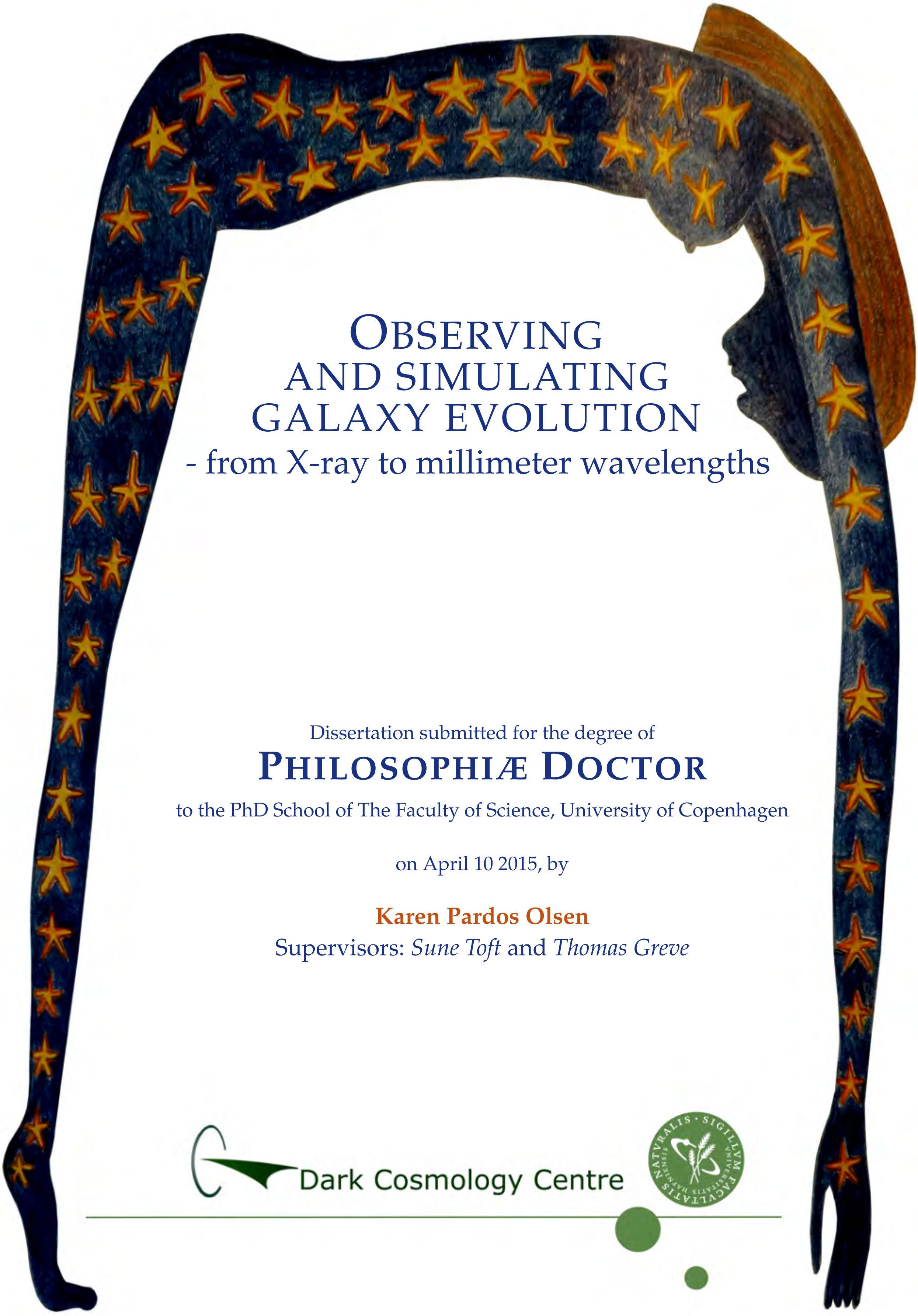

Observing and Simulating Galaxy Evolution

- from X-ray to millimeter wavelengths

Dissertation submitted for the degree of

Philosophiæ Doctor

to the PhD School of The Faculty of Science, University of Copenhagen

on April 10 2015, by

Karen Pardos Olsen

Supervisors: *Sune Toft* and *Thomas Greve*

Dark Cosmology Centre

Cover art:

Nut, goddess of the sky in ancient Egyptian religion. Contrary to most other religions, the sky was feminine and her brother, Geb, personified the Earth. At dusk, Nut would swallow the sun god, Ra, who would pass through her belly during the night and be reborn at dawn. Sometimes she was depicted as a cow, but most of the time as a star-covered nude woman arching over, and protecting, the Earth.

OBSERVING AND SIMULATING GALAXY EVOLUTION

- from X-ray to millimeter wavelengths

ABSTRACT

It remains a quest for modern astronomy to answer what main mechanisms set the star formation rate (SFR) of galaxies. Massive galaxies present a good starting point for such a quest due to their relatively easy detection at every redshift. Since stars form out of cold and dense gas, a comprehensive model for galaxy evolution should explain any observed connection between SFR and the amount and properties of the molecular gas of the interstellar medium (ISM). In proposed models of that kind, an active galactic nucleus (AGN) phase is often invoked as the cause for the decrease or cease of star formation. This thesis consists of models and observations of gas and AGNs in massive galaxies at $z \sim 2$, and how they may affect the overall SFR and the subsequent evolutionary trajectory of massive galaxies to $z = 0$.

For an improved understanding of how observed gas emission lines link to the underlying ISM physics, a new code is presented here; SImulator of GAlaxy Millimeter/submillimeter Emission (`SÍGAME`). By post-processing the outputs of cosmological simulations of galaxy formation with sub-grid physics recipes, `SÍGAME` divides the ISM into different gas phases and derives the density and temperature structure of these, with locally resolved radiation fields. In the **first study**, `SÍGAME` is combined with the radiative transfer code `LIME` to model the spectral line energy distribution (SLED) of CO. A CO SLED close to that of the Milky Way is found for normal star-forming massive galaxies at $z \sim 2$, but 50% smaller $\alpha_{\rm CO}$ factors, with the latter decreasing towards the center of each model galaxy. In a **second study**, `SÍGAME` is adapted to model the fine-structure line of singly ionized carbon, [CII] at $158\,\mu$m, the most powerful emission line of neutral ISM. Applying `SÍGAME` to the same type of galaxies, most [CII] emission can be traced back to the molecular part of their ISM. The observed $L_{\rm [CII]}$-SFR relation at $z > 0.5$ is reproduced and a similar relation is established on kpc scales for the first time theoretically.

A **third study** uncovers the presence of AGNs among massive galaxies at $z \sim 2$, and sheds light on the AGN-host co-evolution by connecting the fraction and luminosity of AGNs with galaxy properties. By analyzing a large survey in X-ray, AGNs of high and low X-ray luminosity are extracted among massive galaxies at $z \sim 2$ via AGN classification methods, and stacking techniques of non-detections, in X-ray. Consequently, it is found that about every fifth massive galaxy, quenched or not, contain an X-ray luminous AGN. Interestingly, an even higher fraction of low-luminosity AGNs reside in the X-ray undetected galaxies, and preferentially in the quenched ones, lending support to the importance of AGNs in impeding star formation during galaxy evolution.

Contents

1

Background

Do not feel lonely, the entire Universe is inside you. - Rumi[1]

While Europeans were taking their medieval nap, Arabs carried astronomy forward. Not only did they collect and combine the astronomy from e.g. Greece, Egypt and India into one mathematical language, they also made contributions to the Ptolemaic system and created instruments such as celestial globes, astrolabs and large observatories. Their motivation was mostly a practical one of wanting to determine prayer times and the direction to Mecca to high accuracy. But what might the Arabs have thought for themselves while looking up at the stars? While this will remain unknown, we now know that most of that tinkling in the sky comes from our home, the Milky Way. Stars in the Milky Way are organized in a slowly rotating disk of spiral arms, embraced by an additional spheroidal component, the bulge. If you are lucky, you can even see a diffuse and 'milky' band, which is the combined light from millions of unresolved stars in this disk. What you can't see with your naked eye, is all the gas and dust out of which new stars are born. Nor can you see the dark matter, emitting no light at all and believed to inhabit a large sphere embracing the Milky Way entirely. We call such an assembly of baryonic and dark matter a galaxy, and the Universe is full of them. Understanding how these galaxies form and evolve while making room for us[2], is one of the fundamental aims of modern astronomy. This thesis is about the gas and the black hole component in galaxies. A theoretical model is developed to simulate the amount and state of gas in galaxies as well as its emission. A separate study uncovers the fraction of massive galaxies dominated by the powerful energetics created by their central black hole, during an important cosmic epoch. Together, these projects offer a better view of galaxy evolution and will be useful for predicting and interpreting future observations.

1.0.1 Setting the scale

The finite speed of light is of great value to astronomers, because it allows us to look back in time. In fact, astronomical distances, both within and between galaxies, are measured in light years (ly; the distance light can travel in 1 year) or parsecs ($1\,\mathrm{pc} = 3.26\,\mathrm{ly}$). On top of that, the expansion of the Universe causes light to 'stretch' as it traverses the great expanses between galaxies. The amount of 'stretching' serves as a label on every photon, saying how far it has been traveling. We call this 'the redshift of light', z, and often use it as a measure of

[1] Persian poet and Sufi mystic of the 13th century
[2] In at least one case

distance from us or age of the Universe. Fig. 1.1 provides a quick callibration between age of the Universe and redshift.

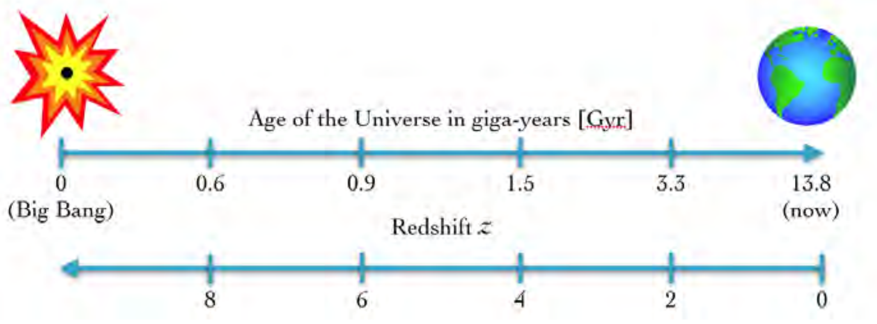

Figure 1.1 A scale comparing age of the Universe with redshift, across its total lifespan of $\sim$ 13.8 Gyr. Note that the redshift drops with age in a exponential-like behaviour, meaning that the Universe reached half its age at quite low redshift, $z \approx 0.7$. Photons decoupled from matter at $z = 1{,}100$, only $\sim$ 378,000 yr after the Big Bang, and that is as far back as we can observe. The ages have been calculated according to the now generally accepted spatially flat ΛCDM cosmology model, that describes the composition of the Universe with just six parameters (fixed here to the most recent results by the Planck Collaboration et al., 2015).

1.0.2 The cosmic web of galaxies

Galaxies are not evenly distributed in space, but rather follow the underlying cosmic web of dark matter that attracts the gas via gravitation. Fig. 1.2 is a map carried out by Colless et al. (2001) of galaxies close to the MW and out to $z \approx 0.3$ over a total sky area of 2000 deg^2 or almost 5 % of the total sky. Like a Swiss cheese, there are regions with very low density of galaxies (so-called voids) and other regions with many galaxies living close together (clusters) connected by filaments and sheets. It has been confirmed by observations, that in the latter, highly concentrated regions, galaxies are prone to interact and possibly merge into even bigger ones. Galaxies are therefore not isolated systems that go about their own business, but are constantly influenced by their surroundings via e.g. mergers, tidal strippings and gas inflow from the Intra Cluster Medium (ICM). In some of the following sections we will describe their internal components and inner workings, treating them as isolated systems, but one should never forget that galaxies in general interact with their surroundings.

1.1 'Normal star-forming galaxies'

Galaxies come in a great variety from containing few stars (dwarf galaxies) to containing many stars (massive galaxies), from compact to extended, from star-forming to inactive (quiescent in the following) and with different compositions of stars, gas, dust and dark matter. That said, most of them follow a basic rule: The more stars they have, the more stars they form. In other words, plotted in a star formation rate (SFR) vs. stellar mass (M_*) diagram, most galaxies fall on a power law relation called the 'main sequence' (MS). The evolution of this sequence with cosmic time has been investigated recently by Speagle et al. (2014) who compiled 25 studies from the existing literature to find that the MS evolves towards higher SFR as we look back in time. This is shown in Fig. 1.3 with best fits to the observations at different redshifts, without plotting individual galaxies for the sake of simplicity.

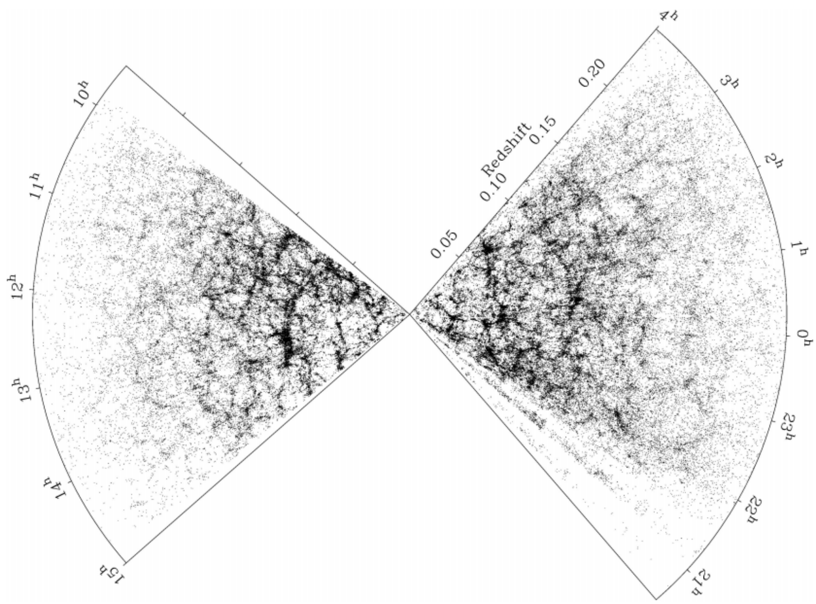

Figure 1.2 Map of galaxies around us and out to $z \approx 0.3$ from the 2dF Galaxy Redshift Survey by (Colless et al., 2001) who studied two strips on the sky, one in the northern (left) and one in the southern (right) hemisphere.

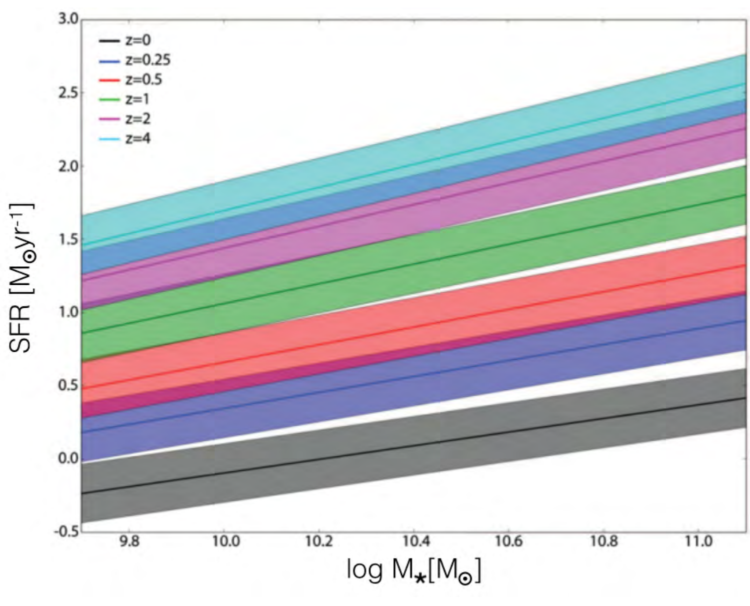

Figure 1.3 Main sequence evolution. Power law fits to star-forming galaxies in different redshift bins from the compilation study of Speagle et al. (2014). Shaded areas show an estimated 'true' scatter of 0.2 dex.

Hence, like in crazy adolescent years, back in the day galaxies used to produce stars at much higher rates. The slope of the SFR-M_* relations shown in Fig. 1.3 is also called the specific star formation rate, SSFR $=$ SFR$/M_*$, and with very few galaxies at high-redshift, it is still hard to say whether the SSFR continues to rise with redshift or reaches a 'plateau' (Behroozi et al., 2013; Speagle et al., 2014).

1.1.1 THE TURNING POINT AT $z \sim 2$

If one measures SFR per volume, there is a maximum in cosmic SFR density, SFRD, at $z \sim 2$ after which it starts to decline again as shown in Fig. 1.4. The epoch around $z \sim 2$, or about 10 billion years ago, is therefore an interesting one of phase change and one that we are just now beginning to uncover with modern telescopes (see Section 1.5).

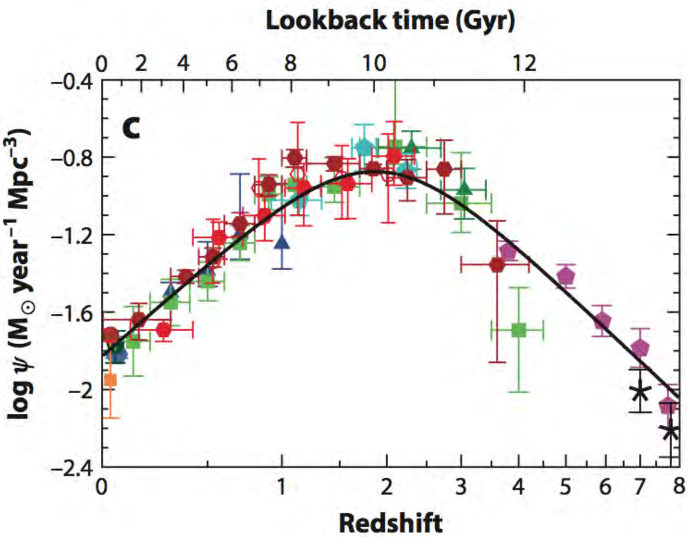

Figure 1.4 The evolution of cosmic SFR density (SFRD) with redshift from the review of Madau & Dickinson (2014).

1.1.2 THE CASE OF 'MASSIVE GALAXIES'

To understand how galaxies evolved since their formation some million years after the Big Bang, we need observations of all types of galaxies from high redshift until now. This task is impeded by the difficulty of resolving a galaxy very far away, because galaxies start to appear very dim and small. The degree at which a large survey (such as the 2dF Survey in Fig. 1.2) is capturing all galaxies of a certain mass, is referred to as 'completeness'. The state-of-the-art Cosmic Assembly Near-IR Deep Extragalactic Legacy Survey (CANDELS), carried out with the Hubble Space Telescope (HST), looks all the way back to the high-redshift universe ($z \sim 8$) with observations of different exposure time (depth). But even in the deep fields of GOODS-South/North, a typical lower mass limit of $10^{10}\,\mathrm{M}_\odot$ must be adopted to ensure $100\,\%$ completeness for studies going out to $z \sim 2.5$ (see e.g. Wuyts et al., 2012). In the smaller Ultra Deep Fields (UDFs), CANDELS can reach the same mass out to $z \sim 3$ due to longer exposure times[3] (Hartley et al., 2013). But galaxies with stellar masses below these limits may exist that these surveys are incapable of detecting with available telescopes and integration time. For this reason, massive (i.e. with high stellar mass) galaxies represent a convenient sample, because

[3]see `http://candels.ucolick.org/survey/files/ferguson_STUC1102_v2.pdf`

they are relatively easy to detect at all redshifts. My work concerns mainly massive galaxies, so this denomination will occur frequently in the present dissertation and the exact mass range will always be defined for each particular study.

1.2 THE INTERSTELLAR MEDIUM (ISM)

Let's return for a moment to the sparkling stars that you may observe on a clear night. What you can't see with your naked eye is all the material filling out the vast spaces in between those stars, the Interstellar Medium or ISM. But it is out of this mixture of gas and dust that stars are born, the stars that expel heavier elements during their explosive deaths, thereby providing the universe with the atoms that we are ultimately made of. Carl Sagan once said that *'we are made of starstuff'*, yet stars would never have been formed had it not been for the gas that was already there. Fig. 1.5 shows an example of what surprises lie in wait once telescopes are tuned to the frequencies at which the gas lights up in the ISM. The blue image is made of stellar light emission from the Antennae Galaxies – two colliding spiral galaxies about 70 million ly away from us – and the red image is a composite of observations with the interferometric array ALMA (to be described in section 1.5).

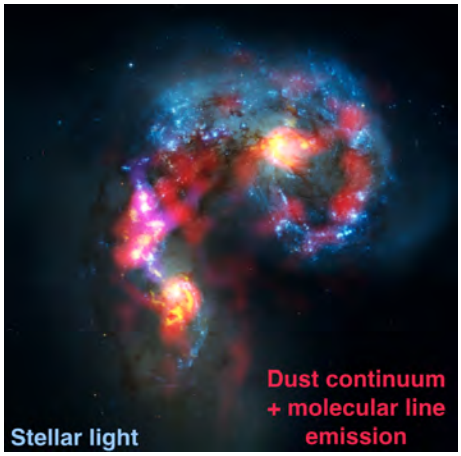

Figure 1.5 The Antennae Galaxies, credit: NASA/ESA HST for the optical image, and ALMA (ESO/NAOJ/NRAO) first science results for the observations of gas and dust at sub-mm wavelengths.

Whether a cloud of gas in a galaxy can fragment and collapse to a density that allows fusion, i.e. the ignition of a new star, depends on the properties of that gas. The efficiency by which the gas forms stars is characterised by the gas depletion time, $t_{\rm dep}$:

$$t_{\rm dep} = m_{\rm gas}/{\rm SFR} \tag{1.1}$$

that is, the time it would take to use up a cloud of mass $m_{\rm gas}$ if the current SFR stayed constant. Naively, one might expect that $t_{\rm dep}$ would be close to the time it takes a cloud to collapse onto itself under the influence of gravity only, also called the free-fall time, $t_{\rm ff}$. But observations show that $t_{\rm dep}$ is typically 1-3 orders of magnitude longer than $t_{\rm ff}$, requiring the existence of processes that slow down the star formation rate resulting from pure gravitation. These processes are broadly gathered under the term 'feedback' from either nearby star formation (see review by Krumholz et al., 2014) or the powerful radiation from an Active Galactic Nucleus (see Section 1.3).

Feedback on star formation is a whole topic in itself under fierce exploration with observations and theoretical models. An example of one strong type of feedback, is the ionizing field from young stars. Stars of masses $> 10\,{\rm M}_*$ emit large quantities of ionizing photons creating large bubbles of expanding hot, ionized gas, that can hit nearby cold clouds and prevent them from collapsing in a type of explosive feedback (Krumholz et al., 2014; Dale et al., 2012).

However, recent simulations by Dale et al. (2012) show that the effect of expanding regions of ionized gas in turbulent clouds depends strongly on the escape velocities in the gas. Fig. 1.6 illustrates, with snapshots from their simulations, how photoionization only has a significant impact in clouds of escape velocities, as set by the cloud mass and size, below about $10\,\mathrm{km\,s^{-1}}$. This example shows that feedback from star formation involves many intercoupled processes. Other types of stellar feedback include those of protostellar outflows, radiation pressure from massive stars, winds from hot stars, supernovae explosions and the mere thermal energy injected into the gas as gravitational potential energy is released during the collapse. In addition, nature most likely combines these mechanisms with the influence of magnetic fields (e.g. Price & Bate, 2009).

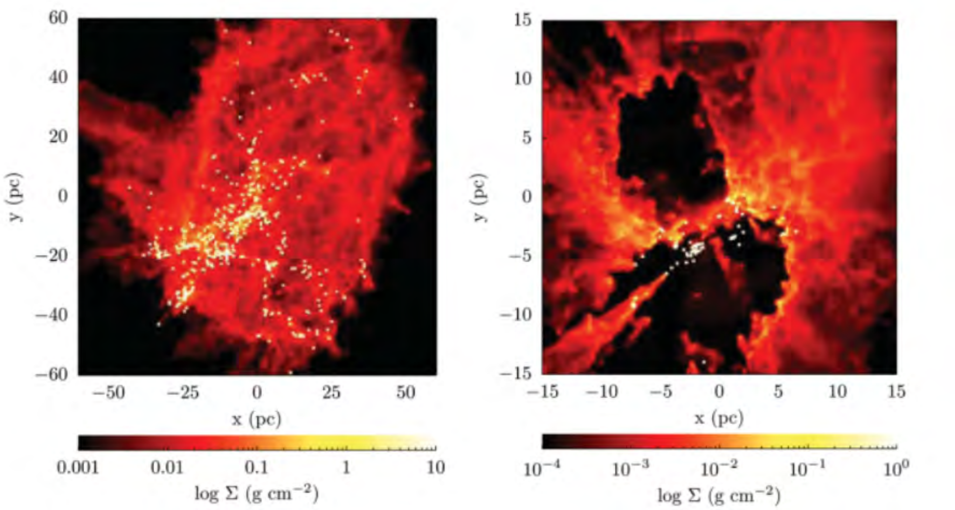

Figure 1.6 *Left:* Column density map of a simulation of star cluster formation in a gas cloud with escape velocity $> 10\,\mathrm{km\,s^{-1}}$. White dots represent individual stars. *Right:* The same but for an escape velocity of $< 10\,\mathrm{km\,s^{-1}}$, in which case star formation is supressed. Adapted from Krumholz et al. (2014).

In principle, being able to observe the composition, turbulence, temperature, density and magnetic fields of the same gas cloud to high angular precision, would provide the building blocks for uniquely defining star formation on small ($< 50\,$pc) scales. Therefore, *being able to characterise the gas in terms of these properties will help explain why some massive galaxies at $z \sim 2$ are quiescent while others are even more star-forming than their local counterparts.*

1.2.1 Chemical composition

Before galaxies formed, the universe was pervaded by a primordial gas of only 4 atomic species; hydrogen (H), helium (He) and a trace of lithium (Li) and beryllium (Be), as well as a few of their isotopes. These were created from about 10 seconds to 20 minutes after the Big Bang[4], but any elements heavier than Lithium and Beryllium had to wait for the formation of the first stars a few hundreds of million years later, in order to be produced. Today, hydrogen and helium continue to be the dominant species found in the local ISM of the MW, with gas mass fractions

[4]see `http://www.astro.ucla.edu/~wright/BBNS.html`

of $\sim 71.5\,\%$ and $\sim 27.1\,\%$ respectively, compared to only $1.4\,\%$ of heavier elements denoted 'metals' (e.g. Przybilla et al., 2008).

All atoms in the ISM can exist in atomic form or be ionized to several degrees or be combined in molecules of increasing complexity (see Tielens 2013 for an overview of just how complicated these molecules can get). For the general life of a galaxy however, only a subset of these species needs to be considered for the structure and thermal state of the ISM relevant for star formation, as we shall see in the next subsections.

1.2.2 Distribution and density

Stars form generally in clusters as the simulated one depicted in Fig. 1.6 (Krumholz et al., 2014). Such constructions of dense knots and long filaments are collectively called Giant Molecular Clouds (GMCs) and are observed to have radii from about 5 to $\sim 100\,$pc in the MW and local galaxies (Blitz et al., 2007). From measuring the broadening of emission lines from the gas and converting those into velocity dispersions, one can get an estimate of the mass, by assuming the cloud to be in virial equilibirum (Roman-Duval et al., 2010):

$$M_{\rm vir} = \frac{1.3{\sigma_{\rm v}}^2 R}{G} \;\Rightarrow\; M_{\rm vir}[{\rm M}_\odot] = 905 \cdot (\sigma_{v,1D}[{\rm km\ s^{-1}}])^2 \cdot R[{\rm pc}] \tag{1.2}$$

This was done by for example Blitz et al. (2007), who found the mass spectrum shown to the left in Fig. 1.7, the data of which can be fitted with a power law of slope -1.71 in the outer MW.

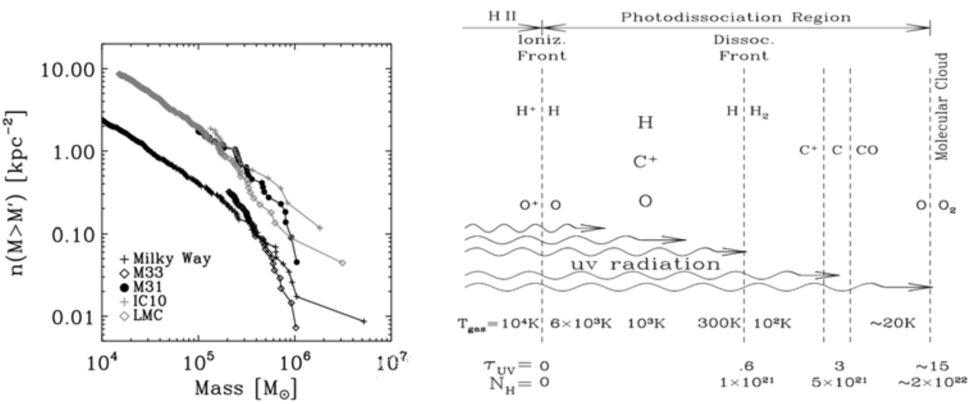

Figure 1.7 *Left:* Mass spectrum of GMCs in the MW and local galaxies (Blitz et al., 2007). *Right:* Schematic overview of the chemical stratification taking place in the PDR of a GMC, from Papadopoulos & Thi (2013).

The reason why all gas in the galaxy is not neutral and forming molecules, is mainly the strong far-ultraviolet (FUV) radiation field from young stars, which ionizes the gas and creates a stratification of the ISM as illustrated on the right-hand side of Fig. 1.7. The region of stratified layers is also referred to as the Photodissociation Region (PDR). In addition to ionizing, the FUV radiation penetrates into the gas and determines its thermal and chemical state. This results in a set of distinct phases of the ISM, that have been observationally identified and are listed in Table 1.1. After the dense, molecular gas, comes the warm and cold neutral medium, often collectively named 'WCNM', and finally, the least dense, ionized gas (HII).

If we take a look at the densities listed in Table 1.1, it is clear that the ISM is in general *very*

Chemical state	Gas phase	n [cm^{-3}]	T_k [K]
Molecular gas	Diffuse H_2	~ 100	~ 50
(17% of total mass)	Dense H_2	$10^3 - 10^6$	$10 - 50$
Atomic gas	Warm HI (WNM)	~ 0.6	~ 5000
(60% of total mass)	Cold HI (CNM)	30	~ 100
Ionized gas	Coronal gas (HIM)	0.004	$10^{5.5}$
(23% of total mass)	HII gas	$0.3 - 10^4$	10^4

Table 1.1 Gas mass fractions, densities and temperatures of the different phases of interstellar gas, adapted from Draine (2011).

diffuse. You would need a cube of $700 \times 700 \times 700$ meters of the densest H_2 gas phase (with density $n_\mathrm{H} \sim 10^6\,\mathrm{cm}^{-3}$) in order to have the same gas mass as present in $1\,\mathrm{cm}^3$ of air at sea level on Earth (with density $\rho \approx 1.2\,\mathrm{kg\,m}^{-3}$).

Gas mass and SFR are related via the Kennicutt-Schmidt (KS) law, which is an observed tight relation between surface density of SFR, Σ_SFR, and gas, Σ_gas. As will be explained in further detail in Part I, the line emission from the CO molecule is particularly well suited for estimating the total gas mass. The KS-law for low and high-z star-forming galaxies was estimated by Genzel et al. (2010) using a large data base of CO line observations and SFRs based on several SFR indicators:

$$\log \Sigma_\mathrm{SFR}\,[\mathrm{M}_\odot\,\mathrm{yr}^{-1}\,\mathrm{kpc}^{-2}] = 1.17 \times \log \Sigma_\mathrm{gas}\,[\mathrm{M}_\odot\,\mathrm{pc}^{-2}] - 3.48 \tag{1.3}$$

However, recent observations show that this correlation might break down already on scales of $\sim 100\,\mathrm{pc}$ (Xu et al., 2015).

1.2.3 THERMAL STATE

The thermal state of the ISM is complicated by the fact that the ISM is never in thermodynamic equilibrium, but rather always subject to a flow of energy. It is constantly being heated, primarily by FUV radiation from young stars, while radiating away the heat via dust emission in the infrared and (mostly FIR) gas emission lines (see Section 1.4 for more on the spectrum of a galaxy). To derive the gas kinetic temperature, T_k, one must therefore consider all relevant heating and cooling mechanisms, calculate their energy rates and search for an equilibrium temperature.

Out in the hot, ionized HII regions (see Table 1.1), gas is heated by photo-ionization of HI gas. FUV photons ionize the hydrogen atoms and the free electrons convert their kinetic energy to heat via collisions with other gas particles. Cosmic rays are very energetic protons, most likely produced in supernovae (Ackermann et al., 2013), and they represent a second radiation field that can heat the gas and penetrate even further into it than FUV photons due to their high energies ($\sim$GeV). Like FUV photons, cosmic rays can ionize the atomic gas and release electrons with kinetic energy, but cosmic rays can also interact with the free electrons, transferring kinetic energy directly via Coulomb interactions.

As for cooling, the gas has several options. First of all, emission lines from hydrogen and heavier elements, in their atomic and ionized states, can remove a great deal of energy, especially at $T_\mathrm{k} > 10^4\,\mathrm{K}$. The cooling rates as function of T_k for the most important elements are shown in Fig. 1.8. The sudden rise in cooling rate at $T_\mathrm{k} \sim 10^4\,\mathrm{K}$ makes sure that the temperature of the HII gas hardly ever exceeds 10^4 K.

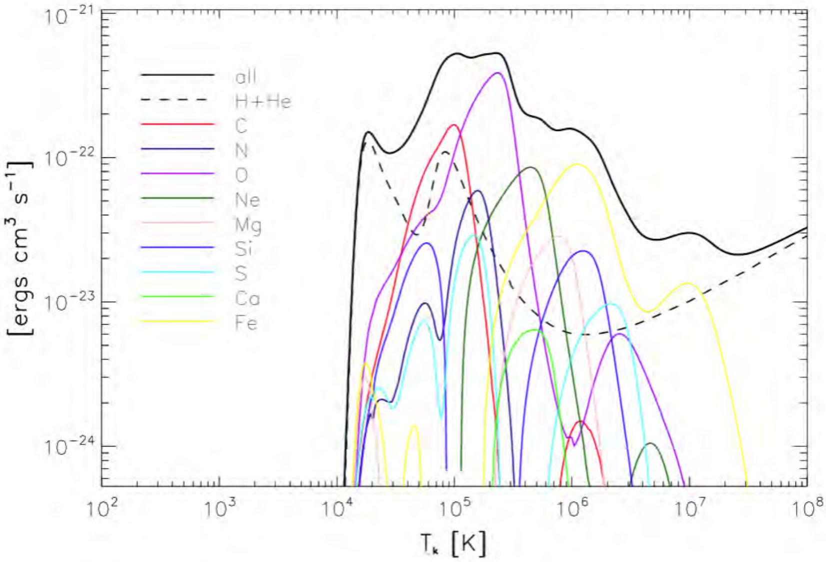

Figure 1.8 Cooling rates of all (black) and individual atoms and ions in the hot ISM as function of temperature. Made with the publicly available code of Wiersma et al. (2009) which takes $T_{\rm k}$ and $n_{\rm H}$ as well as abundances as input.

In addition to these emission lines, electron recombination with ions can cool the gas, as recombining electrons take away kinetic energy from the plasma, a process which is important at temperatures $> 10^3$ K (Wolfire et al., 2003). At similar high temperatures another important cooling mechanism is the scattering of free electrons off of other free ions, whereby free-free emission removes energy from the gas (Draine, 2011).

Combining all of the above heating and cooling mechanisms, we arrive at one equation that describes the balance between the energy rates of heating and cooling:

$$\Gamma_{\rm PI} + \Gamma_{\rm CR,HI} = \Lambda_{\rm ions+atoms} + \Lambda_{\rm rec} + \Lambda_{\rm f-f} \tag{1.4}$$

where $\Gamma_{\rm PI}$ and $\Gamma_{\rm CR,HI}$ are the heating rates for photo-ionization and cosmic ray ionization, respectively, whereas $\Lambda_{\rm ions+atoms}$ is the combined cooling rate from the elements shown in Fig. 1.8. Finally, $\Lambda_{\rm rec}$ and $\Lambda_{\rm f-f}$ are the cooling rates due to recombination and free-free interactions as described above.

In the denser and colder ($T_{\rm k} < 10^4$ K) WCNM, other heating and cooling mechanisms take over. Rather than photo-ionizing the gas, FUV photons now heat the gas more efficiently via the photo-electric effect consisting of a FUV photon knocking loose an electron from the surface of a dust grain, with the same net result: The escaping electron can deposit its kinetic energy as heat in the surrounding gas. The dominating cooling mechanisms in neutral gas are fine-structure line emission from ioinised carbon, [CII], to be discussed in more detail in Section **??** and Part I, and from neutral atomic oxygen, [OI], leading to the following energy rate equation:

$$\Gamma_{\rm PE} + \Gamma_{\rm CR,HI} = \Lambda_{\rm CII} + \Lambda_{\rm OI} \tag{1.5}$$

where $\Gamma_{\rm PE}$ is the heating rate due to the photo-electric effect on dust grains, $\Lambda_{\rm CII}$ is the cooling rate due to [CII] line emission and $\Lambda_{\rm OI}$ is the cooling rate due to [OI] line emission.

In molecular gas, most of the FUV radiation will be attenuated by dust and self-shielding molecules, leaving in some cases cosmic rays as the dominant source of heating. Indeed, it has been suggested that cosmic rays control the initial conditions for star formation in regions of high SFR density where the sites for star formation might be completely UV-shielded (Papadopoulos et al., 2011; Papadopoulos & Thi, 2013). The prescription for cosmic ray heating per hydrogen atom in molecular gas is in principle different from its form in neutral gas, but the two turn out to be very similar (Stahler & Palla, 2005). At increasingly higher temperature, [CII] line cooling gives way for CO line cooling, and at very high densities ($> 10^4\,\mathrm{cm}^{-3}$), cooling by interactions between gas and dust particles can become dominating, as the gas approaches the dust temperature. In molecular gas, line cooling from molecular hydrogen and atomic carbon also contributes to the cooling rate with typically smaller amounts. Summarized in one equation, the thermal equilibrium in molecular gas can hence be approximated by:

$$\Gamma_{\rm PE} + \Gamma_{\rm CR,H_2} = \Lambda_{\rm H_2} + \Lambda_{\rm CO} + \Lambda_{\rm OI} + \Lambda_{\rm CII} + \Lambda_{\rm gas-dust} \tag{1.6}$$

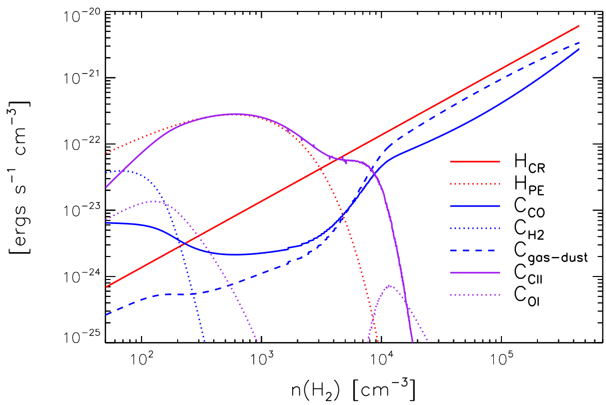

Figure 1.9 Heating and cooling rates in molecular gas. The energy rates shown are calculated at the equilibrium temperature for that density. Calculated for a GMC of mass $m_{\rm GMC} = 10^4\,\mathrm{M}_\odot$, solar metallicity, an interstellar FUV field of 16 Habing units and a cosmic ray ionization rate of $8 \times 10^{-16}\,\mathrm{s}^{-1}$. In the outskirts (low density) of the cloud, [CII] line cooling and photo-electric heating dominate, while in the inner regions (high density), gas-dust cooling and CR heating take over. Made with the `SÍGAME` code (to be described in Part I).

Fig. 1.9 gives an example of the dominant heating and cooling mechanisms mentioned above as functions of density for the interior of a model GMC of mass $m_{\rm GMC} = 10^4\,\mathrm{M}_\odot$ and solar metallicity, immersed in an interstellar FUV field of 16 Habing units and a cosmic ray ionization rate of $8 \times 10^{-16}\,\mathrm{s}^{-1}$.

1.3 The Active Galactic Nucleus (AGN)

Apart from the gas, dust, stars and dark matter that I mentioned in the beginning of this introduction, there is a fifth component in the MW: black holes. A particularly big one or 'supermassive black hole' (SMBH) is hiding at the very center of the MW, and most likely every galaxy, as it became clear in the 90's (Magorrian et al., 1998).

The strong gravitational pull from a SMBH creates a rotating accretion disk of matter (yellow part in Fig. 1.10) from its host galaxy. As gravitational energy is converted into mechanical and electromagnetic energy, gas in the accretion disk is heated to very high temperatures and starts to radiate fiercefully over a broad range of energies, from radio to X-ray (see Krawczynski & Treister, 2013, for a review of the inner workings of these central engines).

Galaxies in which the spectra are dominated by this type of central energy source, are called Active Galactic Nuclei (AGNs). Observationally, AGNs have been classified into two main groups; (Seyfert) type I and type II based on the width of their optical emission lines. Type I AGNs show strong broad emission lines, while type II AGNs have relatively narrow emission lines and softer X-ray emission. In some cases, relativistic jets are produced perpendicularly to the accretion disk and their strong synchroton radiation in radio has led to the classification 'radio-loud' AGNs. AGNs for which the optical light from the host galaxy is outshined by the central disk itself are dubbed quasars (QSOs).

Over the past two decades, observations have led to the Standard Unified Model suggesting that type I and type II AGNs are intrinsically the same class of objects, but viewed from different angles, as pictured in Fig. 1.10 (Bianchi et al., 2012). In this picture, the accretion disk is surrounded by a clumpy torus of gas and dust, and outflow is mainly allowed within the ionisation cone encircling the relativistic jets. A type I AGN is a galaxy inclined so that we see the inner parts of the accretion disk where high orbital speeds result in relatively broad lines. A type II AGN is orientated so that the inner accretion disk is obscured by the clumpy torus and only narrow lines from more distant cold material can be observed.

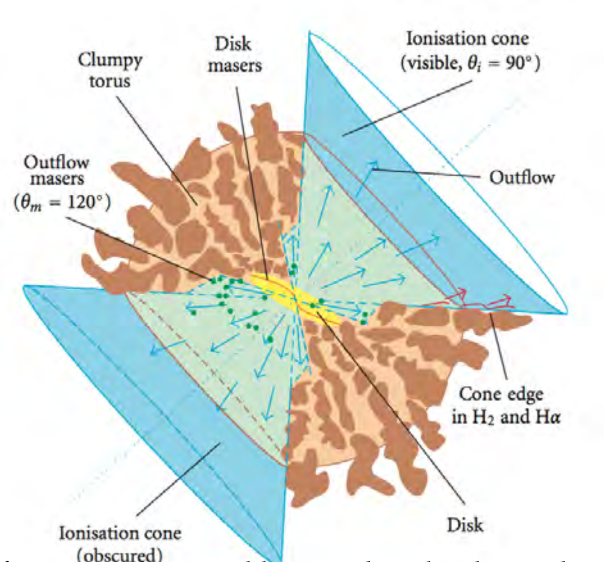

Figure 1.10 Drawing, from the review of (Bianchi et al., 2012), of the inner engine emitting the strong radiation of an AGN, including the disk (yellow) of matter accreting onto the SMBH, the surrounding clumpy torus (brown) and ionization cones (blue), also containing the relativistic jets.

1.3.1 Observing an AGN in X-ray

A tight correlation between optical and X-ray emission of unobscured quasars suggest that all luminous AGNs are intrinsically also X-ray bright (e.g. Steffen et al., 2006; Gibson et al., 2008). But high amounts of obscuring gas and dust in the torus and elsewhere in the host galaxy can decrease the X-ray luminosity or change the spectral slope of the X-ray emission that actually escapes the galaxy, to be discussed further in Section 1.3. Alternative sources for strong X-ray emission in a galaxy are High-Mass X-ray Binary systems (HMXBs), which may be significant in case of high SFR (Ranalli et al., 2003), and halos of hot gas (Mulchaey & Jeltema, 2010).

1.4 The 'spectral fingerprint' of a galaxy

The best way to measure the conditions of gas in the ISM is by taking a 'spectral fingerprint'. Fig. 1.11 is a cartoon version of the spectral energy distribution (SED) of a galaxy if we were able to measure its emission from the smallest wavelengths (x-ray) to the longest ($\sim 1\,\mathrm{cm}$) of interest for the ISM. Furthermore, the SED is shown in the 'rest frame' of the galaxy rather than in the observers frame, in which the SED would be red-shifted to longer wavelengths if the galaxy happened to be at high redshift. The unit is Jansky ($= \mathrm{Jy} = 10^{-26}\,\frac{\mathrm{W}}{\mathrm{m^2 \cdot Hz}}$) which is a typical flux unit in radio astronomy. The SED shown in Fig. 1.11 is that of a typical star-forming spiral galaxy, taken from the publicly available SED templates of Kirkpatrick et al. (2012), with an additional imaginative X-ray flux measurement corresponding to an X-ray luminosity of $L_{0.5-8\,\mathrm{keV}} = 10^{44}\,\mathrm{ergs/s}$.

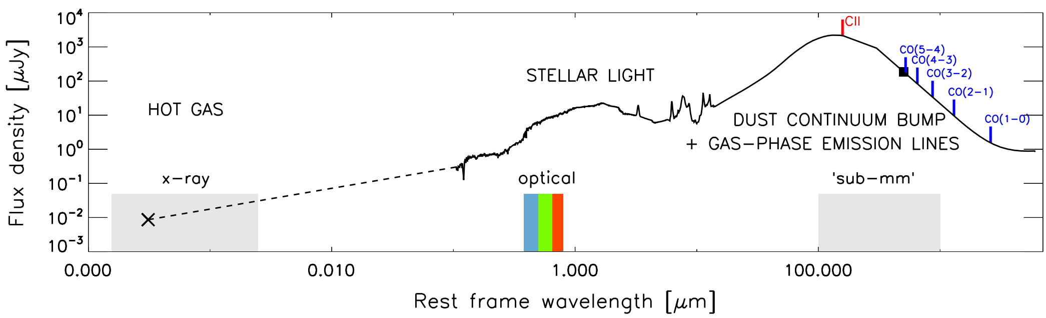

Figure 1.11 The SED of a typical star-forming galaxy at $z = 0$ with indications of the different components contributing to its shape. Also shown are the positions of some important emission lines from the gas, to be described in Part I. The flux has been scaled to the observed $500\,\mu\mathrm{m}$ luminosity of local galaxies for a mass of $10^{10}\,\mathrm{M_\odot}$ as marked with a black square (Groves et al., 2015). SED template of Kirkpatrick et al. (2012): `http://www.astro.umass.edu/~pope/Kirkpatrick2012/`.

First noticeable are the two 'bumps' at wavelengths around $1\,\mu\mathrm{m}$ and $100\,\mu\mathrm{m}$. The first one is dominated by direct stellar light at ultraviolet (UV) to near-infrared (NIR) wavelengths. The UV light is mainly produced by young massive stars recently formed and therefore traces the current SFR well, since massive stars have relatively short lifetimes. On the other hand, the NIR flux is primarily consisting of light from old, less massive stars, making NIR luminosity a good tracer of total stellar mass. Good estimates of SFR and M_* can be made simultaneously by fitting the entire SED with stellar population synthesis models, typically only requiring assumptions about the initial mass function (IMF) of stars as they are born, the SFR history and the metallicity. For example, the SFRs in Fig. 1.4 were created assuming a Salpeter IMF (Salpeter, 1955).

The second bump is caused by dust that absorbs light at many wavelengths, but it is a particularly powerful absorber of far-ultraviolet (FUV; $\sim$ 100-200 nm) radiation, which is re-emitted again in the infrared (IR; $\sim$ 1-1000 μm), thus 'reprocessing' the emitted starlight. The shape of the dust 'bump' can most of the time be approximated by a combination of a modified blackbody (a 'greybody'), fixed at the temperature of the dust, and a power law in the mid-infrared (MIR) as described in detail by Casey (2012) and shown with an example in Fig. 1.12. On top of the dust peak a few important gas emission lines are shown, namely the CO (blue) and [CII] (red) lines, that will be described in detail in Part I.

In order to analyze the gas component of a galaxy, there are basically two relevant regimes

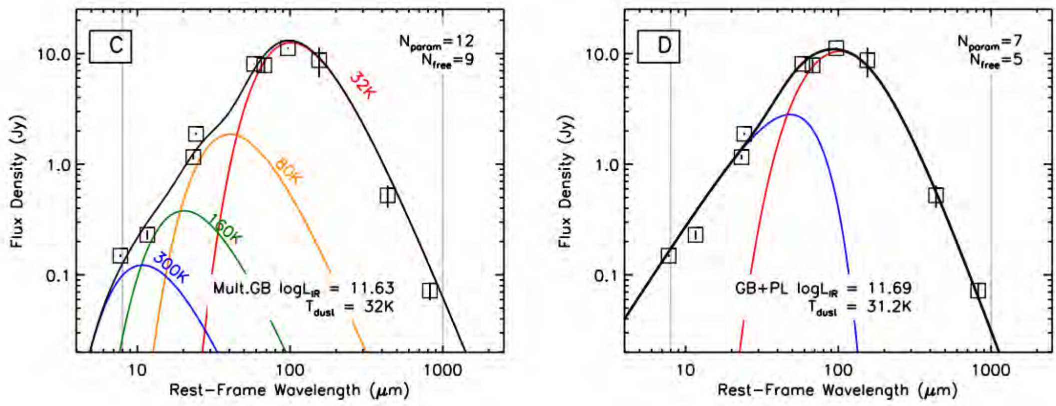

Figure 1.12 Examples of how the spectra in MIR to FIR, caused by dust in a galaxy, can be approximated by either several 'greybodies' of different dust temperature (left) or one greybody combined with a power law at high energies (right). Adapted from Casey (2012) who presented the latter, simplified FIR SED fitting technique.

in wavelength, both of which are indicated with grey areas in the figure:
X-ray regime: Thermal emission from galactic and extra-galactic hot, ionized gas.
Sub-mm regime: Gas emission lines from colder, more neutral gas.
This thesis implements observational and theoretical techniques in both of these regimes, as will be summarized in Section 2.2.

1.5 An exciting time for observations

Facilities for observing gas and dust in galaxies accross cosmic time are experiencing a true revolution, that is gradually opening our eyes towards normal galaxies at high redshifts. Here, I will briefly go through the most important radio and X-ray telescopes in use or preparation.

1.5.1 Radio Telescopes

Probably the most impressive effort in this regard has been the Atacama Large Millimeter Array (ALMA), even if still under contruction. For an idea of its capabilities already in 2011 when the first scientific observations with ALMA began, see the image in Fig. 1.5 made with only 12 antennas. When completed, ALMA will comprise 50 antennas of 12 metres in diameter, acting as a single telescope and with a very high spatial resolution thanks to the art of interferometry. An additional 4 12-m and 12 7-m antennas will create a compact array in the centre. Together, the 66 antennas (each weighing $>$ 100 tons!) can be moved with special designed vehicles into different configurations with maximum antenna distances from 150 m to an astonishing 16 km.

Figure 1.13 A photo of 19 ALMA antennas as they stood ready for the ALMA Early Science cycle. The array is located on the Chajnantor Plateu at 5000 m above sea level in Atacama desert of northern Chile. Credit: ALMA (ESO/NAOJ/NRAO)/W. Garnier (ALMA).

A more extended configuration corresponds to a higher spatial resolution, but also a lower sensitivity towards larger (more extended) sources on the sky, a trade-off that must be considered when planning observations. With bands of high spectral resolution from 312 μm to 3.56 mm (and 2 extra bands going down to about 7.4 mm possibly added in the future), ALMA will be able to detect [CII] and CO lines in a normal galaxy at $z = 3$ in a matter of hours. For the next cycle of observations (Cycle 3, starting in October 2015), ALMA is anticipated to encompass a total of 48 antennas with most receiver bands available.

In the Northern Hemisphere, The NOrthern Extended Millimeter Array (NOEMA[5], former PdBI) will be, upon completion in 2019, the facility in the Northen Hemisphere that comes closest to the capabilities of ALMA, with bands for observing in the 808 μm-3.7 mm range. At longer wavelengths, the Jansky Very Large Array (JVLA) is currently the superior radio interferometer, covering from 0.6 to 30 cm with 27 antennas of diameter 25 m (Napier, 2006). A number of single-dish radio telescopes can also target gas and dust emission at high redshifts; the LMT, IRAM-30m, GBT, Onsala 20+25m, ARO, NMA and APEX to name a few.

An overview of ALMA, EVLA and NOEMA is intended with Fig. 1.14, comparing the position of their frequency bands with the SED (including [CII] and CO lines) of a typical star-forming galaxy at $z = 2$.

The James Webb Space Telescope (JWST), scheduled to launch in 2018, will be an improved version of the famous Hubble Space Telescope (HST, expected to stay in operation until 2020), covering 0.6 to 28 μm with the same resolution in NIR as HST has in the optical.

[5] http://www.iram.fr/IRAMFR/GILDAS/doc/html/noema-intro-html/noema-intro.html

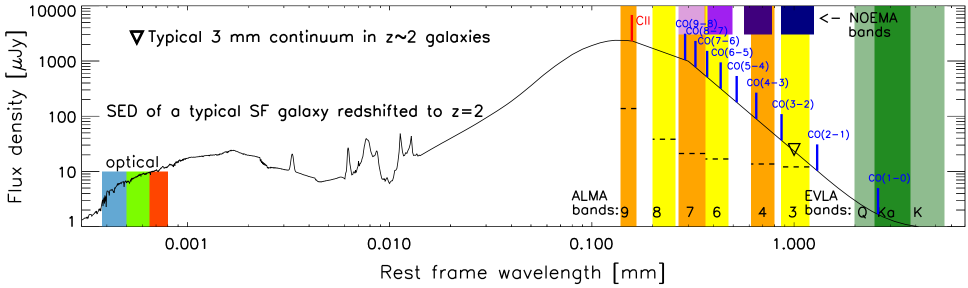

Figure 1.14 The star-forming galaxy SED also used in Fig. **??**, with the frequency bands of some of the worlds best radio interferometers shown in color. The SED has been scaled to 30 μJy at 3 mm, corresponding to typical massive disk galaxies at $z \sim 2$ (Dannerbauer et al., 2009). The dashed lines in the ALMA bands correspond to 3σ after 5 hrs integration time with the full ALMA.

Between the long wavelength range of EVLA/ALMA and the shorter of JWST, ground-based observations are hampered by atmospheric absorption, but new space missions are awaiting approval for adventuring into the MIR 28-312 μm regime. FIRSPEX is a satellite mission to continue the success of the Herschel Space Observatory (*Herschel*), that ran out of fuel in 2013. The primary goal of FIRSPEX is to carry out a wide survey of the MW in [CII], [NII], [CI] and CO$(6-5)$[6], possibly detecting nearby galaxies as well that are redshifted into these bands. SPICA is a similar mission, of ~ 2 orders of magnitude higher sensitivity in the FIR than *Herschel* and wavelength coverage from 5 to $\sim 210\,\mu$m (Goicoechea & Nakagawa, 2011).

1.5.2 X-ray Telescopes

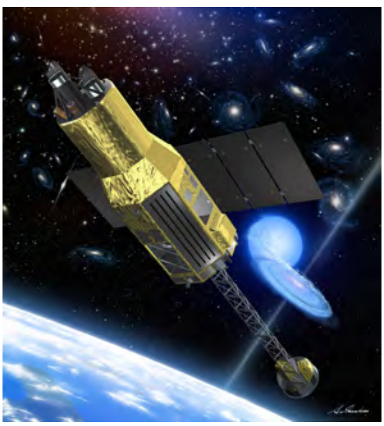

Figure 1.15 An illustration of the upcoming ASTRO-H when in orbit at an altitude of about 5-600 km. From the mission home page: `http://astro-h.isas.jaxa.jp/en/`.

To observe an AGN in X-ray, one has to escape the obscuring atmosphere of the Earth, which has led to many space missions since the beginnings of the 1980's.

The *Chandra* X-ray $(0.1-10\,\text{keV})$ observatory has been in orbit around the Earth since 1999, and has dedicated 2 and 4 Ms to observing the *Chandra* Deep Field North and South respectively (CDF-N and CDF-S). The large covering areas of roughly $450\,\text{arcmin}^2$ for each have proven ideal for detecting AGNs at redshifts $z \approx 0.1 - 5.2$ (Bauer et al., 2004; Xue et al., 2011). Similar missions, though of lower spatial resolution, include the XMM-Newton, ROSAT and Suzaku. At higher energies, the nuclear spectroscopic telescope array Nustar has been observing from space at $3-79\,\text{keV}$ since 2012.

The ASTRO-H mission (see Fig. 1.15) is the latest in a long row of Japanese X-ray satellites, though ASTRO-H is being developed in a collaboration between Japanese (ISAS/JAXA) and US (NASA/GSFC) institutions. It will among other things investigate the X-ray reflection signatures of AGN, with increased sensitivity for the soft X-rays as compared to *Chandra*

[6]FIRSPEX webpage: `http://astroweb1.physics.ox.ac.uk/~dar/FIR/firspex4.html`

(Reynolds et al., 2014). Astrosat is India's first dedicated astronomy satellite and has the advantage of allowing simultaneous multi-wavelength observations at UV and X-ray wavelengths. It will have two bands for detecting X-rays (3-80 keV and 10-150 keV), and a large effective area in the hard X-ray band to facilitate studies of highly variable sources such as AGN (Paul, 2013).

1.6 Galaxy simulations

With so many coupled mechanisms in a galaxy on scales from sub-parsecs to kilo-parsecs, the advantage of running numerical simulations of galaxy evolution has proven tremendous. Galaxy simulations can be roughly divided into two kinds: Cosmological simulations that start out with the small density pertubations of dark matter shortly after the Big Bang, and more idealized disk simulations that start out with an analytical density profile for the galaxy and allow gravitational and electromagnetic forces to perturb the galaxy in time. I will focus on the former kind as that is what my theoretical projects build on (see Parts I and II).

The series of images in Fig. 1.16 illustrate how a cosmological simulation works, with snapshots, from high redshift ($z = 4$) and until now ($z = 0$), of the dark matter structures and the resulting gas mass distribution. In the present ΛCDM cosmological model, dark matter formed structures (or 'minihalos') before baryonic gas could cool and collapse. Cosmological simulations therefore focus on modeling an underlying dark matter structure (left-hand side of Fig. 1.16) at the same time as the baryonic component of the universe is allowed to condense in these structures via gravity, dissipation and radiation (right-hand side of Fig. 1.16). As the universe ages, filaments and knots in the dark matter density distribution become more pronounced and infalling gas cools enough to form stars and galaxies in regions of high concentration.

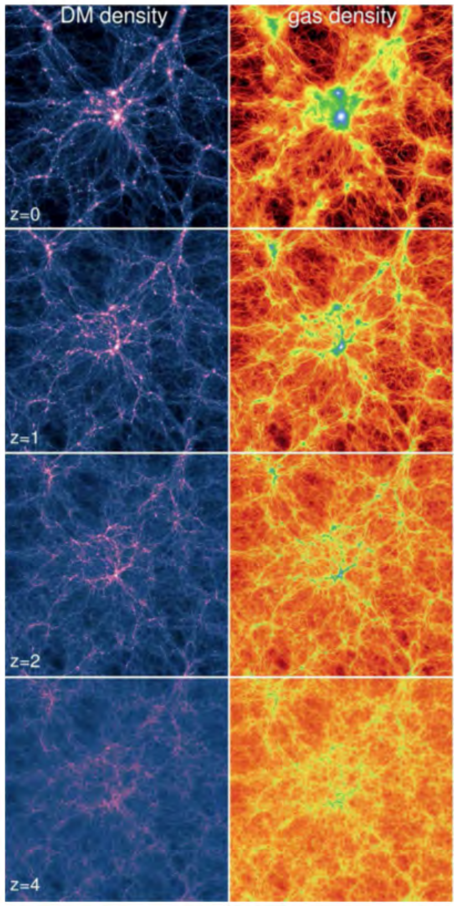

Figure 1.16 106.5 Mpc wide on each side, column density maps are shown of simulated dark matter (left) and gas column densities (right) from $z = 4$ until now (bottom to top). Brightest colors in the column density plot correspond to a density of $\sim 10^4\,\mathrm{M_\odot/kpc^3}$. The images are from the Illustris Project – one of the most comprehensive cosmological hydrodynamical simulations of galaxy formation to date (Vogelsberger et al., 2014). The recently developed moving-mesh code `AREPO` (Springel, 2010) was used to follow DM and gas dynamics.

The universe is then believed to have proceeded via hierarchical structure formation, in which small gravitationally bound structures, such as stars and galaxies, form first, followed by groups, clusters and superclusters of galaxies, not to mention the cosmic web in between them (c.f. Fig 1.2).

It was soon realized though, that these large-scale simulations with resolutions going down to kpc-scales, could not capture the actual physics inside galaxies, where the most important processes take place on $< 1\,\mathrm{pc}$ scales. In particular, simulations on smaller scales proved that localized feedback is needed in order to avoid overpredicting the star formation rate and to agree with the observed IMF of star clusters (Tasker, 2011; Krumholz et al., 2011; Hopkins et al., 2011). Made possible by an increasing computing power and technology, cosmological galaxy simulations have seen two big 'revolutions' since their beginning in the early 90's as illustrated in Fig. 1.17, of which we are in the middle of the last one, the 'zoom-in' simulations.

1.6.1 'Zoom-in' simulations

The concept behind 'zoom-in' simulations is to select a galaxy at low redshift in a cosmological simulation of low resolution ($\gtrsim 1\,\mathrm{kpc}$), and trace the particles (or cells) comprising it back in time to the beginning of the simulation. A re-simulation is then initiated with much higher resolution, but only following the particles/cells that end up in the galaxy of interest. This re-simulation may take days or months, but provides the opportunity to follow star formation on realistic scales, while staying in agreement with the overall large scale structure. Two computational techniques exist for treating the gas hydrodynamically at the necessary resolution:
Smoothed Particle Hydrodynamic (SPH) simulations: The gas is represented by particles with properties such as mass, density and temperature in addition to a smoothing kernel that roughly speaking smears the particles out across a volume in space. Resolution is increased simply by increasing the number of particles while reducing their mass in order to keep mass conservation.
Adaptive Mesh Refinement (AMR) simulations: The gas is divided into cells that can be subdivided in areas where higher resolution is needed. All interactions between gas cells take place as mass/temperature/pressure exchange through the cell partition walls.

Examples of SPH codes include GADGET and GASOLINE, whereas ART, ENZO and RAMSES are AMR codes. Kim et al. (2014) presented, with the AGORA project, a comparison of these in terms of resolution, physics of the ISM, feedback and galactic outflows. But see also Springel (2010) for a novel combination of the two methods.

1.6.2 The callibration to $z = 0$

While the initial conditions for galaxy formation and evolution are relatively strict, by e.g. measurements of the Cosmic Microwave Background (CMB), and the final endpoint is anchored with $z = 0$ observations, what goes on in between is less well-defined by observations. Common tests for the evaluation of a cosmological simulation focus on how well it can reproduce the observed main sequence and luminosity functions at low- to high-z. Although simulations on the whole agree with observations, a discrepancy still persists at the time of maximum cosmic star formation ($1 \lesssim z \lesssim 3$), where the simulated main sequence is a factor $\sim 2-3$ below the observed one (e.g. Furlong et al., 2014). Possible explanations include an IMF that changes with redshift and galaxy properties (rather than staying fixed to the locally observed one as most simulations assume), or feedback from stellar winds, supernovae and AGN that is not properly accounted for in simulations (e.g. Davé, 2008; Narayanan & Davé, 2012; Sparre et al., 2015). Until more resolved observations of ISM at $z \gtrsim 2$ are obtained, simulations of galaxy evolution are forced to make, and be inhibitted by, extrapolations to high-z of local ISM physics and star-formation laws. Some of these restrictions will be discussed in Part I.

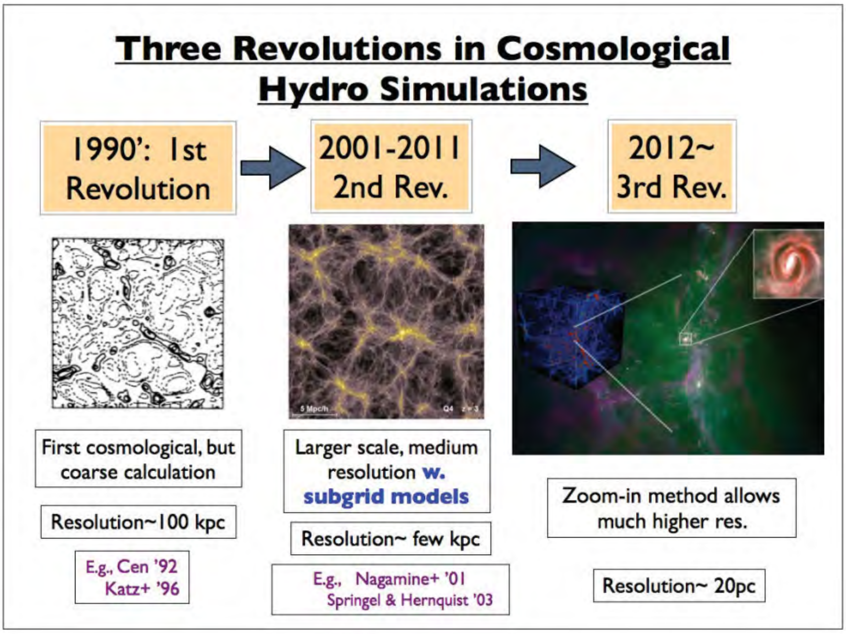

Figure 1.17 Schematic overview of the history of cosmological galaxy simulations and their improvements over the past two decades, with references, as presented in the review by Nagamine (2014).

1.7 References

Ackermann, M., Ajello, M., Allafort, A., et al. 2013, Science, 339, 807
Bauer, F. E., Alexander, D. M., Brandt, W. N., et al. 2004, AJ, 128, 2048
Behroozi, P. S., Wechsler, R. H., & Conroy, C. 2013, ApJ, 770, 57
Bianchi, S., Maiolino, R., & Risaliti, G. 2012, Advances in Astronomy, 2012, 17
Blitz, L., Fukui, Y., Kawamura, A., et al. 2007, Protostars and Planets V, 81
Casey, C. M. 2012, MNRAS, 425, 3094
Colless, M., Dalton, G., Maddox, S., et al. 2001, MNRAS, 328, 1039
Dale, J. E., Ercolano, B., & Bonnell, I. A. 2012, MNRAS, 424, 377
Dannerbauer, H., Daddi, E., Riechers, D. A., et al. 2009, ApJL, 698, L178
Davé, R. 2008, MNRAS, 385, 147
Draine, B. T. 2011, Physics of the Interstellar and Intergalactic Medium
Furlong, M., Bower, R. G., Theuns, T., et al. 2014, ArXiv e-prints
Genzel, R., Tacconi, L. J., Gracia-Carpio, J., et al. 2010, MNRAS, 407, 2091
Gibson, R. R., Brandt, W. N., & Schneider, D. P. 2008, ApJ, 685, 773
Goicoechea, J. R., & Nakagawa, T. 2011, in EAS Publications Series, Vol. 52, EAS Publications Series, ed. M. Röllig, R. Simon, V. Ossenkopf, & J. Stutzki, 253–258
Groves, B. A., Schinnerer, E., Leroy, A., et al. 2015, ApJ, 799, 96
Hartley, W. G., Almaini, O., Mortlock, A., et al. 2013, MNRAS, 431, 3045
Hopkins, P. F., Quataert, E., & Murray, N. 2011, MNRAS, 417, 950
Kim, J.-h., Abel, T., Agertz, O., et al. 2014, ApJS, 210, 14
Kirkpatrick, A., Pope, A., Alexander, D. M., et al. 2012, ApJ, 759, 139
Krawczynski, H., & Treister, E. 2013, Frontiers of Physics, 8, 609
Krumholz, M. R., Klein, R. I., & McKee, C. F. 2011, ApJ, 740, 74

Krumholz, M. R., Bate, M. R., Arce, H. G., et al. 2014, Protostars and Planets VI, 243
Madau, P., & Dickinson, M. 2014, ARA&A, 52, 415
Magorrian, J., Tremaine, S., Richstone, D., et al. 1998, AJ, 115, 2285
Mulchaey, J. S., & Jeltema, T. E. 2010, ApJ, 715, L1
Nagamine, K. 2014, in American Institute of Physics Conference Series, Vol. 1594, American Institute of Physics Conference Series, ed. S. Jeong, N. Imai, H. Miyatake, & T. Kajino, 41–45
Napier, P. J. 2006, in Astronomical Society of the Pacific Conference Series, Vol. 356, Revealing the Molecular Universe: One Antenna is Never Enough, ed. D. C. Backer, J. M. Moran, & J. L. Turner, 65
Narayanan, D., & Davé, R. 2012, MNRAS, 423, 3601
Papadopoulos, P. P., & Thi, W.-F. 2013, in Advances in Solid State Physics, Vol. 34, Cosmic Rays in Star-Forming Environments, ed. D. F. Torres & O. Reimer, 41
Papadopoulos, P. P., Thi, W.-F., Miniati, F., & Viti, S. 2011, MNRAS, 414, 1705
Paul, B. 2013, International Journal of Modern Physics D, 22, 41009
Planck Collaboration, Ade, P. A. R., Aghanim, N., et al. 2015, ArXiv e-prints
Price, D. J., & Bate, M. R. 2009, MNRAS, 398, 33
Przybilla, N., Nieva, M.-F., & Butler, K. 2008, ApJ, 688, L103
Ranalli, P., Comastri, A., & Setti, G. 2003, A&A, 399, 39
Reynolds, C., Ueda, Y., Awaki, H., et al. 2014, ArXiv e-prints
Roman-Duval, J., Jackson, J. M., Heyer, M., Rathborne, J., & Simon, R. 2010, ApJ, 723, 492
Salpeter, E. E. 1955, ApJ, 121, 161
Sparre, M., Hayward, C. C., Springel, V., et al. 2015, MNRAS, 447, 3548
Speagle, J. S., Steinhardt, C. L., Capak, P. L., & Silverman, J. D. 2014, ApJS, 214, 15
Springel, V. 2010, MNRAS, 401, 791
Stahler, S. W., & Palla, F. 2005, The Formation of Stars (Wiley)
Steffen, A. T., Strateva, I., Brandt, W. N., et al. 2006, AJ, 131, 2826
Tasker, E. J. 2011, ApJ, 730, 11
Tielens, A. G. G. M. 2013, Reviews of Modern Physics, 85, 1021
Vogelsberger, M., Genel, S., Springel, V., et al. 2014, MNRAS, 444, 1518
Wiersma, R. P. C., Schaye, J., & Smith, B. D. 2009, MNRAS, 393, 99
Wolfire, M. G., McKee, C. F., Hollenbach, D., & Tielens, A. G. G. M. 2003, ApJ, 587, 278
Wuyts, S., Förster Schreiber, N. M., Genzel, R., et al. 2012, ApJ, 753, 114
Xu, C. K., Cao, C., Lu, N., et al. 2015, ApJ, 799, 11
Xue, Y. Q., Luo, B., Brandt, W. N., et al. 2011, ApJS, 195, 10

2

INTRODUCTION TO THIS THESIS

2.1 EVOLUTION OF MASSIVE GALAXIES ACROSS COSMIC TIME

With the previous brief description of the internal composition of galaxies and the observational and theoretical tools used for characterising them, we are now ready to take a look at the populations of massive galaxies so far uncovered and the current status on creating a consistent picture for their evolution with cosmic time.

2.1.1 HIGH-REDSHIFT MASSIVE GALAXY POPULATIONS

An important fact to bear in mind when studying galaxy evolution, is that we are never observing *the same* galaxy at various epochs in the life of the universe. At each redshift, the most we can do is observe galaxies in a snapshot of their lifetime, and often any evolutionary connection between galaxies observed at different redshifts is hampered by different selection techniques and incompleteness (we cannot detect all galaxies at every redshift, cf. Section 1.1.2).

The ideal way of classifying galaxies at all redshifts would be to measure their entire SED (like the one shown in Fig. 1.11) via spectroscopy. But since this would be very time-consuming, clever methods have been developed to first select a candidate group of the galaxies that might be of interest, and then perform high-resolution spectroscopy on these. Such methods typically build on photometry – measuring the total flux through a limited set of photometric bands by applying filters that only allow certain ranges in wavelength. For selecting galaxies of a certain mass, the K-band (centered on $2.2\,\mu$m in the NIR) is particularly useful since it captures light from primarily old stellar populations that dominate the mass budget of most galaxies. Therefore, a lower cut in K-band luminosity directly translates into a minimum stellar mass Cimatti (2003). Follow-up spectroscopy can then determine the redshift, stellar mass and SFR to higher precision with SED fitting methods (see Man et al., 2012; Cimatti et al., 2004, for applications of this method). This method works out to $z \sim 4$ where the K-band starts to trace rest-frame UV light, which unlike NIR or optical, is dominated by the strong radiation from young stars, and is therefore a tracer of the amount of current star formation rather than stellar mass.

At $z \gtrsim 3$, another way to classify galaxies is typically via their current amount of star formation. This star formation can be either un-obscured, as revealed in rest-frame UV, or – in galaxies of high dust amount – obscured resulting in high FIR luminosities (dust continuum 'bump' in Fig. 1.11), or a combination of the two. Two examples of the first approach are the

Lyman Break Galaxies (LBGs) and BzK-selected galaxies, whereas the second approach has revealed a group of very dusty galaxies, the Sub-mm Galaxies (SMGs) or nowadays, Dusty Star-forming Galaxies (DSFGs; Casey et al., 2014).

LBGs are selected to have a strong break and reduced flux at the wavelength $< \lambda = 912\,\text{Å}$This break is caused by neutral hydrogen gas residing inside the galaxy and in the Inter Galactic Medium (IGM), absorbing light at wavelengths below $912\,\text{Å}$, the threshold for ionizing hydrogen. The LBG technique requires that the galaxy be UV bright (relatively star-forming) and not dust-obscured (Steidel et al., 2003). The advantage of the LBG technique is that it makes a preselection of not only SFR but also redshift, by restricting the location of the break. Carilli et al. (2008) used a method called 'stacking' (see application of this in X-ray in Part II), to find that LBGs at $z \sim 3$ have SFRs of $31 \pm 7\,\mathrm{M}_{\odot}\ \mathrm{yr}^{-1}$, that is, not very high on the MS at that redshift (c.f. Fig. 1.3).

The BzK-selection takes advantage of absorption in stellar atmospheres creating a strong break at $\sim 4000\,\text{Å}$ so that three photometric bands (B, z and K) can effectively be used to select galaxies at $1.4 \lesssim z \lesssim 2.5$ and roughly estimate their SFR (Daddi et al., 2004). Similar groups of color-selected galaxies are those of 'BX' and 'BM' galaxies, selected via their color in the three UV and optical filters U_n, G and $\mathcal{R}$ (Adelberger et al., 2004; Steidel et al., 2004). The color criteria for 'BX' galaxies restricts them to lie at $2.0 \leq z \leq 2.5$, while the 'BM' galaxies lie at $1.5 \leq z \leq 2.0$. Both techniques give rise to slightly higher SFRs than the BzK-selection would, as shown by Reddy et al. (2005) using X-ray inferred bolometric SFRs.

SMGs on the other hand, are selected for having a strong rest-frame NIR emission, and were first detected with the ground-based instrument SCUBA at 850 μm (e.g. Smail et al., 1997; Hughes et al., 1998; Barger et al., 1999), soon followed by surveys including the use of instruments such as MAMBO at 1.2 mm and AzTEC at 1.1 mm (Coppin et al., 2005; Chapman et al., 2005; Greve et al., 2008; Perera et al., 2008). The advantage of looking in the rest-frame $1-3$ mm wavelength range at high redshift, is that the flux stays roughly the same owing to the effect of 'negative K-correction' as illustrated in Fig. 2.1. Due to this effect, SMGs have been identified mainly at $z \sim 2$ but with a tail extending up to $z \sim 5$ (Chapman et al., 2005; Wardlow et al., 2011; Simpson et al., 2014). Converting the high IR luminosities to dust-obscured SFRs, implies SFRs of $\sim 100 - 1000\,\mathrm{M}_{\odot}\ \mathrm{yr}^{-1}$ (Karim et al., 2013). For the most part, SMGs display disturbed stellar morpohologies and/or kinematics as compared to normal non-interacting rotating disks, suggesting recent or ongoing merger events (e.g. Conselice et al., 2003; Chen et al., 2015). The disturbed signatures are backed up by molecular emission line observations of clumps of dense and highly star-forming gas in SMGs (e.g. Tacconi et al., 2008; Riechers et al., 2011; Hodge et al., 2012).

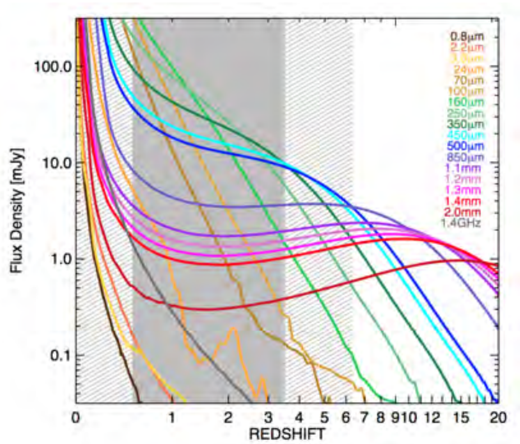

Figure 2.1 Observed flux densities for a typical dusty, star-forming galaxy as presented in the review by Casey et al. (2014). Note the nearly-constant flux density in the ~ 1 mm bands accross $1 \lesssim z \lesssim 10$ redshift range.

2.1.2 OBSERVING GALAXIES AT $z > 4$ VIA THEIR GAS EMISSION LINES

In the early ($z > 4$) universe, very few normal star-forming galaxies have so far been detected, typically via the LBG technique (see Behroozi et al., 2013, for a compilation), and even fewer quiescent galaxies have been discovered at $z \gtrsim 2.5$, with the most distant ones at $z \sim 3$ (Gobat et al., 2012; Fan et al., 2013). Only one galaxy at $z > 7$ has so far had its redshift determined from spectroscopy of its stellar continuum. But the galaxy A1689-zD1 at $z = 7.5 \pm 0.2$, has now been detected in dust emission with ALMA resulting in a combined (UV+IR) SFR of $\sim 12\,\mathrm{M}_\odot\,\mathrm{yr}^{-1}$ (Watson et al., 2015), i.e. a normal star-forming galaxy. In addition to dust continuum, ALMA can also detect line emission from the gas, thereby determining redshifts and characterizing the ISM at the same time for normal star-forming galaxies (see more on this in the Outlook section of Part I). An example of such an emission line, is [CII] from singly ionized carbon, which is expected to be the most luminous cooling line in neutral gas. We return with a more detailed description of [CII] in Chapter 6, but mention here that at $z \sim$ 5-7, the [CII] line falls in bands 6-7 of ALMA, currently the most sensitive millimeter interferometer by an order of magnitude, and therefore a promising tool for detecting [CII] in normal star-forming galaxies at $z \sim 6$. Indeed, it has been detected in and around normal star-forming galaxies at $z \sim 5 - 7$ (Maiolino et al., 2015; Capak et al., 2015). *Our only way of characterizing the ISM of high-z galaxies might very well be to observe emission lines from the gas.*

2.1.3 THE RED AND DEAD

The local galaxy population is bimodal in terms of UV-to-optical color, with a distinct group of blue, star-forming galaxies and another of red, quiescent galaxies (Strateva et al., 2001; Schawinski et al., 2014). This is shown with color-mass diagrams in Fig. 2.2 for low redshift galaxies. The connection between color and star formation activity is a result of younger stars having relatively bluer colors than old stars, which emit their light predominantly at longer (optical and NIR) wavelengths. Historically, the red and blue galaxies are also called 'early' and 'late'-type galaxies from the morphological classification of Hubble (1926). In general, late type galaxies display stellar disks with spiral arms and exponential light profiles whereas the stellar light from early-type galaxies (or sometimes named ellipticals) is more concentrated with even structures and no clear sign of spiral arms. But detailed observations or their stellar populations have later shown that this naming makes sense, since the nearby red galaxies most likely formed much earlier than the blue ones (e.g. Kartaltepe et al., 2014), although that does not imply an evolutionary link between the two in itself. As always, dust plays an important role and can make star-forming galaxies appear red by absorbing the blue light and re-emitting it in the FIR. Indeed Sodré et al. (2013) showed that some local galaxies with extremely red colors, are reddened by dust more than by older (redder) stellar populations. But the diagrams in Fig. 2.2 have been corrected for reddening by dust, by measuring the dust extinction in optical light.

In between the red and the blue group, lies the 'green valley' with very few galaxies. There is a discussion about how many of these green galaxies are actually late-type galaxies being quenched (Pan et al., 2013; Schawinski et al., 2007) and how many are early-type galaxies with star formation initiated recently in a sort of 'rejuvenation' (Fang et al., 2012). In the context of the MS introduced in Section 1.1, the blue galaxies lie on the MS relation, while the red galaxies lie below and at high stellar mass.

By now, the division into quiescent or star-forming has been observationally confirmed out to $z \sim 3$, (Kriek et al., 2008; Williams et al., 2009; Viero et al., 2013; Man et al., 2014), but that

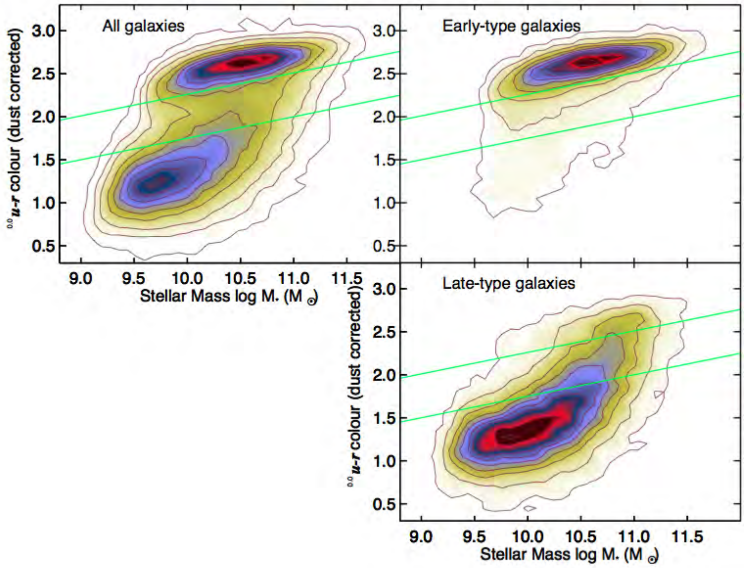

Figure 2.2 The UV-optical color bimodality of $0.02 < z < 0.05$ galaxies, as measured by Schawinski et al. (2014) using the SDSS+*GALEX*+Galaxy Zoo data. The '0.0' in $^{0.0}u$ refers to the K-correction of the observed color to $z = 0$ (see Section 2.1.1). Green lines indicate the 'green valley' in between the two galaxy populations.

still leaves the question: *When did the onset of the red sequence take place and what caused it?*

2.1.4 Quenching star formation

AGNs are one of the preferred hypothesized mechanisms for quenching star formation, as radiation, winds and jets from the central accreting black hole can remove the gas or heat it so that contraction of molecular clouds cannot take place (see Fabian 2012 and McNamara & Nulsen 2007 for a reviews on models and observational evidence). A distinction is made between 'quasar mode', by which feedback from an AGN ejects all gas from the galaxies (Granato et al., 2004), and 'radio mode', during which powerful jets heat the circumgalactic medium to such high temperatures that further accretion of cold gas onto the galaxy is prevented (Croton et al., 2006). Semi-analytical simulations, by e.g. Di Matteo et al. (2005), show how reasonable descriptions of the AGN feedback on star formation in elliptical galaxies can reproduce the observed local mass function.

In addition to quenching by AGNs (possibly ignited by a major merger), the environment in which the galaxy lives is believed to raise further quenching mechanisms. This suspicion came from observations showing that galaxies in clusters are in general more quenched and passive than field galaxies (Verdugo et al., 2008). Similar to AGNs, most of these proposed internal/external mechanisms have to do with the removal, distribution or heating of gas, i.e. the fuel for further star formation. This can happen via galaxy-galaxy interactions or influence by the Intra Cluster Medium (ICM) itself. The following are some of the more popular environmental quenching mechanisms, but see reviews by e.g. Boselli & Gavazzi (2006) and Blanton & Moustakas (2009) for a much more complete overview: i) Harassment, when during close encounters or direct mergers, galaxies alter each others' morphology (Moore et al., 1998); iii) Ram pressure stripping, where galaxies traveling through the ICM at high speed have their

ISM shock-heated and eventually stripped off, ending up in the cluster as seen in observations of individual cases and proposed by several simulations (e.g. Steinhauser et al., 2012; Bösch et al., 2013; Ebeling et al., 2014); ii) Tidal stripping, by which galaxies passing through the ICM feel the global tidal field of their host, significantly altering their morphologies (Villalobos et al., 2014); iv) Cosmological 'starvation' or 'strangulation', when the hot gas halo around a galaxy is removed due to hydrodynamical interactions with the ICM, and further infall of gas is prevented causing the galaxy to slowly run out of fuel on time scales of a few Gyr (Balogh et al., 2000; Bekki et al., 2002; Feldmann & Mayer, 2015); v) Compactness quenching, as suggested by observations of satellites in the outskirts of haloes, that show a strong correlation between quenching and compactness of the galaxy (Woo et al., 2015).

These last types of quenching mechanisms are also referred to collectively as 'satellite quenching', because they primarily happen to satellite galaxies in a cluster. However, it has been hypothesized that satellite quenching and that of AGN (also called 'mass-quenching'), are actually manifestations of the same underlying process (Carollo et al., 2014; Knobel et al., 2015).

2.1.5 CONNECTING THE DOTS

The fact that the red sequence is already in place at $z \sim 2$, means that we have to push even further out in redshift in order to find the onset of this 'dead' population, and with that, hopefully also the 'murder weapon'. In addition, half of the most massive galaxies ($M_* > 10^{11}$ $M_\odot$) at $z \approx 2$ are already compact and quiescent galaxies (CQGs) with old stellar populations (e.g. Toft et al., 2007; van Dokkum et al., 2008; Szomoru et al., 2012). The stellar spectra suggest that major starburst events took place in CQGs some 1-2 Gyr prior to the time of observation, but were quenched by mechanisms either internal or external (or both) to the galaxy (e.g. Gobat et al., 2012; Whitaker et al., 2013; van de Sande et al., 2013). So far, very few have CQGs have been found in the present-day universe (e.g. Trujillo et al., 2009; Taylor et al., 2010), though see also Graham et al. (2015) who suggest that CQGs could be hiding in the local universe as the bulges of spheroidal galaxies having grown an additional (2D) disk over the past 9-11 Gyr.

It is still an open question what kind of galaxy evolution leads to the CQGs observed at $z \sim 2$, and how they increased in size, without increasing their SFR significantly, down to $z \sim 0$, for which a size increase by a factor of $\sim 3-6$ is required [e.g.][]Trujillo et al. (2006); Toft et al. (2007); Szomoru et al. (2012). Basically, three formation scenarios have been put forth:
i) Massive CQGs formed in a monolithic way, assembling most of their mass at $z > 2-3$ and then 'puffed up' (by adiabatic expansion) into the big, red ellipticals we see today (e.g. Bezanson et al., 2009; Damjanov et al., 2009).
ii) A similar scenario to i), but CQGs enhanced their size from $z \sim 2$ to 0 by inside-out growth, most likely due to merging with other small galaxies (minor merging), following a type of hierarchical structure formation like the dark matter (Naab et al., 2009; Oser et al., 2012). The minor merging scenario is in good agreement with the observed metallicity gradients (Kim & Im, 2013) and stellar kinematics (e.g. van de Sande et al., 2013; Arnold et al., 2014) in $z = 0$ quiescent galaxies.
iii) The third possibility, requires a bit more thought. Compared to star-forming galaxies, local quiescent galaxies are more massive at the same SFR but also slightly smaller at the same mass, for redshifts out to $z \sim 2$. This can be seen in Fig. 2.3 which shows the main sequence of galaxies, including the quiescent ones below it, from $z \sim 0$ to $z \sim 2$. The average size of the quiescent population could grow with time simply if recently quenched (larger) star-forming

galaxies are constantly being added to the sample as time moves forward (Trujillo et al., 2012; Poggianti et al., 2013; Krogager et al., 2014, e.g.). This hypothesis also goes under the name 'progenitor bias'. However, Belli et al. (2015) argued that, for at least half of all CQGs at $z = 2$, the increase in size until $z = 1.5$ must have taken place via growth rather than additions of increasingly larger galaxies to the sample.

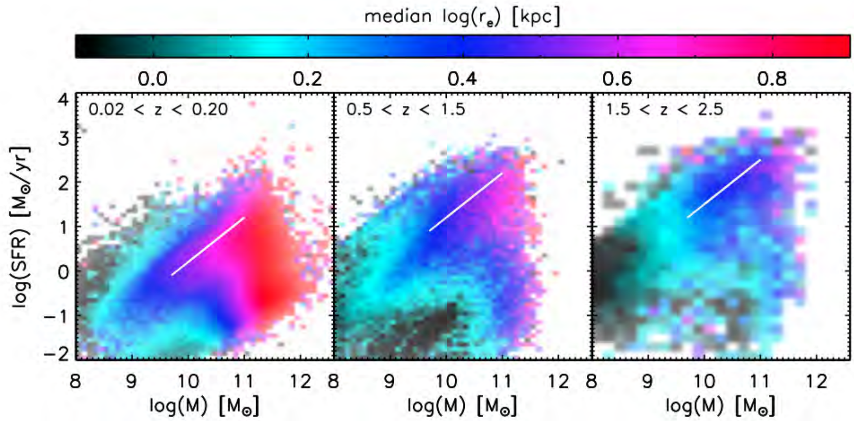

Figure 2.3 Galaxy SFR-mass diagrams in three redshift bins, colorcoded by size which is expressed as a circularized effective radius from fitting a Sérsic profile to the rest frame visible or NIR depending on redshift. From Wuyts et al. (2011), who study galaxies from various large samples, including CANDELS (see Section 1.1.2).

The potential quenching by AGNs has led to the idea of a fast evolutionary path from compact starbursting galaxy at $z \sim 3$ to a galaxy quenched by AGN feedback some $1 - 2$ Gyr later and, via size-growth, to a larger, however still quiescent galaxy at $z = 0$. This is illustrated in Fig. 2.4 as an 'early-track' route (Barro et al., 2013). In addition, Barro et al. (2013) suggest a late-track evolutionary path, by which larger $z \sim 2$ star-forming galaxies slowly turn off star formation between $z = 2$ and $z = 0$, without passing through a compact phase. This idea was expanded upon by Williams et al. (2014), who suggest that massive, compact galaxies take the fast route and quench sooner than the normally-sized LBGs at $z \sim 2 - 3$.

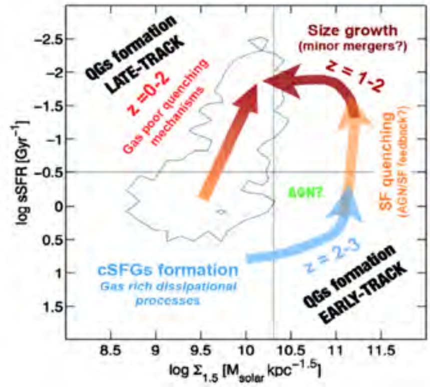

Figure 2.4 Two suggested evolutionary paths from star-forming galaxies at $z = 2 - 3$ to quiescent galaxies at $z = 0$ (Barro et al., 2013).

Galaxy mergers present the kind of violent events that are required for the 'early-track' route. In particular, simulations have shown that gas-rich (wet) mergers can lead to bursts of star formation, but that gas is driven towards the center via dissipation and may ignite an AGN. Wet mergers can increase the stellar mass but leave a more compact remnant, whereas gas-poor (dry) mergers can build up a galaxy in mass and size without altering star formation too much (see Lin et al., 2008, and references therein). In addition, major mergers are those between galaxies of similar mass whereas minor mergers are those in which the stellar masses differ by a factor of at least ~ 4 (Man et al., 2014).

In order to find the actual progenitors (and descendants for that matter) of the CQGs, we have to look outside the MS, consisting of normal galaxies. Fig. 2.5 illustrates an evolutionary sequence connecting $z \gtrsim 3$ SMGs through compact quiescent $z \sim 2$ galaxies to local elliptical ones (Hopkins et al., 2006; Ricciardelli et al., 2010; Toft et al., 2014; Marchesini et al., 2014). Here, gas-rich major mergers in the early universe trigger a short time period (42^{+40}_{29} Myr) of high SFR in the form of a nuclear dust-enshrouded starbursts, that we observe as an SMG. That star formation is subsequently quenched either due to gas exhaustion, feedback from the starburst itself or the ignition of an AGN. What is left behind, is a compact stellar remnant that is observed as a CQG about a Gyr after, at $z \sim 2$. Finally, the CQGs grow gradually, and primarily through minor merging, into the elliptical galaxies that we observe today.

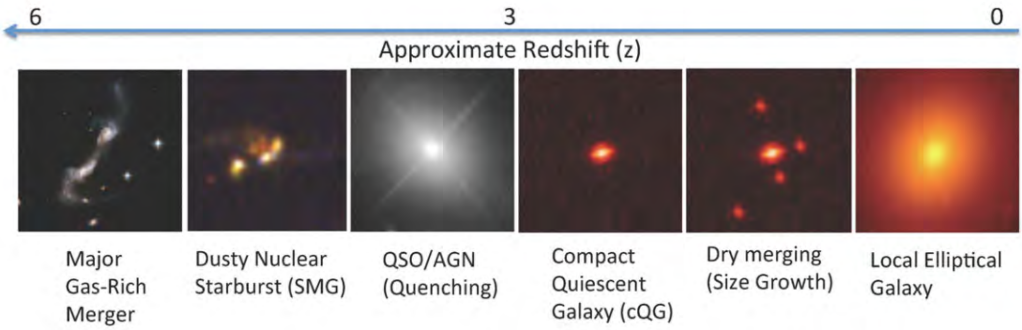

Figure 2.5 The proposed evolutionary sequence by Toft et al. (2014) going from major gas-rich mergers at high redshift (left) to local elliptical quiescent galaxies (right).

But observations of merger rates in massive galaxies at $z \sim 3-0$ show that major and minor merging is not enough to bring the CQGs to the sizes of locally observed early-type galaxies, suggesting that other mechanisms are needed for the size growth (Man et al., 2014). And, as summarized in Section 2.1.4, there are many alternative ways to quench star formation in addition to the powerful feedback of an AGN. *In order to understand evolution of massive galaxies at high redshifts, it is fundamental to find out which of these mechanisms dominate and when.*

2.2 THIS THESIS

In conclusion, we would be much closer to a complete picture of the evolution of massive galaxies, if we could answer the question of how CQGs at $z \sim 2$ quenched their star formation and when. Since gas mass and star formation are so closely entwined, we see that this question translates into:

At what rate did galaxies acquire and use up their gas mass?

2.2.1 ALL EYES ON THE GAS

Most of the above-mentioned mechanisms depend in one way or another on gas amount, as summarized below:

• The gas content together with the amount of in/outflow of gas sets the fuel available for star formation and thereby a 1st order estimate of how long the galaxy can continue producing stars at the current SFR.

• Removal or heating of this gas is what quenches star formation, and is an important milestone in the life of massive galaxies.

• Mergers and the resulting triggering of an AGN, are often invoked as a quenching mechanism, but the outcome of a merger depends critically on how gas-rich the merging galaxies are.

Yet even the most basic knowledge of the gas content, the gas mass fraction defined as $f_{\rm gas} = M_{\rm gas}/(M_{\rm gas} + M_*)$ is unknown at $z \gtrsim 2$. The general consensus is that galaxies at higher redshift were definitely more gas-rich, but the very few observations at $z > 3$ make this statement hard to quantify, as Fig. 2.6 illustrates.

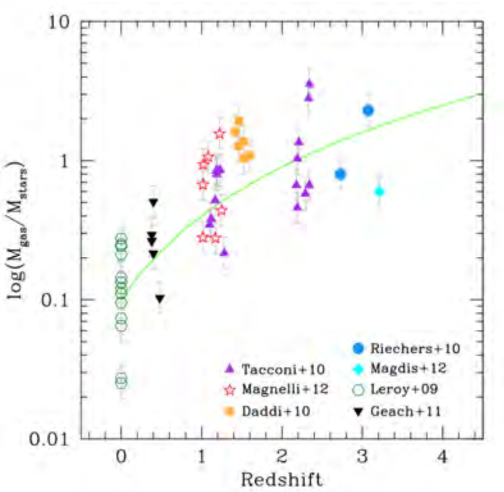

Figure 2.6 Evolution of the gas to stellar mass ratio, $M_{\rm gas}/M_*$, with redshift for star-forming disk galaxies with $M_* > 10^{10}\,M_\odot$ (Carilli & Walter, 2013).

Another topic related to the gas and under current debate, is whether the KS law (introduced in Section 1.2.2) might be different in normal galaxies compared to starburst galaxies or mergers, as shown in Fig. 2.7 (though such conclusions depend critically on how the gas mass is determined, a topic we return to in Part I).

A huge missing piece to the puzzle is therefore knowledge of the gas (and dust) in massive galaxies, especially at $z \gtrsim 2$. The premonition, shared by several research groups, is that future observations of the gas and dust content, morphology and dynamics in high-z MS and quiescent galaxies, will solve the puzzle (Carilli & Walter, 2013; Blain, 2015). As put by Glazebrook (2013): *'...we need to consider the fuel as well as the fire'*. As mentioned in 1.5, it is now possible with radio telescopes such as ALMA, JVLA and NOEMA to access the high-redshift domain where the red sequence must have formed.

To answer the above questions, we not only need to observe the gas at high redshift in more detail, we also need to know how to interpret those observations better.

2.2.2 Quick summary of my projects

I have worked on improving our knowledge of the evolutionary state of massive galaxies at $z = 2$, with regard to 3 aspects:

- Amount and distribution of molecular gas in the ISM
  A key species for studying the gas in the ISM was already introduced in Chapter 1 (Sec-

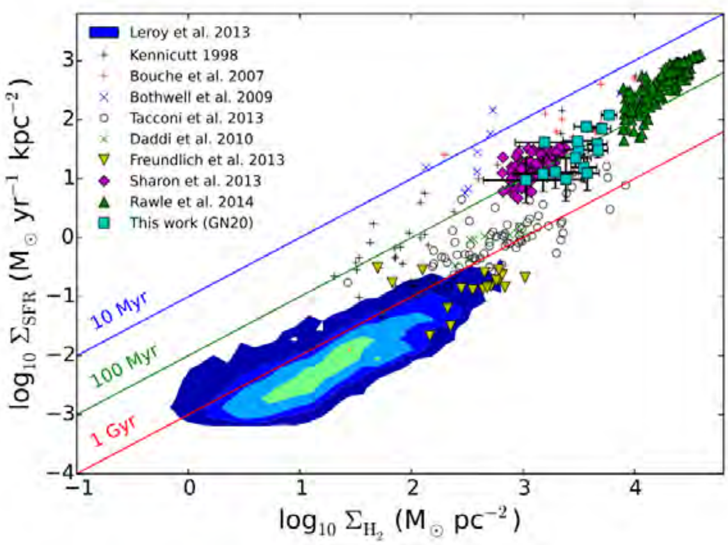

Figure 2.7 The KS law for different galaxy types at high and low redshift from the work of Hodge et al. (2015) who carried out resolved CO(2-1) observations of the $z = 4.05$ SMG GN20, shown with cyan squares. GN20 lies significantly above the relation for local MS galaxies (contours), together with two other strongly lensed, resolved SMGs (magenta diamonds and green triangles), unresolved SMGs (blue crosses and red plus-signs) and local ultraluminous infrared galaxies (ULIRGs; black plus-signs). Close to the local MS galaxies are $z \sim 1.2$ massive star-forming galaxies (yellow upside-down triangles), $z \sim 1-3$ color-selected galaxies (black open circles) and $z \sim 1.5$ BzK galaxies (green crosses). See references for these observations in Hodge et al. (2015).

tion 1.2.2) and will be described in detail in Part I: carbonmonoxide (CO). I used galaxy simulations and developed sub-grid procedures that could be combined with radiative transfer calculations in order to improve predictions for the use of CO lines to estimate the amount and distribution of molecular gas in the ISM of normal star-forming galaxies at $z \sim 2$ (`SÍGAME`, see Part I Chapter 3).

- Tracing SFR on local and global scales
  The line emission of C^+ has been used to trace SFR and various phases of the ISM, including neutral and ionized gas, but it holds many mysteries with its exact origin still unknown. Combining galaxy simulations with sub-grid procedures, I developed a method for modeling [CII] line emission in order to study its origin in the ISM, and make predictions for its use as a star formation tracer at $z \sim 2$ (`SÍGAME`, see Part I Chapter 5).

- Importance of AGNs in massive galaxies at $z \sim 2$
  By analyzing *Chandra* X-ray data from a sample of galaxies at $1.5 \lesssim z \lesssim 2.5$, including the stacked signal from low-luminosity sources, I derive the fraction of luminous and low-luminosity AGNs in star-forming as well as in quiescent massive galaxies (see Part II).

At the beginning of the following chapters some additional background is provided on the specific techniques used in the above listed project, and each chapter will be followed by a list of references.

2.3 References

Adelberger, K. L., Steidel, C. C., Shapley, A. E., et al. 2004, ApJ, 607, 226
Arnold, J. A., Romanowsky, A. J., Brodie, J. P., et al. 2014, ApJ, 791, 80
Balogh, M. L., Navarro, J. F., & Morris, S. L. 2000, ApJ, 540, 113
Barger, A. J., Cowie, L. L., Smail, I., et al. 1999, AJ, 117, 2656
Barro, G., Faber, S. M., Pérez-González, P. G., et al. 2013, ApJ, 765, 104
Behroozi, P. S., Wechsler, R. H., & Conroy, C. 2013, ApJ, 770, 57
Bekki, K., Couch, W. J., & Shioya, Y. 2002, ApJ, 577, 651
Belli, S., Newman, A. B., & Ellis, R. S. 2015, ApJ, 799, 206
Bezanson, R., van Dokkum, P. G., Tal, T., et al. 2009, ApJ, 697, 1290
Blain, A. W. 2015, ArXiv e-prints
Blanton, M. R., & Moustakas, J. 2009, ARA&A, 47, 159
Bösch, B., Böhm, A., Wolf, C., et al. 2013, A&A, 549, A142
Boselli, A., & Gavazzi, G. 2006, PASP, 118, 517
Capak, P. L., Carilli, C., Jones, G., et al. 2015, ArXiv e-prints
Carilli, C. L., & Walter, F. 2013, ARA&A, 51, 105
Carilli, C. L., Lee, N., Capak, P., et al. 2008, ApJ, 689, 883
Carollo, C. M., Cibinel, A., Lilly, S. J., et al. 2014, ArXiv e-prints
Casey, C. M., Narayanan, D., & Cooray, A. 2014, Phys. Rep., 541, 45
Chapman, S. C., Blain, A. W., Smail, I., & Ivison, R. J. 2005, ApJ, 622, 772
Chen, C.-C., Smail, I., Swinbank, A. M., et al. 2015, ApJ, 799, 194
Cimatti, A. 2003, in The Mass of Galaxies at Low and High Redshift, ed. R. Bender & A. Renzini, 124
Cimatti, A., Daddi, E., Renzini, A., et al. 2004, Nature, 430, 184
Conselice, C. J., Chapman, S. C., & Windhorst, R. A. 2003, ApJ, 596, L5
Coppin, K., Halpern, M., Scott, D., Borys, C., & Chapman, S. 2005, MNRAS, 357, 1022
Croton, D. J., Springel, V., White, S. D. M., et al. 2006, MNRAS, 365, 11
Daddi, E., Cimatti, A., Renzini, A., et al. 2004, ApJ, 617, 746
Damjanov, I., McCarthy, P. J., Abraham, R. G., et al. 2009, ApJ, 695, 101
Di Matteo, T., Springel, V., & Hernquist, L. 2005, Nature, 433, 604
Ebeling, H., Stephenson, L. N., & Edge, A. C. 2014, ApJ, 781, L40
Fabian, A. C. 2012, ARA&A, 50, 455
Fan, L., Fang, G., Chen, Y., et al. 2013, ApJ, 771, L40
Fang, J. J., Faber, S. M., Salim, S., Graves, G. J., & Rich, R. M. 2012, ApJ, 761, 23
Feldmann, R., & Mayer, L. 2015, MNRAS, 446, 1939
Glazebrook, K. 2013, in IAU Symposium, Vol. 295, IAU Symposium, ed. D. Thomas, A. Pasquali, & I. Ferreras, 368–375
Gobat, R., Strazzullo, V., Daddi, E., et al. 2012, ApJ, 759, L44
Graham, A. W., Dullo, B. T., & Savorgnan, G. A. D. 2015, ArXiv e-prints
Granato, G. L., De Zotti, G., Silva, L., Bressan, A., & Danese, L. 2004, ApJ, 600, 580
Greve, T. R., Pope, A., Scott, D., et al. 2008, MNRAS, 389, 1489
Hodge, J. A., Carilli, C. L., Walter, F., et al. 2012, ApJ, 760, 11
Hodge, J. A., Riechers, D., Decarli, R., et al. 2015, ApJ, 798, L18
Hopkins, P. F., Hernquist, L., Cox, T. J., et al. 2006, ApJS, 163, 1
Hubble, E. P. 1926, ApJ, 64, 321
Hughes, D. H., Serjeant, S., Dunlop, J., et al. 1998, Nature, 394, 241
Karim, A., Swinbank, A. M., Hodge, J. A., et al. 2013, MNRAS, 432, 2

Kartaltepe, J. S., Mozena, M., Kocevski, D., et al. 2014, ArXiv e-prints
Kim, D., & Im, M. 2013, ApJ, 766, 109
Knobel, C., Lilly, S. J., Woo, J., & Kovač, K. 2015, ApJ, 800, 24
Kriek, M., van der Wel, A., van Dokkum, P. G., Franx, M., & Illingworth, G. D. 2008, ApJ, 682, 896
Krogager, J.-K., Zirm, A. W., Toft, S., Man, A., & Brammer, G. 2014, ApJ, 797, 17
Lin, L., Patton, D. R., Koo, D. C., et al. 2008, ApJ, 681, 232
Maiolino, R., Carniani, S., Fontana, A., et al. 2015, ArXiv e-prints
Man, A. W. S., Toft, S., Zirm, A. W., Wuyts, S., & van der Wel, A. 2012, ApJ, 744, 85
Man, A. W. S., Zirm, A. W., & Toft, S. 2014, ArXiv e-prints
Marchesini, D., Muzzin, A., Stefanon, M., et al. 2014, ApJ, 794, 65
McNamara, B. R., & Nulsen, P. E. J. 2007, ARA&A, 45, 117
Moore, B., Lake, G., & Katz, N. 1998, ApJ, 495, 139
Naab, T., Johansson, P. H., & Ostriker, J. P. 2009, ApJ, 699, L178
Oser, L., Naab, T., Ostriker, J. P., & Johansson, P. H. 2012, ApJ, 744, 63
Pan, Z., Kong, X., & Fan, L. 2013, ApJ, 776, 14
Perera, T. A., Chapin, E. L., Austermann, J. E., et al. 2008, MNRAS, 391, 1227
Poggianti, B. M., Moretti, A., Calvi, R., et al. 2013, ApJ, 777, 125
Reddy, N. A., Erb, D. K., Steidel, C. C., et al. 2005, ApJ, 633, 748
Ricciardelli, E., Trujillo, I., Buitrago, F., & Conselice, C. J. 2010, MNRAS, 406, 230
Riechers, D. A., Carilli, L. C., Walter, F., et al. 2011, ApJ, 733, L11
Schawinski, K., Thomas, D., Sarzi, M., et al. 2007, MNRAS, 382, 1415
Schawinski, K., Urry, C. M., Simmons, B. D., et al. 2014, MNRAS, 440, 889
Simpson, J. M., Swinbank, A. M., Smail, I., et al. 2014, ApJ, 788, 125
Smail, I., Ivison, R. J., & Blain, A. W. 1997, ApJ, 490, L5
Sodré, L., Ribeiro da Silva, A., & Santos, W. A. 2013, MNRAS, 434, 2503
Steidel, C. C., Adelberger, K. L., Shapley, A. E., et al. 2003, ApJ, 592, 728
Steidel, C. C., Shapley, A. E., Pettini, M., et al. 2004, ApJ, 604, 534
Steinhauser, D., Haider, M., Kapferer, W., & Schindler, S. 2012, A&A, 544, A54
Strateva, I., Ivezić, Ž., Knapp, G. R., et al. 2001, AJ, 122, 1861
Szomoru, D., Franx, M., & van Dokkum, P. G. 2012, ApJ, 749, 121
Tacconi, L. J., Genzel, R., Smail, I., et al. 2008, ApJ, 680, 246
Taylor, E. N., Franx, M., Glazebrook, K., et al. 2010, ApJ, 720, 723
Toft, S., van Dokkum, P., Franx, M., et al. 2007, ApJ, 671, 285
Toft, S., Smolčić, V., Magnelli, B., et al. 2014, ApJ, 782, 68
Trujillo, I., Carrasco, E. R., & Ferré-Mateu, A. 2012, ApJ, 751, 45
Trujillo, I., Cenarro, A. J., de Lorenzo-Cáceres, A., et al. 2009, ApJ, 692, L118
Trujillo, I., Förster Schreiber, N. M., Rudnick, G., et al. 2006, ApJ, 650, 18
van de Sande, J., Kriek, M., Franx, M., et al. 2013, ApJ, 771, 85
van Dokkum, P. G., Franx, M., Kriek, M., et al. 2008, ApJ, 677, L5
Verdugo, M., Ziegler, B. L., & Gerken, B. 2008, A&A, 486, 9
Viero, M. P., Moncelsi, L., Quadri, R. F., et al. 2013, ApJ, 779, 32
Villalobos, Á., De Lucia, G., & Murante, G. 2014, MNRAS, 444, 313
Wardlow, J. L., Smail, I., Coppin, K. E. K., et al. 2011, MNRAS, 415, 1479
Watson, D., Christensen, L., Knudsen, K. K., et al. 2015, Nature, 519, 327
Whitaker, K. E., van Dokkum, P. G., Brammer, G., et al. 2013, ApJ, 770, L39
Williams, C. C., Giavalisco, M., Cassata, P., et al. 2014, ApJ, 780, 1

Williams, R. J., Quadri, R. F., Franx, M., van Dokkum, P., & Labbé, I. 2009, ApJ, 691, 1879
Woo, J., Dekel, A., Faber, S. M., & Koo, D. C. 2015, MNRAS, 448, 237
Wuyts, S., Förster Schreiber, N. M., van der Wel, A., et al. 2011, ApJ, 742, 96

Part I

Modeling the ISM of $z \sim 2$ massive galaxies with SÍGAME

3

Observing and modeling CO emission lines in galaxies

3.1 Why CO?

Due to the high abundance of hydrogen, the most common molecule to find in the ISM, is by far H_2. But in terms of observing cold molecular gas, H_2 is practically invisible, because the lack of an electric dipole moment means that the lowest possible rotational transitions of H_2 are electric quadrupole moments with very high energy. The first rotational transition, S(0), is at $510\,K$, meaning that even the lowest roational transitions can only be excited in shock waves, FUV-rich PDRs or regions affected by turbulent dissipation (Ingalls et al., 2011).

The second most abundant molecule is carbonmonoxide, CO, consisting of one carbon and one oxygen atom. The abundance relative to H_2, $[CO/H_2]$, is roughly 10^{-4} in MW ISM as has been determined via observations of early cold cores in the MW (Glover & Mac Low, 2011; Liu et al., 2013) and simulations of molecular clouds with $n_H \gtrsim 1000\,\mathrm{cm}^{-3}$ (Glover & Mac Low, 2011).

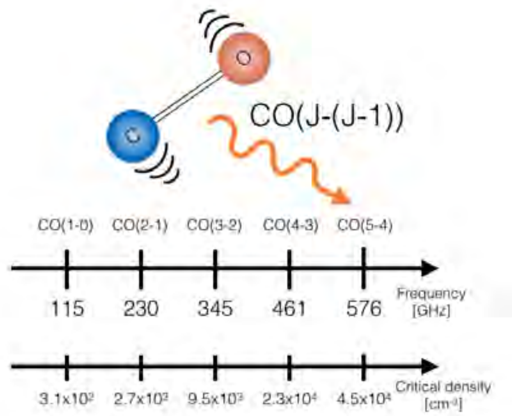

Figure 3.1 Illustration of the rotating CO molecules together with the frequencies of the first 5 rotational lines of the CO molecular are shown. Below are critical densities as calculated by Greve et al. (2014) for a kinetic temperature of $T_k = 40\,K$ and assuming H_2 to be the main collision partner.

CO is the most used molecule for observing molecular gas, since its rotational transitions conveniently sample the typical densities and temperatures inside GMCs. To prope the very densest parts of GMCs, other molecular tracers exist with higher critical densities (again see Tielens 2013 for an overview of most detected molecules, and Aalto 2013 for a subset of the denser gas tracers), but the low CO lines have proven excellent for capturing the mayority of the molecular gas.

Fig. 3.1 provides an illustration of the rotating CO molecule, together with the frequencies and critical densities of the first 5 transitions. Also, the positions of the first 5 transitions on a typical SED can be seen in Fig. 1.11. In GMCs, the excitation of CO molecules to higher rotational levels is believed to come mainly from collisions with H_2 molecules. The population of the various rotional levels are therefore determined by density and temperature (how fast the molecules are moving) of the gas. The amount of flux in each rotational transition creates a CO Spectral Line Energy Distribution (SLED) or 'CO ladder' which can take on different shapes depending on the gas properties.

3.2 Observations of CO line emission

At $z \sim 2$, the vast majority of CO observations have been of extreme galaxies, such as submillimeter galaxies (SMGs) with very high SFRs or quasi-stellar objects (QSOs) containing powerful AGNs. Only a few galaxies on the "main sequence of star formation" (MS, e.g. Wuyts et al., 2011), have been observed in CO. These are typically massive ($10^{10} - 10^{11}\,\mathrm{M}_\odot$) galaxies selected by the BzK technique to be moderately star-forming with SFR$\simeq 10 - 500\,\mathrm{M}_\odot\,\mathrm{yr}^{-1}$, i.e. specific SFR (SSFR) of around $0.5\,\mathrm{Gyr}^{-1}$. The molecular gas of SMGs and QSOs is highly excited with peak fluxes at the CO(5-4) and CO(6-5) transitions, which is evidence of dense and possibly warm gas (Papadopoulos et al., 2012), but little is known for the normal star-forming galaxies observed in CO to date. The only such galaxies, with 4 observed CO transitions, are the BzK-selected galaxies BzK$-$4171, BzK$-$16000 and BzK$-$21000 (Daddi et al., 2014). These galaxies were previously believed to contain mainly gas reminiscent to that of the Milky Way (MW) (Dannerbauer et al., 2009; Aravena et al., 2014), but new CO$(5-4)$ observations by Daddi et al. (2014) require a second component of higher density and possibly higher temperature.

With instruments of high spatial resolution, it has recently become possible to resolve galaxies at $z \gtrsim 2$ on kiloparsec scales, as shown with the VLA by e.g. Walter et al. (2007) when observing low-J CO transitions. Scales of $1\,\mathrm{kpc}$ require a resolution of $\sim 0.1''$ at $z = 2$, achievable with ALMA for higher CO lines that are not redshifted below its bands.

When measuring the CO ladder of galaxies with different compositions, SFR and AGN activity, a huge variety emerges. Fig. 3.2 compares the rather low-excitation ladder of the MW to the CO ladders of SMGs and QSOs which peak at increasingly higher J-values. An upper limit as to how steep the ladder can be, is reached if the gas is in Local Thermal Equilibrium (LTE), in which case the level populations just follow a Boltzmann distribution set by the gas kinetic temperature and no radiative transitions are considered. For gas in LTE, the CO ladder would grow as J^2 as indicated in Fig. 3.2 in blue. But in general, the local kinetic temperature is not equal to the temperature of the radiation field, and the high J-levels are less populated.

3.2.1 The X_{CO} factor

Probably the widest use of CO emission lines, is the estimation of total molecular gas mass. The low critical density ($\sim 300\,\mathrm{cm}^{-3}$) of the first CO(1-0) transition makes it a tracer of most gas in a GMC. In order to convert from CO(1-0) line intensity and column density of H_2, the CO-H_2 conversion factor (X_{CO} or 'X-factor') gives the H_2 column density per CO(1-0) intensity unit:

$$X_{\mathrm{CO}}\,[\mathrm{cm}^{-2}/(\mathrm{K\,km\,s}^{-1})^{-1}] = \mathrm{N(H_2)/W_{(CO(1-0))}} \tag{3.1}$$

A similar conversion factor exists between total H_2 gas mass amount and CO line luminosity:

$$\alpha_{\mathrm{CO}}\,[\mathrm{M}_\odot/(\mathrm{K\,km\,pc}^{-2})^{-1}] = \mathrm{M(H_2)/L_{CO(1-0)}} \tag{3.2}$$

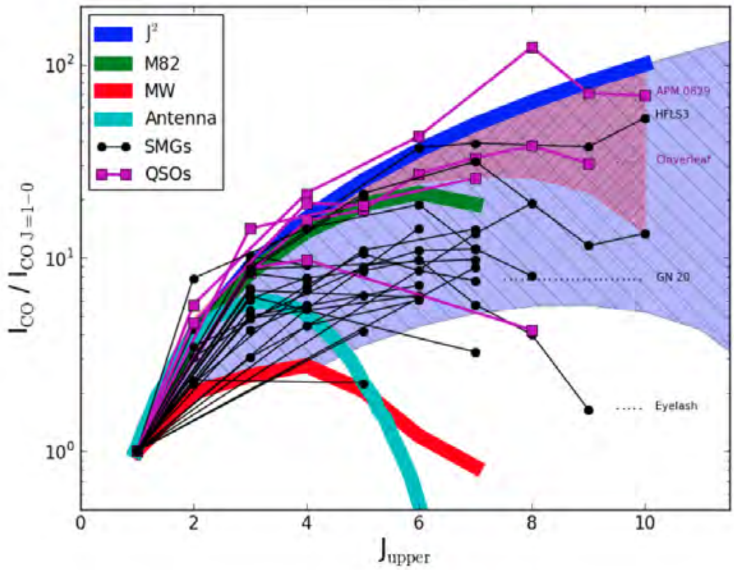

Figure 3.2 Observed CO ladders for different galaxies, normalized to the CO(1-0) transition. From the review of Casey et al. (2014).

The most common way of inferring their values, is to estimate the gas mass from either (i) the CO line width assuming the GMCs are in virial equilibrium (cf. eq. 1.2), (ii) the dust mass assuming a dust-to-gas mass ratio, or (iii) γ-ray emission from cosmic ray interactions with H_2 (see references in Narayanan et al., 2012). In the inner disk of the MW, they are relatively constant at $X_{\rm CO} \approx 2 \times 10^{20}\,{\rm cm^{-2}}/({\rm K\,km\,s^{-1}})^{-1}$ and $\alpha_{\rm CO} \approx 4.3\,{\rm M_\odot}/({\rm K\,km\,pc^{-2}})^{-1}$ (from the comprehensive review on the X-factor by Bolatto et al., 2013).

But recent observations, at low and high redshift, show that $X_{\rm CO}$ must be lower in galaxies of high-surface density environments, and larger in low-metallicity environments. This has led to the belief that maybe there exists two versions of the KS star formation relation, one for gas-rich mergers and another for star-forming normal disk galaxies (Genzel et al., 2010). Based on detailed modeling, Narayanan et al. (2012) came up with a function for $X_{\rm CO}$ that depends on CO line luminosity and metallicity. With this prescription for $X_{\rm CO}$ a single continous KS star formation relation can be drawn for starbursts and normal disk galaxies at low and high redshift as shown in Fig. 3.3. However, see the work of Hodge et al. (2015), implying that SMGs really can have more efficient star formation on small scales, regardless of the choice of conversion factor.

3.3 Modeling of CO emission lines

The CO ladder of a galaxy can be modeled by combining galaxy simulations (either zoom-in versions of cosmological simulations or isolated galaxy models, cf. Section 1.6) with sub-grid prescriptions for the GMC structure and radiative transfer codes or LVG models for the transport of CO line emission through the ISM. Over the past decade in particular, detailed modeling of CO emission has been developed, the basic steps of which can be summarised as follows: (1) Simulate a galaxy with dark matter, stars and atomic gas (if possible, with a multiphase molec-

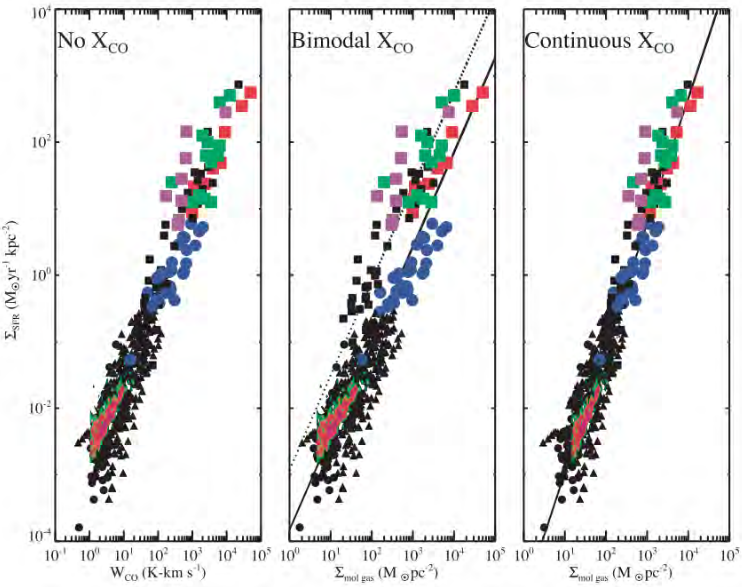

Figure 3.3 The effect of using an effectively bimodal $X_{\rm CO}$ factor (mid panel; $\alpha_{\rm CO} = 4.5$ for local disks, 3.6 for high-z disks and $0.8\,{\rm M_\odot}/({\rm K\,km\,pc^{-2}})^{-1}$ for mergers) or a continuous one (right panel) on the KS law (Narayanan et al., 2012).

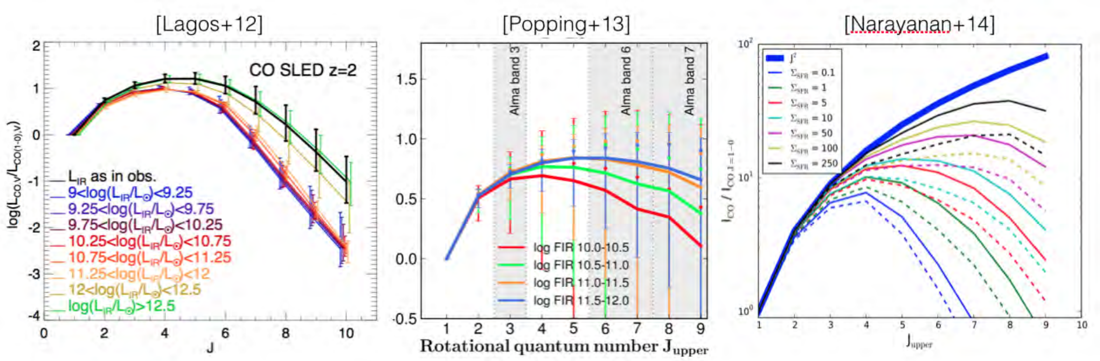

Figure 3.4 Examples of simulated CO ladders for different galaxy types. *Left:* The shape of CO ladders for $z = 2$ galaxies, binned according to infrared ($8 - 1000\,\mu$m) luminosity, $L_{\rm IR}$, as predicted by Lagos et al. (2012), *Middle:* The same as in the left panel according to the method of Popping et al. (2014), *Right:* CO ladders parameterized by $\Sigma_{\rm SFR}$ for simulations of resolved (solid) and unresolved (dashed) cases, as derived by Narayanan & Krumholz (2014).

ular gas), (2) Apply semi-analytical physical recipes to estimate the amount and state of dust and molecular gas, (3) Calculate the radiative transfer of selected CO lines. A full description of such a process can be found in Narayanan et al. (2008b), who investigated the signatures in CO morphology and line profile of outflows created by active galactic nuclei (AGNs) and starbursts. The same method has been used to study other aspects of the ISM, such as the Kennicutt-Schmidt relation and the $X_{\rm CO}$ factor which relates velocity-integrated CO line intensity to H_2 column density, in low- and high-redshift galaxies (e.g., Narayanan et al., 2011; Narayanan & Hopkins, 2013). By running smoothed particle hydrodynamical (SPH) simulations with the GADGET-3 code, Narayanan et al. (2011) were able to follow the evolution with time of a multiphase ISM in isolated disk galaxies undergoing a merger, allowing the gas to cool down to temperatures of $\sim 10\,\mathrm{K}$. Lagos et al. (2012) simulated the CO emission of quiescently star-forming as well as starburst galaxies at redshifts ranging from $z = 0$ to $z = 6$ by coupling cosmological galaxy formation simulations with the tabulated output of a code describing photon dominated regions (PDRs). Lagos et al. (2012) found that the global velocity-integrated CO line intensity peaks at higher rotational transitions with increasing infrared (IR) luminosity (J-level 4 to 5 when median L_{IR} of the sample goes from about $1.3 \sim 10^9$ to $8 \times 10^{12}\,L_{\odot}$). In a similar study, Popping et al. (2014) found that models of normal star-forming galaxies at high redshift have much higher rotational transitions than their local counterparts. Finally, the modeling of CO lines from a large set of simulated disk galaxies, recently carried out by Narayanan & Krumholz (2014) showed that the CO line energy distribution can be parameterised better with respect to SFR surface density compared to total SFR. Simulated CO SLEDs in in Fig. 3.4 provide examples of these previous works. However simulations of resolved CO line emission have been lacking.

4

CO EMISSION FROM SIMULATED MASSIVE $z = 2$ MAIN SEQUENCE GALAXIES (PAPER I)

4.1 AIM OF THIS PROJECT

We wanted to expand on previous modeling done by other groups of CO emission lines from galaxies at high redshift by developing a method that is more reliably on scales within the galaxy, in order to look at radial gradients of the $X_{\rm CO}$ factor and CO line ratios. This would provide a preview for what instruments might one day observe in 'normal' star-forming galaxies at $z = 2$.

With this project, we present a new numerical framework for simulating the line emission of normal star-forming galaxies. The code – SImulator of GAlaxy Millimeter/submillimeter Emission (`SÍGAME`[1]) – combines (non-)cosmological (SPH or grid-based) simulations of galaxy formation with subgrid prescriptions for the H_2/HI fraction and thermal balance throughout the ISM, down to parsec scales. `SÍGAME` accounts for a FUV and cosmic ray intensity field that vary with local SFR density within the galaxy. `SÍGAME` can be applied to any galaxy simulated in the SPH formalism, though currently restricted to galaxies dominated by star formation processes rather than AGN and with mean metallicities above about $0.01 Z_{\odot}$. Here, we adapt the code to cosmological SPH simulations of three massive, normal star-forming galaxies at $z = 2$ (i.e., so-called main-sequence galaxies), and model their CO rotational line spectrum using a publically available 3D radiative transfer code. We show that `SÍGAME` reproduces observed low-J CO line luminosities and provides new estimates of the $X_{\rm CO}$ factor for main-sequence galaxies at $z \sim 2$, while at the same time predicting their CO line luminosities at high-J ($J_{\rm up} > 6$) transitions where observations are yet to be made.

The structure of this chapter is as follows. Section 4.2 describes the cosmological SPH simulations used, along with the basic properties of the three star-forming galaxies extracted from the simulations. A detailed description of `SÍGAME` is presented in Section 4.3. The CO emission maps and spectra obtained after applying `SÍGAME` to the three simulated galaxies are presented in Section 4.4, where we also compare to actual CO observations of similar galaxies at $z \sim 2$. Section 4.5 discusses the strengths and weaknesses of `SÍGAME` in the context of other molecular line (CO) simulations and recent observations. Finally, in Section 4.6 we summarise the main steps of `SÍGAME`, and list its main findings and predictions regarding the CO line emis-

[1] `SÍGAME` in Spanish translates as 'follow me' - which in this context refers to the pursue of line emission through a galaxy.

sion from massive, star-forming galaxies at $z \simeq 2$. We adopt a flat cold dark matter (ΛCDM) scenario with $\Omega_m = 0.3$, $\Omega_\Lambda = 0.7$ and $h = 0.65$.

4.2 Cosmological Simulations

4.2.1 SPH simulations

We employ a cosmological TreeSPH code for simulating galaxy formation and evolution, though in principle, grid-based hydrodynamic simulations could be incorporated equally well. The TreeSPH code used for the simulations is in most respects similar to the one described in Sommer-Larsen et al. (2005) and Romeo et al. (2006). A cosmic baryon fraction of $f_\mathrm{b} = 0.15$ is assumed, and simulations are initiated at a redshift of $z = 39$. The implementation of star formation and stellar feedback, however, has been manifestly changed.

Star formation is assumed to take place in cold gas ($T_\mathrm{k} \lesssim 10^4\,\mathrm{K}$) at densities $n_\mathrm{H} > 1\,\mathrm{cm}^{-3}$. The star formation efficiency (or probability that a gas particle will form stars) is formally set to 0.1, but is, due to effects of self-regulation, considerably lower. Star formation takes place in a stochastic way, and in a star formation event, 1 SPH gas particle is converted completely into 1 stellar SPH particle, representing the instantaneous birth of a population of stars according to a Chabrier (2003) stellar initial mass function (IMF; Chabrier (2003)) – see further below.

The implementation of stellar feedback is based on a subgrid super-wind model, somewhat similar to the 'high-feedback' models by Stinson et al. (2006). These models, though, build on a supernova blast-wave approach rather than super-wind models. Both types of models invoke a Chabrier (2003) IMF, which is somewhat more top-heavy in terms of energy and heavy-element feedback than, e.g., the standard Salpeter IMF. The present models result in galaxies characterized by reasonable $z = 0$ cold gas fractions, abundances and circum-galactic medium abundance properties. They also improve considerably on the "angular momentum problem" relative to the models presented in, e.g., Sommer-Larsen et al. (2003). The models will be described in detail in a forthcoming paper (Sommer-Larsen et al. 2014, in prep.).

4.2.2 The model galaxies

Three model galaxies, hereafter referred to as G1, G2 and G3 in order of increasing SFR, were extracted from the above SPH simulation and re-simulated using the 'zoom-in' technique described in (e.g., Sommer-Larsen et al., 2003). The emphasis in this paper is on massive ($M_* \gtrsim 5 \times 10^{10}\,\mathrm{M}_\odot$) galaxies, and the three galaxies analyzed are therefore larger, rescaled versions of galaxies formed in the $10/h$ Mpc cosmological simulation described in Sommer-Larsen et al. (2003). The linear scale-factor is of the order 1.5, and since the CDM power spectrum is fairly constant over this limited mass range the rescaling is a reasonable approximation.

Galaxy G1 was simulated at fairly high resolution, using a total of 1.2×10^6 SPH and dark matter particles, while about 9×10^5 and 1.1×10^6 particles were used in the simulations of G2 and G3, respectively. For the G1 simulation, the masses of individual SPH gas, stellar and dark matter particles are $m_\mathrm{SPH} = m_* \approx 6.3 \times 10^5\ h^{-1}\mathrm{M}_\odot$ and m_DM=$3.5 \times 10^6\ h^{-1}\mathrm{M}_\odot$, respectively. Gravitational (cubic spline) softening lengths of 310, 310 and 560 h^{-1}pc, respectively, were employed. Minimum gas smoothing lengths were about $50\,h^{-1}$pc. For the lower resolution simulations of galaxies G2 and G3, the corresponding particle masses are $m_\mathrm{SPH} = m_* \approx 4.7 \times 10^6\ h^{-1}\mathrm{M}_\odot$ and $m_\mathrm{DM} = 2.6 \times 10^7\ h^{-1}\mathrm{M}_\odot$, respectively, and the gravitational softening lengths were 610, 610 and 1090 h^{-1}pc. Minimum gas smoothing lengths were about 100 h^{-1}pc.

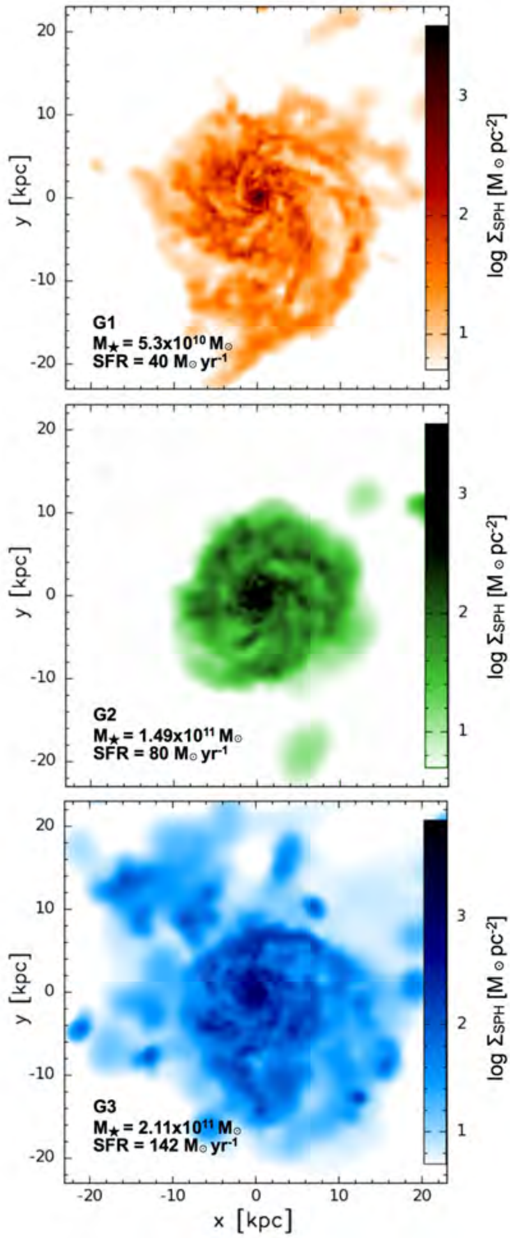

Figure 4.1 SPH gas surface density maps of the three model galaxies G1 (top), G2 (middle), and G3 (bottom) viewed face-on. The stellar masses and SFRs of each galaxy are indicated (see also Table 4.1). The maps have been rendered with the visualization tool SPLASH version 2.4.0 (Price, 2007) using the gas smoothing lengths provided by the simulations.

Due to effects of gravitational softening, typical velocities in the innermost parts of the galaxies (typically at radii less than about $2\epsilon_{\rm SPH}$, where $\epsilon_{\rm SPH}$ is the SPH and star particle gravitational softening length) are somewhat below dynamical values (see, e.g. Sommer-Larsen et al., 1998). The dynamical velocities will be of the order $v_{\rm dyn} = \sqrt{GM(R)/R}$, where G is the gravitational constant, R is the radial distance from the centre of the galaxy and $M(R)$ is the total mass located inside of R. Indeed, it turns out that for the simulated galaxies considered in this paper SPH particle velocities inside of $2\epsilon_{\rm SPH}$ are only about 60-70% of what should be expected from dynamics. To coarsely correct for this adverse numerical effect, for SPH particles inside of $2\epsilon_{\rm SPH}$ the velocities are corrected as follows: For SPH particles of total velocity less than $v_{\rm dyn}$, the tangential component of the velocity is increased such that the total velocity becomes equal to $v_{\rm dyn}$. Only the tangential component is increased in order not to create spurious signatures of merging. With this correction implemented, the average ratio of total space velocity to dynamical velocity of all SPH particles inside of $2\epsilon_{\rm SPH}$ equals unity.

Figure 4.1 shows surface density maps of the SPH gas in G1, G2, and G3, i.e., prior to any post-processing by SÍGAME. The gas is seen to be strongly concentrated towards the centre of each galaxy and structured in spiral arms containing clumps of denser gas. The spiral arms reach out to a radius of about 20 kpc in G1 and G3, with G2 showing a more compact structure that does not exceed $R \sim 15$ kpc. Table 4.1 lists key properties of these galaxies, namely SFR, stellar mass (M_*), SPH gas mass ($M_{\rm SPH}$), SPH gas mass fraction ($f_{\rm SPH} = M_{\rm SPH}/(M_* + M_{\rm SPH})$), and metallicity Z'. These quantities were measured within a radius ($R_{\rm cut}$, also given in Table 4.1) corresponding to where the radial cumulative stellar mass function has flattened out. The metallicity is in units of solar metallicity and is calculated from the abundances of C, N, O, Mg, Si, S, Ca and Fe in the SPH simulations, and adjusted for the fact that not all heavy metals have been included according to the solar element abundancies measured by Asplund et al. (2009).

Table 4.1 Physical properties of the three simulated galaxies G1, G2, and G3

	SFR	M_*	$M_{\rm SPH}$	$f_{\rm SPH}$	Z'	$R_{\rm cut}$
	[$M_\odot$ yr^{-1}]	[10^{11} $M_\odot$]	[10^{10} $M_\odot$]			[kpc]
G1	40	0.53	2.07	29%	1.16	20
G2	80	1.49	2.63	14%	1.97	15
G3	142	2.11	4.66	11%	1.36	20

Notes. All quantities are determined within a radius $R_{\rm cut}$, which is the radius where the cumulative radial stellar mass function of each galaxy becomes flat. The gas mass ($M_{\rm SPH}$) is the total SPH gas mass within $R_{\rm cut}$. The metallicity ($Z' = Z/Z_\odot$) is the mean of all SPH gas particles within $R_{\rm cut}$.

The location of our three model galaxies in the SFR-M_* diagram is shown in Figure 4.2 along with a sample of 3754 $1.4 < z < 2.5$ main-sequence galaxies selected in near-IR from the NEWFIRM Medium-Band Survey (Whitaker et al., 2011). The latter used a Kroupa IMF but given its similarity with a Chabrier IMF no conversion in the stellar mass and SFR was made (cf., Papovich et al. (2011) and Zahid et al. (2012) who use conversion factors of 1.06 and 1.13, respectively). Also shown are recent determinations of the main-sequence relation at $z > 1$ (Daddi et al., 2007; Elbaz et al., 2007; Rodighiero et al., 2010). When comparing to the relation at $z = 2$ of Daddi et al. (2007), G1, G2, and G3 are seen to lie at the massive end of the sequence, albeit somewhat on its lower (i.e., 'passive') side. This latter tendency is also found among a subset of CO-detected BX/BM galaxies at $z \sim 2 - 2.5$ (Tacconi et al., 2013), highlighted in Figure 4.2 along with a handful of $z \sim 1.5$ BzK galaxies also detected in CO (Daddi et al., 2010). The BX/BM galaxies are selected by a UGR colour criteria (Adelberger et al., 2004), while the BzK galaxies are selected by the BzK colour criteria (Daddi et al., 2004). Based on the above we

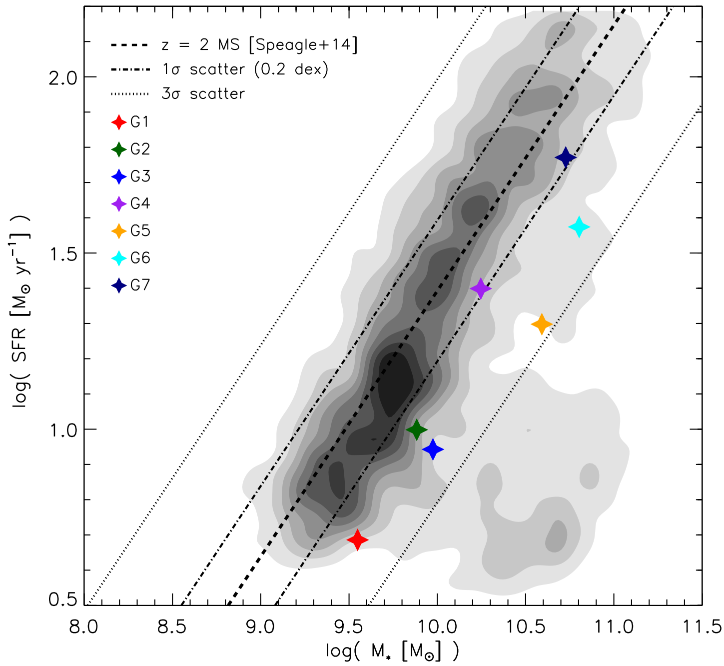

Figure 4.2 Position of the three model galaxies studied here (G1, G2 and G3 with red, green and blue stars respectively), on a SFR–M_* diagram. The grey filled contours show the $z \sim 2$ number density of 3754 $1.4 < z < 2.5$ galaxies from the NEWFIRM Medium-Band Survey (Whitaker et al., 2011). The dashed, dash-dotted and dotted lines indicate the SFR–M_* relation at $z = 2$ (Daddi et al., 2007), $z = 1$ (Elbaz et al., 2007) and $z > 1.5$ (Rodighiero et al., 2010), respectively. Also shown are six $z \sim 1.4 - 1.6$ BzK galaxies (black circles; Daddi et al. 2010) and 14 $z \sim 2 - 2.5$ Bx/BM galaxies (black crosses; Tacconi et al. 2013). The BzK galaxies are from top to bottom: BzK−12591, BzK−21000, BzK−16000, BzK−17999, BzK−4171 and BzK−2553 (following the naming convention of Daddi et al. 2010).

conclude that, in terms of stellar mass and SFR, our three model galaxies are representative of the star-forming galaxy population detected in CO at $z \sim 2$.

4.3 Modeling the ISM with SÍGAME

4.3.1 Methodology overview

Here we give an overview of the major steps that go into SÍGAME, along with a brief description of each. The full details of each step are given in subsequent sections and in appendices A.1 through A.3. We stress, that SÍGAME operates entirely in the post-processing stage of an SPH simulation, and can in principle easily be adapted to any given SPH galaxy simulation as long as certain basic quantities are known for each SPH particle in the simulation, namely: position ($\vec{r}$), velocity ($\vec{v}$), atomic hydrogen density ($n_{\rm H}$), metallicity (Z'), kinetic temperature ($T_{\rm k}$), smoothing length (h), and star formation rate (SFR). The key steps involved in SÍGAME are:

1. Cooling of the SPH gas. The initially hot ($T_{\rm k} \sim 10^{3-7}$ K) SPH gas particles are cooled to temperatures typical of the warm neutral medium ($\lesssim 10^4$ K) by atomic and ionic cooling

lines primarily.

2. Inference of the molecular gas mass fraction ($f'_{\rm mol} = m_{\rm H_2}/m_{\rm SPH}$) of each SPH particle after the initial cooling in step 1. $f'_{\rm mol}$ for a given SPH particle is calculated by taking into account its temperature, metallicity, and the local cosmic ray and FUV radiation field impinging on it.

3. Distribution of the molecular gas into GMCs. Cloud masses and sizes are obtained from random sampling of the observed GMC mass-spectrum in nearby quiescent galaxies and applying the local GMC mass-size relation.

4. GMC thermal structure. A radial density profile is adopted for each GMC and used to calculate the temperature structure throughout individual clouds, taking into account heating and cooling mechanisms relevant for neutral and molecular gas, when exposed to the local cosmic ray and attenuated FUV fields.

5. Radiative transport of CO lines. Finally, the CO line spectra are calculated separately for each GMC with a radiative transfer code and accumulated on a common velocity axis for the entire galaxy.

Determining the temperature (step *i*) and the molecular gas mass fraction (step *ii*) of a warm neutral gas SPH particle cannot be done independently of each other, but must be solved for simultaneously in an iterative fashion (see Sections 4.3.2 and 4.3.3). As already mentioned, we shall apply `SÍGAME` to the SPH simulations of galaxies G1, G2, and G3 described in Section 4.2, and in doing so we will use them to illustrate the workings of the code.

4.3.2 The Warm and Cold Neutral Medium

In SPH simulations of galaxies the gas is typically not cooled to temperatures below a few thousand Kelvin (Springel & Hernquist, 2003). This is illustrated in Figure 4.3, which shows the SPH gas temperature distribution (dashed histogram) in G1 (for clarity we have not shown the corresponding temperature distributions for G2 and G3, both of which are similar to that of G1). Minimum SPH gas temperatures in G1, G2 and G3 are about 1200 K, 3100 K and 3200 K, respectively, and while temperatures span the range $\sim 10^{3-7}$ K, the bulk ($\sim 80-90\%$) of the gas mass in all three galaxies is at $T_{\rm k} \lesssim 10^5$ K.

At such temperatures all gas will be in atomic or ionised form and H atoms that attach to grain surfaces via chemical bonds (chemisorbed) will evaporate from dust grains before H_2 can be formed. H_2 can effectively only exist at temperatures below $\sim 10^3$ K, assuming a realistic desorption energy of 3×10^4 K for chemisorbed H atoms (see Cazaux & Spaans, 2004). The first step of `SÍGAME` is therefore to cool some portion of the hot SPH gas down to $T_{\rm k} \lesssim 10^3$ K, i.e., a temperature range characteristic of a warm and cold neutral medium for which we can meaningfully employ a prescription for the formation of H_2.

`SÍGAME` employs the standard cooling and heating mechanisms pertaining to a hot, partially ionised gas. Cooling occurs primarily via emission lines from H, He, C, O, N, Ne, Mg, Si, S, Ca, and Fe in their atomic and ionised states, with the relative importance of these radiative cooling lines depending on the temperature (Wiersma et al., 2009). In addition to these emission lines, electron recombination with ions can cool the gas, as recombining electrons take away kinetic energy from the plasma, a process which is important at temperatures $> 10^3$ K (Wolfire et al., 2003). At similar high temperatures another important cooling mechanism is the scattering of free electrons off other free ions, whereby free-free emission removes energy from the gas (Draine, 2011). Working against the cooling is heating caused by cosmic rays via the expulsion of bound electrons from atoms or the direct kinetic transfer to free electrons via Coulomb interactions (Simnett & McDonald, 1969). Since this cooling step is targeted towards the hot, ionised gas, we shall ignore photo-ionization as a heating process, but include it in the subsequent temperature calculations (see Section 4.3.4).

We arrive at a first estimate of the temperature of the neutral medium by requiring energy rate equilibrium between the above mentioned heating and cooling mechanisms:

$$\Gamma_{\rm CR,HI} = \Lambda_{\rm ions+atoms} + \Lambda_{\rm rec} + \Lambda_{\rm f-f}, \tag{4.1}$$

where $\Lambda_{\rm ions+atoms}$ is the cooling rate due to atomic and ionic emission lines, $\Lambda_{\rm rec}$ and $\Lambda_{\rm f-f}$ are the cooling rates from recombination processes and free-free emission as described above, and $\Gamma_{\rm CR,HI}$ is the cosmic ray heating rate in atomic, partly ionised, gas. The detailed analytical expressions employed by SÍGAME for these heating and cooling rates are given in appendix A.1.

The abundances of the atoms and ions, listed above, entering the $\Lambda_{\rm ions+atoms}$ cooling term either have to be calculated in a self-consistent manner as part of the SPH simulation or set by hand. For our set of galaxies, the SPH simulations follow the abundances of H, C, N, O, Mg, Si, S, Ca and Fe, while for the abundances of He and Ne, we first find the mass fractions, $f_{\rm He}$ and $f_{\rm Ne}$, by scaling the corresponding solar mass fractions with what is left:

$$\begin{aligned} f_{\rm He} &= \left(1 - \sum f_i\right) \times \frac{f_{\rm He,\odot}}{f_{\rm He,\odot} + f_{\rm Ne,\odot}} \\ f_{\rm Ne} &= \left(1 - \sum f_i\right) \times \frac{f_{\rm Ne,\odot}}{f_{\rm He,\odot} + f_{\rm Ne,\odot}}, \end{aligned} \tag{4.2}$$

where i runs over the elements followed by the simulation, and we use $f_{\rm He,\odot} = 0.2806$ and $f_{\rm Ne,\odot} = 10^{-4}$ as used by Wiersma et al. (2009).

$\Gamma_{\rm CR,HI}$ depends on the *primary* cosmic ray ionization rate ($\zeta_{\rm CR}$), a quantity that is set by the number density of supernovae since they are thought to be the main source of CRs (Ackermann et al., 2013). In SÍGAME, this is accounted for by parameterizing $\zeta_{\rm CR}$ as a function of the *local* star formation rate density (SFRD) as it varies across the simulated galaxy. The details of this parameterization are deferred to Section 4.3.4.

It is important to emphasize that a) the ionization fraction of the gas depends on the *total* cosmic ray ionization rate (i.e., $\zeta_{\rm CR}$ corrected for secondary ionizations of H and He), the gas temperature ($T_{\rm k}$), and H I density ($n_{\rm HI}$); and b) these quantities are interdependent (see Pelupessy (2005)). In other words, for a fixed $\zeta_{\rm CR}$, all terms in eq. 4.1 depend on $T_{\rm k}$, $n_{\rm HI}$, and the electron density ($n_{\rm e}$), see appendix A.1. The latter is calculated taking into account the ionization of H and He (with a procedure kindly provided by I. Pelupessy; see also Pelupessy (2005)), and is a function of both $T_{\rm k}$ and $\zeta_{\rm CR}$. Since, $n_{\rm HI}$ is set by the molecular gas mass fraction ($f'_{\rm mol}$), which in turn also depends on $T_{\rm k}$ (see Section 4.3.3 on how $f'_{\rm mol}$ is calculated), eq. 4.1 has to be solved in an iterative fashion until consistent values for $T_{\rm k}$, $n_{\rm e}$, and $f'_{\rm mol}$ are reached. Example solutions are given in Figure A.1 in Appendix A.1.

The temperature distribution that results from solving eq. 4.1 for every SPH particle in the G1 simulation is shown in Figure 4.3 (very similar distributions are obtained for G2 and G3). The gas has been cooled to $T_{\rm k} \lesssim 10^4$ K, with temperatures extending down to 25, 30 and 27 K

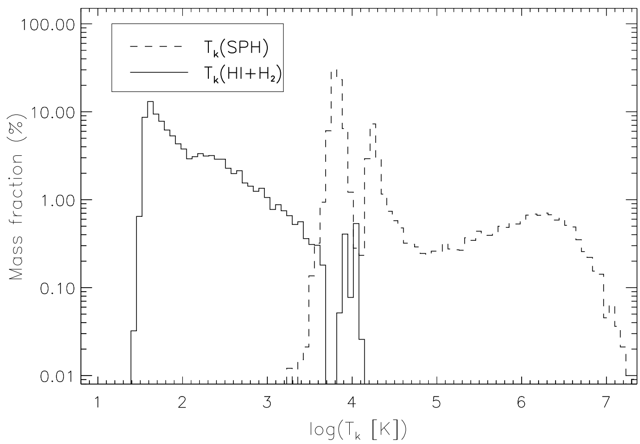

Figure 4.3 The distributions of gas kinetic temperature before (dashed histogram) and after (solid histogram) applying the heating and cooling mechanisms of eq. 4.1 to galaxy G1. The original hot SPH gas is seen to span a temperature range from about 10^3 K up to $\sim 10^7$ K, while once the gas has been cooled the temperature distribution only barely exceeds $\sim 10^4$ K.

respectively for G1, G2 and G3. We identify this gas as the warm neutral medium (WNM) and the cold neutral medium (CNM), and it is from this gas phase that we shall construct our molecular gas phase in the subsequent sections.

4.3.3 HI TO H$_2$ CONVERSION

For the determination of the molecular gas mass fraction associated with each SPH gas particle we use the prescription of Pelupessy et al. (2006), inferred by equating the formation rate of H$_2$ on dust grains with the destruction rate by UV photoionization and taking into account the self-shielding capacity of H$_2$ and dust extinction. We ignore H$_2$ production in the gas phase (cf., Christensen et al., 2012) since only in diffuse low metallicity ($\lesssim 0.1 Z_\odot$) gas is this thought to be the dominant formation route (Norman & Spaans, 1997), and so should not be relevant in our model galaxies that have mean metallicities $Z' > 1$ (see Table 4.1) and very little gas exists at $Z' < 0.1$ (see Figure A.3 in Appendix A.3). We adopt a steady-state for the H I$\rightarrow$H$_2$ transition, meaning that we ignore any time dependence owing to temporal changes in the UV field strength and/or disruptions of GMCs, both of which can occur on similar time scales as the H$_2$ formation. This has been shown to be a reasonable assumption for environments with metallicities $\gtrsim 0.01\, Z_\odot$ (Narayanan et al., 2011; Krumholz & Gnedin, 2011).

The first step is to derive the FUV field strength, G_0, which sets the H I$\rightarrow$H$_2$ equilibrium. In SÍGAME, G_0 consists of a spatially varying component that scales with the local SFRD ($\mathrm{SFRD_{local}}$) in different parts of the galaxy on top of a constant component set by the total stellar mass of the galaxy. This is motivated by Seon et al. (2011) who measured the average FUV field strength in the Milky Way ($G_{0\ ,\mathrm{MW}}$) and found that about half comes from star light directly with the remainder coming from diffuse background light. We shall assume that in the MW the direct stellar contribution to $G_{0\ ,\mathrm{MW}}$ is determined by the average SFRD ($\mathrm{SFRD_{MW}}$), while the diffuse component is fixed by the stellar mass ($\mathrm{M_{*,MW}}$). From this assumption, i.e., by calibrating to

MW values, we derive the desired scaling relation for G_0 in our simulations:

$$G_0 = G_{0,\mathrm{MW}} \left(0.5 \frac{\mathrm{SFRD_{local}}}{\mathrm{SFRD_{MW}}} + 0.5 \frac{\mathrm{M}_*}{\mathrm{M}_{*,\mathrm{MW}}} \right), \tag{4.3}$$

where $G_{0\ ,\mathrm{MW}} = 0.6$ Habing (Seon et al., 2011), and $\mathrm{M}_{*,\mathrm{MW}} = 6 \times 10^{10}\ \mathrm{M}_\odot$ (McMillan, 2011). For $\mathrm{SFRD_{MW}}$ we adopt $0.0024\,\mathrm{M}_\odot\ \mathrm{yr}^{-1}\ \ \mathrm{kpc}^{-3}$, inferred from the average SFR within the central 10 kpc of the MW ($0.3\,\mathrm{M}_\odot\ \mathrm{yr}^{-1}$; Heiderman et al., 2010) and within a column of height equal to the scale height of the young stellar disk ($0.2\,\mathrm{kpc}$; Bovy et al., 2012) of the MW disk. $\mathrm{SFRD_{local}}$ is the SFRD ascribed to a given SPH particle, and is calculated as the volume-averaged SFR of all SPH particles within a $5\,\mathrm{kpc}$ radius. Note, that the stellar mass sets a lower limit on G_0, which for G1, G2, and G3 are 0.22, 0.62, and 0.88 Habing, respectively.

Next, the gas upon which the FUV field impinges is assumed to reside in logotropic clouds, i.e., clouds with radial density profiles given by $n(r) = n_{\mathrm{H,ext}}\,(r/R)^{-1}$, where $n_{\mathrm{H,ext}}$ is the density at the cloud radius R. From Pelupessy et al. (2006) we then have that the molecular gas mass fraction, including heavier elements than hydrogen, of each cloud is given by[2]:

$$f'_{\mathrm{mol}} \equiv \frac{m_{\mathrm{mol}}}{m_{\mathrm{SPH}}} = \exp\left[-4 \frac{A_{\mathrm{v}}^{(\mathrm{tr})}}{\langle A_{\mathrm{v}} \rangle} \right]. \tag{4.4}$$

Here $\langle A_{\mathrm{v}} \rangle$ is the area-averaged visual extinction of the cloud and $A_{\mathrm{v}}^{(\mathrm{tr})}$ is the extinction through the outer layer of neutral hydrogen.

The mean extinction $\langle A_{\mathrm{v}} \rangle$ is calculated as:

$$\langle A_{\mathrm{v}} \rangle = 0.22 Z' \frac{n_{\mathrm{ds}}}{100\,\mathrm{cm}^{-3}} \left(\frac{P_{\mathrm{e}}/k_{\mathrm{B}}}{10^4\,\mathrm{cm}^{-3}\mathrm{K}} \right)^{1/2}, \tag{4.5}$$

where the boundary pressure of each cloud, P_{e}, enters through a pressure normalized density-size relation of which n_{ds} is the normalization constant (here set to $1520\,\mathrm{cm}^{-2}$ following Pelupessy et al., 2006). The boundary pressure is caused by thermal as well as macroscopic motions, i.e.:

$$P_{\mathrm{e}} = n_{\mathrm{e}} k_{\mathrm{B}} T_{\mathrm{k}} + \frac{1}{3} m_{\mathrm{H}} n_{\mathrm{H,ext}} \sigma_v^2 / k_{\mathrm{B}}, \tag{4.6}$$

where σ_{v} is the local gas velocity dispersion, which for a given SPH particle is the mean velocity dispersion of its neighbouring particles within two smoothing lengths, weighted by mass, density and the cubic spline kernel (see also Monaghan, 2005). For a logotropic density profile, the external density is given by $n_{\mathrm{H,ext}} = 2/3 \langle n_{\mathrm{H}} \rangle$, where $\langle n_{\mathrm{H}} \rangle$ is the average cloud density, which we approximate with the original SPH gas density.

For $A_{\mathrm{v}}^{(\mathrm{tr})}$, the following expression is provided by Pelupessy et al. (2006):

$$A_{\mathrm{v}}^{(\mathrm{tr})} = 1.086 \nu \xi_{\mathrm{FUV}}^{-1} \times \ln \left[1 + \frac{\frac{G_0}{\nu \mu S_{\mathrm{H}}(T_{\mathrm{k}})} \sqrt{\frac{\xi_{\mathrm{FUV}}}{Z' T_{\mathrm{k}}}}}{n_{\mathrm{H,ext}}/135\,\mathrm{cm}^{-3}} \right], \tag{4.7}$$

where ξ_{FUV} is the ratio between dust FUV absorption cross section (σ) and the effective grain surface area (σ_d), and is set to $\xi_{\mathrm{FUV}} = \sigma/\sigma_{\mathrm{d}} = 3$. $S_{\mathrm{H}} = (1 + 0.01 T_{\mathrm{k}})^{-2}$ is the probability

[2] We will use lower case m when dealing with individual SPH particles. Furthermore, f'_{mol} is not to be confused with f_{mol} describing the total molecular gas mass fraction of a galaxy and to be introduced in Section 4.4.

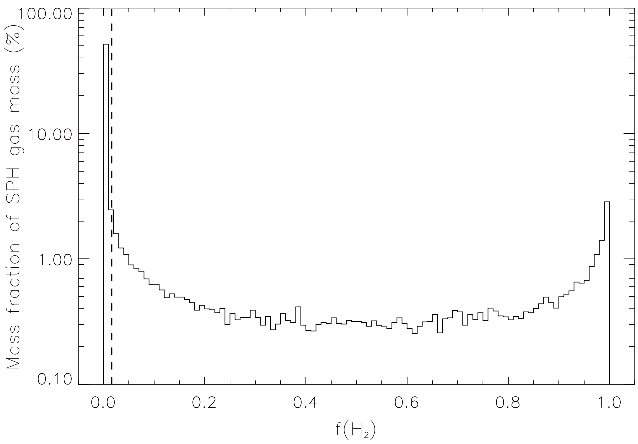

Figure 4.4 The distribution of the H_2 gas mass fraction of the SPH particles in G1 calculated according to eq. 4.4 (solid line histogram). Similar distributions are found for G2 and G3. The lower limit on $f'_{\rm mol}$, defined as described in Section 4.3.4, is indicated by the dashed vertical line.

that HI atoms stick to grain surfaces, where T_k is the kinetic gas temperature (determined in an iterative way as explained in Section 4.3.2). Furthermore, $\nu = n_{\rm H,ext}R\sigma(1+n_{\rm H,ext}R\sigma)^{-1}$, and μ (set to 3.5 as suggested by Pelupessy et al., 2006) is a parameter which incorporates the uncertainties associated with primarily $S_{\rm H}$ and $\sigma_{\rm d}$.

Following the above prescription SÍGAME determines the molecular gas mass fraction and thus the molecular gas mass ($m_{\rm mol} = f'_{\rm mol}m_{\rm SPH}$) associated with each SPH particle. Depending on the environment (e.g., G'_0, Z', T_k, P_e,...), the fraction of the SPH gas converted into H_2 can take on any value between 0 and 1, as seen from the $f'_{\rm mol}$ distribution of G1 in Figure 4.4. Overall, the total mass fraction of the SPH gas in G1, G2, and G3 (i.e., within $R_{\rm cut}$) that is converted to molecular gas is 24 %, 48 % and 33 %, respectively.

4.3.4 STRUCTURE OF THE MOLECULAR GAS

Molecular gas is known to clump on scales $\lesssim 100\,$pc, significantly below the typical resolution in simulations of galaxy evolution, thus posing a general problem when modelling molecular emission lines (Narayanan et al., 2011; Popping et al., 2014; Narayanan & Krumholz, 2014). In relatively undisturbed, moderately star-forming galaxies, molecular gas is believed to be distributed in giant molecular clouds (GMCs) of sizes $\sim 6-60\,$pc with internal substructures similar to those observed in the MW (Kauffmann et al., 2010), and as suggested by simulations (e.g. Vázquez-Semadeni et al., 2010). Having determined the molecular gas mass fractions, SÍGAME proceeds by distributing the molecular gas into GMCs, and calculates the masses and sizes, along with the internal density and temperature structure, for each GMC as described in the following.

GMC masses and sizes

The molecular gas associated with a given SPH particle is divided into a number of GMCs with masses randomly extracted from the GMC mass function observed in the MW disk and Local Group galaxies: $\frac{dN}{dm_{\rm GMC}} \propto m_{\rm GMC}^{-\beta}$ with $\beta = 1.8$ (Blitz et al., 2007). Lower and upper mass cut-offs at $10^4\,{\rm M}_\odot$ and $10^6\,{\rm M}_\odot$, respectively, are enforced in order to span the mass range observed by Blitz et al. (2007). For G1, typically $\lesssim 30$ GMCs are created in this way per SPH particle, while for G2 and G3, which were run with SPH gas particles masses almost an order of magnitude higher, as much as ~ 100 GMCs can be extracted from a given SPH particle. Figure 4.5 shows the resulting mass distribution of all the GMCs in G1, along with the distribution of molecular mass associated with the SPH gas particles prior to it being divided into GMCs. The net effect of re-distributing the H_2 mass into GMCs is a mass distribution dominated by relatively low masses, which is in contrast to the SPH H_2 mass distribution which tended to be more skewed toward high gas masses. Note, the lower cut-off at $m_{\rm GMC} = 10^4\,{\rm M}_\odot$ implies that if the molecular gas mass associated with an SPH particle (i.e., $m_{\rm mol} = f'_{\rm mol} m_{\rm SPH}$) is less than this lower limit it will not be re-distributed into GMCs. Since $m_{\rm SPH}$ is constant in our simulations ($6.3 \times 10^4\,h^{-1}\,{\rm M}_\odot$ for G1 and $4.7 \times 10^6\,h^{-1}\,{\rm M}_\odot$ for G2 and G3, see Section 4.2.2) the lower limit imposed on $m_{\rm GMC}$ translates directly into a lower limit on $f'_{\rm mol}$ (0.016 for G1 and 0.002 for G2 and G3, shown as a dashed vertical line for G1 in Figure 4.4). As a consequence, 0.2, 0.005 and 0.01 % of the molecular gas in G1, G2, and G3, respectively, does not go into GMCs. These are negligible fractions, however, and the molecular gas they represent can be safely ignored.

The GMCs are placed randomly around the position of their 'parent' SPH particle, albeit with an inverse proportionality between displacement distance and mass of the GMC. The latter is done in order to retain the mass distribution of the original galaxy simulation as best as possible. The GMCs are assigned the same bulk velocity, $\bar{v}$, Z', G_0 and $\zeta_{\rm CR}$ as their 'parent' SPH particle.

The sizes of the GMCs were inferred from the local mass-size relation determined from measurements of the CO line widths and angular sizes of GMCs in the MW and several Local Group galaxies (e.g., Larson, 1981; Solomon et al., 1987; Heyer et al., 2001; Blitz et al., 2007). Adopting the relation by Solomon et al. (1987), GMC size is related to mass by:

$$R_{\rm eff}[{\rm pc}] = \sqrt{m_{\rm GMC}[{\rm M}_\odot]/540} \tag{4.8}$$

where $R_{\rm eff}$ is the *effective radius* defined as $\pi {R_{\rm eff}}^2 = \Delta l \Delta b$ where Δl and Δb are the extensions (FWHM) of the cloud in projected Galactic longitude and latitude. Figure 4.6 shows the resulting distribution of cloud sizes ($R_{\rm eff}$) for G1. Upper and lower limits on cloud sizes of $\sim 30\,{\rm pc}$ and $\sim 4\,{\rm pc}$, respectively, are set by the maximum and minimum GMC masses.

GMC density structure

The internal density structure of GMCs is highly complex and non-spherically symmetric, yet observations suggest that it can be approximated by a radial density profile of the form: $\rho(R) \propto R^{-1}$ (Young et al., 2003). `SÍGAME` adopts a Plummer density profile, which is approximately inversely proportional to R in the inner parts, but has a finite central density (e.g., Gieles et al.,

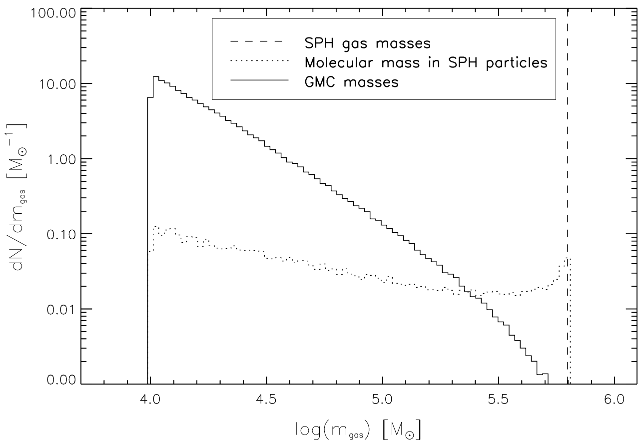

Figure 4.5 The distribution of GMC masses (solid histogram) in galaxy G1 after applying our GMC mass prescription described in §4.3.4. For comparison, we also show the distribution of molecular gas masses (dotted histogram) prior to the molecular gas being distributed in GMCs but after the HI to H_2 conversion applied to the SPH gas particles (§4.3.3). The dashed vertical line indicates the (fixed) SPH gas particle mass, i.e., the gas mass resolution of the simulation (6.3×10^5 $M_\odot$).

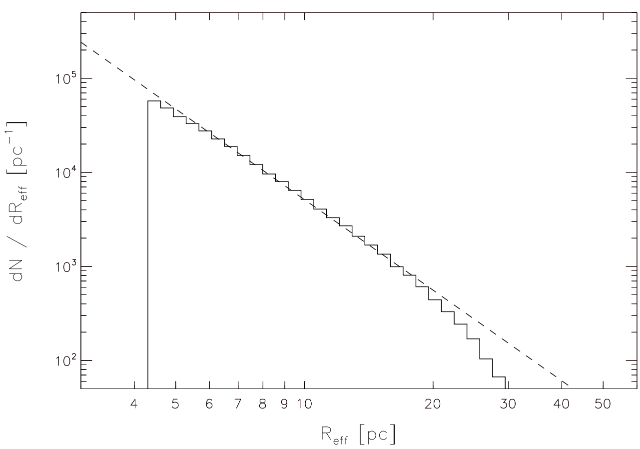

Figure 4.6 The distribution of GMC effective radii (solid histogram) in G1. Similar distributions are found for G2 and G3. The dashed line shows the best-fit power-law to the distribution: $\frac{dN}{dR_{\text{eff}}} \propto R_{\text{eff}}{}^{-3.2}$. From observations of clouds in the outer Galactic disk, found a mass distribution with a power-law slope of -3.2 ± 0.1 over a similar mass range as ours.

2006; Miettinen et al., 2009):

$$n_{\mathrm{H}_2}(R)[\mathrm{cm}^{-3}] = 20.23 \frac{3 m_{\mathrm{GMC}}[\mathrm{M}_\odot]}{4\pi 1.36 (R_p\,[\mathrm{pc}])^3} \left(1 + \frac{R^2}{R_p^2}\right)^{-5/2}, \tag{4.9}$$

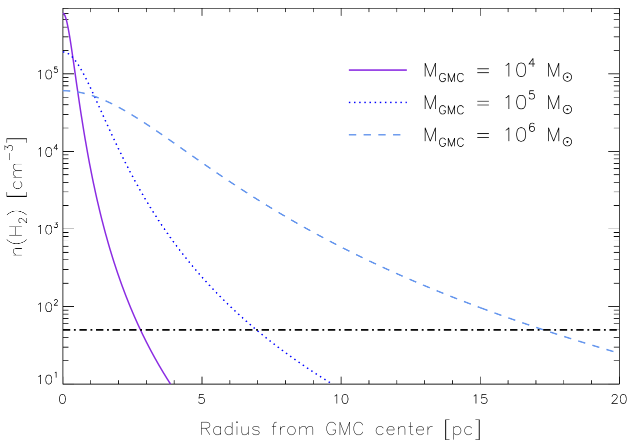

Figure 4.7 Radial Plummer density profiles (eq. 4.9) for GMCs with masses 10^4 (solid), 10^5 (dotted) and $10^6\,M_\odot$ (dashed), and corresponding Plummer radii of 0.4, 1.4, and 4.3 pc. The horizontal dot-dashed line marks the n_{H_2} value ($50\,\mathrm{cm}^{-3}$) below which CO is assumed to photo-dissociate.

where R_p is the so-called Plummer radius, which we set to $R_p = 0.02R_{\rm eff}$. The latter allows for a broad range in gas densities throughout the clouds, from $\sim 10^6\,\mathrm{cm}^{-3}$ in the central parts to a few $10\,\mathrm{cm}^{-3}$ further out, as seen in Figure 4.7 which shows the density profiles for GMCs with masses of 10^4, 10^5 and $10^6\,M_\odot$. The factor 1.36 in the denominator accounts for the presence of helium in the GMC.

GMC thermal structure

Having established the masses, sizes, and density structure of the GMCs, SÍGAME next solves for the kinetic temperature throughout the clouds. This means balancing the relevant heating and cooling mechanisms as a function of cloud radius.

GMCs are predominantly heated by FUV photons (via the photo-electric effect) and cosmic rays. For the strength of the FUV field impinging on the GMCs, we take the previously calculated values at the SPH gas particle position (eq. 4.3). We shall assume that the cosmic ray ionization rate scales in a similar manner, having its origin in supernovae and therefore also being closely related to nearby star formation and the total stellar mass of the galaxy:

$$\zeta_{\rm CR} = \zeta_{\rm CR,MW}\left(0.5\frac{\rm SFRD_{local}}{\rm SFRD_{MW}} + 0.5\frac{M_*}{M_{*,MW}}\right) \tag{4.10}$$

where $\rm SFRD_{local}$, $\rm SFRD_{MW}$ and $M_{*,\rm MW}$ are as described in Section 4.3.3, and $\zeta_{\rm CR}$ is scaled to the 'canonical' MW value of $\zeta_{\rm CR\ ,MW} = 3\times10^{-17}\,\mathrm{s}^{-1}$ (e.g. Webber, 1998). While the FUV radiation is attenuated by dust and therefore does not heat the GMC centres significantly, cosmic rays can easily penetrate into the UV-shielded central gas and heat as well as ionise it (Papadopoulos et al., 2011). For this reason we will attenuate the FUV field, but not the cosmic ray field, assuming that the latter keeps the same intensity throughout the GMCs. The extinction of the FUV field at a certain point within a GMC is derived by integrating the Plummer density profile from that point and out to the cloud radius, which is taken to be $R_{\rm eff}$ from eq. 4.8, and converting this H column density (derived from the density profile, corrected by a factor $1/1.36$ to account for elements heavier than hydrogen) into an extinction with $A_{\rm V} = N_{\rm H}/2.2 \times 10^{21}\,{\rm cm}^{-2}$ (Güver & Özel, 2009). This extinction is then converted into a dust-attenuated FUV field (Black & Dalgarno, 1977):

$$G_{0,\rm att} = G_0 e^{-1.8 A_{\rm V}} \tag{4.11}$$

We calculate the temperature throughout each GMC via the following heating and cooling rate balance:

$$\Gamma_{\rm PE} + \Gamma_{\rm CR,H_2} = \Lambda_{\rm H_2} + \Lambda_{\rm CO} + \Lambda_{\rm OI} + \Lambda_{\rm CII} + \Lambda_{\rm gas-dust} \tag{4.12}$$

$\Gamma_{\rm PE}$ is the photo-electric heating by FUV photons, and $\Gamma_{\rm CR,H_2}$ is the cosmic ray heating in molecular gas. $\Lambda_{\rm H_2}$ is the cooling rate of the two lowest H_2 rotational lines (S(0) and S(1)), and $\Lambda_{\rm CO}$ is the cooling rate of the combined CO rotational ladder. $\Lambda_{\rm gas-dust}$ is the cooling rate due to interactions between gas molecules and dust particles, which only becomes important at densities above $10^4\,{\rm cm}^{-3}$ (e.g., Goldsmith, 2001; Glover & Clark, 2012). $\Lambda_{\rm CII}$ and $\Lambda_{\rm OI}$ are the cooling rates due to [CII] and [[OI]] line emission, respectively, the strongest cooling lines in neutral ISM. The abundances of carbon and oxygen used in the prescriptions for their cooling rates, scale with the cloud metallicity, while the CO cooling scales with the relative CO to neutral carbon abundance ratio, set by the molecular density (see Appendix A.2).

The dust temperature, $T_{\rm dust}$, used for $\Lambda_{\rm gas-dust}$ in eq. 4.12 is set by the equilibrium between absorption of FUV and the emission of IR radiation by the dust grains. We adopt the approximation given by Tielens (2005):

$$T_{\rm dust} \simeq 33.5 \left(\frac{1\mu{\rm m}}{a}\right)^{0.2} \left(\frac{G_{0,\rm att}}{10^4}\right)^{0.2} {\rm K}, \tag{4.13}$$

where $G_{0,\rm att}$ is the dust-attenuated FUV field (eq. 4.11) and a is the grain size, which we set to $1\,\mu$m for simplicity. Values for $T_{\rm dust}$ using eq. B.2 range from 0 to 8.9 K, but we enforce a lower limit on $T_{\rm dust}$ equal to the $z = 2$ CMB temperature of $8.175\,{\rm K}$. $T_{\rm dust}$ is therefore essentially constant ($\sim 8 - 9\,{\rm K}$) throughout the inner region of the GMC models, similar to the value of $T_{\rm dust} = 8\,{\rm K}$ adopted by Papadopoulos & Thi (2013) for CR-dominated cores. Analytical expressions for all of the above heating and cooling rates are given in Appendix A.2, which also shows their relative strengths as a function of density for two example GMCs (Figure A.2).

Figure A.4 in Appendix A.3 shows the resulting $T_{\rm k}$ versus $n_{\rm H_2}$ behaviour for 80 GMCs spanning a broad range of GMC masses, metallicities, and star formation rate densities. As seen in the displayed GMC models, some general trends can be inferred from the $T_{\rm k} - n_{\rm H_2}$ diagrams. At fixed metallicity and mass, an increase in FUV radiation field, G_0 (and therefore also CR ionization rate, $\zeta_{\rm CR}$), leads to higher temperatures throughout the models. In the outer regions this is due primarily to the increased photoelectric heating, while in the inner regions, heating by the unattenuated cosmic rays takes over as the dominating heating mechanism (Figure A.2). Keeping G_0 (and $\zeta_{\rm CR}$) fixed, lower $T_{\rm k}$-levels and shallower $T_{\rm k} - n_{\rm H_2}$ gradients are found in GMCs with higher metallicities, Z'. Both these trends are explained by the fact that the [CII] and [OI] cooling rates scale linearly with Z' (see Appendix A.2).

Moving from the outskirts and inward towards the GMC centres (i.e., towards higher densities), $T_{\rm k}$ drops as the attenuation of G_0 reduces the photoelectric heating. However, the transition from the cooling by [CII] to the less efficient cooling mechanism by CO lines, causes a local increase in $T_{\rm k}$ at $n_{\rm H_2} \sim 10^3 - 10^{4.5}\,{\rm cm^{-3}}$, as also seen in the more detailed GMC models by Glover & Clark (2012). The exact density at which this 'bump' in $T_{\rm k}$ depends strongly on the mass of the GMC, which is an effect of the chosen mass distribution within the GMCs. Our choice of the Plummer model for the radial density profile means that the extinction, $A_{\rm V}$, at a certain density increases with GMC mass. This in turn decreases the FUV heating, and as a result the $T_{\rm k} - n_{\rm H_2}$ curve moves to lower densities with increasing GMC mass.

As the density increases towards the cloud centres (i.e., $n_{\rm H_2} \gtrsim 10^4\,{\rm cm^{-3}}$) molecular line cooling and also gas-dust interactions become increasingly efficient and start to dominate the cooling budget, bringing the temperature down to the CMB temperature in most cases (Figure A.2).

In the inner parts ($n_{\rm H_2} \gtrsim 10^{4.5}\,{\rm cm^{-3}}$) the $T_{\rm k} - n_{\rm H_2}$ curves are seen to be insensitive to changes in Z', which is expected since the dominant heating and cooling mechanisms in these regions do not depend on Z'. Eventually, in the very central regions of the clouds, the gas reaches temperatures close to that of the ambient CMB radiation field, irrespective of the overall GMC properties and the conditions at the surface.

GMC grid models

The $T_{\rm k} - n_{\rm H_2}$ curve for a given GMC is determined by the following basic quantities:

- The FUV radiation, G_0, and with that the cosmic ray field strength, $\zeta_{\rm CR}$ (proportional to G_0), together governing the heating of the gas.
- The GMC mass ($m_{\rm GMC}$), which determines the effective radius of a cloud (eq. 4.8) and thus its density profile (eq. 4.9).
- The local metallicity (Z'), which influences the fraction of H_2 gas and plays an important role in cooling the gas.

Of these, G_0 and $\zeta_{\rm CR}$ are set by the local star formation rate density (SFRD$_{\rm local}$) and the total stellar mass (M_*) according to eqs. 4.3 and 4.10, Z' is is taken directly from the simulations while $m_{\rm GMC}$ is extracted randomly from a probability distribution as explained in Section 4.3.4. The distributions of SFRD$_{\rm local}$, $m_{\rm GMC}$, Z', G_0 and $\zeta_{\rm CR}$ for each of the galaxies G1, G2 and G3 are shown in Figure A.3.

There are more than $100,000$ GMCs in a single model galaxy and, as Figure A.3 shows, they span a wide range in G_0, $m_{\rm GMC}$, and Z'. Thus, in order to shorten the computing time, we calculated $n_{\rm H_2}$ and $T_{\rm k}$ profiles for a set of only 630 GMCs, chosen to appropriately sample the above distributions at certain grid values (listed in Table 4.2, and marked by vertical black lines in Figure A.3). $T_{\rm k} - n_{\rm H_2}$ curves were calculated for each possible combination of the parameter grid values listed in Table 4.2 giving us 630 GMC grid models. Every GMC in our simulations was subsequently assigned the $T_{\rm k} - n_{\rm H_2}$ curve of the GMC grid model closest to it in our (G_0, $m_{\rm GMC}$, Z') parameter space.

Table 4.2 Grid parameter values

G_0 [Habing]	0.5, 1, 4, 7, 10, 13, 16, 19, 23, 27
$\log(m_{\rm GMC}/{\rm M_\odot})$	4.0, 4.25, 4.5, 4.75, 5.0, 5.25, 5.5, 5.75, 6.0
$\log(Z/Z_\odot)$	-1, -0.5, 0, 0.5, 1, 1.4, 1.8

4.3.5 RADIATIVE TRANSFER OF CO LINES

With the internal density and temperature structure of each of the 630 grid GMCs determined according to the above prescriptions, we only need a CO abundance in order to solve for the radiative transport of the CO rotational lines. SÍGAME assumes the density of CO follows that of the H_2 gas with a fixed CO abundance equal to the Galactic value of $[CO/H_2] = 2 \times 10^{-4}$ (Lee et al., 1996; Sofia et al., 2004, and see Section 4.5 for a justification of this value) everywhere in the GMCs except for $n_{H_2} < 50\,\mathrm{cm}^{-3}$, where CO is no expected to survive photo-dissociation processes (e.g. Narayanan et al., 2008a). Now we are ready to solve the radiative transfer for each GMC individually and derive the emerging CO line emission from the entire galaxy.

Individual GMCs

For the CO radiative transfer calculations we use a slightly modified version of the LIne Modeling Engine (LIME ver. 1.4; Brinch & Hogerheijde (2010)) - a 3D molecular excitation and radiative transfer code. LIME has been modified in order to take into account the redshift dependence of the CMB temperature, which is used as boundary condition for the radiation field during photon transport, and we have also introduced a redshift correction in the calculation of physical sizes as a function of distance. We use collision rates for CO (assuming H_2 as the main collision partner) from Yang et al. (2010). In LIME, photons are propagated along grid lines defined by Delaunay triangulation around a set of appropriately chosen sample points in the gas, each of which contain information on n_{H_2}, T_k, σ_v, $[CO/H_2]$ and $\bar{v}$. SÍGAME constructs such a set of sample points throughout each GMC: about 5000 points distributed randomly out to a radius of $40\,\mathrm{pc}$, i.e., beyond the effective radius of all GMCs in G1, G2, and G3 (Figure 4.6) and in a density regime below the threshold density of $50\,\mathrm{cm}^{-3}$ adopted for CO survival (see previous paragraph). The concentration of sample points is set to increase towards the centre of each GMC where the density and temperature vary more drastically.

For each GMC, LIME generates a CO line data cube, i.e., a series of CO intensity maps as a function of velocity. The velocity-axis consists of 50 channels, each with a spectral resolution of $1.0\,\mathrm{km\,s}^{-1}$, thus covering the velocity range $v = [-25, +25]\,\mathrm{km\,s}^{-1}$. The maps are $100\,\mathrm{pc}$ on a side and split into 200 pixels, corresponding to a linear resolution of $0.5\,\mathrm{pc/pixel}$ (or an angular resolution of $5.9 \times 10^{-5}\,''/\mathrm{pixel}$ at $z = 2$). Intensities are corrected for arrival time delay and redshifting of photons.

Figure A.5 shows the area- and velocity-integrated CO Spectral Line Energy Distributions (SLEDs) for the same 80 GMCs used in Section 4.3.4 to highlight the $T_\mathrm{k} - n_{H_2}$ profiles (Figure A.4). The first thing to note is that the CO line fluxes increase with m_GMC, which is due to the increase in size, i.e., surface area of the emitting gas, with cloud mass (Section 4.3.4). Turning to the shape of the CO SLEDs, a stronger G_0 (and ζ_CR) increases the gas temperature and thus drives the SLEDs to peak at higher J-transitions. Only the higher, $J_\mathrm{up} > 4$, transitions are also affected by metallicity, displaying increased flux with increased Z' for $Z' \gtrsim 1$ and $G_0 \gtrsim 1$. For GMCs with high G_0, the high metallicity levels thus cause the CO SLED to peak at $J_\mathrm{up} > 8$.

The effects of dust

Dust absorbs the UV light from young O and B stars and re-emits in the far-IR, leading to possible 'IR pumping' of molecular infrared sources. However, due to the large vibrational level spacing of CO, the molecular gas has to be at a temperature of at least $159\,\mathrm{K}$, for significant

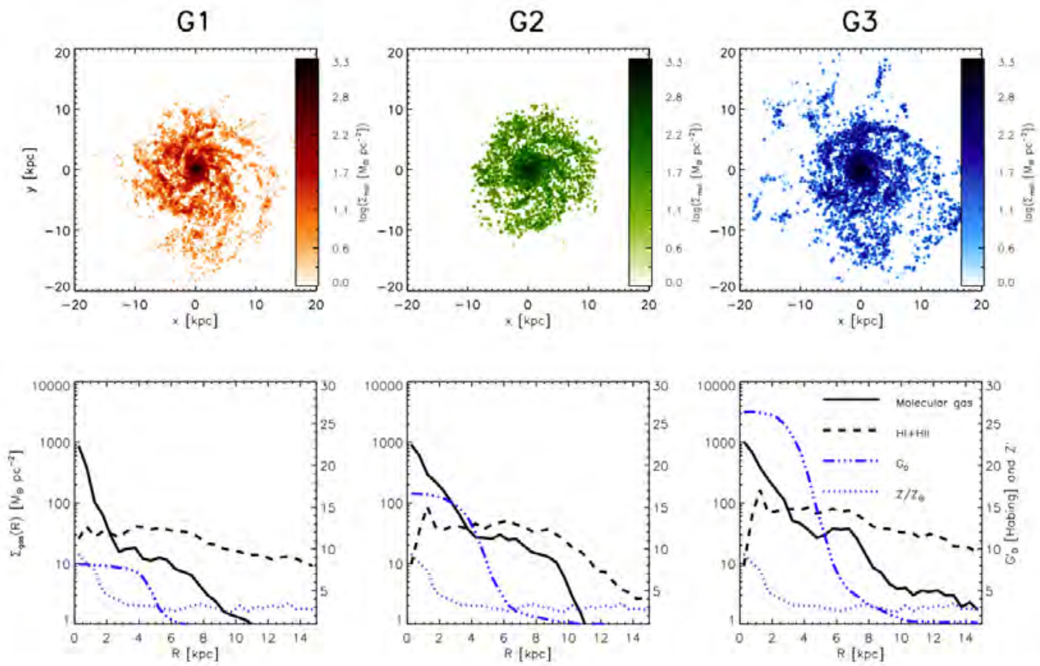

Figure 4.8 Top row: Molecular surface density maps of our model galaxies seen face-on. The maps have been smoothed using a circular Gaussian with full width at half maximum (FWHM) of 3 pixels corresponding to 0.24 kpc. Comparing to the SPH gas density maps in Figure 4.1 the molecular gas surface density maps are seen to trace the same spiral arms and inner disk as well as a few dense clumps further out. Bottom row: azimuthally averaged radial profiles of the HI +HII (dashed curve) and molecular (solid curve) gas surface densities, of the mean metallicity (dotted curve) and of G_0 (dot-dashed curve) – determined from 50 radial bins stretching from 0 to 15 kpc from the centre of each galaxy. The molecular gas is the result of applying the recipes in Section 4.3.3 to the SPH simulations presented in Section 4.2.2, while the HI +HII gas is the initial SPH gas mass minus the derived molecular gas mass, including a contribution from heavier elements. We estimate G_0 by averaging over the FUV fields impinging on all GMCs in each radial bin.

IR pumping of the CO rotational lines to take place, when assuming a maximum filling factor of 1, as shown by Carroll & Goldsmith (1981). Most of the gas in our GMC models is at temperatures below $100\,\mathrm{K}$, with only a small fraction of the gas, in the very outskirts, of the GMCs reach $T_\mathrm{k} > 159\,\mathrm{K}$, as seen in Figure A.4 in Appendix A.3. This happens only if the metallicity is low ($Z' \leq 0.1$) or in case of a combination between high FUV field ($G_0 \geq 4$) and moderate metallicity. On the other hand, the CO emission lines could be subject to dust extinction, which is however only important in extremely dust-enshrouded sources such as Arp 220 (Papadopoulos et al., 2010), and therefore not significant for our set of normal galaxies.

Upon these reflections, we have chosen not to include dust in the radiative transfer calculations of each GMC, although we mention that `LIME` is fully capable of including a dust component, provided that a table of dust opacities as function of wavelength be supplied together with the input model.

4.3.6 Combining the GMC line profiles in a galaxy

The CO emission line profile is derived for each galaxy GMC by assigning to it the GMC model that corresponds to the nearest grid point (in log space for m_GMC and Z'). The total line profiles of the galaxies are derived by adding the line profiles of individual GMCs to a common velocity axis at their respective projected velocities within each galaxy. This assumes that the molecular line emission from each GMC is radiatively decoupled from all other GMCs, which is a reasonable assumption due to the large velocity gradients through the galaxies (σ_v of $\sim 200-500\,\mathrm{km\,s^{-1}}$ in our model galaxies) and the relatively small internal turbulent line widths expected for the GMC (typically $\sim 1-3\,\mathrm{km\,s^{-1}}$ for Galactic GMCs; Heyer et al., 2009).

CO moment 0 maps are constructed by overlaying a grid of 500×500 pixels on each galaxy and adding the area-integrated CO line profiles from all GMCs within each pixel to a common velocity axis and integrating this line profile in velocity. This way, we create maps with a fixed width of 20 kpc and a resolution of ~ 80 pc. By integrating in area instead of velocity, we create total line profiles, and by further integrating these line profiles in velocity space, the CO SLED for the entire galaxy can be derived. All this will be examined in the following section and the results discussed further in Section 4.5.

4.4 SIMULATING MASSIVE $z = 2$ MAIN SEQUENCE GALAXIES

In this section we examine the H_2 surface density and CO emission maps resulting from applying `SÍGAME` to the three SPH galaxy simulations G1, G2, and G3 (Section 4.2), and we compare with existing CO observations of main sequence galaxies at $z \sim 1-2.5$.

4.4.1 TOTAL MOLECULAR GAS CONTENT AND H_2 SURFACE DENSITY MAPS

The total molecular gas masses of G1, G2 and G3 – obtained by summing up the GMC masses associated with all SPH particles within each galaxy (i.e., $M_{\rm mol} = \sum m_{\rm GMC} = \sum f'_{\rm mol} m_{\rm SPH}$) – are 4.9×10^9, 1.3×10^{10}, and $1.5\times10^{10}\,\mathrm{M_\odot}$, respectively, corresponding to about 24, 49 and 32 % of the original total SPH gas masses of the galaxies[3]. The global molecular gas mass fractions (i.e., $f_{\rm mol} = M_{\rm mol}/(M_* + M_{\rm mol})$ are 8.5, 7.8 and 6.8 % for G1, G2, and G3, respectively.

For the high-redshift samples we use for comparison in Figure 4.10, $f_{\rm mol}$ assumes mean values of; 59 ± 23 % for the $z\sim 1-1.3$ SFGs of Magnelli et al. (2012), 57 ± 6 % for the $z\sim1.5$ BzKs of Daddi et al. (2010), 48 ± 14 % for the $z\sim1-2.2$ SFGs of Tacconi et al. (2013) and 52 ± 20 % for the $z\sim2-2.5$ BX/BM galaxies of Tacconi et al. (2013). The mean for all these galaxies is $\sim 47\%$ or $\sim 5.5-6.8$ times above that of our galaxies. In comparison, local star-forming galaxies are relatively gas-poor as shown by Saintonge et al. (2011), who estimated molecular masses for a sample of nearby star-forming galaxies by applying a MW-like $\alpha_{\rm CO}$ factor to 119 detections in CO$(1-0)$ and to a stack of 103 non-detections. Correcting their molecular masses for the contribution from helium (1.36), the mean $f_{\rm mol}$ is only $\sim 6.7\pm4.5$ %. While our model galaxies have molecular gas mass fractions about a factor 6 below $z\sim1-2.5$ star-forming galaxies, they are within the observed range for the local counterparts. The main cause for this discrepancy between our model galaxies and observations made at $z\sim2$, is most likely the relatively low SPH gas mass fractions to begin with, i.e. $f_{\rm SPH} = M_{\rm SPH}/(M_* + M_{\rm SPH}) = 9-26\,\%$, restricting $f_{\rm mol}$ to be below these values.

The molecular surface density ($\Sigma_{\rm mol}$) maps of G1, G2, and G3, depicting the average $\Sigma_{\rm mol}$ within pixels $80\,\mathrm{pc}\times80\,\mathrm{pc}$ in size, are shown in Figure 4.8 (top panels). The pixel size was chosen in order to avoid resolving the GMCs, which have typical sizes of $R_{\rm eff}\approx 4-30$ pc (see Section 4.3.4).

[3]These global molecular-to-SPH gas mass fractions are calculated as $M_{\rm mol}/M_{\rm SPH} = \sum m_{\rm GMC}/\sum m_{\rm SPH}$, where the sums are over all SPH particles.

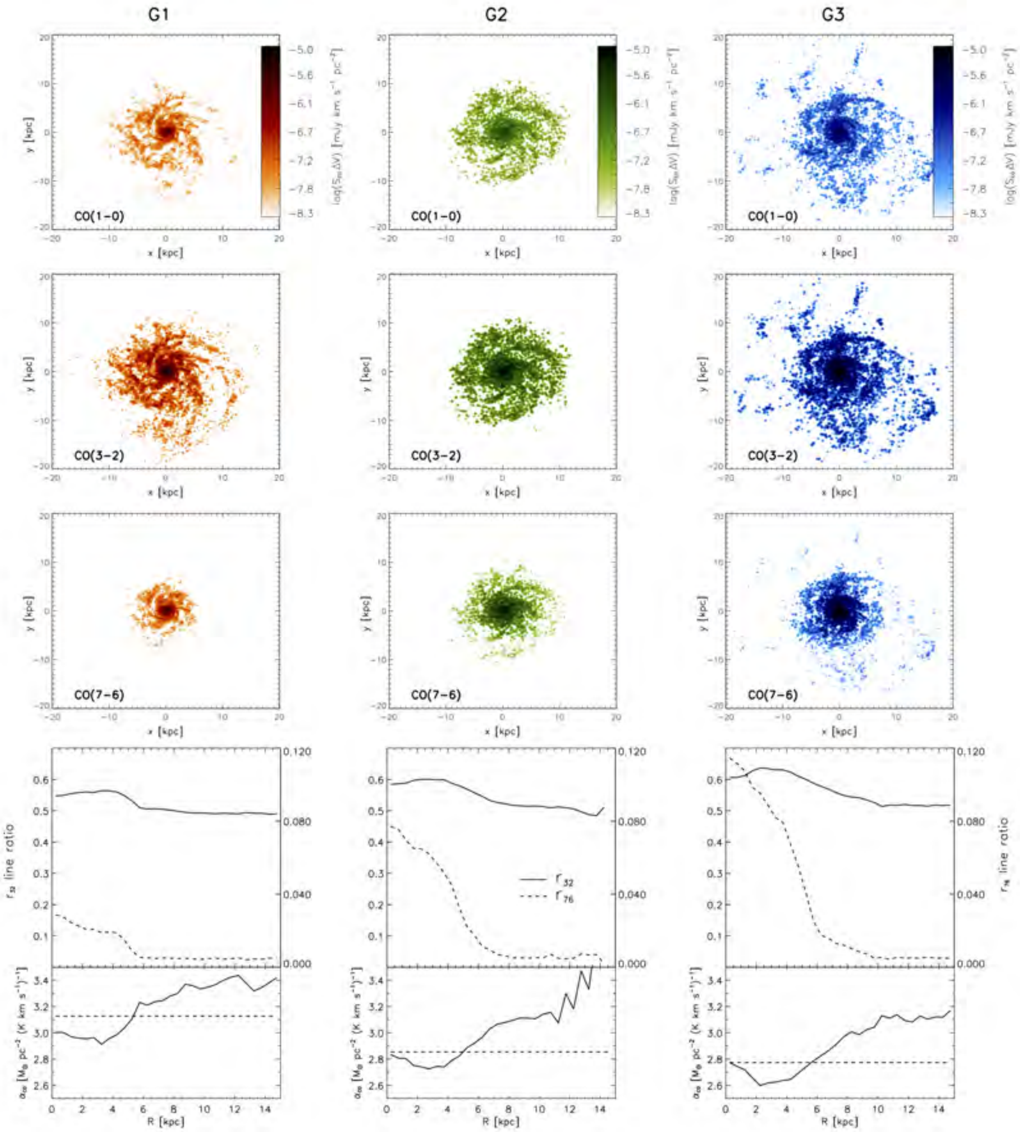

Figure 4.9 The top three rows show the moment zero maps of the CO(1−0), CO(3−2) and CO(7−6) emission from G1, G2 and G3. The CO maps have been smoothed using a circular Gaussian with full width at half maximum (FWHM) of 3 pixels corresponding to 0.24 kpc, and as with the SPH and molecular gas surface density maps, a logarithmic scale has been applied in order to better display extended emission. The bottom row shows the azimuthally averaged CO 3−2/1−0 and 7−6/1−0 brightness temperature line ratios (denoted r_{32} and r_{76}, respectively) as functions of projected radius for each of the three galaxies. A radial bin-size of 0.5 kpc was used. Also shown are the azimuthally averaged radial profiles of CO-to-H_2 conversion factor $\alpha_{\rm CO}(R) = \Sigma_{\rm H_2}/I_{\rm CO(1-0)}$ in units of $\rm M_{\odot}\ pc^{-2}\,(K\,km\,s^{-1})^{-1}$ with a dashed line indicating the global $\alpha_{\rm CO}$ factor.

Some molecular gas is seen to extend out to radii of $\sim 10\,\rm kpc$ and beyond, but generally the molecular gas concentrates within the inner regions of each galaxy. Thus, the distribution of molecular gas broadly follows the central disk and spiral arms where the SPH surface density ($\Sigma_{\rm SPH}$) is also the highest (Figure 4.1). The correspondence is far from one-to-one, however, as seen by the much larger extent of the SPH gas, i.e., regions where H_2 has not formed despite the presence of atomic and ionized gas. This point is further corroborated in the bottom panels of Figure 4.8, which show azimuthally-averaged radial surface density profiles of the molecular gas and of the HI +HII gas, both including a contribution from heavier elements. In order to compare values of $\Sigma_{\rm HI+HII}$and $\Sigma_{\rm mol}$ with observations, we set the radial bin width to $0.5\,{\rm kpc}$ – the typical radial bin size used for nearby spirals in the work of Leroy et al. (2008)[4]. The radially binned $\Sigma_{\rm mol}$ reaches $\sim 800-1000\,{\rm M_\odot\ pc^{-2}}$ in the central regions of our simulated galaxies, which is comparable to observational estimates of $\Sigma_{\rm mol}$ (of several $100\,{\rm M_\odot\ pc^{-2}}$) towards the centres of nearby spirals (Leroy et al., 2008). In all three galaxies, the HI +HII surface density dips within the central $\sim 1-2\,{\rm kpc}$, coinciding with a strong peak in $\Sigma_{\rm mol}$. Thus, despite the marked increase in the FUV radiation field towards the centre (the radial profile of G_0 is shown as dash-dotted line in Figure 4.8), the formation of H_2 driven by the increase in gas pressure is able to overcome photo-dissociative destruction of H_2 by FUV photons. The central H_2 surface densities are similar for all galaxies and is a direct consequence of very similar SPH gas surface densities in the centre combined with molecular gas mass fractions approaching 1. From $R \sim 2\,{\rm kpc}$ and out to $\sim 10\,{\rm kpc}$, the HI +HII surface density remains roughly constant with values of ~ 40, ~ 70 and $\sim 100\,{\rm M_\odot\ pc^{-2}}$ for G1, G2 and G3, respectively.

Radial profiles of the HI and molecular gas surface density that are qualitatively very similar to our simulations have been observed in several nearby star-forming disk galaxies (e.g., Leroy et al., 2008; Bigiel et al., 2008). In local galaxies, however, the HI surface density, including helium, rarely exceeds $\sim 10\,{\rm M_\odot\ pc^{-2}}$, while in our simulations we find HI +HII surface densities that are $4-10\times$higher, indicating that there is a substantial fraction of ionised gas in our model galaxies.

4.4.2 CO line emission maps and resolved excitation conditions

Moment zero maps of the CO(1−0), CO(3−2) and CO(7−6) emission from G1, G2 and G3 are shown in Figure 4.9. Comparing with the H_2 surface density maps in Figure 4.8, both the CO(1−0) and CO(3−2) emission are seen to trace the H_2 gas distribution well, while the CO(7−6) emission is restricted to the central $\sim 7\,{\rm kpc}$ of the galaxies.

Also shown in Figure 4.9 (bottom row) are the azimuthally averaged CO 3−2/1−0 and 7−6/1−0 brightness temperature line ratios (denoted r_{32} and r_{76}, respectively) as a function of radius for G1, G2 and G3. The profiles show that the gas is clearly more excited in the central $\sim 5\,{\rm kpc}$, where typical values of r_{32} and r_{76} are $\sim 0.55-0.65$ and $\sim 0.005-0.05$, respectively, compared to $r_{32} \sim 0.5$ and $r_{76} < 0.01$ further out in the disk. This radial behaviour of the line ratios does not reflect the H_2 gas surface density, which peaks towards the centre rather than flattens, and gradually trails off out to $R \sim 12\,{\rm kpc}$ instead of dropping sharply at $R \sim 4-6\,{\rm kpc}$ (Figure 4.9). Rather, r_{32} and r_{76} seem to follow closely the behaviour of G_0 (and thus $\zeta_{\rm CR}$), which makes sense since G_0 and $\zeta_{\rm CR}$ are the most important factors for the internal GMC temperature distribution (Figure A.4). The central values for r_{32} and r_{76} increase when going from G1 to G3, as expected from the elevated levels of star formation density (and of G_0 and $\zeta_{\rm CR}$, accordingly) towards the centre. Beyond $\sim 6\,{\rm kpc}$ the line ratios are constant (~ 0.5 and < 0.01) and the same for all three galaxies, due to relatively similar FUV fields here.

At high-z, resolved observations of single CO lines are starting to appear (e.g. Genzel et al., 2013; Hodge et al., 2014), but since resolved excitation studies using multiple lines have so

[4]The H_2 surface density maps in Fig. 4.8 are averaged over areas $80\times 80\,{\rm pc}$ in size, and therefore give higher peak surface densities than the radial profiles which are averaged over $\sim 0.5\,{\rm kpc}$ wide annuli.

far not been obtained, we instead compare our results to local quiescent and extreme galaxies. The increased CO(3−2)/CO(1−0) line ratios towards the centres, are in agreement with observations of nearby galaxies as those carried out by Dumke (2000). Geach & Papadopoulos (2012) modeled two extreme cases of gas conditions, and found that while r_{32} might only be ~ 0.13 in quiescent environments, it is typically ~ 0.88 in denser gas. Mao et al. (2010) observed 125 nearby galaxies of different types and found r_{32} to be 0.61 ± 0.16 in normal galaxies, but > 0.89 in starbursts and (U)LIRGs. Iono et al. (2009) and Papadopoulos et al. (2012) finds slightly lower r_{32} in their samples of (U)LIRGs, with mean values of 0.48 ± 0.26 and 0.67 ± 0.62 respectively. In light of these observations, the r_{32} radial profiles of our model galaxies, suggest a denser, ULIRG-like environment in the central ($R < 5$ kpc) region together with a more quiescent and diffuse gas phase further out in the disk of $z = 2$ normal star-forming galaxies.

4.4.3 THE CO-TO-H_2 CONVERSION FACTOR

The CO-to-H_2 conversion factor ($\alpha_{\rm CO}$) connects CO(1−0) line luminosity (in surface brightness temperature units) with the molecular gas mass ($M_{\rm mol}$) as follows:

$$\alpha_{\rm CO} = \frac{M_{\rm mol}}{L'_{\rm CO(1-0)}}, \tag{4.14}$$

From the CO$(1-0)$ surface brightness and H_2 surface density maps of our model galaxies, we calculate $\alpha_{\rm CO}$ in radial bins surrounding the galaxy centres (Figure 4.9). The resulting radial $\alpha_{\rm CO}$ factors for our model galaxies lie in the range of $\sim 3-4\,{\rm M}_\odot\ {\rm pc}^{-2}\,({\rm K\,km\,s^{-1}})^{-1}$, and show a clear transition from lower $\alpha_{\rm CO}$-values inside the central $R \sim 5$ kpc to higher values at $R \gtrsim 6$ kpc. The drop in $\alpha_{\rm CO}$ from the disk average to the central value is about $\sim 1.1 - 1.2$, and while the same trend is present, observed $\alpha_{\rm CO}$ profiles drop by a higher factor. Recently, Blanc et al. (2013) measured a drop in $\alpha_{\rm CO}$ by a factor of two when going from $R \sim 7$ kpc to the centre of the Sc galaxy NGC 628, by using a constant gas depletion timescale in order to convert SFR surface densities into gas masses. Similarly, Sandstrom et al. (2013) found a drop by a factor of on average ~ 2 from $\alpha_{\rm CO}$ averaged across the galaxy disks to $\alpha_{\rm CO}$ of the central $R \leq 1$ kpc in 26 nearby spiral galaxies, by converting inferred dust masses into gas masses.

One could expect $\alpha_{\rm CO}$ to be correlated with Z', as higher metallicity means higher C and O abundances as well as more dust that help shielding H_2 formation sites from FUV radiation, and thereby increase the amount of CO, possibly lowering $\alpha_{\rm CO}$. On the other hand, although a higher FUV field leads to more ionization and photo-dissociation, it also increases the gas temperatures, which translates into more excited CO molecules and again a lower $\alpha_{\rm CO}$ factor. Comparison of the $\alpha_{\rm CO}$ radial profiles with those of G_0 and Z' in the bottom panel of Figure 4.8, suggests that the transition in $\alpha_{\rm CO}$ is caused by a change in G_0 rather than a change in Z', since G_0 generally starts to drop at around $R \sim 6$ kpc while Z' already drops drastically at 1 kpc from the centre. Our modeling therefore implies that $\alpha_{\rm CO}$ is controlled by G_0 rather than Z' in normal star-forming galaxies at $z \sim 2$, in agreement with the observations by Sandstrom et al. (2013) who do not find a strong correlation with Z'.

From the total molecular gas masses and CO$(1-0)$ luminosities of our galaxies, we derive their global $\alpha_{\rm CO}$ factors. This gives global values of $\alpha_{\rm CO} = 3.1, 2.8$ and $2.8\,{\rm M}_\odot\ {\rm pc}^{-2}\,({\rm K\,km\,s^{-1}})^{-1}$ for G1, G2 and G3, respectively. These values are lower (by a factor ~ 0.6) than the global Milky Way value of $\alpha_{\rm CO,MW} \simeq 4.4 \pm 0.9\,{\rm M}_\odot\,{\rm pc}^{-2}\,({\rm K\,km\,s^{-1}})^{-1}$, calibrated from dynamical, dust, and γ-ray studies (e.g., Strong & Mattox, 1996; Dame et al., 2001; Pineda et al., 2008), and higher than the typical mergers/starburst $\alpha_{\rm CO}$-values ($\sim 0.2 \times \alpha_{\rm CO,MW}$) inferred from CO dynamical studies of local ULIRGs (e.g., Solomon et al., 1997; Downes & Solomon, 1998; Bryant & Scoville, 1999) and $z \sim 2$ SMGs (e.g., Tacconi et al., 2008). Our $\alpha_{\rm CO}$-values are, however, identical to those inferred from dynamical modeling of $z \sim 1.5$ BzKs ($\alpha_{\rm CO} = 3.6 \pm 0.8\,{\rm M_\odot\,pc^{-2}\,(K\,km\,s^{-1})^{-1}}$; Daddi et al., 2010).

On the other hand, the $\alpha_{\rm CO}$ factors of the $z \sim 1-1.3$ star-forming galaxies studied by Magnelli et al. (2012) and occupying the same region of the M_*–SFR plan as our model galaxies, are $\sim 5-20\,{\rm M_\odot\,pc^{-2}\,(K\,km\,s^{-1})^{-1}}$ when converting dust masses to gas masses using a metallicity-dependent gas-to-dust ratio. Magnelli et al. (2012) find that the same galaxies have relatively low dust temperatures of $\lesssim 28\,{\rm K}$ compared to the galaxies further above the main sequence of Rodighiero et al. (2010). The fact that the main-sequence galaxies of Magnelli et al. (2012) are all of near-solar metallicity as ours, cf. Table 4.1, suggests that other factors, such as dust temperature caused by strong FUV radition, can be more important than metallicity in regulating $\alpha_{\rm CO}$.

4.4.4 Global CO line luminosities and spectral line energy distributions

The global CO SLEDs of G1, G2 and G3 are shown in Figure 4.10 in three different incarnations: 1) total CO line luminosities ($L'_{\rm CO_{J,J-1}}$), 2) brightness temperature ratios ($T_{\rm B,CO_{J,J-1}}/T_{\rm B,CO_{1,0}} = L'_{\rm CO_{J,J-1}}/L'_{\rm CO_{1,0}}$) and 3) line intensity ratios ($I_{\rm CO_{J,J-1}}/I_{\rm CO_{1,0}} = L'_{\rm CO_{J,J-1}}/L'_{\rm CO_{1,0}} \times (\nu_{\rm CO_{J,J-1}}/\nu_{\rm CO_{1,0}})^2$). In Figure 4.10 we have also compiled all relevant CO observations of normal star-forming galaxies at $z \sim 1-3$ to date in order to facilitate a comparison with our simulated CO SLEDs of such galaxies. Samples are the same as in Figure 4.2, but including an additional 7 star-forming galaxies (SFGs) at $z \sim 1.2$ (Magnelli et al., 2012) and another 39 SFGs at $z \sim 1-1.5$ (Tacconi et al., 2013). The first sample of galaxies are all detected in CO(2−1) as well as in *Herschel*/PACS bands, and have $\log M_* = 10.36 - 11.31$ and SFR$\sim 29 - 74\,{\rm M_\odot\ yr^{-1}}$. The sample from Tacconi et al. (2013) comes from the Extended Growth Strip International Survey (EGS), is covered by the CANDELS and 3D-HST programs ($J - H$ bands and Hα respectively), and has $\log M_* = 10.40 - 11.23$ and SFR$\sim 28 - 630\,{\rm M_\odot\ yr^{-1}}$.

First, we compare the total CO(3−2) luminosities of our model galaxies with those of the $z \sim 2-2.5$ BX/BM galaxies of Tacconi et al. (2013), which are not only closest in redshift to our model galaxies but also occupy the same region of the SFR−M_* plane (see Figure 4.2). We find that G2 and G3, the two most massive ($M_* > 10^{11}\,{\rm M_\odot}$) and star-forming (SFR $\gtrsim 80\,{\rm M_\odot\ yr^{-1}}$) galaxies of our simulations, have CO(3−2) luminosities of $\sim 2.5-3.3\times10^9\,{\rm K\,km\,s^{-1}\ pc^2}$, which is $\sim 3.5-4.7$ times lower than the average CO(3−2) luminosity of the BX/BM galaxies ($\sim 1.2 \pm 0.9 \times 10^{10}\,{\rm K\,km\,s^{-1}\ pc^2}$). For G1, the offset is about a factor of ~ 14. For the $z \sim 1.5$ BzKs, the offset in $L'_{\rm CO}$ from our model galaxies is even larger. Our G2 and G3 simulations, however, are able to reproduce the CO luminosities of the $z \simeq 1-1.5$ SFGs observed by Magnelli et al. (2012) and Tacconi et al. (2013), which span a range in CO(2−1) and CO(3−2) luminosities of $(3.6-12.5)\times10^9$ and $(1.4-41.3)\times10^9\,{\rm K\,km\,s^{-1}\,pc^2}$, respectively. As mentioned in Section 4.4.1, the molecular gas mass fractions of our galaxies is about a factor 6 below the mean of the observed galaxies at $z \sim 1-2.5$ with which we compare. We can make a rough correction for this by scaling the CO line luminosities up by the same factor, in order to account for the missing gas. By doing so, all CO line luminosities of our model galaxies come to lie within the observed ranges at CO$(2-1)$ and CO$(3-2)$ and less than 2σ away from the mean of each

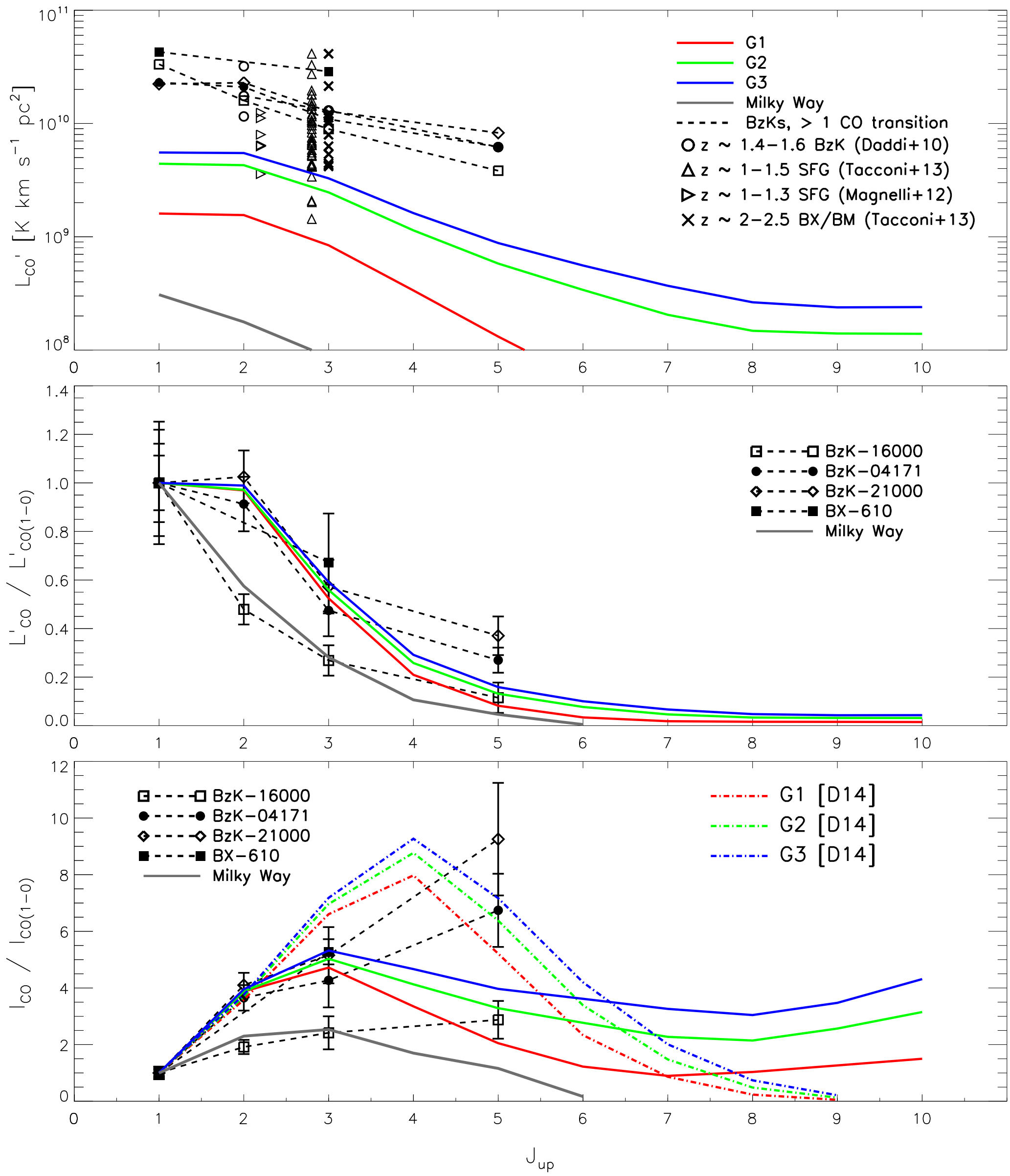

Figure 4.10 Global CO SLEDs of our three model galaxies G1, G2 and G3 shown as red, green and blue solid curves, respectively. The SLEDs are given as absolute line luminosities in units of K km s^{-1} pc^{-2} (top panel), as brightness temperature ratios normalized to the CO(1−0) transition (middle panel), and as velocity-integrated intensity ratios normalized to CO(1−0) (bottom panel). The model CO SLEDs are compared with observations of $z \sim 1.4 - 1.6$ BzK galaxies (CO(1−0) and CO(2−1); Dannerbauer et al., 2009; Daddi et al., 2010, 2014; Aravena et al., 2010, 2014), $z \sim 1 - 1.5$ star-forming galaxies (CO(3−2); empty triangles; Tacconi et al., 2013), $z \sim 1 - 1.3$ star-forming galaxies (CO(1−0) and CO(2−1); rightfacing triangles; Magnelli et al., 2012), and $z \sim 2 - 2.5$ BX/BM galaxies (CO(3−2); crosses; Tacconi et al., 2013). Also shown is the global CO SLED of the Milky Way (grey line; Fixsen et al., 1999). Three BzK galaxies (BzK−16000, BzK−4171, and BzK−21000) have been observed in CO$(1-0)$ and at least one additional transition to date, and are highlighted by connecting dashed lines. Also shown in the bottom panel, with dash-dotted lines, are the line ratio predictions of Narayanan & Krumholz (2014) (D14), calculated for the $\Sigma_{\rm SFR}$ of our galaxies (see text).

observed sample.

Differences in the global CO excitation conditions between G1, G2 and G3 are best seen in the CO(1−0) normalized luminosity (and intensity) ratios, i.e., middle (and bottom) panel in Figure 4.10). The CO SLEDs of all three galaxies follow each other quite closely up to the $J = 3-2$ transition where the SLEDs all peak. At higher J, the SLEDs diverge more and more until $J_{\rm up} = 6$ after which they remain at a relatively constant separation from each other. While the metallicity distributions in G1, G2 and G3 are similar (see Figure A.3), the rise in G_0 presents a likely cause to the increasing high-J flux when going from G1 to G3, as higher G_0 leads to more flux primarily in the $J > 4$ transitions (see Figure A.5).

Our simulated galaxies are seen to have CO 2−1/1−0, 3−2/1−0, and 5−4/1−0 brightness temperature ratios of $r_{21} \simeq 1$, $r_{32} \simeq 0.6$, and $r_{54} \simeq 0.2$, respectively. The first two ratios compare extremely well with the line ratios measured for BzK−4171 and BzK−21000, i.e., $r_{21} \simeq 0.9-1$, and $r_{32} \simeq 0.5-0.6$ (Dannerbauer et al., 2009; Aravena et al., 2010; Daddi et al., 2010, 2014), and suggest that our simulations are able to emulate the typical gas excitation conditions responsible for the excitation of the low-J lines in normal $z \sim 1-3$ SFGs. In contrast, $r_{54} = 0.3-0.4$ observed in BzK−4171 and BzK−21000 (Daddi et al., 2014), is nearly 2× higher than our model predictions. Daddi et al. (2014) argue that this is evidence for a component of denser and possibly warmer molecular gas, not probed by the low-J lines. In this picture, we would expect CO(4−3) to probe both the cold, low-excitation gas as well as the dense and possibly warm star-forming gas traced by the CO(5−4) line; and we would expect CO(6−5) to be arising purely from this more highly excited phase and thus departing even further from our models. Thus, although our G2 and G3 simulations do a good job at matching the low-J CO lines up to $J_{\rm up} = 3$, it would seem the method has problems at higher CO transitions, where it only predicts a rise in flux for transitions above $J_{\rm up} \sim 8$.

However, significant scatter in the CO line ratios of main-sequence galaxies is to be expected, as demonstrated by the significantly lower line ratios observed towards BzK−16000: $r_{21} \simeq 0.4$, $r_{32} \simeq 0.3$, and $r_{54} \simeq 0.1$ (Aravena et al., 2010; Daddi et al., 2010, 2014) and, in fact, the average r_{54} for all three BzK galaxies above ($\simeq 0.2$; Daddi et al. (2014)) is consistent with our models. It may be that G2 and G3, and perhaps even G1, are more consistent with the CO SLEDs of the bulk $z \sim 1-3$ main-sequence galaxies. We stress, that to date, no $z \sim 1-3$ main sequence galaxies have been observed in the $J = 4-3$ nor the $6-5$ transitions, and observations of these lines, along with low- and high-J lines in many more BzK and main-sequence $z \simeq 1-3$ galaxies are needed in order to fully delineate the global CO SLEDs in a statistically robust way.

4.5 Comparison with other models

`SÍGAME` relies on subgrid physics to describe the molecular gas in high-z galaxies, e.g., cloud masses, their density and temperature structure etc. It is assumed that the scaling and thermal balance equations that have been established and calibrated to GMC complexes in our own Milky Way can be extrapolated to the ISM conditions in high-z galaxies. Similarly, all other numerical simulations made to date of the molecular gas in galaxies and their CO line emission rely to smaller or larger degree on subgrid physics (e.g., Narayanan et al., 2006; Pelupessy et al., 2006; Greve & Sommer-Larsen, 2008; Christensen et al., 2012; Lagos et al., 2012; Muñoz & Furlanetto, 2013; Narayanan & Krumholz, 2014; Lagos et al., 2012; Popping et al., 2014). In this section we will highlight and discuss some of the differences in the subgrid physics between

SÍGAME and other simulations.

First, however, we compare the SÍGAME CO SLEDs of G1, G2, and G3 with those predicted by other CO emission simulations of similar main-sequence galaxies. A direct comparison with SÍGAME can be made in the case of the models presented by Narayanan & Krumholz (2014), where the global CO SLED is parametrised as a function of the SFR surface density ($\Sigma_{\rm SFR}$). The SFR surface densities (averaged over the inner $5\,{\rm kpc}$) of G1, G2, and G3 are 0.11, 0.21, and $0.34\,{\rm M_\odot\ yr^{-1}\ kpc^{-2}}$, respectively, and the corresponding CO SLEDs inferred from the Narayanan & Krumholz (2014) parametrisation are shown as dash-dotted lines in Figure 4.10 (bottom panel). The SLEDs of Narayanan & Krumholz (2014) all peak at $J = 4-3$ and not $3-2$ as our SLEDs, and the line flux ratios are significantly higher at transitions between $J = 3-2$ and $6-5$. While a direct comparison is not possible, we note that (Lagos et al., 2012) provide CO SLED predictions for $z = 2$ main-sequence galaxies are in agreement with those of Narayanan & Krumholz (2014), when comparing galaxies of similar infrared luminosities as ours. Converting SFRs to infrared luminosities with the Kennicutt (1998) conversion factor adapted to a Chabrier IMF, $L_{\rm IR}/L_\odot = {\rm SFR}/[{\rm M_\odot\,yr^{-1}}] \times 10^{10}$ (see Daddi et al., 2010), our simulated galaxies G1, G2 and G3 have $L_{\rm IR}$ of 0.40, 0.80 and $1.4 \times 10^{12} L_\odot$, respectively, which is in the bottom of the range typically observed for BzK galaxies ($L_{\rm IR}$ from 0.6 to $4.0 \times 10^{12} L_\odot$; Daddi et al., 2010). For galaxies with infrared luminosities $L_{\rm IR} \sim 10^{11.25} - 10^{12}\,L_\odot$, corresponding to the range of $L_{\rm IR}$ in our simulated galaxies, Lagos et al. (2012) predict CO SLEDs that peak in the CO$(4-3)$ transition, that is, again implying slightly more excited gas than SÍGAME does. Popping et al. (2014) find an interesting trend with redshift in their semi-analytical study of MS galaxies at $z = 0$, 1.2 and 2; Galaxies with far-infrared (FIR) luminosities of $\log{(L_{\rm FIR}/L_\odot)} = 11-12$ peak at CO$(3-2)$ or CO$(4-3)$ at $z = 0$, but at CO$(6-5)$ at $z = 2$. Our galaxies lie in the same FIR luminosity range ($\log{(L_{\rm FIR}/L_\odot)} = 11.4 - 11.9$ when converting $\rm L_{IR}$ to $\rm L_{FIR}$ by dividing by 1.7; Chapman et al., 2000), but again SÍGAME predicts less excited gas when comparing to the $z \sim 2$ MS galaxies of Popping et al. (2014).

• *Implementation of G_0 and $\zeta_{\rm CR}$*

SÍGAME stands out from most other simulations to date in the way the FUV radiation field and the CR flux that impinge on the molecular clouds are modelled and implemented. Most simulations adopt a fixed, galaxy-wide value of G_0 and $\zeta_{\rm CR}$, scaled by the total SFR or average gas surface density across the galaxy (e.g., Lagos et al., 2012; Narayanan & Krumholz, 2014). SÍGAME refines this scheme by determining a spatially varying G_0 (and $\zeta_{\rm CR}$) set by the local SFRD, as described in Section 4.3.3. By doing so, we ensure that the molecular gas in our simulations is calorimetrically coupled to the star formation in their vicinity. If we adopt the method of Narayanan & Krumholz (2014) and calculate a global value for G_0 by calibrating to the MW value, using ${\rm SFR_{MW}} = 2\,{\rm M_\odot\ yr^{-1}}$ and $G_{0,\rm MW} = 0.6\,$Habing, our galaxies would have G_0 ranging from about 12 to 42, whereas, with the SFR surface density scaling of Lagos et al. (2012), global G_0 values would lie between about 6 and 9. For comparison, the locally determined G_0 in our model galaxies spans a larger range from 0.3 to 27 (see Figure A.3). Narayanan & Krumholz (2014) determines the global value of $\zeta_{\rm CR}$ as $2 \times 10^{-17} Z' {\rm s^{-1}}$, corresponding to values of $3.7 - 6.2 \times 10^{-17}{\rm s^{-1}}$ in our model galaxies, when using the mass-weighted mean of Z' in each galaxy. Typical values adopted in studies of ISM conditions are around $(1-2) \times 10^{-17}{\rm s^{-1}}$ (Wolfire et al., 2010; Glover & Clark, 2012), but again, the local values of $\zeta_{\rm CR}$ in our galaxies span a larger range, from 1.3×10^{-17} to $1.3 \times 10^{-15}\,{\rm s^{-1}}$.

As a test we ran SÍGAME on G1, G2 and G3 adopting fixed global values of G_0 and $\zeta_{\rm CR}$ equal to those derived from the method of Narayanan & Krumholz (2014), i.e., $G_0 = [12, 24, 42]\,{\rm Habing}$

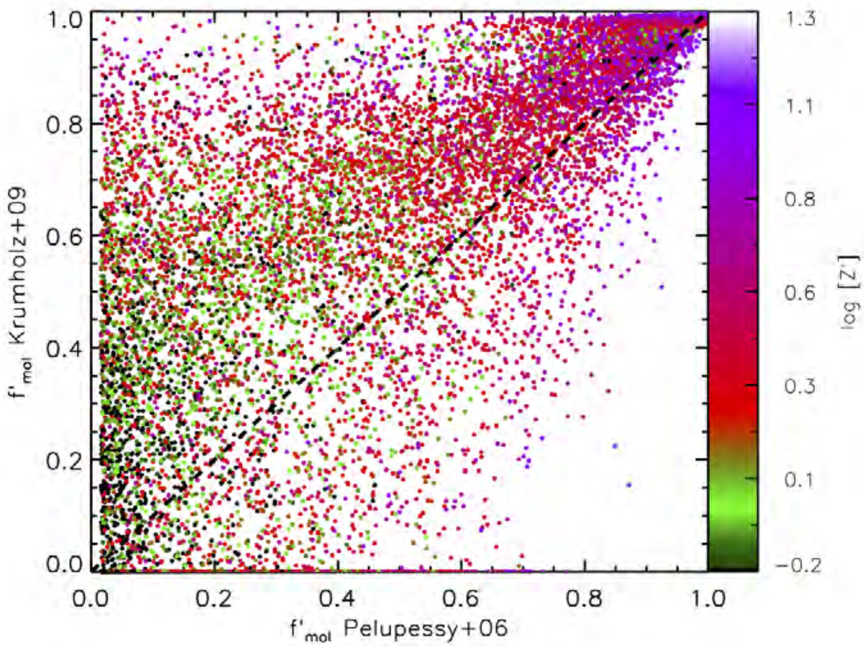

Figure 4.11 Comparison of two methods for calculating the molecular gas mass fraction, $f'_{\rm mol}$: That of Pelupessy et al. (2006) used in this work (abscissa) and that of Krumholz et al. (2009) (ordinate) used by e.g., Narayanan & Krumholz (2014), color-coded by metallicity.

and $\zeta_{\rm CR} = [3.7, 6.2, 4.3] \times 10^{-17}\,{\rm s}^{-1}$ for G1, G2, and G3, respectively. The peak J-value of the CO SLED does not change, but the luminosity at $J_{\rm upper} \gtrsim 2$ grows when keeping G_0 and $\zeta_{\rm CR}$ fixed as compared to when using eq. 4.3 and 4.10. That way, the $J_{\rm upper} = 4-6$ luminosities are ~ 1.2, $1.3-1.5$ and $1.4-2.1$ higher for G1, G2 and G3.

• *The molecular gas mass fraction*

In SÍGAME the molecular gas mass fraction ($f'_{\rm mol}$) is calculated following the work by Pelupessy et al. (2006), in which $f'_{\rm mol}$ depends on temperature, metallicity, local FUV field, and boundary pressure on the gas cloud in question. Other methods exist, such as those of Blitz & Rosolowsky (2006) and Krumholz et al. (2009) (K09). Most recently, Narayanan & Krumholz (2014) applied the K09 model in order to derive the H_2 gas mass, and we compare this method to that of Pelupessy et al. (2006) (P06), used by SÍGAME, in Figure 4.11. Both methods produce higher $f'_{\rm mol}$ for increasingly more metal-rich gas, as expected since higher metallicity leads to more dust onto which the H_2 molecules can form. The K09 method tends to give larger values of $f'_{\rm mol}$ than the P06 method, for all metallicities as the colours of Figure 4.11 show. This leads to systematically higher total molecular gas masses when using the method of K09 instead of P06. In particular, the molecular gas mass fractions, $f_{\rm mol} = M_{\rm mol}/(M_* + M_{\rm mol})$, of G1, G2 and G3 increase from 8.5, 7.8 and 6.8 % to 9.8, 10.3 and 9.5 % respectively. While significant, the elevated values for $f_{\rm mol}$ of our model galaxies are still below those typically observed for star-forming galaxies at $z \sim 2$ (see Section 4.4.1).

A common feature of the above H I $\longrightarrow H_2$ prescriptions is that they assume an instantaneous HI to H_2 conversion, once the conditions for H_2 formation are met. By actually incorporating their HI $\longrightarrow$$H_2$ subgrid model in an N-body/SPH dwarf galaxy simulation, Pelupessy et al. (2006) find that typical timescales for H_2 cloud formation are of order $\sim 10^7$ yr. Such timescales are comparable to a wide variety of processes that can potentially alter or even fully disrupt typical molecular clouds, leading to the conclusion that modeling of the HI $\longrightarrow$$H_2$ transition should be time-dependent, in order to embrace such phenomena as clump-clump collisions and star formation, which can drive H_2 formation in both directions. Relying on the findings of Narayanan et al. (2011) and Krumholz & Gnedin (2011), the static solution for H_2 formation is a valid approximation for $Z' > 0.01$, which is the case for the three model galaxies studied here, but restricts `SÍGAME` to the domain of galaxies with at least $Z' \sim 0.01$.

• *CO abundance*

For the density of CO, we assumed that CO follows the structure of H_2 gas, and adopted a constant Galactic abundance of $[\mathrm{CO/H_2}] = 2 \times 10^{-4}$. In reality, H_2 gas can self-shield better than the CO gas, creating an outer region or envelope of 'CO-dark' gas (Bolatto et al., 2008). Observations in the Milky Way by Pineda et al. (2013) indicate that the amount of dark gas grows with decreasing metallicity and the resulting absence of CO molecules. By modeling a dynamically evolving ISM with cooling physics and chemistry incorporated on small scales, Smith et al. (2014) showed that in a typical MW-like disk of gas, the dark gas mass fraction, f_{DG}, defined as having $W_{\mathrm{CO}} < 0.1\,\mathrm{K\,km\,s^{-1}}$, is about 42 %, but up to 62 % in a radiation field ten times that of the solar neighbourhood. While Smith et al. (2014) keept metallicity constant throughout the disk, Wolfire et al. (2010) found f_{DG} values of about $0.5 - 0.7$ for the low metallicity cases with $Z' = 0.5$, however using a 1D PDR model only. Such studies show, that $[\mathrm{CO/H_2}]$ is lower in regions of low metallicity and/or intense FUV fields, effectively leading to underestimates of the α_{CO} conversion factor when not accounted for in models. Since in this paper we have restricted our simulations to main-sequence galaxies with solar or higher than solar metallicities, adopting a constant Galactic [CO/H_2] seems a reasonable choice, but see Lagos et al. (2012), Narayanan et al. (2012) and Narayanan & Krumholz (2014) for alternative approaches.

• *GMC density and thermal structure*

When solving for the temperature structure of each GMC, `SÍGAME` includes only the most dominant atomic and molecular species in terms of heating and cooling efficiencies. In this approximation, we also neglect X-ray irradiation and turbulence, leaving these for a future study. We have, however, checked our $T_{\mathrm{k}} - n_{\mathrm{H_2}}$ curves in Figure A.4 against those of Glover & Clark (2012), who performed time-resolved, high-resolution ($\delta m \simeq 0.05 - 0.5\,\mathrm{M_\odot}$) SPH simulations of individual FUV irradiated molecular clouds using a chemical network of 32 species (see their Figure 2). Overall, there is great similarity in the T_{k} vs. $n_{\mathrm{H_2}}$ behaviour of the two sets of simulations. This includes the same main trend of decreasing temperature with increasing hydrogen density, as well as the local increase in T_{k} at $\sim 10^3 - 10^4\,\mathrm{cm^{-3}}$ and the subsequent decrease to $T_{\mathrm{k}} < 10\,\mathrm{K}$ at $n_{\mathrm{H_2}} > 10^{5.5}\,\mathrm{cm^{-3}}$. Thus, our GMCs models, despite their simplified density profiles and chemistry, seem to agree well with much more detailed simulations and we take this as an indication that they also mimic the conditions in real molecular clouds well.

4.6 CONCLUSIONS

In this chapter we have presented `SÍGAME`, a code that simulates the molecular line emission of galaxies via a detailed post-processing of the outputs from cosmological SPH simulations.

A sequence of subgrid prescriptions are applied to a simulation snapshot in order to derive the molecular gas density and temperature from the SPH particle information such as SFR, gas density, temperature and metallicity. `SÍGAME` stands out from other methods of its kind by combining cosmological galaxy simulations with the following aspects:

1. *Local FUV field and cosmic ray ionization rate*
   In `SÍGAME`, the energetics of the ISM are driven by the local star formation rate density, which is what sets the local FUV and cosmic ray field, i.e. G_0 and $\zeta_{\rm CR}$ respectively, and thus the heating and ionization of the gas. Unlike other simulations, `SÍGAME` can therefore be used to study resolved properties within a galaxy, as for example line ratios and $\alpha_{\rm CO}$ factors.

2. *Multiphase ISM*
   The partly ionised gas in the SPH simulation is first cooled down to a cold neutral phase by including only heating by cosmic rays, counter-balanced by cooling via metal line emission, recombination processes and free-free emission. In a second cooling step, `SÍGAME` determines the internal radial temperature profile of each GMC by considering cosmic ray heating and photo-electric heating by FUV photons as wells as cooling by H_2, CO, OI, [CII] lines in addition to gas-dust interactions.

3. *Radiative transfer on sub-parsec scales*
   We constructed a grid of GMC models that probe a large range in $m_{\rm GMC}$, Z' and G_0. On each model, the novel radiative transfer code `LIME` was employed for determining the CO line emission, so that `SÍGAME` can interpolate in [$m_{\rm GMC}$,Z',G_0] - space and sum up the emission in several CO lines for an entire galaxy in a few minutes.

We have used `SÍGAME` to create line emission velocity-cubes of the full CO rotational ladder for three cosmological N-body/SPH simulations of massive ($M_* \gtrsim 10^{10.5}\,{\rm M}_\odot$) main-sequence galaxies at $z = 2$.

Molecular gas is produced more efficiently towards the centre of each galaxy, and while HI surface gas densities (including helium) do not exceed $\sim 100\,{\rm M}_\odot$ pc^{-2} anywhere in the disk, central molecular gas surface densities reach $\sim 1000\,{\rm M}_\odot$ pc^{-2} on spatial scales of $80\,{\rm pc} \times 80\,{\rm pc}$, in good agreement with observations made at similar spatial resolution. This strong increase in molecular surface density is brought on by a similar increase in total gas surface density, overcoming the increase in photo-dissociating FUV field towards the centre of each galaxy.

Turning to the CO emission, the velocity-integrated moment 0 maps reveal distinct differences in the various transitions as molecular gas tracers. The morphology of molecular gas in our model galaxies is well reproduced in CO(1-0), but going to higher transitions, the region of CO emitting gas shrinks towards the galaxy centres. The global CO SLEDs of our simulated galaxies all peak at $J = 3-2$, indicating a dominating low-excitation gas. Recent CO($5-4$) observations of $z \sim 1.5$ BzK galaxies seem to suggest that these galaxies actually peak at higher J, presenting an important test case that we will be following closely in the future in order to benchmark `SÍGAME` fully at $z \sim 2$ before moving to e.g. higher redshifts. The CO line luminosities of our model galaxies, are typically $2-3\sigma$ below the mean of corresponding observed samples at redshifts $z \sim 1-2.5$. The low luminosities are most likely a consequence of molecular gas mass fractions in our galaxies about 6 times below the observed values in star-forming galaxies at $z = 1-2.5$. Roughly adjusting for this discrepancy, by multiplying the CO line luminosities by a factor of 6, our model galaxies come within the range of observed CO($2-1$)

and CO($3-2$) luminosities. The low CO luminosities of our model galaxies can therefore be explained by low molecular gas mass fractions, to a large part due to relatively low SPH gas mass fractions to begin with ($9-26\,\%$).

Combining the derived H_2 gas masses with the CO($1-0$) line emission found, we investigate local variations in the CO-H_2 conversion factor $\alpha_{\rm CO}$. The radial $\alpha_{\rm CO}$ profiles all show a decrease towards the galaxy centres, dropping by a factor of $\sim 1.1-1.2$ in the central $R \leq 1\,$kpc region compared to the disk average, and the main driver being the FUV field rather than a gradient in density or metallicity. We believe that the primary reason as to why our galaxies do not display a gradient as steep as that typically observed locally (~ 2), is the assumption of a constant $[{\rm CO/H_2}]$ abundance ratio. Global $\alpha_{\rm CO}$ factors range from 2.8 to $3.1\,{\rm M_\odot}$ ${\rm pc^{-2}}\,({\rm K\,km\,s^{-1}})^{-1}$ or about 0.6 times the MW-value, but closer to values for $z\sim 1.5$ normal star-forming galaxies identified with the BzK colour criteria.

The CO luminosity ratios of CO $3-2/1-0$ and $7-6/1-0$ (r_{32} and r_{76} respectively) drop off in radius about where the FUV radiation drops in intensity, and thus likely controlled by FUV field as $\alpha_{\rm CO}$. The global ratios of $r_{21}\simeq 1$ and $r_{32}\simeq 0.6$ agree very well with observations of BzK galaxies, while the r_{54} of about 0.2 is low compared to recent observations in BzK$-$4171 and BzK$-$21000. However, more observations of $J_{\rm up}>3$ lines towards high-z main-sequence galaxies, such as the BzKs, are still needed in order to determine the turn-over in their CO SLEDs and better constrain the gas excitation.

SÍGAME is in principle able to simulate the emission from a broad range of molecular and atomic lines in the far-IR/mm wavelength regime provided measured collision rates, such as those found in the LAMDA database[5], are available. For more on future applications of SÍGAME, see the Outlook chapter after the following chapter.

[5] http://www.strw.leidenuniv.nl/moldata/, Schöier et al. (2005)

4.7 References

Aalto, S. 2013, in IAU Symposium, Vol. 292, IAU Symposium, ed. T. Wong & J. Ott, 199–208

Ackermann, M., Ajello, M., Allafort, A., et al. 2013, Science, 339, 807

Adelberger, K. L., Steidel, C. C., Shapley, A. E., et al. 2004, ApJ, 607, 226

Aravena, M., Carilli, C., Daddi, E., et al. 2010, ApJ, 718, 177

Aravena, M., Hodge, J. A., Wagg, J., et al. 2014, MNRAS, 442, 558

Asplund, M., Grevesse, N., Sauval, A. J., & Scott, P. 2009, ARA&A, 47, 481

Bigiel, F., Leroy, A., Walter, F., et al. 2008, AJ, 136, 2846

Black, J. H., & Dalgarno, A. 1977, ApJs, 34, 405

Blanc, G. A., Schruba, A., Evans, II, N. J., et al. 2013, ApJ, 764, 117

Blitz, L., Fukui, Y., Kawamura, A., et al. 2007, Protostars and Planets V, 81

Blitz, L., & Rosolowsky, E. 2006, ApJ, 650, 933

Bolatto, A. D., Leroy, A. K., Rosolowsky, E., Walter, F., & Blitz, L. 2008, ApJ, 686, 948

Bolatto, A. D., Wolfire, M., & Leroy, A. K. 2013, ARA&A, 51, 207

Bovy, J., Rix, H.-W., & Hogg, D. W. 2012, ApJ, 751, 131

Brinch, C., & Hogerheijde, M. R. 2010, A&A, 523, A25

Bryant, P. M., & Scoville, N. Z. 1999, AJ, 117, 2632

Carroll, T. J., & Goldsmith, P. F. 1981, ApJ, 245, 891

Casey, C. M., Narayanan, D., & Cooray, A. 2014, Phys. Rep., 541, 45

Cazaux, S., & Spaans, M. 2004, ApJ, 611, 40

Chabrier, G. 2003, PASP, 115, 763

Chapman, S. C., Scott, D., Steidel, C. C., et al. 2000, MNRAS, 319, 318

Christensen, C., Quinn, T., Governato, F., et al. 2012, MNRAS, 425, 3058

Daddi, E., Cimatti, A., Renzini, A., et al. 2004, ApJ, 617, 746

Daddi, E., Dickinson, M., Morrison, G., et al. 2007, ApJ, 670, 156

Daddi, E., Bournaud, F., Walter, F., et al. 2010, ApJ, 713, 686

Daddi, E., Dannerbauer, H., Liu, D., et al. 2014, ArXiv e-prints

Dame, T. M., Hartmann, D., & Thaddeus, P. 2001, ApJ, 547, 792

Dannerbauer, H., Daddi, E., Riechers, D. A., et al. 2009, ApJL, 698, L178

Downes, D., & Solomon, P. M. 1998, ApJ, 507, 615

Draine, B. T. 2011, Physics of the Interstellar and Intergalactic Medium (Princeton University Press)

Dumke, M. 2000, in Astronomical Society of the Pacific Conference Series, Vol. 221, Stars, Gas and Dust in Galaxies: Exploring the Links, ed. D. Alloin, K. Olsen, & G. Galaz, 15

Elbaz, D., Daddi, E., Le Borgne, D., et al. 2007, A&A, 468, 33

Fixsen, D. J., Bennett, C. L., & Mather, J. C. 1999, ApJ, 526, 207

Geach, J. E., & Papadopoulos, P. P. 2012, ApJ, 757, 156

Genzel, R., Tacconi, L. J., Gracia-Carpio, J., et al. 2010, MNRAS, 407, 2091

Genzel, R., Tacconi, L. J., Kurk, J., et al. 2013, ApJ, 773, 68

Gieles, M., Portegies Zwart, S. F., Baumgardt, H., et al. 2006, MNRAS, 371, 793

Glover, S. C. O., & Clark, P. C. 2012, MNRAS, 421, 9

Glover, S. C. O., & Mac Low, M.-M. 2011, MNRAS, 412, 337

Goldsmith, P. F. 2001, ApJ, 557, 736

Greve, T. R., & Sommer-Larsen, J. 2008, A&A, 480, 335

Greve, T. R., Leonidaki, I., Xilouris, E. M., et al. 2014, ApJ, 794, 142

Güver, T., & Özel, F. 2009, MNRAS, 400, 2050

Heiderman, A., Evans, II, N. J., Allen, L. E., Huard, T., & Heyer, M. 2010, ApJ, 723, 1019

Heyer, M., Krawczyk, C., Duval, J., & Jackson, J. M. 2009, ApJ, 699, 1092
Heyer, M. H., Carpenter, J. M., & Snell, R. L. 2001, ApJ, 551, 852
Hodge, J. A., Riechers, D., Decarli, R., et al. 2014, ArXiv e-prints
—. 2015, ApJ, 798, L18
Ingalls, J. G., Bania, T. M., Boulanger, F., et al. 2011, ApJ, 743, 174
Iono, D., Wilson, C. D., Yun, M. S., et al. 2009, ApJ, 695, 1537
Kauffmann, J., Pillai, T., Shetty, R., Myers, P. C., & Goodman, A. A. 2010, ApJ, 712, 1137
Kennicutt, Jr., R. C. 1998, ARA&A, 36, 189
Krumholz, M. R., & Gnedin, N. Y. 2011, ApJ, 729, 36
Krumholz, M. R., McKee, C. F., & Tumlinson, J. 2009, ApJ, 699, 850
Lagos, C. d. P., Bayet, E., Baugh, C. M., et al. 2012, MNRAS, 426, 2142
Larson, R. B. 1981, MNRAS, 194, 809
Lee, H.-H., Bettens, R. P. A., & Herbst, E. 1996, A&As, 119, 111
Leroy, A. K., Walter, F., Brinks, E., et al. 2008, AJ, 136, 2782
Liu, T., Wu, Y., & Zhang, H. 2013, ApJ, 775, L2
Magnelli, B., Saintonge, A., Lutz, D., et al. 2012, A&A, 548, A22
Mao, R.-Q., Schulz, A., Henkel, C., et al. 2010, ApJ, 724, 1336
McMillan, P. J. 2011, MNRAS, 414, 2446
Miettinen, O., Harju, J., Haikala, L. K., Kainulainen, J., & Johansson, L. E. B. 2009, A&A, 500, 845
Monaghan, J. J. 2005, Reports on Progress in Physics, 68, 1703
Muñoz, J. A., & Furlanetto, S. R. 2013, MNRAS, 435, 2676
Narayanan, D., Cox, T. J., Shirley, Y., et al. 2008a, ApJ, 684, 996
Narayanan, D., & Hopkins, P. F. 2013, MNRAS, 433, 1223
Narayanan, D., Krumholz, M., Ostriker, E. C., & Hernquist, L. 2011, MNRAS, 418, 664
Narayanan, D., & Krumholz, M. R. 2014, MNRAS, 442, 1411
Narayanan, D., Krumholz, M. R., Ostriker, E. C., & Hernquist, L. 2012, MNRAS, 421, 3127
Narayanan, D., Cox, T. J., Robertson, B., et al. 2006, ApJL, 642, L107
Narayanan, D., Cox, T. J., Kelly, B., et al. 2008b, ApJs, 176, 331
Norman, C. A., & Spaans, M. 1997, ApJ, 480, 145
Papadopoulos, P. P., Isaak, K., & van der Werf, P. 2010, ApJ, 711, 757
Papadopoulos, P. P., & Thi, W.-F. 2013, in Advances in Solid State Physics, Vol. 34, Cosmic Rays in Star-Forming Environments, ed. D. F. Torres & O. Reimer, 41
Papadopoulos, P. P., Thi, W.-F., Miniati, F., & Viti, S. 2011, MNRAS, 414, 1705
Papadopoulos, P. P., van der Werf, P. P., Xilouris, E. M., et al. 2012, MNRAS, 426, 2601
Papovich, C., Finkelstein, S. L., Ferguson, H. C., Lotz, J. M., & Giavalisco, M. 2011, MNRAS, 412, 1123
Pelupessy, F. I. 2005, PhD thesis, Leiden Observatory, Leiden University, P.O. Box 9513, 2300 RA Leiden, The Netherlands
Pelupessy, F. I., Papadopoulos, P. P., & van der Werf, P. 2006, ApJ, 645, 1024
Pineda, J. E., Caselli, P., & Goodman, A. A. 2008, ApJ, 679, 481
Pineda, J. L., Langer, W. D., Velusamy, T., & Goldsmith, P. F. 2013, A&A, 554, A103
Popping, G., Somerville, R. S., & Trager, S. C. 2014, MNRAS, 442, 2398
Price, D. J. 2007, Publications of the Astronomical Society of Australia, 24, 159
Rodighiero, G., Cimatti, A., Gruppioni, C., et al. 2010, A&A, 518, L25
Romeo, A. D., Sommer-Larsen, J., Portinari, L., & Antonuccio-Delogu, V. 2006, MNRAS, 371, 548

Saintonge, A., Kauffmann, G., Kramer, C., et al. 2011, MNRAS, 415, 32
Sandstrom, K. M., Leroy, A. K., Walter, F., et al. 2013, ApJ, 777, 5
Schöier, F. L., van der Tak, F. F. S., van Dishoeck, E. F., & Black, J. H. 2005, A&A, 432, 369
Seon, K.-I., Edelstein, J., Korpela, E., et al. 2011, ApJs, 196, 15
Simnett, G. M., & McDonald, F. B. 1969, ApJ, 157, 1435
Smith, R. J., Glover, S. C. O., Clark, P. C., Klessen, R. S., & Springel, V. 2014, MNRAS, 441, 1628
Sofia, U. J., Lauroesch, J. T., Meyer, D. M., & Cartledge, S. I. B. 2004, ApJ, 605, 272
Solomon, P. M., Downes, D., Radford, S. J. E., & Barrett, J. W. 1997, ApJ, 478, 144
Solomon, P. M., Rivolo, A. R., Barrett, J., & Yahil, A. 1987, ApJ, 319, 730
Sommer-Larsen, J., Götz, M., & Portinari, L. 2003, ApJ, 596, 47
Sommer-Larsen, J., Romeo, A. D., & Portinari, L. 2005, MNRAS, 357, 478
Sommer-Larsen, J., Vedel, H., & Hellsten, U. 1998, MNRAS, 294, 485
Springel, V., & Hernquist, L. 2003, MNRAS, 339, 289
Stinson, G., Seth, A., Katz, N., et al. 2006, MNRAS, 373, 1074
Strong, A. W., & Mattox, J. R. 1996, A&A, 308, L21
Tacconi, L. J., Genzel, R., Smail, I., et al. 2008, ApJ, 680, 246
Tacconi, L. J., Neri, R., Genzel, R., et al. 2013, ApJ, 768, 74
Tielens, A. G. G. M. 2005, The Physics and Chemistry of the Interstellar Medium (Cambridge University Press)
—. 2013, Reviews of Modern Physics, 85, 1021
Vázquez-Semadeni, E., Colín, P., Gómez, G. C., Ballesteros-Paredes, J., & Watson, A. W. 2010, ApJ, 715, 1302
Walter, F., Riechers, D. A., Carilli, C. L., et al. 2007, in Astronomical Society of the Pacific Conference Series, Vol. 375, From Z-Machines to ALMA: (Sub)Millimeter Spectroscopy of Galaxies, ed. A. J. Baker, J. Glenn, A. I. Harris, J. G. Mangum, & M. S. Yun, 182
Webber, W. R. 1998, ApJ, 506, 329
Whitaker, K. E., Labbé, I., van Dokkum, P. G., et al. 2011, ApJ, 735, 86
Wiersma, R. P. C., Schaye, J., & Smith, B. D. 2009, MNRAS, 393, 99
Wolfire, M. G., Hollenbach, D., & McKee, C. F. 2010, ApJ, 716, 1191
Wolfire, M. G., McKee, C. F., Hollenbach, D., & Tielens, A. G. G. M. 2003, ApJ, 587, 278
Wuyts, S., Förster Schreiber, N. M., van der Wel, A., et al. 2011, ApJ, 742, 96
Yang, B., Stancil, P. C., Balakrishnan, N., & Forrey, R. C. 2010, ApJ, 718, 1062
Young, C. H., Shirley, Y. L., Evans, II, N. J., & Rawlings, J. M. C. 2003, ApJs, 145, 111
Zahid, H. J., Dima, G. I., Kewley, L. J., Erb, D. K., & Davé, R. 2012, ApJ, 757, 54

5

Observing and modeling [CII] emission lines

5.1 Why [CII]?

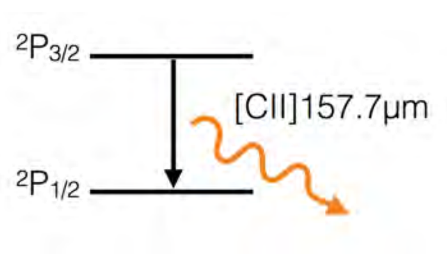

Figure 5.1 The two level system of ionized carbon leading to the line emission at $\sim$ 158 μm. The excitation happens via collisions with either electrons, atoms or molecules.

Being the fourth most common element after hydrogen in the Milky Way (MW), it comes as no surprise that carbon is nearly ubiquitous thoughout the various phases of the ISM in star-forming galaxies (e.g. Dartois & Muñoz-Caro, 2007; Esteban et al., 2014; James et al., 2014). Much of that carbon is ionized by the ultraviolet (UV) radiation permeating the ISM, due to the low ionization potential of carbon (11.3 eV cf. 13.6 eV for hydrogen). As a result, singly ionized carbon (CII) is found in regions of ionised as well as neutral gas. In both regions, the $^2P_{3/2}$-$^2P_{1/2}$ fine structure transition of CII can be collisionally excited by electrons (e^-), atoms (HI) or molecules (H_2), depending on the gas phase, resulting in an emission line at 157.714 μm or 1900.5369 GHz (hereafter [CII]). The critical densities of [CII] are only 16 cm^{-3}, 2400 cm^{-3} and 4800 cm^{-3} for collisions with e^-, HI and H_2 respectively at a temperature of 500 K (Goldsmith et al., 2012). Together, these facts are what makes [CII] one of the strongest cooling lines of the ISM, with a line luminosity equivalent to $\sim 0.1 - 1\%$ of the far-infrared (FIR) luminosity of galaxies (e.g. Stacey et al., 1991; Brauher et al., 2008).

5.2 Observations of [CII] emission in galaxies

Due to high atmospheric opacity at these frequencies, observations of [CII] in the local Universe must be done at high altitudes or in space. Indeed, the very first detections of [CII] towards Galactic objects (Russell et al., 1980; Stacey et al., 1983; Kurtz et al., 1983) and other galaxies (Crawford et al., 1985; Stacey et al., 1991; Madden et al., 1992) were done with airborne observatories such as the NASA Lear Jet and the Kuiper Airborne Observatory. The advent of the Infrared Space Observatory (ISO) allowed for the first systematic [CII] surveys of local galaxies (e.g. Malhotra et al., 1997; Luhman et al., 1998, 2003). Detections of [CII] at high-z have also become feasible over recent years with ground-based facilities (Hailey-Dunsheath et al., 2010; Stacey et al., 2010), as well as the *Herschel* Space Observatory (see the recent review by Casey et al., 2014).

5.2.1 THE [CII] DEFICIT

Early observations and modeling suggested that [CII] is predominantly associated with Photodissociation Regions (PDRs) in the outskirts of molecular clouds exposed to intense far-ultraviolet (FUV) ratiation, hence predicting a strong correlation between [CII] luminosity, $L_{[\mathrm{CII}]}$, and that of reprocessed FUV light as measured in far-infrared (FIR), L_{FIR} (Tielens & Hollenbach, 1985; Crawford et al., 1985). However, a deficit in $L_{[\mathrm{CII}]}$ relative to L_{FIR} was soon observed towards local ultraluminous infrared galaxies (ULIRGs) and high-z galaxies dominated by an AGN (e.g. Malhotra et al., 1997; Luhman et al., 1998; Malhotra et al., 2001; Luhman et al., 2003; Díaz-Santos et al., 2013; Farrah et al., 2013). Some indications suggest that this '[CII] deficit' persists at high-z, with the ratio extending to other FIR lines (e.g. Graciá-Carpio et al., 2011), though the existence of a high-z deficit is debated (Hailey-Dunsheath et al., 2010; Wagg et al., 2010; De Breuck et al., 2011; Ferkinhoff et al., 2011; Swinbank et al., 2012). Magdis et al. (2014) find that intermediate $z \sim 0.3$ ULIRGs actually fall on the relation for local normal galaxies measured by Malhotra et al. (2001), suggesting that high-z ULIRGs are in fact scaled-up versions of local star-forming galaxies, rather than the disturbed systems resulting from mergers that are typically associated with local $z < 0.2$ ULIRGs. The [CII] deficit increases with higher dust temperatures on both global and resolved scales in local galaxies (e.g Croxall et al., 2012; Díaz-Santos et al., 2013; Herrera-Camus et al., 2015), shown with an example in Fig. 5.2, suggesting that dust plays a crucial role in controlling the $L_{[\mathrm{CII}]}/L_{\mathrm{FIR}}$ ratio.

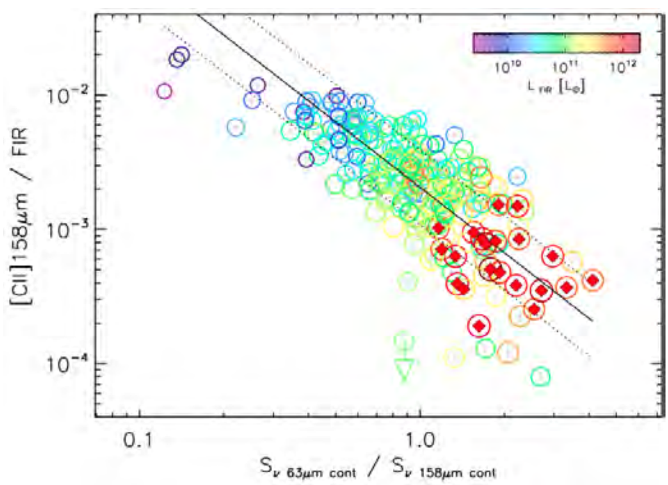

Figure 5.2 The [CII] deficit as investigated and plotted by Díaz-Santos et al. (2013) for local luminous infrared galaxies (LIRGs). Deviation from the global [CII]-FIR relation increases with dust temperature corresponding to increasing 60/100 μm color.

Various scenarios have been put forward as causing the [CII] deficit (see a summary of these in e.g. Malhotra et al., 2001; Herrera-Camus et al., 2015), but a consesus has not been achieved with observations and models so far. Favoured scenarios causing the [CII] deficit are ones in which the efficiency of the FUV light to heat the gas is decreased or obscuring dust absorbs the FUV radiation before it reaches the potential sources of [CII] emission. Such scenarios include i) large HII regions created by high ionization parameters where most of the FUV radiation is absorbed by dust rather than goes to heating the gas via photo-ionization (e.g. Tielens & Hollenbach, 1985; Abel et al., 2009; Graciá-Carpio et al., 2011; Croxall et al., 2012), ii) high levels of grain charging, primarily in PDRs, which decrease the efficiency of photoelectric heating of the gas by FUV radiation (e.g. Malhotra et al., 2001; Croxall et al., 2012; Ibar et al., 2015), and iii) dust-bounded clouds or PDRs in ULIRGs, where high dust masses in the HII regions absorb most FUV light before it reaches regions with more ionized carbon (Luhman et al., 2003; Farrah et al., 2013; Abel et al., 2009).

5.2.2 CONTRIBUTING GAS PHASES TO [CII] EMISSION

Knowing the relative contributions to $L_{[\mathrm{CII}]}$ from different gas phases in the ISM would help sorting out in the possible causes for the [CII] deficit. But observations of [CII] emission alone, will not readily give away information on the different ISM phases contributing, unless combined with some other gas tracer such as [NII] (122 μm) (Malhotra et al., 2001) or HI (21 cm) as well as CO line emission as done by Pineda et al. (2013) for the MW, in order to separate contributions from ionized, neutral and molecular gas. Updated in Pineda et al. (2014), the ISM phases considered are found to contribute with rougly amounts to the total $L_{[\mathrm{CII}]}$ with 30 % from dense PDRs, 25 % from cold HI, 25 % from CO-dark H_2 gas and 20 % from ionized gas. Observing 60 normal, star-forming galaxies in [CII] and [NII], Malhotra et al. (2001) estimated that a rough mean of 50 % of $L_{[\mathrm{CII}]}$ comes from ionized gas and the rest from PDRs. Even larger PDR contributions were found in the giant HII region N11 in the Large Magellanic Cloud (LMC), by Lebouteiller et al. (2012) who conclude, from comparison of [CII] with [NII], that 95 % of $L_{[\mathrm{CII}]}$ arises in diffuse PDRs, whereas dense PDRs are better traced by [OI], also considered the second most important cooling line in neutral gas.

5.2.3 [CII] AS A STAR FORMATION RATE TRACER

Since [CII] is sensitive to the local FUV field which itself probes OB star formation activity, it was early on suggested that $L_{[\mathrm{CII}]}$ correlates with SFR of a galaxy, and observations soon revealed a $L_{[\mathrm{CII}]}$-SFR correlation for nearby galaxies (Stacey et al., 1991; Leech et al., 1999; Boselli et al., 2002). More comprehensive studies were performed by de Looze et al. (2011); De Looze et al. (2014) and Farrah et al. (2013) for modest star-forming galaxies and ULIRGs in the local Universe. The scatter in the $L_{[\mathrm{CII}]}$-SFR relation is substantial though, apparently irregardless of the overall galaxy classification (Sargsyan et al., 2012), and increasing towards low metallicity, warm dust temperatures and large filling factors of ionized, diffuse gas (De Looze et al., 2014).

With the Photodetector Array Camera & Spectrometer (PACS) on board *Herschel*, resolved observations of [CII] in local galaxies became possiple (e.g. De Looze et al., 2014; Herrera-Camus et al., 2015; Kapala et al., 2015), and the advent of the Atacama Large Millimeter Array (ALMA) promises to make such detections and observations relatively routine, even at high-z (e.g. Wang et al., 2013). The $L_{[\mathrm{CII}]}$-SFR relation has now also observed on kpc-scales in local galaxies as a kind '[CII] KS relation' between surface density of SFR, Σ_{SFR}, and that of [CII] luminosity, $\Sigma_{[\mathrm{CII}]}$ (e.g. De Looze et al., 2014; Herrera-Camus et al., 2015; Kapala et al., 2015). Kapala et al. (2015) concluded that [CII] traces SFR in the spiral arms of the Andromeda Galaxy (M31) similarly to what is seen in larger samples of more distant galaxies, although with a significant contribution to [CII] from outside star-forming regions. and a shallower slope of the $\Sigma_{[\mathrm{CII}]}$-Σ_{SFR} relation on $\sim 50\,$pc scales than on kpc scales. For the MW, Pineda et al. (2014) find that only the combined emission of all gas phases, leads to a slope of the $\Sigma_{[\mathrm{CII}]}$-Σ_{SFR} relation in agreement with extragalactic observations. But the $\Sigma_{[\mathrm{CII}]}$-Σ_{SFR} relation for local galaxies also suffers from a great deal of scatter. De Looze et al. (2014) find, when observing 32 local dwarf galaxies on kpc-scales, that this scatter is most likely due to internal ISM conditions, rather than large variations within individual galaxies. Analyzing 46 nearby (mostly spiral) galaxies from the *Herschel* KINGFISH sample, Herrera-Camus et al. (2015) succeeded in reducing the scatter on the $\Sigma_{[\mathrm{CII}]}$-Σ_{SFR} relation at warm IR colors, by deriving a set of IR color adjustments that can be applied to normal, star-forming galaxies in the absence of strong AGNs. But a firm physical reason for the scatter is still missing.

Metallicity is a potentially important factor for the $L_{[\mathrm{CII}]}$-SFR, as an increase in metallicity translates into a higher mass fraction of carbon and dust, both of which affect the $L_{[\mathrm{CII}]}$-SFR relation. Similar to De Looze et al. (2014), Herrera-Camus et al. (2015) found an increased scatter around the $L_{[\mathrm{CII}]}$-SFR relation at low metallicities, implying that at low metallicities, a non-negligible fraction of the neutral gas cooling takes place via the [OI] $63\,\mu$m cooling line instead the [CII] line. In M31, Kapala et al. (2015) see an increasing trend in $L_{[\mathrm{CII}]}/L_{\mathrm{TIR}}$ with radius as expected if $L_{[\mathrm{CII}]}$ itself dependeded strongly on metallicity, since M31 excibits a clearly decreasing metallicity with radius (Sanders et al., 2012). However, Kapala et al. (2015) cannot rule out other factors such as stellar density and radiation field strength. Kramer et al. (2013) found a sharp increase in $L_{[\mathrm{CII}]}/L_{\mathrm{FIR}}$ at $R \sim 4.5\,$kpc in M33, but dismiss metallicity as the sole cause, due to the rather shallow metallicity gradient in M33 (Magrini et al., 2010). The effect of low metallicity together with the disruption of molecular clouds is also becoming an important subject for studies of the Epoch of Reionization (EoR) at $z \sim 6$, as a possible explanation for several non-detections of normal star-forming galaxies. Examples include the lensed Lyα emitter at $z = 6.56$ and the Himiko galaxy at $z \sim 6.5$ forming stars at a rate of ≈ 10 and $\sim 100\ \mathrm{M}_{\odot}\ \mathrm{yr}^{-1}$, respectively (Kanekar et al., 2013; Ouchi et al., 2013), and more recently 3 Lyman Break Galaxies at $z \sim 7$ of SFR $\sim 10\,\mathrm{M}_{\odot}\ \mathrm{yr}^{-1}$ (Maiolino et al., 2015).

5.3 MODELING [CII] EMISSION

How the physical conditions of the ISM control the [CII] emission can be investigated by applying sub-grid treatment to the gas in semi-analytical (Popping et al., 2013; Muñoz & Furlanetto, 2013) or fully hydrodynamical (Nagamine et al., 2006; Vallini et al., 2013) simulations of galaxy evolution. In their models of [CII] emission in high-z galaxies Nagamine et al. (2006) found that [CII] emission depends significantly on the amount of neutral gas. Vallini et al. (2013) improved on the method of Nagamine et al. (2006), by implementing radiative transfer of the UV field and higher resolution simulations of a single $z = 6.6$ Lyα emitter, though only at two fixed metallicities ($Z = Z_{\odot}$ and $Z = 0.02Z_{\odot}$). Popping et al. (2013) managed to reproduce the [CII] deficit for all FIR luminosities at $z > 1$ as well as the $L_{[\mathrm{CII}]}$-FIR correlation at $z = 0$, however with the simplification of averaging galaxy properties across annuli in the galactic disks. Muñoz & Furlanetto (2013) modeled $z > 6$ Lyα emitters, slightly overpredicting the [CII] while underpredicting the CO line emission, when compared to the few observations available, but demonstrating that line modeling during the Epoch of Reionization is possible. In addition, other works have concentrated on single clouds employing either radiative transfer (Abel et al., 2009) or an escape probability approach (Goldsmith et al., 2012) to derive the [CII] strength.

6

SIMULATING [CII] LINE EMISSION AT $z = 2$ (PAPER II)

6.1 AIM OF THIS PROJECT

As described in the previous chapter, simulations hold promise in aiding interpretation of the [CII] emission. In this chapter, an expansion and improvement of SÍGAME is presented, enabling the simulation of [CII] emission from galaxies, with the principle goal of understanding the dominant sites of origin of [CII] emission in modestly star-forming galaxies. Much of the formalism and methodology of SÍGAME stay unchanged and the reader is referred to the previous Chapter I for those details. However, instead of making use of a radiative transfer code, the [CII] emission is calculated analytically for each ISM phase separately. SÍGAME in its new form is then applied to a cosmological SPH simulation of 7 massive star-forming galaxies on the main-sequence at $z \sim 2$ in order to simulate their [CII] emission. By modeling the internal structure of the molecular gas on scales down to about $\sim 0.5\,\mathrm{pc}$, we investigate the origin of the $L_{[\mathrm{CII}]}$-SFR relation on global as well as resolved scales and how metallicity affects the $L_{[\mathrm{CII}]}$/SFR radial gradient for normal galaxies of different SFR at $z = 2$. Throughout, a flat cosmology is adopted with $\Omega_{\mathrm{M}} = 0.27, \Omega_{\Lambda} = 0.73$, and $h = 0.71$ (Spergel et al., 2003).

6.2 METHODOLOGY OVERVIEW

This section gives an overview of our multi-phased ISM model. To a large extent the model follows the steps laid out in Chapter 4, in that it is applied at the post-processing stage of an SPH simulation. As input, the ISM model requires: the position ($[x, y, z]$), velocity ($[v_x, v_y, v_z]$), total gas mass (m_{SPH}), hydrogen density (n_{H}), kinetic temperature (T_{k}), smoothing length (h), star formation rate (SFR), metallicity (Z) as well as the relative abundances of carbon ([C/H]) and oxygen ([O/H]). In addition, the model also requires an electron fraction, x_{e}.

The key steps involved in this process are illustrated in Fig. 6.1 and briefly listed below (with full details given in subsequent sections):

1. The SPH gas is separated into an ionized and a neutral phase as dictated by the electron fraction provided by the GADGET-3 simulation (Section 6.4).

2. The neutral gas is divided into giant molecular clouds (GMCs) according to the observed mass function of GMCs in the MW and nearby quiescent galaxies. The GMCs are mod-

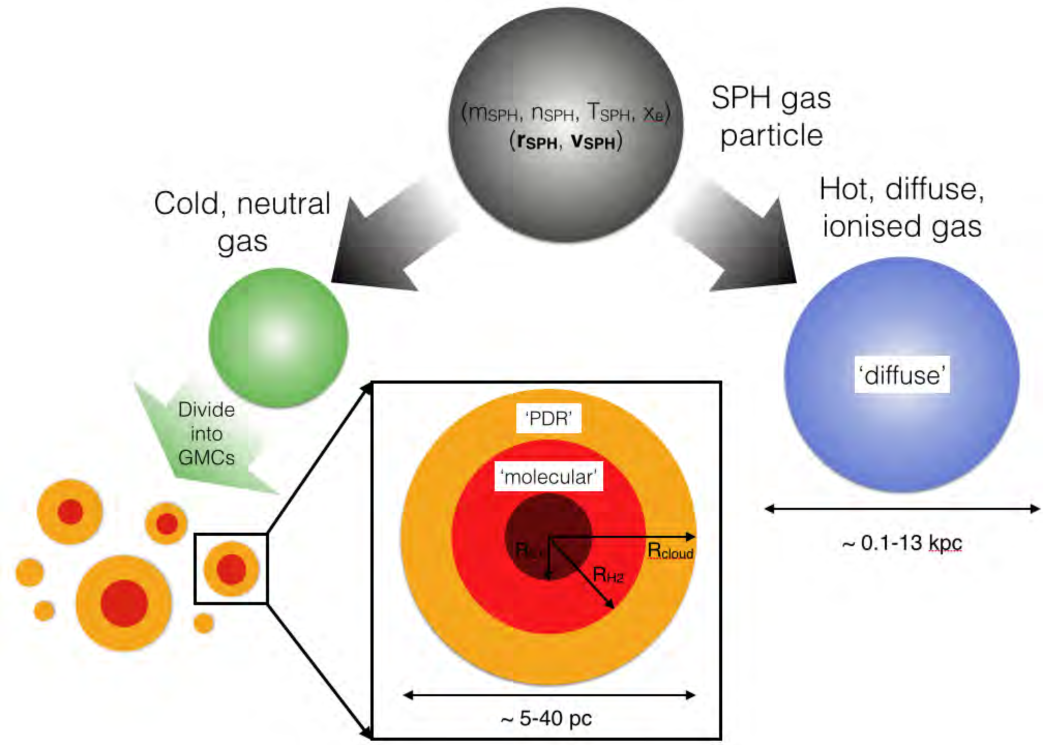

Figure 6.1 Schematic illustrating the sub-grid procedures applied to the SPH simulation described in Section 6.3. In Section 6.4.1, we go through the left-hand side, in which the neutral part of each SPH gas particle is divided into GMCs, the interior of each GMC is stratified in concentric shells and their ionization state and thermal balance is derived. In Section 6.4.2, we turn to the right-hand side of Fig. 6.1, modeling the diffuse, ionised gas.

elled as logotropic spheres with their radii derived according to a local GMC mass-size relation.

3. Each GMC is assumed to consist of three spherically symmetric regions: 1) an inner molecular (H_2) region where carbon is only found in its neutral (CI) form[1], 2) an outer molecular region where both CI and C^+ can exist, and 3) a largely neutral atomic layer of HI, HII and ionized carbon. The last region mimics the UV-stratified PDRs observed at the surfaces of molecular clouds (Hollenbach & Tielens, 1999). The relative extent of these regions within each cloud, and thus the densities at which they occur, ultimately depends on the strength of the impinging FUV and cosmic ray fields. The temperatures are calculated from thermal balance equations.

4. The remaining ionised gas of the SPH simulation is divided into HII clouds of radius equal to the smoothing lengths, temperature equal to that of the SPH simulation and constant density.

[1]In reality, the innermost regions of GMCs also contain dense clumps of carbon in molecular form (CO), but this is not relevant for the [CII] emission, hence SÍGAME does not attempt to resolve these clumps but assumes that all carbon is in the form of CI here.

Table 6.1 Global properties of the seven simulated galaxies used for this work at $z = 2$.

	G1	G2	G3	G4	G5	G6	G7
M_* [$10^{10}\,M_\odot$]	0.354	0.765	0.945	1.76	3.91	6.36	5.34
M_{gas} [$10^{10}\,M_\odot$]	0.362	0.672	1.25	1.43	2.52	1.72	2.14
$M_{\rm neutral}$ [$10^{10}\,M_\odot$]	0.085	0.129	0.565	0.20	0.286	0.392	0.285
SFR [$M_\odot$ yr^{-1}]	4.85	9.96	8.77	25.06	19.86	37.50	59.04
$\Sigma_{\rm SFR}$ [$M_\odot$ yr^{-1} kpc^{-2}]	0.0039	0.0079	0.0070	0.020	0.0158	0.0298	0.0469
Z'	0.46	0.85	0.64	1.00	1.02	1.73	1.67

All quantities have been calculated at $z = 2$ within a fixed cut-out radius of $R_{\rm cut} = 20$ kpc, which is the radius at which the accumulated stellar mass function of each galaxy flattens. $M_{\rm neutral}$ is the mass of neutral gas, resulting from the electron fraction attached to all SPH gas particles in the simulation. The metallicity ($Z' = Z/Z_\odot$) is the mean of all SPH gas particles within $R_{\rm cut}$.

5. Finally, the [CII] emission is calculated for 3 separate regions: The molecular region in GMCs, the PDR region of GMCs and the surrounding HII regions. The emission profiles from these regions are studied individually and summed to arrive at a total galaxy [CII] luminosity.

The SPH simulation used to test out this scheme, is described in the following section, and our model galaxies taken from this simulation are presented in Section 6.3.1.

6.3 SPH SIMULATIONS

Our simulations are evolved with an extended version of the GADGET-3 cosmological SPH code (Springel 2005 and Huang et al. 2015, in prep.). It includes cooling processes using the primordial abundances as described in Katz et al. (1996), with additional cooling from metal lines assuming photo-ionization equilibrium from Wiersma et al. (2009). We use the more recent 'pressure-entropy' formulation of SPH which resolves mixing issues when compared with standard 'density-entropy' SPH algorithms (see Saitoh & Makino, 2013; Hopkins, 2013, for further details). Our code additionally implements the time-step limiter of Saitoh & Makino (2009); Durier & Dalla Vecchia (2012) which improves the accuracy of the time integration scheme in situations where there are sudden changes to a particle's internal energy. To prevent artificial fragmentation (Schaye & Dalla Vecchia, 2008; Robertson & Kravtsov, 2008), we prohibit gas particles from cooling below their effective Jeans temperature which ensures that we are always resolving at least one Jeans mass within a particle's smoothing length. This is very similar to adding pressure to the interstellar medium as in Springel & Hernquist (2003); Schaye & Dalla Vecchia (2008), except instead of directly pressurizing the gas we prevent it from cooling and fragmenting below the Jeans scale.

We stochastically form stars within the simulation from molecular gas following a Schmidt (1959) law with an efficiency of 1% per local free-fall time (Krumholz & Tan, 2007; Lada et al., 2010). The molecular content of each gas particle is calculated via the equilibrium analytic model of Krumholz et al. (2008, 2009); McKee & Krumholz (2010). This model allows us to regulate star formation by the local abundance of H_2 rather than the total gas density, which confines star formation to the densest peaks of the interstellar medium. Further implementation details can be found in Thompson et al. (2014). Galactic outflows are implemented using the hybrid energy/momentum-driven wind (ezw) model fully described in Davé et al. (2013); Ford et al. (2015). We also account for metal enrichment from Type II supernovae (SNe), Type Ia SNe, and AGB stars as described in Oppenheimer & Davé (2008).

6.3.1 SPH SIMULATIONS OF $z = 2$ MAIN SEQUENCE GALAXIES

For this work we use the cosmological zoom-in simulations presented in Thompson et al., 2015 in prep., and briefly summarize them here. Initial conditions were generated using the MUSIC code (Hahn & Abel, 2011) assuming cosmological parameters consistent with constraints from the *Planck* (Planck Collaboration et al., 2013) results, namely $\Omega_m = 0.3, \Omega_\Lambda = 0.7, H_0 = 70, \sigma_8 = 0.8, n_s = 0.96$. Six target halos were selected at $z = 2$ from a low-resolution N-body simulation consisting of 256^3 dark-matter particles in a $(16h^{-1}\mathrm{Mpc})^3$ volume with an effective comoving spatial resolution of $\epsilon = 1.25\,h^{-1}$ kpc. Each target halo is populated with higher resolution particles at $z = 249$, with the size of each high resolution region chosen to be $2.5\times$ the maximum radius of the original low-resolution halo. The majority of halos in our sample are initialized with a single additional level of refinement ($\epsilon = 0.625\,h^{-1}$kpc), while the two smallest halos are initialized with two additional levels of refinement ($\epsilon = 0.3125\,h^{-1}$kpc).

The six halos produce seven massive star-forming galaxies at $z = 2$ that are free from all low-resolution particles within the virial radius of their parent halo. Masses range from 3.6×10^9 to $6.6\times10^{10}\,\mathrm{M}_\odot$ and their star formation rates from $5-60\,\mathrm{M}_\odot\ \mathrm{yr}^{-1}$. We hereafter label these galaxies G1,G2, ..., G7, in order of increasing stellar mass (M_*). Relevant global properties for each can be found in Table 6.1.

The SFRs of our simulated galaxies agree with the specific SFRs of $z\sim2$ BzKs as measured by Daddi et al. (2007), though slightly below the MS $z\simeq2$ main sequence (MS) of star forming galaxies as determined more recently by (Speagle et al., 2014). Fig. 6.2 shows the positions of G1, ..., G7 on an M_*-SFR diagram and how they lie below, but within 3σ of the Speagle et al. (2014) relation. This offset is not unexpected given the difficulty currently afflicting most SPH simulations in reaching the specific star formation rates (sSFR =SFR/M_*) observed at $z = 2$ (e.g. Furlong et al., 2014). However, this may also be caused by It has been proposed that this problem may be solved in the near future by including a better model for the Initial Mass Function (IMF) or feedback from stellar winds, supernovae and AGN (e.g. Davé, 2008; Narayanan & Davé, 2012; Sparre et al., 2015).

6.4 MODELING THE ISM

SÍGAME was originally crafted for modeling the molecular part of the ISM, with focus However, here we are interested in the entire ISM rather than just the molecular phase, and the resulting modifications to SÍGAME are explained in this section. As illustrated with the schematic in Fig. 6.1, our sub-gridding procedure starts by splitting each SPH particle into an ionised (blue) and a neutral gas component, the latter of which is further divided into a molecular layer (red) and a PDR region (orange). As mentioned in Section 6.2, we use the electron fractions, x_e, attached to each SPH particle to divide the gas into an ionized and a neutral component:

$$m_{\mathrm{HII}} = x_\mathrm{e}\cdot m_{\mathrm{SPH}} \tag{6.1}$$

$$m_{\mathrm{neutral}} = (1-x_\mathrm{e})\cdot m_{\mathrm{SPH}}. \tag{6.2}$$

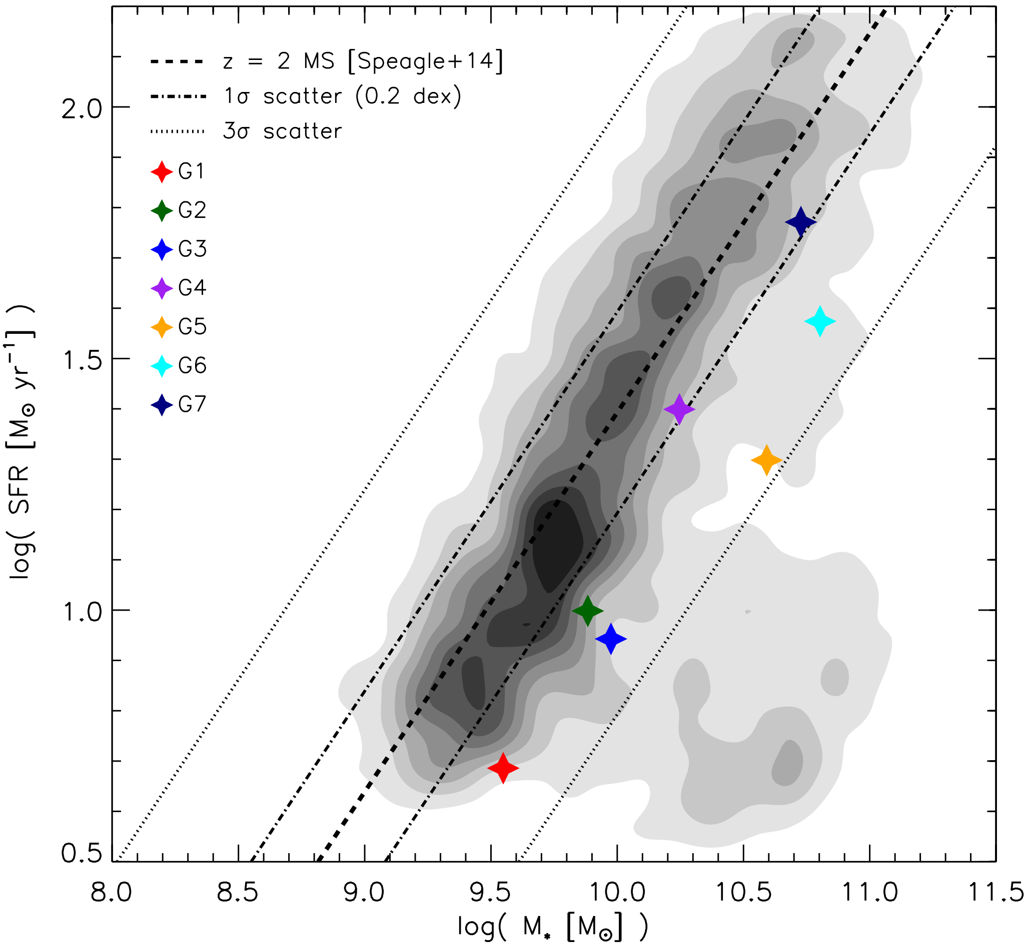

Figure 6.2 The SFR–M$_*$ relation at $z \simeq 2$ as determined by Speagle et al. (2014) (dashed line) with the location of our seven model galaxies highlighted (filled stars). For comparison we also show the locus defined by 3754 $1.4 < z < 2.5$ galaxies from the NEWFIRM Medium-Band Survey (grey filled contours), with masses and SFRs calculated using a Kroupa IMF (Whitaker et al., 2011). Dot-dashed and dotted lines indicate the 1σ and 3σ scatter around the relation of Speagle et al. (2014).

The electron fraction from GADGET-3 gives the density of electrons relative to that of hydrogen, $n_{\rm e}/n_{\rm H}$, and can therefore reach values of ~ 1.16 in the cases where helium is also ionised. For the above equations we have normalised $x_{\rm e}$ by its maximum value so as to not exceed the total gas mass in the simulation.

6.4.1 Giant Molecular Clouds

Masses and sizes

The neutral gas mass, $m_{\rm neutral}$, associated with a given SPH particle is divided into GMCs by randomly sampling the observed GMC mass function as observed in the MW disk and Local Group galaxies: $\frac{dN}{dm_{\rm GMC}} \propto m_{\rm GMC}^{-\beta}$ with $\beta = 1.8$ (Blitz et al., 2007). A lower and upper cut in mass of $10^4\,{\rm M}_\odot$ and $10^6\,{\rm M}_\odot$, respectively, are enforced in order to span the range of GMC masses observed by Blitz et al. (2007). Up to 40 GMCs are created per SPH particle but typically most ($> 90\%$) of the SPH particles are split into four GMCs or less. A histogram of the initial SPH particle gas masses (dashed) together with histograms of their neutral gas masses (dotted) and the resulting GMC masses (solid) are shown in Fig. 6.3. The SPH particle masses do not go below the lower GMC mass limit of $10^4\,{\rm M}_\odot$, but the extracted neutral masses, $m_{\rm neutral}$, sometimes do, and we discard these neutral masses in the GMC sub-gridding procedure. For galaxies G1 and G2, that are of highest resolution in our sample, this descarded neutral amounts to $\sim 6\,\%$ of the total neutral mass, while only $0.005-0.015\,\%$ in the remaining five galaxies, and we shall assume that it does not affect our results significantly.

The GMCs are spatially distributed within 0.2 times the smoothing length of the original SPH particle, at random angles but with a radial displacement that scales inversely with GMC mass in order to retain a spatial distribution of the gas close to the original. In order to ensure preservation of the gas kinematics as well, all GMCs associated with a given SPH particle are given the same bulk velocity, namely that of the parent SPH particle.

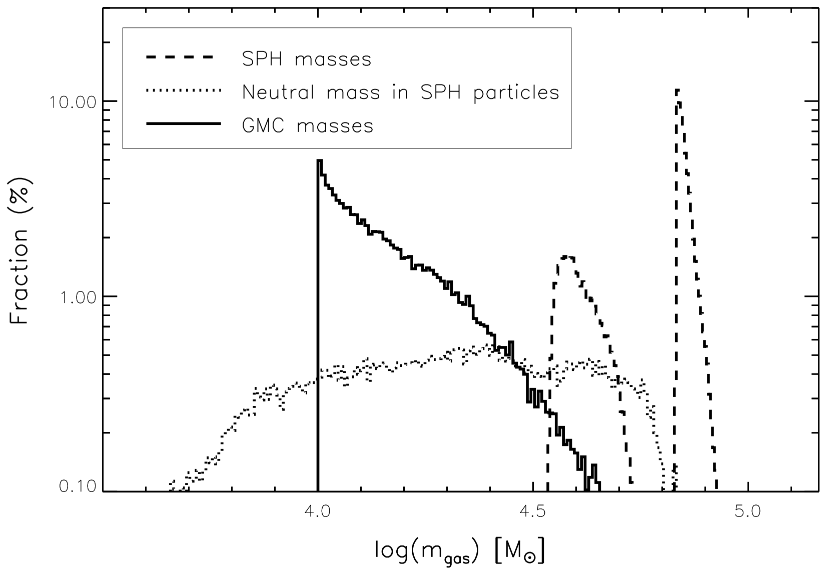

Figure 6.3 The distribution of SPH gas particle masses (dashed histogram) in G1. The distribution peaks at two characteristic masses ($\sim 10^{4.6}\,{\rm M}_\odot$ and $\sim 10^{4.85}\,{\rm M}_\odot$), where the lower mass peak represents gas particles left over from the first generation of stars in the simulation. The dotted histogram shows the corresponding neutral gas mass distribution of the SPH particles obtained from eq. 6.2, going all the way down to 0. GMCs are extracted from the neutral gas following the prescription in Section 6.4.1 and the resulting GMC mass distribution is shown as the solid histogram.

GMC sizes, $R_{\rm cloud}$, are obtained from the mass-size scaling relationship of Solomon et al. (1987):

$$R_{\rm cloud}[{\rm pc}] = \sqrt{m_{\rm GMC}[{\rm M}_\odot]/540}. \tag{6.3}$$

We assume a logotropic density profile for the total hydrogen number density of the GMCs:

$$n_{\rm H}(R) = n_{\rm H,ext}\left(\frac{R_{\rm cloud}}{R}\right), \tag{6.4}$$

where $n_{\rm H}(R > R_{\rm cloud}) = 0$ and the external density, $n_{\rm H,ext}$, is given by 2/3 of the average hydrogen density:

$$n_{\rm H,ext} = 2/3\langle n\rangle = 2/3\frac{m_{\rm GMC}}{4/3\pi m_{\rm H}{R_{\rm cloud}}^3}. \tag{6.5}$$

Internal GMC structure

Having defined the total hydrogen density profile with the expression in eq. 6.4, Fig. 6.4 is an example of a GMC model in galaxy G1. From the center of the GMC and out to $R_{\rm H_2}$, hydrogen is in molecular form and the gas number density is therefore given by the dotted line in Fig. 6.4. Beyound $R_{\rm H_2}$, hydrogen is found as HI and HII (dash-dotted and dash-dot-dotted lines) out to $R_{\rm cloud}$, the size of the GMC.

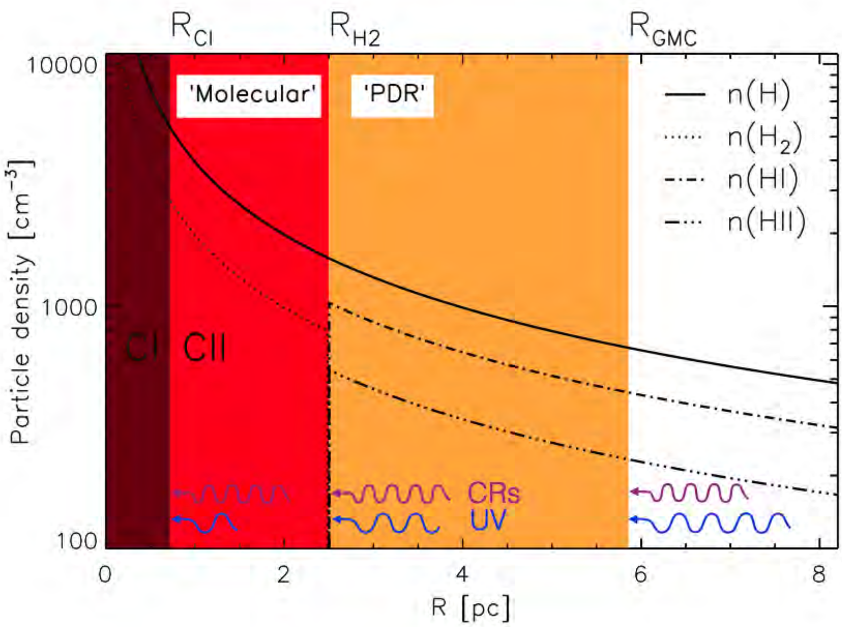

Figure 6.4 Density profiles of the species relevant for our modeling of the [CII] emission for a GMC of mass $\sim 4.5 \times 10^4\,{\rm M}_\odot$ and radius $\sim$ 11 pc in galaxy G1. Dark red ('CI') indicates the region with neutral carbon, whereas singly ionised carbon can exist further out in the red ('Molecular') and orange ('PDR') regions. At the bottom, arrows show how the cosmic rays penetrate all the way to the innermost layer, while UV radiation is attenuated by dust inside the GMC.

The size of the molecular region, $R_{\rm H_2}$, when adopting the logotropic density profile (eq. 6.4), is related to the total molecular gas mass fraction[2], $f'_{\rm mol}$, of each GMC as:

$$f'_{\rm mol} = \frac{m_{\rm mol}}{m_{\rm GMC}} = \frac{\int_0^{R(\rm H_2)} \rho_{\rm ext} \frac{R_{\rm GMC}}{R} 4\pi R^2 dR}{\int_0^{R_{\rm GMC}} \rho_{\rm ext} \frac{R_{\rm GMC}}{R} 4\pi R^2 dR} \tag{6.6}$$

$$= \frac{\int_0^{R(\rm H_2)} R\, dR}{\int_0^{R_{\rm GMC}} R\, dR} = \left(\frac{R(\rm H_2)}{R_{\rm GMC}}\right)^2 \tag{6.7}$$

$$\Rightarrow r_{\rm H_2} = \sqrt{f'_{\rm mol}}, \tag{6.8}$$

where $r_{\rm H_2}$ is the fractional radius[3], $r_{\rm H_2} = R_{\rm H_2}/R_{\rm cloud}$. We calculate $f'_{\rm mol}$ from H I $\leftrightarrow$ $\rm H_2$ equilibrium with the analytical framework of Pelupessy et al. (2006), as explained in Chapter 4. The value of $f'_{\rm mol}$ depends directly on density, $n_{\rm H}$, electron fraction, $x_{\rm e}$, velocity dispersion, $\sigma_{\rm v}$, FUV radiation field, G_0 (in Habing units) metallicity Z', kinetic gas temperature, $T_{\rm k}$, and, indirectly, the cosmic ray ionization rate, $\zeta_{\rm CR}$, via the temperature. The calculation of these quantities is described in the following.

• $n_{\rm H}$. The total hydrogen density at any point within the GMCs is calculated with eq. 6.4.

• $\sigma_{\rm v}$. For the velocity dispersion we use the $\sigma_{\rm v}$-size relation of Galactic disk GMCs (Oka et al., 2001):

$$\sigma_v[\text{km s}^{-1}] = 1.0 \times \left(\frac{\sqrt{\pi}}{3.4} R_{\rm cloud}[\text{pc}]\right). \tag{6.9}$$

• $x_{\rm e}$. We calculate the electron fraction with the help of `CLOUDY` v13.03, under the simple assumption that mainly cosmic rays are responsible for the ionization, and that ionisation by attenuated FUV radiation can be neglected inside the GMCs (see more in Appendix B.2 on this derivation of $x_{\rm e}$).

• G_0. The local FUV ionizing radiation field, G_0, together with the cosmic ionization rate, $\zeta_{\rm CR}$, play a crucial role in determining both of the fractional radii, $R_{\rm H_2}$ and $R_{\rm CI}$, and also in setting the themal balance inside the GMCs. However, G_0 nor the ionization field, $\zeta_{\rm CR}$, come out in a direct way from the simulation. We use `SÍGAME` to estimate G_0 as described in Chapter 4. This method scales the FUV field to the MW value in regions with SFR density, SFRD, corresponding to that of the MW, and scales G_0 with the local SFRD in the simulation as well as the total stellar mass relative to that of the MW.

The FUV field is expected to be attenuated by dust when moving into the GMC, and we assume that this attenuation has the shape of $\exp(-\xi_{\rm FUV}\, A_v)$ where $\xi_{\rm FUV}$ is a factor accounting for the difference in opacity between visual and FUV, set equal to 3.02 as in Röllig et al. (2006). From full strength at GMC radius, we then calculate the dust-attenuated FUV field, $G_{0,\rm att}$, as:

$$G_{0,\rm att}(R_{\rm cloud}) = G_0 \tag{6.10}$$

$$G_{0,\rm att}(R_{\rm H_2}) = G_0 e^{-\xi_{\rm FUV} A_v(R_{\rm H_2})} \tag{6.11}$$

$$G_{0,\rm att}(R_{\rm CI}) = G_0 e^{-\xi_{\rm FUV} A_v(R_{\rm CI})}, \tag{6.12}$$

where $A_v(R_{\rm CI})$ is $A_v(r_{\rm CI})$ to be derived in eq. 6.17 and $A_v(R_{\rm H_2})$ comes from the work of Pelu-

[2] $f'_{\rm mol}$ not to be confused with the molecular gas mass fraction of the entire galaxy, $f_{\rm mol}$.
[3] Please note that radius in units of the GMC radius is denoted with r whereas actual radii in pc are denoted with capital R.

pessy et al. (2006) (again, see Chapter 4 for its implementation).

• Z'. The metallicity is assumed constant throughout each GMC and inherited from the parent SPH particle.

• T_k. We defer the calculation of T_k at R_{H_2} to Section 6.4.1.

• ζ_CR. The bulk of MW cosmic rays are believed to originate in the energetic supernovae explosions (Blasi, 2013), which is our reason for scaling ζ_CR with the local SFR density only:

$$\zeta_\mathrm{CR} = \zeta_\mathrm{CR,MW} \cdot \frac{\mathrm{SFRD}_\mathrm{local}}{\mathrm{SFRD}_\mathrm{MW}}, \tag{6.13}$$

where $\mathrm{SFRD}_\mathrm{local}$ is estimated everywhere by averaging within a surrounding sphere of radius 2 kpc and ζ_CR is scaled to the 'canonical' MW value of $\zeta_{,\mathrm{MW}} = 3\times10^{-17}\,\mathrm{s}^{-1}$ (e.g. Webber, 1998). Due to their high energy and hence penetration capacity, we will assume that the cosmic rays maintain their full intensity throughout the GMCs (Papadopoulos et al., 2011).

As for carbon, the total carbon mass fraction is kept constant throughout the GMC at the value of its parent SPH particle. Consequently, the density profile of carbon atoms follows that of total hydrogen in Fig. 6.4. Inside the molecular region, R_CI (also marked in Fig. 6.4), marks the size of the neutral carbon region, or the radius at which the density of atomic carbon equals the density of ionized carbon; $n_\mathrm{CI} = n_\mathrm{CII}$. Gas of non-zero metallicity outside this radius will contain ionized carbon and thus contribute to the [CII] luminosity. We expect R_CI be smaller than R_{H_2} because hydrogen selfshields better than carbon. However, it happens that R_CI is equal or slightly larger than R_{H_2}. In these cases ($\sim 6-53\,\%$ of the GMC mass), we shall assume that CII only exists outside R_{H_2}, in the PDR region.

For the neutral carbon region, we apply the work of Röllig et al. (2006) (but see also Pelupessy & Papadopoulos, 2009), which considers the following dominant reaction channels for the formation and destruction of C^+:

$$\mathrm{C}^0 + \nu \rightarrow \mathrm{C}^+ + \mathrm{e}^- \tag{6.14}$$
$$\mathrm{C}^+ + \mathrm{e}^- \rightarrow \mathrm{C}^0 + \nu \tag{6.15}$$
$$\mathrm{C}^+ + \mathrm{H}_2 \rightarrow \mathrm{CH}_2^+ + \nu. \tag{6.16}$$

By equating the ionization rate (for eq. 6.14) with the recombination and radiative association rates (for eq. 6.15+6.15), Röllig et al. (2006) shows that r_CI can be found by solving the following equation:

$$\begin{aligned} 5.13\times10^{-10}s^{-1}G_0 \int_1^\infty \frac{e^{-\mu\xi_{FUV}A_v(r_\mathrm{CI})}}{\mu^2}d\mu \\ = n_H(a_C X_\mathrm{C} + 0.5k_C), \end{aligned} \tag{6.17}$$

where the left-hand side of the equation is the ionization rate due to the attenuated FUV field coming from all directions, and the right-hand side is the competing destruction rate of C^+. Extinction through the outer ionized carbon layer is given by $A_v(r_\mathrm{CI}) = 0.724\sigma_{dust}ZnR_\mathrm{cloud}\ln\left({r_\mathrm{CI}}^{-1}\right)$ (Pelupessy & Papadopoulos, 2009), and X_C is the relative carbon abundance which we calculate from the carbon mass fractions of the simulations, the latter of which is shown in histograms in Appendix B.5. The constants $a_C = 3\times10^{-11}\,\mathrm{cm}^{-3}\,\mathrm{s}^{-1}$ and $k_C = 8\times10^{-16}\,\mathrm{cm}^{-3}\,\mathrm{s}^{-1}$ are the recombination and radiative association rate coefficient for the reactions that destroy C^+ (see eqs. 6.15 and 6.16). Replacing σ_{dust} with a dust FUV absorption cross section of

$4.9 \times 10^{-22}\,\mathrm{cm}^2$ (e.g. Mezger et al., 1982) and $nR_{\rm cloud}$ by the pressure-modified Larson-scaling relation of Pelupessy et al. (2006), the integral in eq. 6.17 can be tabulated as a function, F_{int}, of boundary pressure, P_e, Z', and $r_{\rm CI}$ only:

$$\frac{n_H(a_C X_{\rm C} + 0.5k_C)}{3 \times 10^{-10} s^{-1} G_0} = F_{int}(P_e, Z', r_{\rm CI}). \tag{6.18}$$

In practice, we determine $R_{\rm CI}$ based on the external properties to each GMC, while $R_{\rm H_2}$ is calculated in an iterative process together with the temperature calculation at that radius described in the following section.

Internal temperature of the GMCs

We will only probe the temperature at the radii $R_{\rm CI}$, $R_{\rm H_2}$ and $R_{\rm cloud}$ (see previous section and Fig. 6.1 for an overview). This is done by iterations, applying one of the following equations for relevant heating and cooling mechanisms at the given radius:

$$R_{\rm CI} : \Gamma_{\rm PE} + \Gamma_{\rm CR,H_2} = \Lambda_{\rm H_2} + \Lambda_{\rm CI} + \Lambda_{\rm CII} + \Lambda_{\rm gas-dust} \tag{6.19}$$
$$R_{\rm H_2} : \Gamma_{\rm PE} + \Gamma_{\rm CR,H_2} = \Lambda_{\rm H_2} + \Lambda_{\rm CII} + \Lambda_{\rm OI} \tag{6.20}$$
$$R_{\rm cloud} : \Gamma_{\rm PE} + \Gamma_{\rm CR,HI} = \Lambda_{\rm CII} + \Lambda_{\rm OI}. \tag{6.21}$$

Here $\Gamma_{\rm PE}$ is heating associated with the photoelectric ejection of electrons from dust grains immersed in a FUV radiation field, $\Gamma_{\rm CR,H_2}$ is the heating of molecules by cosmic rays in molecular gas environments and $\Gamma_{\rm CR,HI}$ that from cosmic rays in atomic gas. On the cooling side are line cooling by atoms and molecules as well as cooling from gas-dust interactions, $\Lambda_{\rm gas-dust}$. References to and more detailed description of these heating and cooling rates can be found in Appendix B.3. Both $\Gamma_{\rm CR,H_2}$, $\Gamma_{\rm PE}$ and $\Lambda_{\rm CII}$ (at least in the PDRs) depend on the electron fraction, $x_{\rm e}$, which is calculated with `CLOUDY` as described in Section 6.4.1.

We solve simultaneously and iteratively for $r_{\rm H_2}$ and $r_{\rm CI}$ as well as $n_{\rm H}$ and $T_{\rm k}$ at the $R_{\rm CI}$, $R_{\rm H_2}$ and $R_{\rm cloud}$ boundaries shown in Fig. 6.1. The final $r_{\rm CI}$ and $r_{\rm H_2}$ fractional radii are presented in GMC-mass-weighted histograms in Fig. 6.5. Likewise, GMC-mass-weighted histograms of the resulting temperatures and hydrogen densities at each boundary are shown in Fig. 6.6 for galaxy G1.

6.4.2 THE DIFFUSE, IONISED GAS

The remaining gas, not part of the neutral gas described in the previous section, is assumed to be fully ionised, and distributed in large, unattenuated clouds. The size of these HII complexes is approximated by the smoothing length of the original SPH particle. Furthermore we assume the gas to be evenly distributed and isothermal at the temperature of the simulation, $T_{\rm k,SPH}$.

6.5 THE [CII] LINE EMISSION

The [CII] line emission originates in different regions of a galaxy, from the diffuse and neutral medium to the denser gas in the outer layers of GMCs, where carbon is ionized by the FUV radiation from nearby stars. We consider the three contributing regions named and illustrated in Fig. 6.1 and listed here according to increasing distance from GMC centers and decreasing

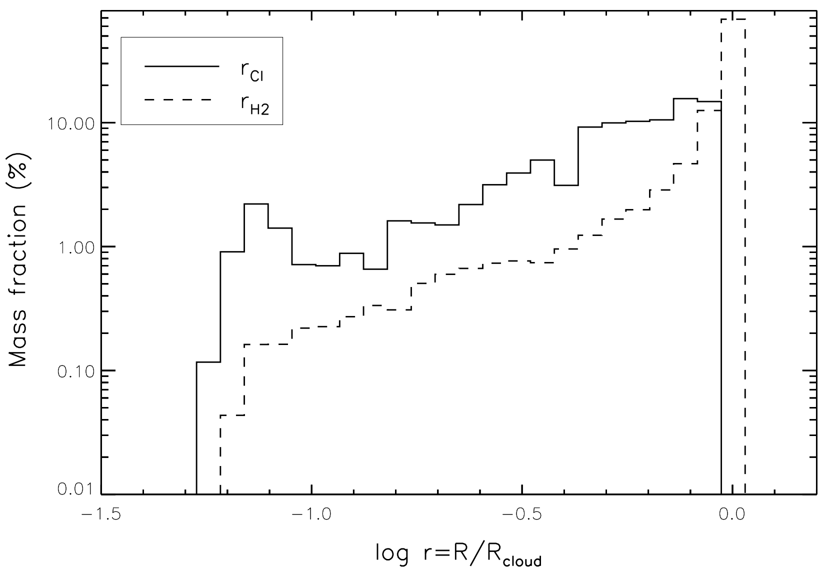

Figure 6.5 GMC-mass-weighted histograms of $r_{\rm CI}$ and $r_{\rm H_2}$, the outer radii to the neutral carbon region and the H_2 region respectively, divided by the GMC radii, $R_{\rm cloud}$, for all GMCs in galaxy G1 (see Section 6.3.1). The few GMCs for which no solution yields $R_{\rm CI} < R_{\rm H_2}$, have been removed from this plot.

hydrogen density:

- Molecular region (red): C^+ layer of GMCs containing molecular gas. [CII] is excited via collisions with H_2 molecules.

- PDR region (orange): C^+ layer of GMCs containing partially ionised hydrogen. [CII] is excited via collisions with primarily atomic hydrogen.

- Diffuse region (blue): Diffuse, ionized gas outside GMCs. [CII] is excited via collisions with primarily electrons.

The total [CII] luminosity, $L_{\rm [CII]}$, is the total [CII] luminosity from these 3 regions.

6.5.1 Integration of the [CII] line emission

The [CII] luminosity of a volume of gas can be found by integrating the [CII] cooling rate per volume, $\Lambda_{\rm CII}$:

$$L_{\rm [CII]} = \int \Lambda_{\rm CII}\, dV. \tag{6.22}$$

The cooling rate is set by the temperature, density and chemical composition of the gas as well as the radiation field hitting the gas from the outside. We derive [CII] cooling rates in each of the 3 gas regions by employing the framework and terminology provided by Goldsmith et al.

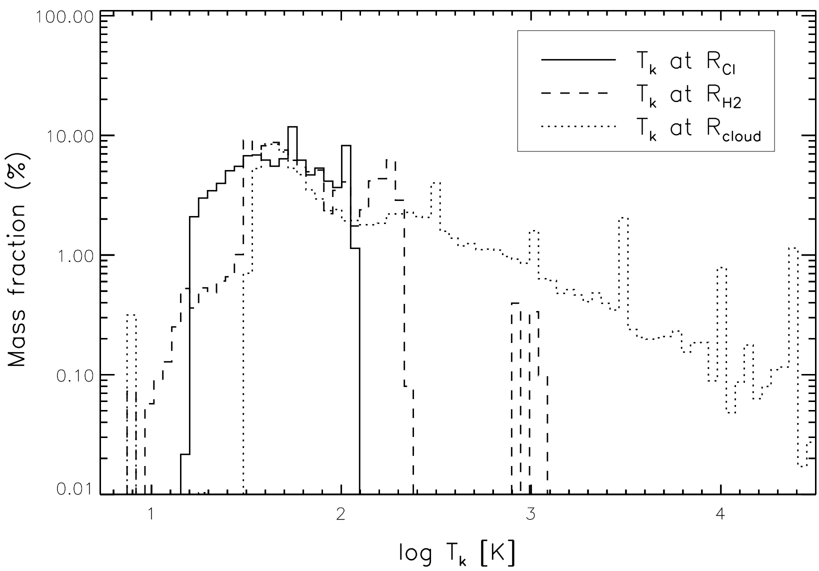

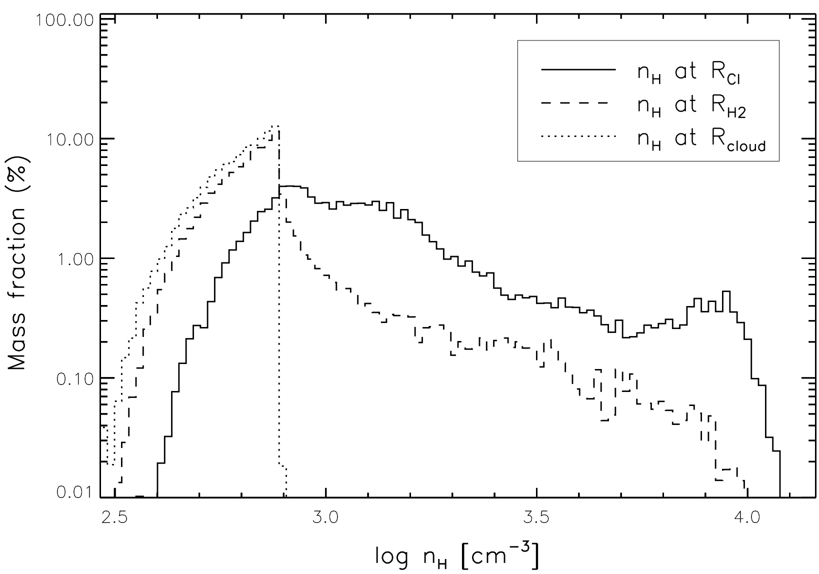

Figure 6.6 GMC-mass-weighted histograms of temperature (*top*) and density (*bottom*) in model galaxy G1 at the three GMC layer boundaries considered (see Fig. 6.1 for definition of layers). As one moves in towards the center of the GMCs from $R_{\rm cloud}$ to $R_{\rm CI}$, the distribution of temperatures goes to lower values while density increases. The few GMCs for which no solution yields $R_{\rm CI} < R_{\rm H_2}$, have been removed from this plot.

(2012), writing the general [CII] cooling rate as:

$$\Lambda_{\rm CII} = A_{ul}\beta f_u n_{\rm CII} h\nu, \tag{6.23}$$

where A_{ul} is the Einstein rate of spontaneous emission of $2.3 \times 10^{-6}\,\mathrm{s}^{-1}$ for [CII][4], β is a correction factor in the case of optically thick emission, f_u is the fraction of singly ionized carbon in the upper $^2P_{3/2}$ level, n_{CII} is the density of singly ionized carbon, h is the Planck constant and ν is the frequency of [CII] (1900.537 GHz).

For the density of singly ionized carbon, we tabulate the output from `CLOUDY` v13.03, using solar abundances and a wide range in electron temperature, hydrogen density, local cosmic ray ionization rate, ζ_{CR}, and FUV field, G_0 (see Appendix B.1 for more on this). The upper state fraction, f_u, is determined by radiative processes as well as collisional excitation and deexcitation. The latter can be with electrons, atomic hydrogen or molecular hydrogen depending on the state of the gas, leading to a total deexcitation rate, C_{ul}, of:

$$C_{ul} = R_{ul}(e^-)n_{e^-} + R_{ul}(\mathrm{HI})n_{\mathrm{HI}} + R_{ul}(\mathrm{H_2})n_{\mathrm{H_2}}, \tag{6.24}$$

where R_{ul} are the respective collision rate coeffecients.

Full expressions for the collision rate coefficients and the derivation of Λ_{CII} in gas of different optical depth can be found in Appendix B.4. Instead, we focus the remainder of this section on how eq. 6.22 is implemented in the various gas regions.

6.5.2 [CII] EMISSION FROM MOLECULAR REGIONS

The [CII] luminosity from the molecular region is an integral from the outer radius of the neutral carbon region to the outer radius of the molecular hydrogen region:

$$\begin{aligned} L_{[\mathrm{CII}],\mathrm{mol}} &= \int_0^{2\pi}\int_0^{\pi}\int_{R(\mathrm{CI})}^{R(\mathrm{H_2})} \Lambda_{\mathrm{CII}} R^2 \sin\theta dR d\theta d\phi \\ &= 4\pi \int_{R(\mathrm{CI})}^{R(\mathrm{H_2})} \Lambda_{\mathrm{CII}} R^2 dR. \end{aligned} \tag{6.25}$$

We solve the integral numerically by splitting the layer up into 100 radial bins. The total hydrogen density in each bin is dictated by the logotropic density profile as shown in Fig. 6.4, and all hydrogen that is not ionized is assumed fully molecular. That leaves collisions with $\mathrm{H_2}$ molecules as the main collision partner for $\mathrm{C^+}$ ions. To get an upper limit on the luminosity, we adopt the temperature, electron fraction and FUV radiation field at the outer boundary, $R_{\mathrm{H_2}}$, for all radial bins.

6.5.3 [CII] EMISSION FROM PDRS

For the partially ionised gas composing the PDRs in the outskirts of the GMCs, we use a method essentially similar to that described in the previous subsection for molecular gas. Only now, the integral goes from the outer radius of the molecular hydrogen region to the GMC

[4]Einstein coefficient for spontaneous emission taken from the LAMDA database: `http://www.strw.leidenuniv.nl/~moldata/`, Schöier et al. (2005)

radius:

$$L_{[\mathrm{CII}],\mathrm{PDR}} = \int_0^{2\pi}\int_0^{\pi}\int_{R(\mathrm{H}_2)}^{R_{\mathrm{GMC}}} \Lambda_{\mathrm{CII}} R^2 \sin\theta dR d\theta d\phi$$
$$= 4\pi \int_{R(\mathrm{H}_2)}^{R_{\mathrm{GMC}}} \Lambda_{\mathrm{CII}} R^2 dR. \quad (6.26)$$

Again, that layer is divided into 100 radial bins over which the temperature, electron fraction and G_0 are kept fixed to the outer boundary value (i.e. no attenuation of the FUV field), and the density of atomic hydrogen and electrons follow the logotropic density profile sketched in Fig. 6.4. We assume that no molecular hydrogen exists in this layer.

6.5.4 [CII] EMISSION FROM DIFFUSE, IONISED REGIONS

As explained in Section 6.4.2, the ionised gas mass is distributed evenly within a spherical cloud of radius R_{HII} set equal to the smoothing length of the SPH particle. We work out Λ_{CII} in the same way as for the molecular gas and PDRs, this time assuming a constant density across the diffuse gas region, so that the total [CII] luminosity is simply the cooling rate multiplied by the volume of the diffuse gas:

$$L_{[\mathrm{CII}],\mathrm{HII}} = \Lambda_{\mathrm{CII}} \frac{3}{4}\pi {R_{\mathrm{HII}}}^3. \quad (6.27)$$

6.6 RESULTS AND DISCUSSION

A central problem when interpreting [CII] line emission, is its exact origin. We are now able to attack this problem theoretically with our simulated galaxies sampling the normal star-forming galaxies at $z = 2$, having divided the ISM into molecular gas, PDRs and diffuse gas as explained in the previous sections and illustrated in Fig. 6.1. In the following, the relative contributions from these gas phases to the globally integrated as well as the resolved [CII] emission, is revealed.

6.6.1 RADIAL DISTRIBUTIONS OF $L_{[\mathrm{CII}]}$

In Fig. 6.7 we present surface density maps of the SPH gas, and $R < 15$ kpc radial $L_{[\mathrm{CII}]}$ profiles for each model galaxy seen face-on. As evident from the gas maps, our model galaxies are diverse in shape, some merging with satellite galaxies (G1, G2 and G3), others with very clear spiral arms (G4, G5 and G7), bars (G5 and G7) or even a ring of gas at $R \sim 8-10$ kpc (G6 and G7).

The radial $L_{[\mathrm{CII}]}$ profiles are made by summing up all luminosity in concentric rings of width 0.2 kpc, and both total as well as individual gas phase luminosities are shown, plotted in the same way as done by Pineda et al. (2014) (P14), for quick comparison with their observations of the MW. We adopt a similar color-scheme to that of P14 so that: Red corresponds to 'molecular gas' ('CO-dark H_2 gas' + 'dense PDRs' in P14), orange corresponds to 'PDRs' ('HI CNM' in P14) and blue is ionised gas as in P14.

Comparing to the radial [CII] profiles in the MW, the following resemblances can be seen: i) $L_{[\mathrm{CII}],\mathrm{mol}}$ tends to dominates the [CII] luminosity in most of our galaxies (G1, G2, G3 and G4), with $L_{[\mathrm{CII}],\mathrm{PDR}}$ coming next and $L_{[\mathrm{CII}],\mathrm{HII}}$ last. ii) The radial $L_{[\mathrm{CII}],\mathrm{mol}}$ profile extends out to at

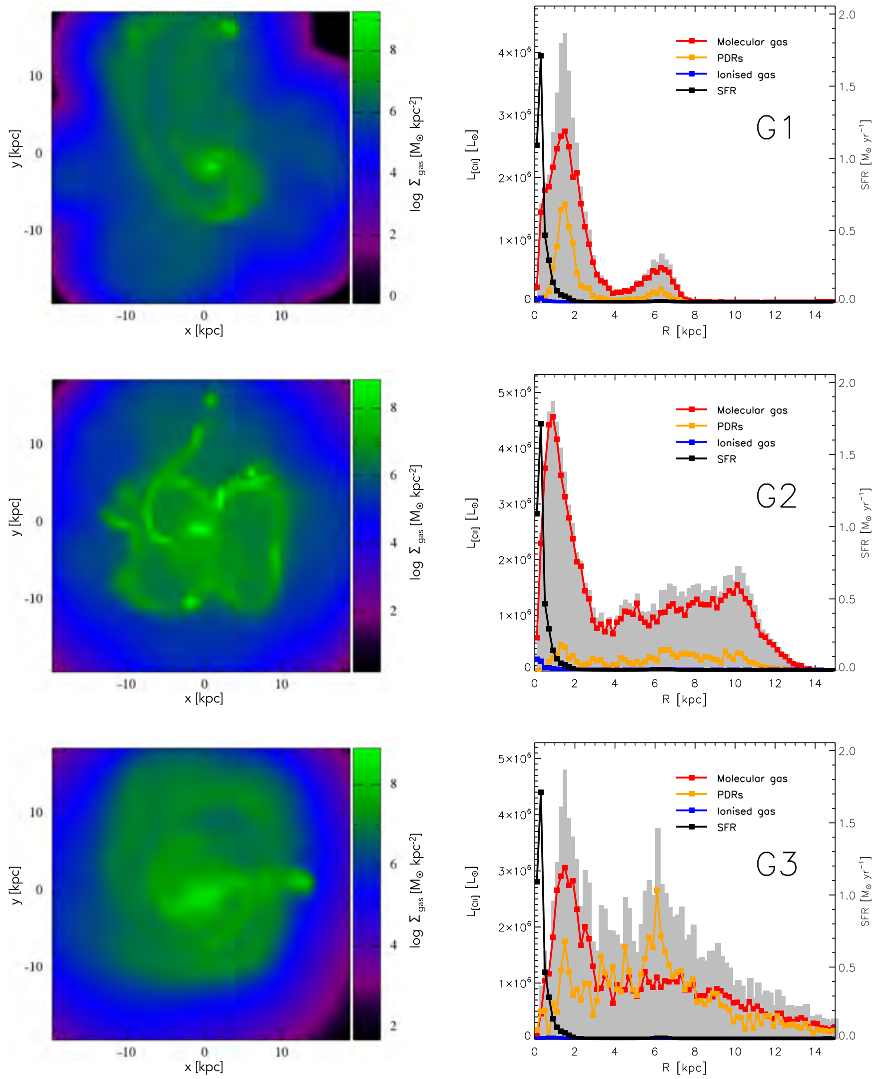

Figure 6.7 *Left:*) SPH gas surface density maps made with SPLASH v2.5.0, and *right:*) Radial profiles of total $L_{[\mathrm{CII}]}$ (grey histogram) as well as contributions from molecular gas (red), PDRs (orange) and ionised gas (blue). The colors have been chosen to ease comparison with the observations of the MW by Pineda et al. (2014), see the text and Fig. 6.9.

least 15 kpc in at least some of our galaxies (G3, G4 and G5). iii) The radial profile of SFR peaks at smaller radii than does the total [CII] profile (in grey).

However, there are also departures from the MW profiles. First of all, our modeled $L_{[\mathrm{CII}]}$ profiles are more concentrated towards the center, peaking at $R \lesssim 2\,\mathrm{kpc}$, whereas the MW profile peaks further out, at $R \sim 5\,\mathrm{kpc}$. In most model galaxies (except G1 and G2), $L_{[\mathrm{CII}],\mathrm{PDR}}$ rises to the level of $L_{[\mathrm{CII}],\mathrm{mol}}$ or there above, whereas in the MW, the observed PDR contribution is always less than the molecular one. This happens in particular to the galaxies of higher SFRs ($\gtrsim 10\,\mathrm{M}_\odot\ \mathrm{yr}^{-1}$), i.e. the ones departing most from the SFR of the MW of $0.68 - 1.45\,\mathrm{M}_\odot\ \mathrm{yr}^{-1}$ (Robitaille & Whitney, 2010).

In integrated luminosities, the molecular gas stands for $\sim 39 - 85\,\%$ of the total $L_{[\mathrm{CII}]}$, the

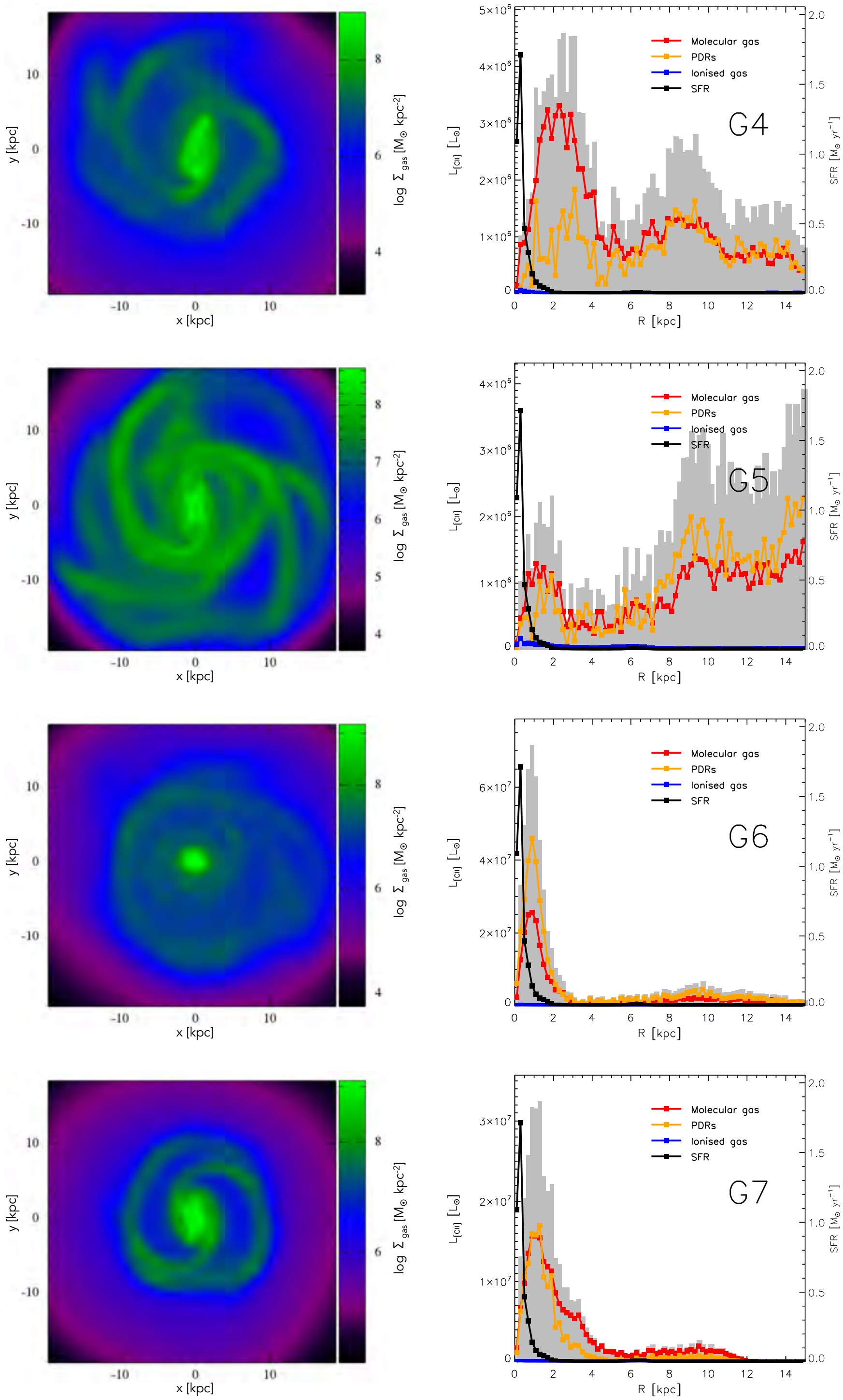

Figure 6.8 Fig. 6.7 continued.

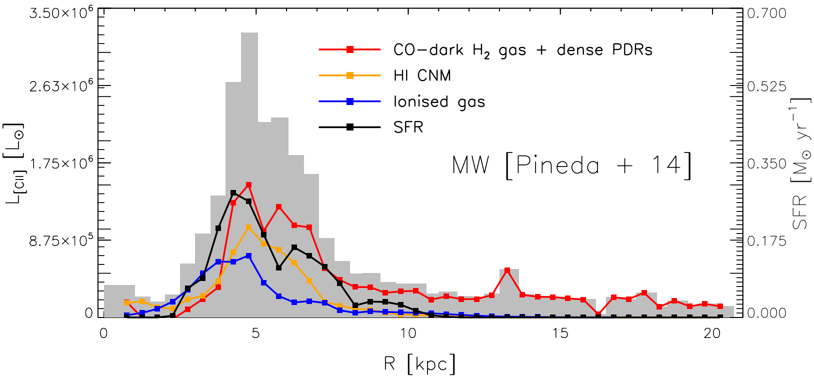

Figure 6.9 Radial $L_{[\mathrm{CII}]}$ profile in the MW (grey histogram) together with contributions from the various ISM phases (red, orange and blue lines) and the radial SFR profile (black line) from the 1.4 GHz intensity distribution, from the work of Pineda et al. (2014).

PDRs for $\sim 12{-}61\,\%$, while the contribution from ionised gas ranges from only $0.2\,\%$ to $\sim 3.4\,\%$. This is in broad agreement with the relative molecular and PDR contributions found by Pineda et al. (2014) for the MW, with corresponding fractions of 55 and 25 %. However, ionised gas in our $z = 2$ galaxies seems to play a less important role than in the MW (20 %), accounting for $< 1\,\%$ of $L_{[\mathrm{CII}]}$ in 5 out of 7 galaxies.

6.6.2 The $L_{[\mathrm{CII}]}$-SFR relation

We now turn to the observed correlation between total SFR and total [CII] luminosity, comparing our 7 model galaxies to observed galaxies at $z \sim 0 - 6.5$ in the top panel of Fig. 6.10.

Also shown is the high-redshift galaxy ($z > 0.5$, SFR $\gtrsim 300\,\mathrm{M}_\odot\,\mathrm{yr}^{-1}$) relation from the study of De Looze et al. (2014) (dashed line; D14 relation) and the best linear fit to the local normal star-forming galaxies (SFR $\lesssim 140\,\mathrm{M}_\odot\,\mathrm{yr}^{-1}$) observed by Malhotra et al. (2001) as given by Magdis et al. (2014) (dotted line; M01 relation). The model galaxies can be fit well by a straight line at a χ^2 of 0.17, leading to a $L_{[\mathrm{CII}]}$-SFR relation with slope 0.86 ± 0.19 which is in almost perfect agreement with the slope of the D14 relation, 0.85 ± 0.14, and within $1\,\sigma$ of the unity-slope of the M01 relation and the slope of 1.02 ± 0.07 measured for the MW by Pineda et al. (2014).

The bottom three panels of Fig. 6.10 give the $L_{[\mathrm{CII}]}$-SFR relation for each gas phase (molecular gas, PDRs and ionised gas) separately, with a linear regression fit in solid line. The slope for the ionized gas of 0.23 is much below that of the D14 relation for the total gas, but a steeper slope in the [CII] brighter molecular and atomic gas helps to recover the observed relation, when adding all gas phases (top panel). This concurs with the conclusions of Pineda et al. (2014), that only when including all phases of the ISM, is the total $L_{[\mathrm{CII}]}$ correlated with a slope consistent with extragalactic observations. However, the individual linear fits to the $L_{[\mathrm{CII}]}$-SFR relation in each gas phase do not correspond very well to the corresponding ones for the MW (dotted lines).

6.6.3 RESOLVED $\Sigma_{[\mathrm{CII}]} - \Sigma_{\mathrm{SFR}}$ RELATION

In Fig. 6.11, we show the combined $\Sigma_{[\mathrm{CII}]}$-Σ_{SFR} relation for all seven simulated galaxies in their face-on configuration. Surface densities were determined within 1 kpc $\times$ 1 kpc regions. Contours reflect the number of regions at a given (Σ_{SFR},$\Sigma_{[\mathrm{CII}]}$)-combination and are given as percentages of the peak number of regions. In the top panel we present the relation when taking into account all ISM phases. Relative to a straight line in log-log, our model galaxies display an excess in $\Sigma_{[\mathrm{CII}]}$ at lower Σ_{SFR}, mainly caused by the molecular gas, as seen in the panel below, but also to some degree arising in the PDRs. The $\Sigma_{[\mathrm{CII}]}$-Σ_{SFR} relation for the ionised gas, has a slope very close to the total relation, but offset to lower [CII] surface brightness. All gas phases are subject to substantial scatter, however we attempt to fit the total relation with a combination of two power laws at the end of this section.

First, we compare the total gas contribution to $\Sigma_{[\mathrm{CII}]}$ in the top panel to the power-law fits to three resolved surveys of nearby galaxies: 1) the 50 pc-scale relation for M31 (K15; dot-dashed line), 2) the kpc-scale relations for low-metallicity dwarf galaxies (D14; dashed line), and 3) the kpc-scale relations for spiral galaxies (H15; dotted line). Regarding the observations by H15, we adopt the raw $\Sigma_{[\mathrm{CII}]}$ measurements rather than the IR-color-corrected ones.

Some caution is called for when comparing our simulations to resolved observations, primarily regarding the determination of Σ_{SFR} on $\leq$ kpc-scales. The aforementioned studies all measure both obscured (from 24 μm) and un-obscured (from either FUV or Hα) SFRs in order to estimate the total Σ_{SFR} and, while intrinsic uncertainties are inherent in the empirical 24 μm/FUV/Hα $\rightarrow$ SFR callibrations, the Σ_{SFR} values should therefore be directly comparable to those from our simulations. An important source of uncertainty is likely to be the choice of scale over which Σ_{SFR} is determined. In particular, the emission from old stellar populations in diffuse regions with no ongoing star formation can lead to overestimates of the SFR when using the above empirical SFR callibrations (D14). K15 and H15 both account for this by subtracting the expected cirrus emission from old stars in 24 μm, according to the method presented in Leroy et al. (2012). It becomes particularly challenging to estimate Σ_{SFR} on 50 pc-scales, where the 24 μm cirrus estimation of Leroy et al. (2012) cannot readily be used because it was callibrated on 1 kpc scales. However, the diffuse 24 μm is likely resolved out it any case at 50 pc-scales, making the cirrus contribution less of a problem on these scales, as pointed out by K15. K15 points to another problem arising from the possibility of photons leaking between neighbouring stellar populations, meaning that average estimates of the SFR on scales < 50 pc might not represent the true underlying SFR.

Keeping the above limitations in mind, we see from the top panel of Fig. 6.11 that there is an overall agreement between the observed $\Sigma_{[\mathrm{CII}]}$-Σ_{SFR} relations and our modeled one, at least at higher Σ_{SFR} ($\gtrsim 0.01\,\mathrm{M}_{\odot}\ \mathrm{yr}^{-1}$). Of the three observered relations, our models come closest to those found in local spirals, including M31, compared to those of low-metallicity dwarf galaxies. The scatter in our modeled $\Sigma_{[\mathrm{CII}]}$-Σ_{SFR} relation is large as expected from the observational scatter of 0.32, 0.18 and 0.21 dex around the D14, K15 and H15 relations respectively.

An excess in total $\Sigma_{[\mathrm{CII}]}$, similar to what we see at low Σ_{SFR}, is observed by K15, in particular in 2 out of the 5 fields observed in M31. The K15 group ascribes the excess to a diffuse (HII) contribution to [CII], but also possibly a sensitivity issue with *Herschel* causing a larger dispersion in $\Sigma_{[\mathrm{CII}]}$ around Σ_{SFR} at low [CII] surface brightness. Surprisingly, we do not see a strong contribution from the diffuse, HII gas phase at low Σ_{SFR} but rather a dominating molecular contribution.

In Fig. 6.12 we fit the resolved $\Sigma_{\rm [CII]}$-$\Sigma_{\rm SFR}$ relation (top panel of Fig. 6.11) for the sum of all ISM phases with a power law expression of the form:

$$\Sigma_{\rm [CII]} = A_1 \times {\Sigma_{\rm SFR}}^{A_2} + A_3 \times {\Sigma_{\rm SFR}}^{A_4}, \tag{6.28}$$

with fit parameters and χ^2 given in the plot. Also shown are the individual 50 pc size regions in M31 (K15), who observe a similar flattening of the $\Sigma_{\rm [CII]}$-$\Sigma_{\rm SFR}$ relation at low $\Sigma_{\rm SFR}$.

6.7 THE ROLE OF METALLICITY

As explained in Section 5.2.3, an observational effort has been put forward to understand the effect of metallity on the [CII] emission. For this, the [O/H] abundance is typically used as a proxy for metallicity with $Z_{\rm [O/H]} = 12 + \log{\rm [O/H]}$. Our model galaxies excibit SPH-mass-weigthed $Z_{\rm [O/H]}$ values from 8.03 to 8.96, and thus do not really probe the low metallicity range, $Z_{\rm [O/H]} \lesssim 8$, at which an increased scatter in the $L_{\rm [CII]}$-SFR relation is observed (De Looze et al., 2014; Herrera-Camus et al., 2015). Shown in the top panel of Fig. 6.13 is the scatter around the global $L_{\rm [CII]}$-SFR relation (top panel of Fig 6.10) as a function of $Z_{\rm [O/H]}$, with scatter measured as SFR/$L_{\rm [CII]}$ using the SFR directly from the the simulation. In our model galaxies, there is no increase in scatter towards low $Z_{\rm [O/H]}$, as the one observed by e.g. the D14 group, shown with black diamonds. As De Looze et al. (2014) point out, $Z_{\rm O/H}$ does not take into account potential deficits of carbon relative to the [O/H] abundance. Taking advantage of the galaxy simulation, we also looked for a connection between the scatter and $Z_{\rm C/H} = 12 + \log{\rm [C/H]}$ (in green), however finding no signs of a correlation.

Having concluded that the scatter in the $L_{\rm [CII]}$-SFR relation for our model galaxies, with their limited range in metallicity, does not depend on $Z_{\rm [O/H]}$, we move on to look on resolved scales. Defining $\langle Z_{\rm [O/H]}\rangle$ as the SPH-mass-weighted metallicities in regions of kpc-scales, $Z_{\rm [O/H],mw}$, the mean $Z_{\rm [O/H],mw}$ in 1 kpc radial bins, the metallicity drops from central values of $\langle Z_{\rm [O/H]}\rangle \sim 9$ to ~ 8.2 at $R > 10$ kpc. The outskirts of our galaxies hence resemble the metal-poor HII regions in the LMC and the SMC with $Z_{\rm [O/H]} = 8.4$ and 8.1, respectively as presented by Pagel (2003). The observed metallicity gradient in M33 is flatter, from about $Z_{\rm [O/H]} \approx 8.5$ in the center to 8.1 at $R = 8.5$ kpc (Magrini et al., 2010). But the steeper metallitiicy gradients in our $z = 2$ model galaxies is in agreement with claims that this gradient has flattened from $z = 2.2$ and until now by a factor of ~ 2.6 for galaxies of similar stellar mass and SFR (e.g. Jones et al., 2013).

In the bottom panel of Fig. 6.13, we plot the resolved scatter, SFR/$L_{\rm [CII]}$, as a function of radius for kpc^2-size regions in all model galaxies, color-coded by SPH-mass-weighted metallicity. An overall decrease of SFR/$L_{\rm [CII]}$ with radius takes place in all our model galaxies, in agreement with the increasing radial trend of $L_{\rm [CII]}/L_{\rm TIR}$ observed in M33 and M31 (Kramer et al., 2013; Kapala et al., 2015). Relatively high $L_{\rm [CII]}/L_{\rm TIR}$ values are also observed in the metal-poor HII regions of the LMC/SMC by (Israel & Maloney, 2011), who ascribe the high ratios to the combined effects of the low metallitiicy and dust content of these clouds.

A more influential factor on [CII]/$L_{\rm TIR}$ might be dust temperature (see introduction) but we are with the current model incapable of modeling dust temperatures and hence defer this subject for future improvements on the method (see Appendix B.3.1 for the method used to calculate $T_{\rm dust}$ adopted here).

6.8 Caveats

Possibly the most important choice in this work, is the assumption of an ISM structure similar to that observed for the MW, meaning that we force all molecular gas to follow the observed structure for local GMCs. This choice comes from the fact that detailed observations of ISM structure have so far been restricted to the MW, but see also Bolatto et al. (2008) and Hughes et al. (2010) who find evidence for slightly larger GMC radii in nearby dwarf or low-metallicity galaxies. However for lack of more detailed observations, we choose to adopt the MW-like GMC picture, in line with similar studies at $z \sim 2$ (Narayanan et al., 2011; Lagos et al., 2012; Popping et al., 2013).

Our calculations are based on one snapshot of a cosmological simulation, from which we infer the molecular gas in post-processing. Ideally, one should follow the build-up and destruction of molecular gas in time, as the timescale associated with H_2 formation is comparable to the timescales of the relevant processes that disrupt or alter GMCs (Pelupessy et al., 2006), but such analytic approximations, as the static one used here, have been shown by e.g. Narayanan et al. (2011) and Krumholz & Gnedin (2011) to be reasonable at metallicities above $0.01\,\mathrm{Z}_\odot$. The mass fraction of GMCs with Z< 0.01 is below $6\,\%$ in our model galaxies, except in galaxies G1, G3 and G5, where the fractions are ~ 12, 44 and $16\,\%$ respectively (see also SPH-mass-weighted histograms in Appendix B.5). Galaxies G1, G3 and G5 are expected to have lower metallicities due to their relatively low SFR, and present cases in which time-dependent study might be necessary, but we leave this for a future study.

The neutral gas mass fractions of our galaxies, are quite low compared to local normal star-forming galaxies. With the approach given in Section 6.4, 11-23 % of the SPH gas mass is considered neutral and further sub-divided into GMCs, (red and orange regions in Fig. 6.1) whereas 77-89 % remains diffuse and ionised (blue regions in Fig. 6.1). This corresponds to molecular gas mass fractions, $f_{\rm mol}$, of $\sim 3-14\,\%$ in our model galaxies, if assuming that $M_{\rm neutral} \approx M_{\rm mol}$. At $z \sim 0.4$, normal star-forming galaxies of SFRs $\sim 30-60\,\mathrm{M}_\odot\,\mathrm{yr}^{-1}$ were found by Geach et al. (2011) to have $f_{\rm mol} \sim 10-34\,\%$ (although only upper limits could be achieved for two galaxies with the lowest SFR of less than $34\,\mathrm{M}_\odot\,\mathrm{yr}^{-1}$). At $z \sim 2$ however, $f_{\rm mol}$ is expected to be even larger, as shown by (Tacconi et al., 2013) who measure a mean value of $\langle f_{\rm mol}\rangle = 47\,\%$ in a sample of 15 $z \sim 2.3$ galaxies of moderate SFRs ($\sim 62-382\,\mathrm{M}_\odot\,\mathrm{yr}^{-1}$) and stellar masses of $5.7-24\times10^{10}\,\mathrm{M}_\odot$, i.e. similar to our model galaxies (see Table 6.1). Daddi et al. (2010) report even higher molecular gas mass fractions of $50-65\,\%$ for their 6 $z \sim 1.5$ BzK-selected galaxies, with SFRs of $62-400\,\mathrm{M}_\odot\,\mathrm{yr}^{-1}$ and stellar masses of $3.3-11\times10^{10}\,\mathrm{M}_\odot$. The gas mass fractions of our model galaxies range from 21 to 57 %, with an average of $\langle f_{\rm gas}\rangle = 42\,\%$, so we do not expect $f_{\rm mol}$ to exceed this value. Even reaching $\langle f_{\rm mol}\rangle = 42\,\%$, would require that all gas in our model galaxies be neutral, which seems unlikely, but the very low $M_{\rm mol}$-to-$M_{\rm gas}$ fractions resulting from our current approach is an issue that we seek to resolve in the future.

The impinging radiation field on each GMC depends in principle on the number of and distance to nearby young stars, but since galaxy simulations such as ours only provide information on entire stellar populations at a time, we adopt the same method as Popping et al. (2013) of smoothing and scaling the UV and CR radiation field with local SFR density. The choice of smoothing the local SFRD over spheres of radius 2 kpc comes from a desire to avoid large FUV and CR field strengths for which some of our sub-gridding methods may not be valid anymore. However, we also calculated [CII] luminosities for two limiting cases: $R_{\rm SFR} = 1\,\mathrm{kpc}$ and constant [G_0, $\zeta_{\rm CR}$] values across the galaxies. The first case, of resolving the FUV field on 1 rather than 2 kpc scales, results in very similar global and resolved [CII] properties, affirming that the calculations have converged. We refrain from attempting to resolve the FUV field on even smaller scales, as that would mean modeling the light of individual stars, not captured by stellar SPH particles that each represent stellar populations. The effect of keeping G_0 and $\zeta_{\rm CR}$ constant across the galaxies (assuming values that are calculated following the approach of Narayanan & Krumholz, 2014) is to increase the mass fraction of molecular gas in the galaxy centers, where the fixed G_0 value is lower than the resolved one, at the same time as decreasing the amount of molecular gas in the outskirts where an increased G_0 in regions of low SFRD dissociates more of the GMC mass. In particular the decrease in molecular gas in the outskirts, results in a higher fraction of $L_{\rm [C\,II]}$ coming from the PDRs that are more efficient here at cooling via [CII] than the molecular counterpart, giving rise to an overall increase in total $L_{\rm [C\,II]}$ (with factors from 1.23 to 2.26 relative to the default method). We conclude that keeping G_0 and $\zeta_{\rm CR}$ fixed, according to our model, leads to overestimates of the PDR contribution to the total $L_{\rm [C\,II]}$, due to overestimates of G_0 and $\zeta_{\rm CR}$ in the outskirts of the galaxy.

The contribution to $L_{\rm [C\,II]}$ from HII regions is neglegible in all our model galaxies, but we note that this conclusion depends critically on the assumptions made about size (and hence density) of those regions. We chose to use the smoothing lengths, $h \sim 0.1 - 13\,{\rm kpc}$, of the simulation as radius for the HII clouds, as h spans the observed $10 - 1000\,{\rm pc}$ sizes of HII clouds in nearby galaxies (Oey & Clarke, 1997; Hodge et al., 1999). But if, for instance, the sizes of the HII regions is set tot $0.5 \times h$ (which would still be within the observed range), then $L_{\rm [C\,II],H\,II}$ increases by a factor 8-14.

The model galaxies used here only probe $z \sim 2$ galaxies of low SFR and over a narrow range in metallicity, but we intend to evolve the method for use on more diverse galaxies in these respects as well as redshift range.

6.9 CONCLUSION

Based on a simple underlying scheme, we present a new method for modeling [CII] emission in galaxies, capable of separating and tracing [CII] from different gas phases in the ISM. In particular, the ISM is divided into 3 phases; molecular gas regions, PDRs and ionised gas clouds.

The method is applied to a sample of 7 simulated normal star-forming galaxies at $z \sim 2$ for comparison with observations of global $L_{\rm [C\,II]}$, but also for predictions of resolved [CII] observations at high redshift. Based on this test-suite, we propose a global $L_{\rm [C\,II]}$-SFR relation at $z \sim 2$ for normal star-forming galaxies (SFR $\lesssim 100\,{\rm M_\odot\ yr^{-1}}$):

$$L_{\rm [C\,II]}\,[L_\odot] = 1.51 \pm 0.26 \times 10^7 \left(\frac{\rm SFR}{\rm M_\odot\ yr^{-1}}\right)^{0.86\pm0.19}, \tag{6.29}$$

in very good agreement with the observed relation for galaxies at $z > 0.5$ with SFR $\gtrsim 300\,{\rm M_\odot\ yr^{-1}}$ (De Looze et al., 2014).

In line with observations of the MW, we find a dominating [CII] contribution from the molecular gas phase in most of our model galaxies ($\sim 39 - 85\%\,L_{\rm [C\,II]}$), typically followed by that from PDRs ($\sim 12 - 61\%\,L_{\rm [C\,II]}$), while ionised gas accounts for an even smaller [CII] luminosity ($\sim 0.2 - 3.4\%\,L_{\rm [C\,II]}$). However, the ionised gas is in general much less important than the $20\,\%$ found for the MW.

The resolved $\Sigma_{\rm [C\,II]}$-$\Sigma_{\rm SFR}$ relation on kpc-scales resembles that observed locally in spiral galaxies, including M31, with a [CII] excess at low $\Sigma_{\rm SFR}$, caused mostly by the molecular gas.

We combine two power laws to fit the $\Sigma_{[\mathrm{CII}]}$-Σ_{SFR} of our model galaxies, using all kpc^2 regions, leading to the following expression at a χ^2 of 0.17:

$$\Sigma_{[\mathrm{CII}]} = 10^{6.52} \times {\Sigma_{\mathrm{SFR}}}^{0.45} + 10^{5.60} \times {\Sigma_{\mathrm{SFR}}}^{2.48}. \tag{6.30}$$

Finally, we do not see a correlation between mass-weighted metallicity and scatter around the $L_{[\mathrm{CII}]}$-SFR relation, but note that on resolved scales, SFR/$L_{[\mathrm{CII}]}$ does increase with metallicity.

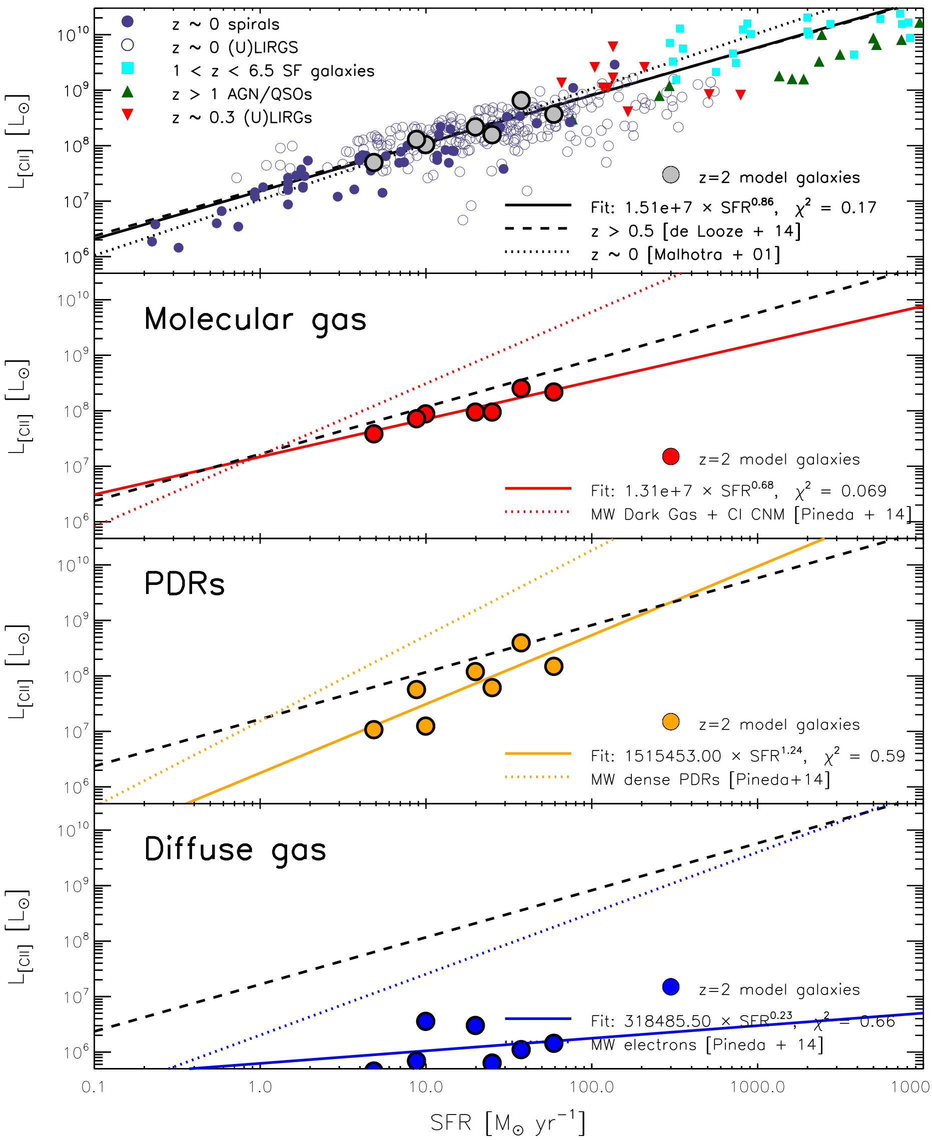

Figure 6.10 Our simulated galaxies (big filled circles) compared with the global $L_{[\mathrm{CII}]}$-SFR relation at $z > 0.5$ as determined by De Looze et al. (2014) (dashed line), and the local normal galaxies by Malhotra et al. (2001) (dotted line). From top to bottom panel, we show contributions from all gas (grey), molecular gas (red), PDRs (orange) and ionised gas (blue). Observations are the same as those used in figure 6 of Magdis et al. (2014), from whom we gratefully received the compilation. The individual observation points include 16 $z \sim 4-7$ QSOs (green triangles; Iono et al., 2006; Walter et al., 2009; Wagg et al., 2010; Gallerani et al., 2012; Wang et al., 2013; Venemans et al., 2012; Carilli et al., 2013; Willott et al., 2013), 54 local spirals (blue filled circles; Malhotra et al., 2001), 240 LIRGs and ULIRGs (blue open circles; Díaz-Santos et al., 2013; Farrah et al., 2013), 25 $1 < z < 6$ star-forming galaxies (cyan squares; De Looze et al., 2014) and 12 $z \sim 0.3$ (U)LIRGs (red triangles Magdis et al., 2014).

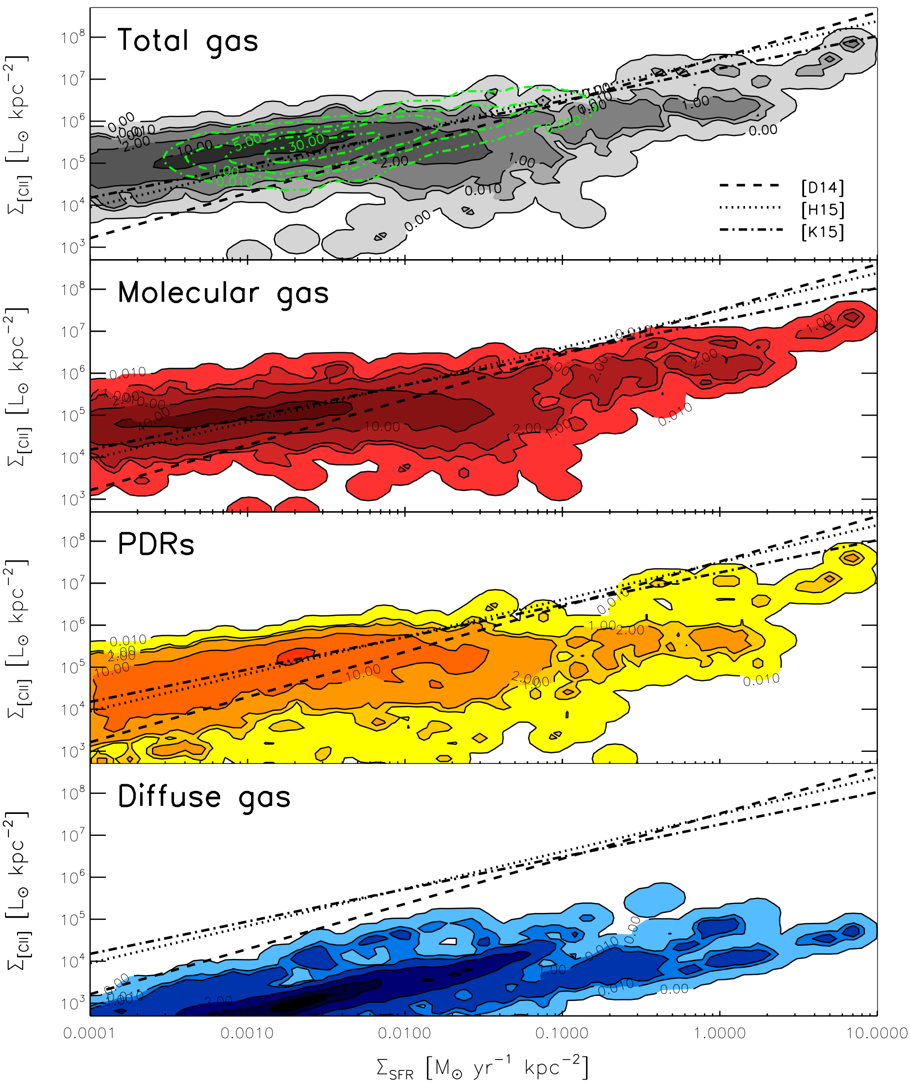

Figure 6.11 Surface brightness of [CII] luminosity, $\Sigma_{[\mathrm{CII}]}$, against surface density of SFR, Σ_{SFR}, for combined gas (top panel) and the three ISM gas phases considered (following 3 panels). Σ_{SFR} and $\Sigma_{[\mathrm{CII}]}$ are determined for kpc^2-sized pixels within all 7 galaxies and the colors indicate the number of pixels with this combination of Σ_{SFR} and $\Sigma_{[\mathrm{CII}]}$ as a percentage of the maximum number of pixels that occurs. The contour levels indicate 0.01, 1, 2, 10, 40 and 70 %. The model galaxies are compared with the combined relation for 5 fields in M31 (dash-dotted line; Kapala et al., 2015), resolved observations of local dwarf galaxies (dashed line; De Looze et al., 2014) and (mostly spiral) galaxies (dotted line; Herrera-Camus et al., 2015). Also shown in green contours are the individual 20 pc regions in M31.

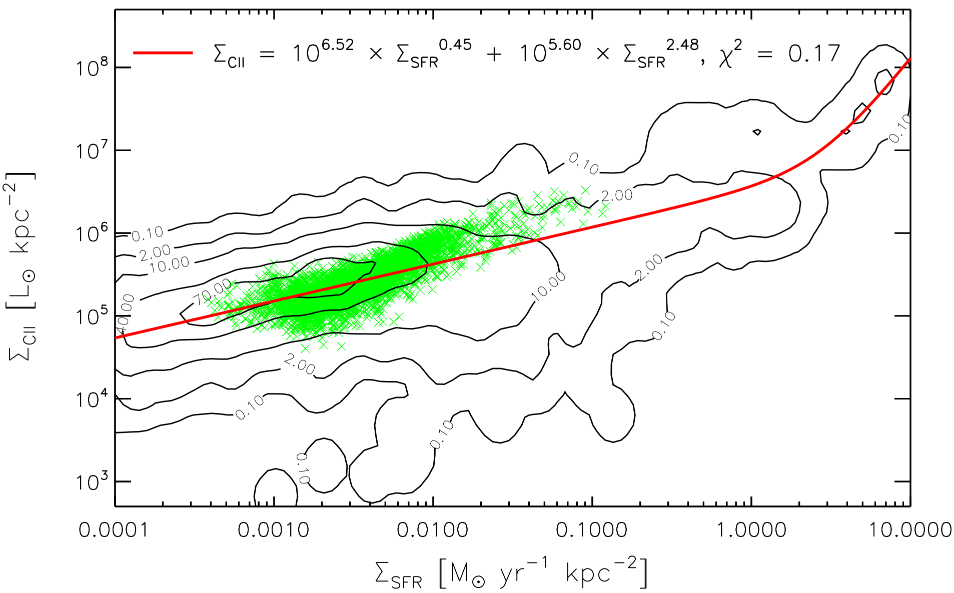

Figure 6.12 Surface brightness of [CII] luminosity, $\Sigma_{[\mathrm{CII}]}$, against surface density of SFR, Σ_{SFR}, for all contributing ISM phases in our model galaxies. Contours are the same as in Fig. 6.11 while this time we also plot the individual kpc^2 regions observed in M33 (K15; green crosses). The red line is a fit to all kpc^2 regions in our model galaxies.

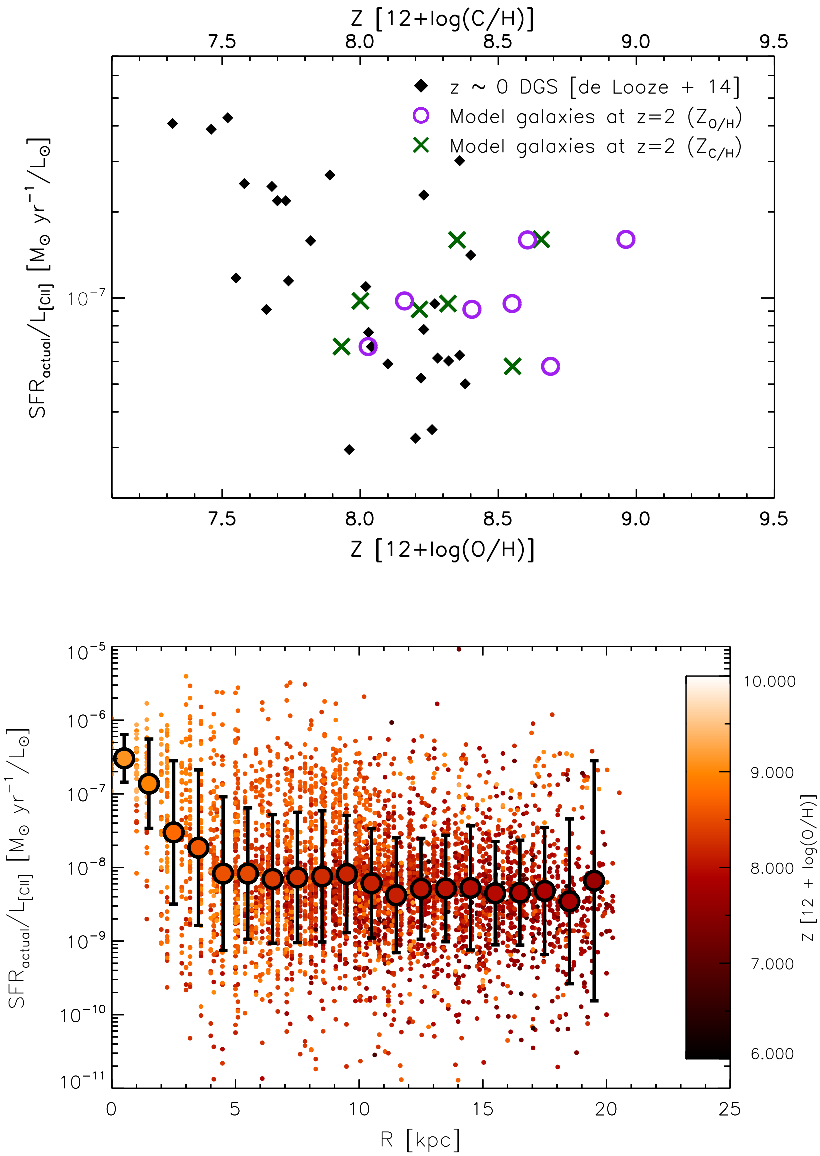

Figure 6.13 *Top:* Scatter around the $L_{[\mathrm{CII}]}$-SFR relation (top panel of Fig. 6.10) as a function of metallicity probed by either the relative oxygen abundance (purple) or the relative carbon abundance directly (green). The scatter in our model galaxies is measured as the actual SFR from the simulation, $\mathrm{SFR}_{\mathrm{actual}}$, divided by derived $L_{[\mathrm{CII}]}$. For comparison, we show the scatter in the global relation for the local dwarf galaxy sample of De Looze et al. (2014), who estimate $\mathrm{SFR}_{\mathrm{actual}}$ from a combination of the FUV and 24 μm SFR tracers. *Bottom:* The same scatter as in the top panel, but resolved in kpc^2-regions in all model galaxies as a function of radius. Mean values in 1 kpc radial bins are shown with filled circles with errorbars corresponding to 1 standard deviation, revealing decreasing trend with radius, coinsiding with lower metallicity (darker colors).

7

OUTLOOK

7.1 IMPROVEMENTS ON SÍGAME

The aim of SÍGAME is to model line emission from the ISM of galaxies at any redshift. Such a code has to be as true as possible to the observations of gas and dust, on small and large scale. At high-z (and assuming that physical laws do not change in time), this turns into a limitation in how well we can resolve the ISM spatially or spectroscopically, sometimes leading to rather crude assumptions based on what can be observed locally. As a recently developed code, SÍGAME has several such assumptions with room for improvement, of which three are listed below.

7.1.1 DUST TEMPERATURES WITH RADIATIVE TRANSFER

With SÍGAME we have demonstrated a new method that takes into account local FUV fields and CR intensities in galaxies. However, our method of scaling these fields to the local SFR and total stellar mass, can be made much more realistic with the inclusion of an actual dust radiative transfer (RT) code. One such code, developed recently, is Hyperion[1] (Robitaille, 2011) for which Powderday[2] can be used as an interface between Hyperion and galaxy formation simulations. And many alternatives exist as evident from the review by Steinacker et al. (2013). Implementing one of these would allow us to self-consistently derive dust temperatures, taking into account anisotropic scattering, absorption and (re-)emission by interstellar dust, all based on the distribution of stars and dust in the galaxy.

7.1.2 ASYMMETRIC GMCS

At present, there exists a gap between simulations of the ISM on galaxy-scales and those on scales relevant for the formation of individual stars. On galaxy-scales, simulations are typically restricted to model star formation using empirical correlations between gas density and star formation rate. However, more detailed simulations are emerging, following dense gas from kpc-scales down to $\sim 0.1\,\mathrm{pc}$ where star clusters are formed (Butler et al., 2014; Dobbs, 2015). With modifications, SÍGAME could be applied to resolved simulations of single star formation such as those of Vázquez-Semadeni et al. (2010, 2011) and Dale et al. (2013), in order to make a more precise grid in CO line intensities as a function of more global parameters. The move

[1] http://www.hyperion-rt.org/
[2] https://bitbucket.org/desika/powderday

from spherically symmetric GMC models towards the clumpy, filamentary clouds observed is an important step forward for SÍGAME.

7.1.3 HEATING BY X-RAYS AND TURBULENT DISSIPATION

Particularly towards the Galactic center, observations demand the presence of non-photon driven heating such as cosmic rays and turbulent dissipation (Ao et al., 2014). But also in normal star-forming GMCs, turbulent dissipation has been suggested as a cause for most of the observed excess in CO lines at $J_{\rm upper} \geq 6$ (Pon et al., 2012, 2014). In AGNs, the circum-nuclear disks can act like an X-ray Dominated Region (XDR), and X-ray heating is therefore important when modeling these central regions (e.g. Aalto et al., 2007; García-Burillo et al., 2010). We have focused our research projects on normal star-forming galaxies, but if SÍGAME is to work more generally on starburst and AGNs, turbulent dissipation and X-ray heating must be included in the model.

7.2 GOING TO HIGHER REDSHIFT

7.2.1 THE EVOLUTION OF $X_{\rm CO}$ WITH REDSHIFT

Gas mass estimates depend crucially on the dust-to-gas mass ratio or the X-factor, $X_{\rm CO}$. At $z \sim 2$, SÍGAME predicts $X_{\rm CO}$ factors about half that of the MW for massive star-forming galaxies, and applying the same method to simulations at higher redshift, we could investigate how $X_{\rm CO}$ changes with redshift. Such predictions will be important for future observational campaigns trying to pin down the evolution of $f_{\rm gas}$ with redshift. $X_{\rm CO}$ could also readily be applied to observations of any CO line, if we knew the shape of the CO ladder beforehand. Narayanan & Hopkins (2012) developed a parametrization of the CO ladder with $\Sigma_{\rm SFR}$ that SÍGAME can now improve on by seeing how it changes at $z > 2$ for normal star-forming galaxies.

7.2.2 THE FULL CALLIBRATION TO NORMAL GALAXIES AT $z \sim 2$

As evident from the study of CO and [CII] line emission in normal star-forming $z \sim 2$ galaxies, we are in need of more observations, in particular of the full CO SLED, in order to test models, such as SÍGAME, and use them to their fullest. I plan to continue my involvement in the HELLO (*Herschel* Extreme Lensing Line Observations) project which takes advantage of powerful lensing (by e.g. foreground groups of galaxies) in order to detect [CII] line emission from normal galaxies at $z \sim 2$. With the high spectral resolution of *Herschel*, kinematic studies of the line profiles are used to estimate rotation speed and gas velocity dispertion (Rhoads et al., 2014). Follow-up observations of CO lines with JVLA and ALMA make these galaxies excellent callibrators for SÍGAME, which itself will help in the interpretation of these future line observations.

7.2.3 GALAXIES DURING THE EPOCH OF RE-IONIZATION

In the early universe, at redshifts above 7, spectroscopic obervations in the FIR might be our only way to characterize the modest MS galaxies responsible for most star formation, that are otherwise proving difficult to capture in rest-frame UV with existing spectrographs. Observing and modeling the gas conditions during the Epoch of Re-ionization (EoR) will enable us to answer questions such as: *How did galaxies first aquire their gas masses? When did the gas become enriched by the first supernovae? What role did the gas play in setting the SFR?*

Observing with band 7 of ALMA, Capak et al. (2015) found $> 3\sigma$ detections of [CII] in a sample of 9 normal (SFR < 3 to $\sim 170\,\mathrm{M}_\odot\,\mathrm{yr}^{-1}$) galaxies at $z \sim 5-6$, of which only 4 are detected in dust continuum, underlining the importance of [CII] as a tracer of the ISM at high redshift. However, many attempts with ALMA (and PdBI) pointing at $z \sim 7$ star-forming MS galaxies for hours, have only resulted in upper limits on both [CII] line emission and dust continuum (Ouchi et al., 2013; Maiolino et al., 2015; Ota et al., 2014; Schaerer et al., 2015; González-López et al., 2014). One preferred explanation is low metallicity because the galaxies might not have had enough time to enrich the primordial gas with metallicities to a degree that their line emission is strong enough for detection (Ouchi et al., 2013; Ota et al., 2014; González-López et al., 2014; Schaerer et al., 2015). Another explanation based on recent simulations, is that molecular clouds in these primeval systems are destroyed and dispersed by strong stellar feedback, pushing most of the carbon to higher ionization states (Maiolino et al., 2015; Vallini et al., 2013). A difference in PDR structure or physical states of the ISM between star-forming galaxies at high-redshift and local ones, might also be enough to explain the low luminosity in [CII] and FIR (Ota et al., 2014).

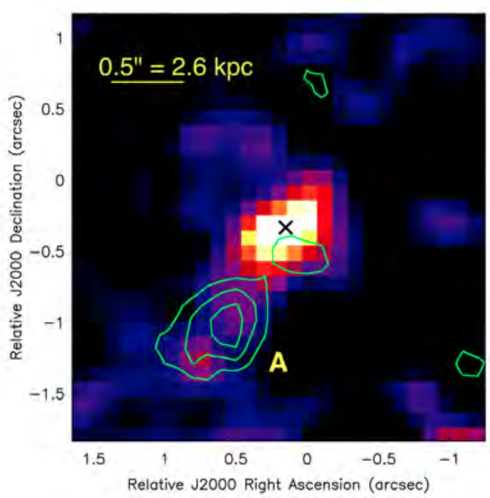

Figure 7.1 Image in rest frame UV stellar continnum and Lyα emission of the $z = 7.109$ galaxy BDF3299. Green contours show the levels of 2, 3 and 4 times the noise per beam in the [CII] map. The detected clump at 4 kpc distance from the galaxy center (black cross) is marked 'A' (Maiolino et al., 2015).

Interestingly, Maiolino et al. (2015) detect a strong (7σ) [CII] signal from a position which is offset from the actual galaxy, BDF3299 at $z = 7.109$, as shown in Fig. 7.1. This is interpreted as an accreting/satellite gas clump of neutral gas about 4 kpc from the galaxy itself. At slightly higher redshift, Watson et al. (2015) managed to detect dust continuum emission from the galaxy A1689-zD1 of SFR$\sim 10\,\mathrm{M}_\odot\,\mathrm{yr}^{-1}$. Such observations nourish the hope that we are but few steps away from using [CII] observations to charaterise the gas in normal galaxies and/or the mass assembly from the Circumgalactic Medium (CGM) in the early universe.

With this motivation, I have recently made preliminary attempts at simulating [CII] emission from halos at high redshift, in collaboration with Kristian Finlator, here at the Dark Cosmology Centre. As a simple test, we adopted a NFW profile for the radial halo density profile, and, since little is known about the metal abundance at these redshifts, assumed three values for the abundance of carbon, going from pessimistic to optimistic: $Z'_\mathrm{C} = [10^{-4.5}, 10^{-4}, 10^{-3.5}]$. The resulting rough estimate of [CII] luminosity as a function of halo mass at $z = 6$ is shown in Fig. 7.2 together with a surface brightness map for a halo mass of $5 \times 10^9\,\mathrm{M}_\odot$. With the use of actual cosmological simulations, rather than simple spherically symmetric halo models or constant metallicity and temperature, we can make much more precise predictions for the detectability of the CGM.

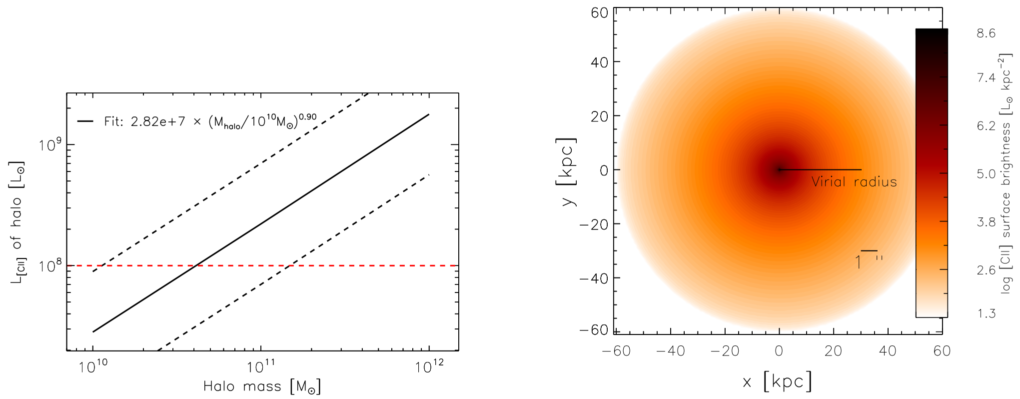

Figure 7.2 *Left:* [CII] luminosity as a function of stellar mass for our fiducial case (solid line) and the optimistic and pessimistic cases (dashed lines). *Right:* Map of [CII] surface brightness from a galaxy of stellar mass 5×10^9 $M_\odot$ at $z = 6$ (corresponding to a halo mass of 2.7×10^{11} $M_\odot$ within the virial radius, marked on the figure.

7.3 References

Aalto, S., Spaans, M., Wiedner, M. C., & Hüttemeister, S. 2007, A&A, 464, 193

Abel, N. P., Dudley, C., Fischer, J., Satyapal, S., & van Hoof, P. A. M. 2009, ApJ, 701, 1147

Ao, Y., Henkel, C., Menten, K. M., et al. 2014, in IAU Symposium, Vol. 303, IAU Symposium, ed. L. O. Sjouwerman, C. C. Lang, & J. Ott, 89–91

Blasi, P. 2013, A&A Rev., 21, 70

Blitz, L., Fukui, Y., Kawamura, A., et al. 2007, Protostars and Planets V, 81

Bolatto, A. D., Leroy, A. K., Rosolowsky, E., Walter, F., & Blitz, L. 2008, ApJ, 686, 948

Boselli, A., Gavazzi, G., Lequeux, J., & Pierini, D. 2002, A&A, 385, 454

Brauher, J. R., Dale, D. A., & Helou, G. 2008, ApJS, 178, 280

Butler, M. J., Tan, J. C., & Van Loo, S. 2014, ArXiv e-prints

Capak, P. L., Carilli, C., Jones, G., et al. 2015, ArXiv e-prints

Carilli, C. L., Riechers, D., Walter, F., et al. 2013, ApJ, 763, 120

Casey, C. M., Narayanan, D., & Cooray, A. 2014, arXiv/1402.1456

Crawford, M. K., Genzel, R., Townes, C. H., & Watson, D. M. 1985, ApJ, 291, 755

Croxall, K. V., Smith, J. D., Wolfire, M. G., et al. 2012, ApJ, 747, 81

Daddi, E., Dickinson, M., Morrison, G., et al. 2007, ApJ, 670, 156

Daddi, E., Bournaud, F., Walter, F., et al. 2010, ApJ, 713, 686

Dale, J. E., Ngoumou, J., Ercolano, B., & Bonnell, I. A. 2013, MNRAS, 436, 3430

Dartois, E., & Muñoz-Caro, G. M. 2007, A&A, 476, 1235

Davé, R. 2008, MNRAS, 385, 147

Davé, R., Katz, N., Oppenheimer, B. D., Kollmeier, J. A., & Weinberg, D. H. 2013, MNRAS, 434, 2645

De Breuck, C., Maiolino, R., Caselli, P., et al. 2011, A&A, 530, L8

de Looze, I., Baes, M., Bendo, G. J., Cortese, L., & Fritz, J. 2011, MNRAS, 416, 2712

De Looze, I., Cormier, D., Lebouteiller, V., et al. 2014, ArXiv e-prints

Díaz-Santos, T., Armus, L., Charmandaris, V., et al. 2013, ApJ, 774, 68

Dobbs, C. L. 2015, MNRAS, 447, 3390

Durier, F., & Dalla Vecchia, C. 2012, MNRAS, 419, 465

Esteban, C., García-Rojas, J., Carigi, L., et al. 2014, MNRAS, 443, 624

Farrah, D., Lebouteiller, V., Spoon, H. W. W., et al. 2013, ApJ, 776, 38
Ferkinhoff, C., Brisbin, D., Nikola, T., et al. 2011, ApJ, 740, L29
Ford, A. B., Werk, J. K., Dave, R., et al. 2015, ArXiv e-prints
Furlong, M., Bower, R. G., Theuns, T., et al. 2014, ArXiv e-prints
Gallerani, S., Neri, R., Maiolino, R., et al. 2012, A&A, 543, A114
García-Burillo, S., Usero, A., Fuente, A., et al. 2010, A&A, 519, A2
Geach, J. E., Smail, I., Moran, S. M., et al. 2011, ApJ, 730, L19
Goldsmith, P. F., Langer, W. D., Pineda, J. L., & Velusamy, T. 2012, ApJS, 203, 13
González-López, J., Riechers, D. A., Decarli, R., et al. 2014, ApJ, 784, 99
Graciá-Carpio, J., Sturm, E., Hailey-Dunsheath, S., et al. 2011, ApJ, 728, L7
Hahn, O., & Abel, T. 2011, MNRAS, 415, 2101
Hailey-Dunsheath, S., Nikola, T., Stacey, G. J., et al. 2010, ApJ, 714, L162
Herrera-Camus, R., Bolatto, A. D., Wolfire, M. G., et al. 2015, ApJ, 800, 1
Hodge, P. W., Balsley, J., Wyder, T. K., & Skelton, B. P. 1999, PASP, 111, 685
Hollenbach, D. J., & Tielens, A. G. G. M. 1999, Reviews of Modern Physics, 71, 173
Hopkins, P. F. 2013, MNRAS, 428, 2840
Hughes, A., Wong, T., Ott, J., et al. 2010, MNRAS, 406, 2065
Ibar, E., Lara-López, M. A., Herrera-Camus, R., et al. 2015, ArXiv e-prints
Iono, D., Yun, M. S., Elvis, M., et al. 2006, ApJ, 645, L97
Israel, F. P., & Maloney, P. R. 2011, A&A, 531, A19
James, B. L., Aloisi, A., Heckman, T., Sohn, S. T., & Wolfe, M. A. 2014, ApJ, 795, 109
Jones, T., Ellis, R. S., Richard, J., & Jullo, E. 2013, ApJ, 765, 48
Kanekar, N., Wagg, J., Ram Chary, R., & Carilli, C. L. 2013, ApJ, 771, L20
Kapala, M. J., Sandstrom, K., Groves, B., et al. 2015, ApJ, 798, 24
Katz, N., Weinberg, D. H., & Hernquist, L. 1996, ApJS, 105, 19
Kramer, C., Abreu-Vicente, J., García-Burillo, S., et al. 2013, A&A, 553, A114
Krumholz, M. R., & Gnedin, N. Y. 2011, ApJ, 729, 36
Krumholz, M. R., McKee, C. F., & Tumlinson, J. 2008, ApJ, 689, 865
—. 2009, ApJ, 693, 216
Krumholz, M. R., & Tan, J. C. 2007, ApJ, 654, 304
Kurtz, N. T., Smyers, S. D., Russell, R. W., Harwit, M., & Melnick, G. 1983, ApJ, 264, 538
Lada, C. J., Lombardi, M., & Alves, J. F. 2010, ApJ, 724, 687
Lagos, C. d. P., Bayet, E., Baugh, C. M., et al. 2012, MNRAS, 426, 2142
Lebouteiller, V., Cormier, D., Madden, S. C., et al. 2012, A&A, 548, A91
Leech, K. J., Völk, H. J., Heinrichsen, I., et al. 1999, MNRAS, 310, 317
Leroy, A. K., Bigiel, F., de Blok, W. J. G., et al. 2012, AJ, 144, 3
Luhman, M. L., Satyapal, S., Fischer, J., et al. 2003, ApJ, 594, 758
—. 1998, ApJ, 504, L11
Madden, S. C., Genzel, R., Herrmann, F., et al. 1992, in Bulletin of the American Astronomical Society, Vol. 24, American Astronomical Society Meeting Abstracts, 1268
Magdis, G. E., Rigopoulou, D., Hopwood, R., et al. 2014, ApJ, 796, 63
Magrini, L., Stanghellini, L., Corbelli, E., Galli, D., & Villaver, E. 2010, A&A, 512, A63
Maiolino, R., Carniani, S., Fontana, A., et al. 2015, ArXiv e-prints
Malhotra, S., Helou, G., Stacey, G., et al. 1997, ApJ, 491, L27
Malhotra, S., Kaufman, M. J., Hollenbach, D., et al. 2001, ApJ, 561, 766
McKee, C. F., & Krumholz, M. R. 2010, ApJ, 709, 308
Mezger, P. G., Mathis, J. S., & Panagia, N. 1982, A&A, 105, 372

Muñoz, J. A., & Furlanetto, S. R. 2013, ArXiv e-prints
Nagamine, K., Wolfe, A. M., & Hernquist, L. 2006, ApJ, 647, 60
Narayanan, D., & Davé, R. 2012, MNRAS, 423, 3601
Narayanan, D., & Hopkins, P. 2012, ArXiv e-prints
Narayanan, D., Krumholz, M., Ostriker, E. C., & Hernquist, L. 2011, MNRAS, 418, 664
Narayanan, D., & Krumholz, M. R. 2014, MNRAS, 442, 1411
Oey, M. S., & Clarke, C. J. 1997, MNRAS, 289, 570
Oka, T., Hasegawa, T., Sato, F., et al. 2001, ApJ, 562, 348
Oppenheimer, B. D., & Davé, R. 2008, MNRAS, 387, 577
Ota, K., Walter, F., Ohta, K., et al. 2014, ApJ, 792, 34
Ouchi, M., Ellis, R., Ono, Y., et al. 2013, ApJ, 778, 102
Pagel, B. E. J. 2003, in Astronomical Society of the Pacific Conference Series, Vol. 304, CNO in the Universe, ed. C. Charbonnel, D. Schaerer, & G. Meynet, 187
Papadopoulos, P. P., Thi, W.-F., Miniati, F., & Viti, S. 2011, MNRAS, 414, 1705
Pelupessy, F. I., & Papadopoulos, P. P. 2009, ApJ, 707, 954
Pelupessy, F. I., Papadopoulos, P. P., & van der Werf, P. 2006, ApJ, 645, 1024
Pineda, J. L., Langer, W. D., & Goldsmith, P. F. 2014, A&A, 570, A121
Pineda, J. L., Langer, W. D., Velusamy, T., & Goldsmith, P. F. 2013, A&A, 554, A103
Planck Collaboration, Ade, P. A. R., Aghanim, N., et al. 2013, ArXiv e-prints
Pon, A., Johnstone, D., & Kaufman, M. J. 2012, ApJ, 748, 25
Pon, A., Johnstone, D., Kaufman, M. J., Caselli, P., & Plume, R. 2014, MNRAS, 445, 1508
Popping, G., Pérez-Beaupuits, J. P., Spaans, M., Trager, S. C., & Somerville, R. S. 2013, ArXiv e-prints
Rhoads, J. E., Malhotra, S., Allam, S., et al. 2014, ApJ, 787, 8
Robertson, B. E., & Kravtsov, A. V. 2008, ApJ, 680, 1083
Robitaille, T. P. 2011, A&A, 536, A79
Robitaille, T. P., & Whitney, B. A. 2010, ApJ, 710, L11
Röllig, M., Ossenkopf, V., Jeyakumar, S., Stutzki, J., & Sternberg, A. 2006, A&A, 451, 917
Russell, R. W., Melnick, G., Gull, G. E., & Harwit, M. 1980, ApJ, 240, L99
Saitoh, T. R., & Makino, J. 2009, ApJ, 697, L99
—. 2013, ApJ, 768, 44
Sanders, N. E., Caldwell, N., McDowell, J., & Harding, P. 2012, ApJ, 758, 133
Sargsyan, L., Lebouteiller, V., Weedman, D., et al. 2012, ApJ, 755, 171
Schaerer, D., Boone, F., Zamojski, M., et al. 2015, A&A, 574, A19
Schaye, J., & Dalla Vecchia, C. 2008, MNRAS, 383, 1210
Schmidt, M. 1959, ApJ, 129, 243
Schöier, F. L., van der Tak, F. F. S., van Dishoeck, E. F., & Black, J. H. 2005, A&A, 432, 369
Solomon, P. M., Rivolo, A. R., Barrett, J., & Yahil, A. 1987, ApJ, 319, 730
Sparre, M., Hayward, C. C., Springel, V., et al. 2015, MNRAS, 447, 3548
Speagle, J. S., Steinhardt, C. L., Capak, P. L., & Silverman, J. D. 2014, ApJS, 214, 15
Spergel, D. N., Verde, L., Peiris, H. V., et al. 2003, ApJS, 148, 175
Springel, V. 2005, MNRAS, 364, 1105
Springel, V., & Hernquist, L. 2003, MNRAS, 339, 289
Stacey, G. J., Geis, N., Genzel, R., et al. 1991, ApJ, 373, 423
Stacey, G. J., Hailey-Dunsheath, S., Ferkinhoff, C., et al. 2010, ApJ, 724, 957
Stacey, G. J., Smyers, S. D., Kurtz, N. T., & Harwit, M. 1983, ApJ, 268, L99
Steinacker, J., Baes, M., & Gordon, K. D. 2013, ARA&A, 51, 63

Swinbank, A. M., Karim, A., Smail, I., et al. 2012, MNRAS, 427, 1066
Tacconi, L. J., Neri, R., Genzel, R., et al. 2013, ApJ, 768, 74
Thompson, R., Nagamine, K., Jaacks, J., & Choi, J.-H. 2014, ApJ, 780, 145
Tielens, A. G. G. M., & Hollenbach, D. 1985, ApJ, 291, 722
Vallini, L., Gallerani, S., Ferrara, A., & Baek, S. 2013, MNRAS, 433, 1567
Vázquez-Semadeni, E., Banerjee, R., Gómez, G. C., et al. 2011, MNRAS, 414, 2511
Vázquez-Semadeni, E., Colín, P., Gómez, G. C., Ballesteros-Paredes, J., & Watson, A. W. 2010, ApJ, 715, 1302
Venemans, B. P., McMahon, R. G., Walter, F., et al. 2012, ApJ, 751, L25
Wagg, J., Carilli, C. L., Wilner, D. J., et al. 2010, A&A, 519, L1
Walter, F., Riechers, D., Cox, P., et al. 2009, Nature, 457, 699
Wang, R., Wagg, J., Carilli, C. L., et al. 2013, ApJ, 773, 44
Watson, D., Christensen, L., Knudsen, K. K., et al. 2015, Nature, 519, 327
Webber, W. R. 1998, ApJ, 506, 329
Whitaker, K. E., Labbé, I., van Dokkum, P. G., et al. 2011, ApJ, 735, 86
Wiersma, R. P. C., Schaye, J., Theuns, T., Dalla Vecchia, C., & Tornatore, L. 2009, MNRAS, 399, 574
Willott, C. J., Omont, A., & Bergeron, J. 2013, ApJ, 770, 13

Part II

The AGN-galaxy co-evolution at $z \sim 2$

8

How to detect an AGN

A general concern when estimating the SFR by fitting the broadband SED of a galaxy with stellar population synthesis models, is the relative dominance of AGN versus star formation. The dominant contributor to the mid-infrared (MIR) light is from UV-light reprocessed by dust, but the UV light can be emitted by either young stars or an AGN. At $z \sim 2$ it is not clear, without the aid of high spatial and spectral resolution, what is causing the observed MIR emission from massive galaxies; is dust in the central regions being heated by AGN activity, is dust across a larger region of the galaxy being heated by star formation, or is a combination of the two scenarios taking place?

X-ray emission, on the other hand, does not suffer from strong dust obscuration. Observing in X-ray can thus lift the apparent degeneracy in interpreting the origin of the MIR light, and thereby help to give the true AGN fraction of a sample of galaxies. A galaxy dominated by AGN activity can be distinguished from a galaxy dominated by star formation by having a harder X-ray spectrum if the AGN is obscured by dust, or by simply having a very high X-ray luminosity, $L_{0.5\text{-}8\,\mathrm{keV}}$. The most heavily obscured 'Compton-thick' AGNs, with column densities $N_\mathrm{H} > 10^{24}\,\mathrm{cm}^{-2}$, might be missed by X-ray selection, but can instead be identified via an excess of MIR emission over that expected from purely star-forming galaxies (e.g., Daddi et al., 2007; Treister et al., 2009).

The shape of the MIR spectrum can also reveal AGNs, as the intense nuclear emission re-emitted by dust leads to a power-law spectrum in the MIR. For this purpose, color cuts have been devised using the *Spitzer* data (e.g., Stern et al., 2005; Donley et al., 2012). While this technique has the capability of detecting even Compton-thick AGNs, otherwise missed in X-ray, it has a low efficiency for low- to moderate-luminosity AGNs and its robustness has yet to be verified at $z \gtrsim 2$ (Cardamone et al., 2008).

In a galaxy where star formation is dominant, the total hard band X-ray luminosity, $L_{2\text{-}10\,\mathrm{keV}}$, can be used to estimate the SFR (e.g., Grimm et al., 2003; Ranalli et al., 2003; Lehmer et al., 2010). An AGN will reveal itself if the X-ray SFR inferred this way is much larger than the SFR derived from other tracers such as Hα, UV, or MIR luminosity. Also, if star formation dominates the radiation output, the $L_x \rightarrow$SFR conversion will give an upper limit on the SFR as has been obtained for sub-mm galaxies (Laird et al., 2010) and for massive, star-forming galaxies at $1.2 < z < 3.2$ (Kurczynski et al., 2012).

At redshifts around 2, high-ionization lines in the rest-frame UV can be used as AGN indicators, but X-ray observations remain a more efficient way of identifying AGNs (Lamareille, 2010).

8.1 X-RAY EMISSION FROM AN AGN

I will focus this section on X-ray emission generated by the accretion of matter onto a SMBH, as described in Section 1.3, since it is this characteristic that I use for detecting AGN in my study of the presence of AGN at high-z (Part II).

Fig. 8.1 shows the X-ray part of the SED of a type I AGN, together with individual contributions from its components, the nature of which is elaborated on below.

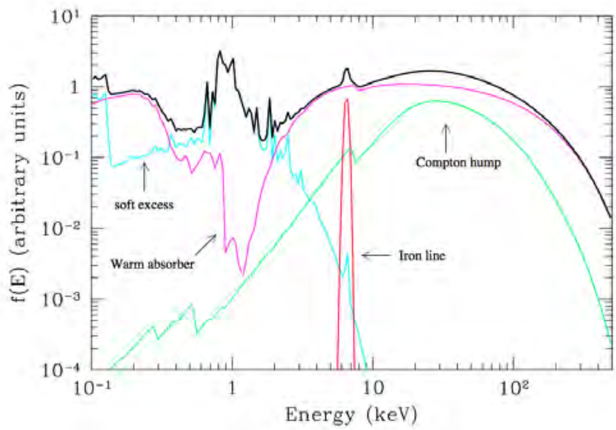

Figure 8.1 The X-ray spectrum (black) of a typical type I AGN, with curves showing the contrution from a primary continuum component (pink) resembling a power law but aborbed at soft energies by warm gas, a cold reflection component (green; Compton hump) and a soft excess (cyan). Also shown is iron Kα emission – the most relevant narrow feature (red), arising in the inner parts of the accretion disk. Figure from the review by Risaliti & Elvis (2004).

At high X-ray energies (~ 30 keV), the SED is dominated by reflection component ('Compton hump') consisting of primary emission from the accretion disk being scattered by ionized gas, i.e. electrons. This component will be largest if the reflector is Compton-thick but smaller in the Compton-thin case in which case some of the incident radiation escapes without interaction (Risaliti & Elvis, 2004). An additional hard component is sometimes present, most likely caused by inverse-Compton scattering of the radio-synchroton photons off of electrons in the relaticistic jet itself. At lower energies ($\lesssim 2$ keV) with an almost universal effective temperature of $\sim 0.1 - 0.2$ keV, a 'soft excess' is often observed but less understood. Models suggest that the strongest soft excesses are found in AGNs with low mass accretion rates Done et al. (2012), and typically atomic processes are invoked to explain the soft excess via either ionized reflectioni with light bending or the remaining part of a high-energy power law subject to ionized absorption (Vasudevan et al., 2014). But also comptonization models have been proposed, in which the soft excess consists of UV/soft-X-ray photons by a population of hot electrons Matt et al. (2014). The joint NuSTAR/XMM program as well as future X-ray missions such as ASTRO-H and ASTROSAT (to be launched this year) are likely to break the degeneracy between these models (see Section 1.5). Finally a warm, ionized absorber exists that reflects the incident continuum without changing its spectral shape.

To first order though, the intrinsic or 'primary' emission from the central engine is a power law extending from 1 to 100 keV, with the slope determined by the different components described. The slope of the power law can be used to determine the amount of obscuration in the AGN, as more obscuration will result in a steeper power law (harder). In order to estimate the column density of obscuring material, one has to take a guess at the spectral slope, Γ, of the

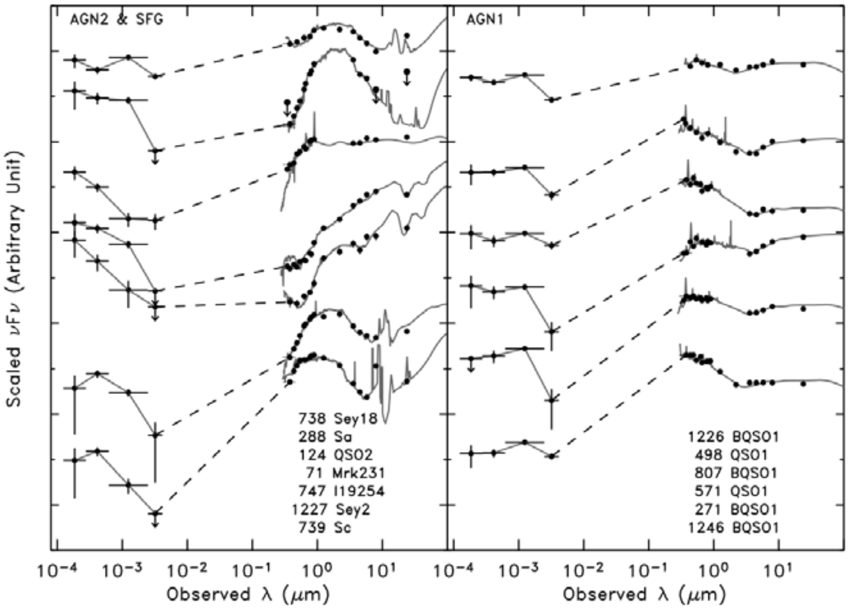

Figure 8.2 X-ray spectra of 13 galaxies from the work of Tajer et al. (2007). *Left:* Top two spectra are consistent with star-forming template SEDs shown, while the following 4 galaxies have type 2 AGN SEDs. *Right:* Type 1 AGN SEDs.

intrinsic emission from the obscured source:

$$dN/dE[\text{photons cm}^{-2}\ \text{s}^{-1}\ \text{keV}^{-1}] \propto E^{-\Gamma} \tag{8.1}$$

where dN is the number of photons with energy in the dE energy range. Note that a harder spectrum has *lower* Γ as shown in the left-hand plot of Fig. 8.3. A value of $\Gamma = 1.9$ is usually adopted, based on observations showing that Γ is roughly constant for large samples of low-luminosity Seyfert galaxies and bright QSOs for redshifts up to ~ 5 (e.g. Nandra & Pounds, 1994; Reeves & Turner, 2000; Piconcelli et al., 2005).

Fig. 8.2 shows 13 SEDs from X-ray to FIR ($100\,\mu$m) of type I and type II AGN with best-fit galaxy templates. The X-ray part consists of data from XMM (see Section 1.5) sampled with 4 bands at 0.3-0.5, 0.5-2, 2-4.5, 4.5-10 and 2-10 keV.

The high angular resolution ($\sim 0.5''$) of *Chandra* combined with the high sensitivity in the deep fields CDF-N and CDF-S (see Section 1.4), makes these fields advategous for searches of AGN at low and high redshift (Bauer et al., 2004; Xue et al., 2011; Treister et al., 2009; Alexander et al., 2011). For those studies, the observed X-ray spectra of *Chandra* are typically divided into a full ($0.5-8$ keV), a soft ($0.5-2$ keV) and a hard ($2-8$ keV) band. A proxy for the powerlaw slope is the 'hardness ratio', HR, defined as:

$$\text{HR} = (H-S)/(H+S) \tag{8.2}$$

where H and S are the counts in hard and soft band respectively. Hardness ratio has the advantage, in comparison to Γ, of avoiding any assumptions regarding the shape of the spectrum.

Assuming an intrinsic obscured power law with $\Gamma = 1.9$, HR converts into a column density that increases with the 'hardness' of the spectrum as shown in the right-hand plot of Fig. 8.3.

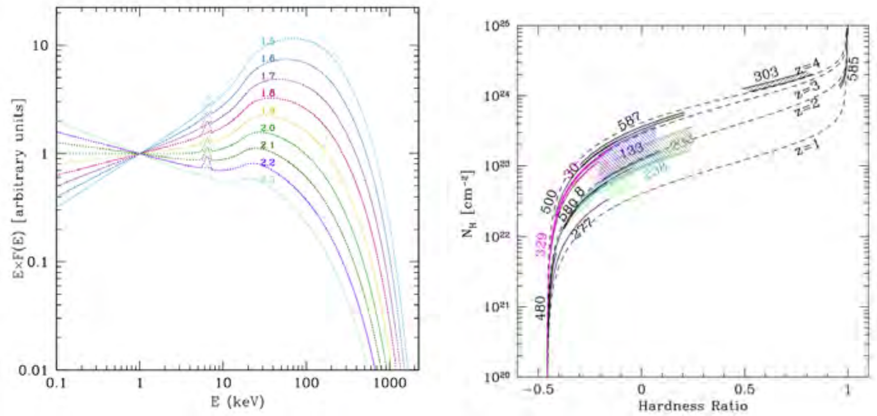

Figure 8.3 Measures of intrinsic power law slope in AGN. *Left:* SED templates for unobscured Seyferts normalized at 1 keV (Gilli et al., 2007). *Right:* Column density of obscuring material as a function of hardness ratio, HR (Treister et al., 2009).

The criteria for finding an AGN are a high full-band X-ray luminosity ($\gtrsim 2 \times 10^{42}$ ergs/s) of a hard spectrum with HR > -0.2 for sources of lower luminosity These criteria are meant to rule out galaxies with SEDs consisten with star formation processes only. However, a third possible origin of a bright X-ray component in the area-integrated SED, is a hot gas halo embracing the galaxy (Mulchaey & Jeltema, 2010). Souch a component can be ruled out, if the observed X-ray source is predominantly point-like, rather than extended.

8.1.1 Previous observations

Several studies of massive $z \sim 2$ galaxies have therefore been made with the aim of uncovering AGN fractions, using the *Chandra* X-ray observatory. Rubin et al. (2004) performed a study of 40 massive ($M_* = (1\text{-}5) \times 10^{11} M_\odot$) red ($J_s - K_s \geq 2.3$) galaxies at $z \gtrsim 2$ by analyzing a 91 ks *Chandra* exposure. Roughly 5% of these were found to host an AGN with intrinsic $L_{2\text{-}10\,\mathrm{keV}} > 1.2 \times 10^{43}\,\mathrm{erg\,s^{-1}}$. Assuming that the stacked X-ray signal from the remaining X-ray undetected galaxies in X-ray comes from star formation alone, they derived a mean SFR broadly consistent with the typical mean SFRs estimated from SED fits. Alexander et al. (2011) analyzed the 4Ms *Chandra* observations of 222 star-forming BzK galaxies ($M_* \sim 10^{10}\text{-}10^{11} M_\odot$, Daddi et al., 2007) in the Chandra Deep Field-South (CDF-S). 10%(23) showed X-ray emission consistent with AGN dominance, of which 5%(11) were found to contain heavily obscured AGNs, 4%(9) to have luminous, unobscured AGNs, and 3 out of 27 low-luminosity systems showed excess variability over that expected from star formation processes, indicating that at least some low-luminosity (rest-frame $L_{2\text{-}10\mathrm{keV}} < 10^{43}\,\mathrm{erg\,s^{-1}}$) systems may contain AGNs.

9

ON THE PREVALENCE OF AGN AT $z \sim 2$ (PAPER III)

9.1 AIM OF THIS PROJECT

The aim of this project was to determine the AGN fraction in massive $z \sim 2$ galaxies, and reveal any differences between quiescent and star-forming galaxies.

9.2 OUR METHOD AND GALAXY SAMPLE

We addressed the matter by analyzing the X-ray emission from a mass-complete ($M_* > 5 \times 10^{10} M_\odot$) sample of $1.5 \leq z \leq 2.5$ galaxies residing in the CDF-S. The CDF-S, observed for $4\,$Ms, is currently the deepest X-ray view of the universe and so provides the best opportunity to study high-z galaxies across a relatively large area ($464.5\,$arcmin^2).

We selected our galaxies from the FIREWORKS[1] catalog (Wuyts et al., 2008), which covers a field situated within the CDF-S and contains photometry in 17 bands from the U band to the MIR. For this study we extracted a mass-complete sample of $M_* > 5 \times 10^{10} M_\odot$ galaxies at $1.5 \leq z \leq 2.5$ in a way similar to that of Franx et al. (2008) and Toft et al. (2009). We used spectroscopic redshifts when available (Vanzella et al., 2008; Xue et al., 2011), and photometric redshifts from the FIREWORKS catalog otherwise. In order to maximize the signal-to-noise (S/N) on results from X-ray stacking (Zheng et al., 2012) and ensure a relatively homogeneous PSF across the *Chandra* field employed, we considered only galaxies that lie within 6′ of the average *Chandra* aimpoint.

We adopted galaxy stellar masses from the SED fitting results of Franx et al. (2008) and Toft et al. (2009). In short, the SED fits were carried out with models by Bruzual & Charlot (2003), choosing the best fit from adopting three different star formation histories (a single stellar population with no dust, an exponentially declining star formation history of timescale $300\,$Myr with dust, and a constant star formation history with dust). In cases where the spectroscopic redshift differed by more than 0.1 from the original FIREWORKS photometric redshift, we re-did the SED fits in FAST[2] using an exponentially declining star formation history with a range of possible timescales from $10\,$Myr to $\sim 1\,$Gyr. As a quality parameter of the SED modeling, we demanded an upper limit on the reduced χ^2_ν of 10 on the best-fit model. The SED fits pro-

[1] http://www.strw.leidenuniv.nl/fireworks/

[2] http://astro.berkeley.edu/~mariska/FAST.html

vide SFR estimates, but we used SFRs derived from rest-frame UV+IR luminosities (see Section 9.2.3) as these include obscured star formation and are subject to less assumptions. From the observed photometry, rest-frame fluxes in U, V, J band and at 2800 Å have been derived using InterRest[3] (Taylor et al., 2009).

We divided the resulting sample of 123 galaxies into quiescent and star-forming galaxies using the rest-frame U, V and J (falling roughly into the observed J, K and IRAC $4.5\,\mu$m bands at $z \sim 2$) colors. Dust-free but quiescent galaxies differ from dust-obscured starburst galaxies in that they obey the following criteria by Williams et al. (2009):

$$U - V > 1.3 \tag{9.1}$$

$$V - J < 1.6 \tag{9.2}$$

$$(U - V) > 0.88 \times (V - J) + 0.49 \tag{9.3}$$

The fraction of quiescent galaxies identified within our sample using this method is $22\% \pm 5\%(27/123)$. This is rather low compared to the 30–50% found by Toft et al. (2009) for the same redshift and mass limit, but under the requirement that the sSFR (=SFR/M_*) from SED fitting is less than $0.03\,\mathrm{Gyr}^{-1}$. If applying this criterion, we would have arrived at a fraction of $42\% \pm 7\%(51/123)$. A possible reason for the discrepancy between the two methods may be that we were using the UVJ criterion in the limits of the redshift range in which it has so far been established. As the redshift approaches 2, the quiescent population moves to bluer $U - V$ colors, possibly crossing the boundaries of Equation (9.3). However, we preferred the UVJ selection technique in contrast to a cut in sSFR, because rest-frame colors are more robustly determined than star formation rates from SED fits.

9.2.1 X-RAY DATA AND STACKING ANALYSIS

The raw X-ray data from the CDF-S survey consist of 54 individual observations taken between 1999 October and 2010 July. We build our analysis on the work of Xue et al. (2011), who combined the observations and reprojected all images. They did so in observed full band (0.5–8 keV), soft band (0.5–2 keV) and hard band (2–8 keV), and the resulting images and exposure maps are publicly available.[4]

We extracted source and background count rates in the X-ray maps for all galaxies using the method of Cowie et al. (2012). Source counts were determined within a circular aperture of fixed radii: $0''.75$ and $1''.25$ at off-axis angles of $\theta \leq 3'$ and $\theta > 3'$ respectively. Background counts were estimated within an annulus 8″–22″ from the source, excluding nearby X-ray sources from the catalog of Xue et al. (2011).

Each galaxy was classified as 'X-ray detected' if detected in at least one band at $\geq 3\sigma$ significance, thereby creating 4 subsamples containing 8 quiescent and detected, 19 quiescent and undetected, 43 star-forming and detected, and 53 star-forming and undetected galaxies.

While the X-ray detected galaxies could be analyzed individually, we stacked the X-ray non-detected galaxies in order to constrain the typical X-ray flux from these. Stacked X-ray images of the 4 subsamples are shown in Figure 9.1 with all galaxies aligned to their K_s band galaxy center positions from FIREWORKS. Representative count rates and associated errors for these stacks were calculated using the optimally weighted mean procedure of Cowie et al.

[3] `http://www.strw.leidenuniv.nl/~ent/InterRest`

[4] `http://www2.astro.psu.edu/users/niel/cdfs/cdfs-chandra.html`

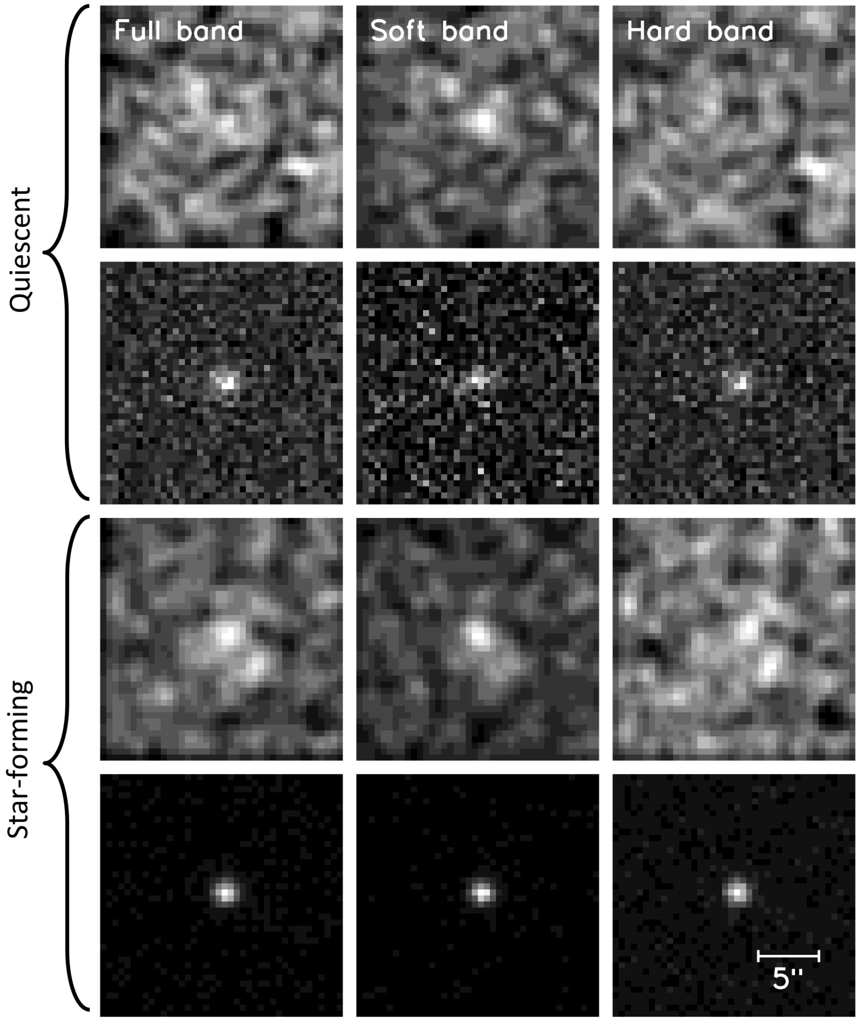

Figure 9.1 Stacked, background-subtracted and exposure-corrected 20″ × 20″ images in the three energy bands (columns) for the individually non-detected (top row) and detected (bottom row) quiescent and star-forming galaxies. Images of the non-detections have been smoothed with a Gaussian of width 2 pixels.

(2012) and tabulated in Table 9.1 together with S/N values.

	Count Rate $\pm 1\sigma$ (10^{-6} s^{-1}) in		
	Full Band	Soft Band	Hard Band
Q	0.71 ± 0.96	2.01 ± 0.41	-1.67 ± 0.86
	(0.7)	(4.9)	(-1.9)
SF	2.51 ± 0.55	1.08 ± 0.24	1.29 ± 0.49
	(4.5)	(4.5)	(2.7)

Table 9.1 Stacking results for Quiescent (Q) and Star-forming (SF) galaxies not detected individually in X-Rays (in Parentheses the corresponding S/N)

The reliability of our chosen method for X-ray stacking and source count extraction was tested with Monte Carlo (MC) simulations. With 500 MC simulations of 53 (corresponding to the number of star-forming galaxies not detected in X-rays) randomly selected positions having no X-ray detections nearby, we obtained a histogram of stacked S/N values that is well fitted by a normal distribution with a center at -0.02 ± 0.8, that is, consistent with no detection. Similar results were obtained using a sample size of 19, the number of quiescent non-detections.

$L_{0.5\text{–}8\,\mathrm{keV}}$ ($\mathrm{erg\,s^{-1}}$)	HR	Classification
$> 3\times10^{42}$	< -0.2	Unobscured AGNs ($N_\mathrm{H} < 10^{22}\ \mathrm{cm^{-2}}$)
$> 3\times10^{42}$	> -0.2 and < 0.8	Moderately obscured AGNs ($10^{22} < N_\mathrm{H} < 10^{24}\ \mathrm{cm^{-2}}$)
$> 3\times10^{42}$	> 0.8	Compton-thick AGNs ($N_\mathrm{H} > 10^{24}\ \mathrm{cm^{-2}}$)
$< 3\times10^{42}$	< -0.2	Star-forming galaxy
$< 3\times10^{42}$	> -0.2	Low-luminosity obscured AGNs or star-forming galaxy

Table 9.2 Classification scheme used in this work, with limits from Szokoly et al. (2004), Wang et al. (2004), and Treister et al. (2009)

We quantified the hardness of the X-ray spectra using the hardness ratio (see eq. 8.2). Assuming a power-law spectrum, we also derived a photon index, Γ, with the online mission count rate simulator WebPIMMS[5] using a Galactic H 1 column density of $8.8 \times 10^{19}\ \mathrm{cm^{-2}}$ (Stark et al., 1992) and not including intrinsic absorption. Whenever the S/N in either soft or hard band was below 2, we used the corresponding 2σ upper limit on the count rate to calculate a limit on both HR and Γ, leading to a limit on the luminosity as well. When neither a hard- nor a soft-band flux was detected with an S/N above 2, a typical faint source value of $\Gamma = 1.4$ (Xue et al., 2011) was assumed, corresponding to HR ~ -0.3 for an intrinsic powerlaw spectrum of $\Gamma = 1.9$ (Wang et al., 2004).

We derived the unabsorbed flux from the count rate by again using the WebPIMMS tool, now with the Γ tied to the observed value of either the individually detected galaxy or the stack in question. With this method, a count rate of $\sim 10^{-5}$ counts $\mathrm{s^{-1}}$ corresponds to a flux of nearly $10^{-16}\ \mathrm{erg\,cm^{-2}\,s^{-1}}$ in full band at a typical value of $\Gamma = 0.8$. Finally, the flux was converted into luminosity in the desired rest-frame bands using XSPEC version 12.0.7 (Arnaud, 1996).

9.2.2 Luminous AGN Identification

In the top panel of Figure 9.2 are shown the rest-frame X-ray full band luminosities, $L_{0.5\text{–}8\,\mathrm{keV}}$, not corrected for intrinsic absorption, versus observed hardness ratio, HR, for all X-ray detected galaxies as well as stacked non-detections. A typical detection limit on $L_{0.5\text{–}8\,\mathrm{keV}}$ has been indicated with a dotted line in Figure 9.2, calculated as two times the background noise averaged over all source positions. A few detected galaxies were found below this limit due to these residing at relatively low z and/or in regions of lower-than-average background. Galaxies with $L_{0.5\text{–}8\,\mathrm{keV}} > 3 \times 10^{42}\ \mathrm{erg\,s^{-1}}$ were selected as luminous AGN, since star-forming galaxies are rarely found at these luminosities (Bauer et al., 2004). In addition, we adopted the HR criteria in Table 9.2 in order to identify obscured and unobscured AGNs.

About $53\%(27/51)$ of the X-ray detected galaxies were identified as luminous AGNs, with 22 moderately to heavily obscured ($-0.2 <$ HR < 0.8) and 5 unobscured (HR < -0.2) AGNs.

[5] http://heasarc.nasa.gov/Tools/w3pimms.html

The rest had X-ray emission consistent with either low-luminosity AGNs or star formation. We did not identify any Compton-thick AGNs directly, but three galaxies had lower limits on their hardness ratios just below HR $= 0.8$, thus potentially consistent with Compton-thick emission (see Table 9.2). In total, we detected a luminous AGN fraction of $22\% \pm 5\%(27/123)$, a fraction which is $23\% \pm 5\%(22/96)$ for the star-forming and $19\% \pm 9\%(5/27)$ for the quiescent galaxies.

Stacking the non-detections resulted in average X-ray source properties that exclude high luminosity AGNs. However, the inferred limits on their HR were consistent with a contribution from low-luminosity AGNs, the importance of which cannot be determined from this plot alone.

9.2.3 X-RAY INFERRED SFR

From the rest-frame hard band luminosity, $L_{2\text{–}10\,\text{keV}}$ it is possible to derive estimates of the SFR, as the number of high-mass X-ray binaries (HMXBs) is proportional to the SFR (Ranalli et al., 2003). Kurczynski et al. (2012) made a comparison of different SFR indicators, by applying three different $L_x \rightarrow$SFR conversions to 510 star-forming BzK galaxies at $1.2 < z < 3.2$, selected as having $L_{2\text{–}10\,\text{keV}} < 10^{43}\,\text{erg}\,\text{s}^{-1}$. While relations by Persic et al. (2004) and Lehmer et al. (2010) overestimated the true SFR (from rest-frame UV and IR light) by a factor of ~ 5, the relation by Ranalli et al. (2003) provided a good agreement at $1.5 < z < 3.2$. But, as pointed out by Kurczynski et al. (2012), all relations might lead to an overestimation due to contamination by obscured AGNs in the sample of SF galaxies. As we did not know the exact amount of obscured AGN contamination in the stacks, we chose to use the following relation by Ranalli et al. (2003) as a conservative estimate of the SFR:

$$\text{SFR}_{2\text{–}10\,\text{keV}} = 2.0 \times 10^{-40}\, L_{2\text{–}10\,\text{keV}} \tag{9.4}$$

with SFR measured in $M_\odot\,\text{yr}^{-1}$ and $L_{2\text{–}10\,\text{keV}}$ in $\text{erg}\,\text{s}^{-1}$. Another reason for not using the more recent relation by Lehmer et al. (2010) is that this relation was constructed for galaxies with SFR $> 9\,M_\odot\,\text{yr}^{-1}$ only, whereas a large part of our sample had very low SFRs as inferred from SED fitting ($< 1\,M_\odot\,\text{yr}^{-1}$). Following Kurczynski et al. (2012), we used the observed soft band flux to probe the rest-frame hard band luminosity. The uncertainty on the SFR is estimated from the error on the observed soft-band flux together with a systematic error in the relation itself of 0.29 dex, as given by Ranalli et al. (2003).

For comparison, the 'true' SFR is inferred from rest-frame UV and IR light, $\text{SFR}_{\text{UV+IR}}$, following the method of Papovich et al. (2006):

$$\text{SFR}_{\text{UV+IR}} = 1.8 \times 10^{-10}(L_{\text{IR}} + 3.3 L_{2800})/L_\odot \tag{9.5}$$

where L_{IR} is the total infrared luminosity and L_{2800} is the monochromatic luminosity at rest-frame 2800 Å. L_{2800} comes from the rest-frame UV flux, $f_{2800\text{Å}}$, and in this context, the errors on $f_{2800\text{Å}}$ are negligible. We derived L_{IR} from the observed $24\,\mu$m flux, $f_{24\mu\text{m}}$, using redshift-dependent multiplicative factors, $a(z)$, from the work of Wuyts et al. (2008), Section 8.2 in that paper):

$$L_{\text{IR}}[L_{\odot,8\text{–}1000\mu\text{m}}] = 10^{a(z)} \cdot f_{24\mu\text{m}} \tag{9.6}$$

The errorbars on L_{IR} derive from the errors on $f_{24\mu\text{m}}$ and we further assume an uncertainty

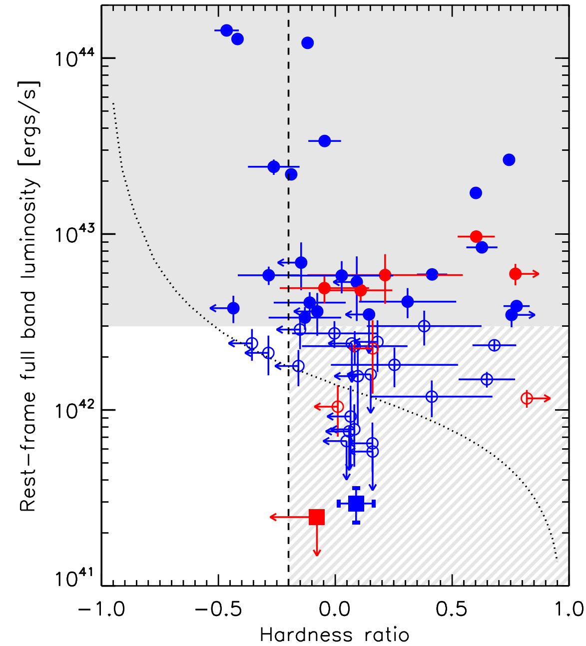

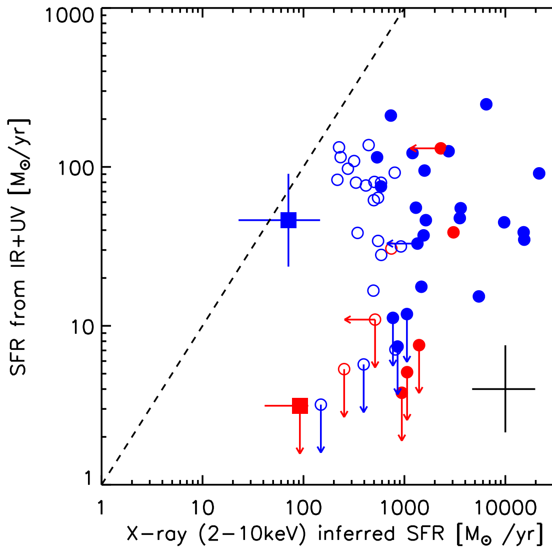

Figure 9.2 Top: $L_{0.5\text{–}8\,\mathrm{keV}}$ vs. HR for all galaxies. Red: quiescent galaxies. Blue: star-forming galaxies. Squares: stacks of non-detected samples. Filled circles: luminous AGNs (selected with the X-ray criteria indicated by a shaded area). Open circles: galaxies dominated by low-luminosity AGNs or star formation processes alone (selected with X-ray criteria indicated by a hatched area). Dashed line: separating obscured ($N_{\mathrm{H}} \gtrsim 10^{22}$ cm^{-2}) from unobscured AGNs. Dotted line: typical detection limit. Errorbars display 2σ errors and limits are indicated with arrows. Bottom: $\mathrm{SFR}_{\mathrm{UV+IR}}$ vs. $\mathrm{SFR}_{2\text{–}10\mathrm{keV}}$ (see the text). Dashed line: equality. Typical errors on X-ray detected galaxies are shown in the lower right corner. Symbols are as above.

of 0.3 dex in the relation of Papovich et al. (2006) as found by Bell (2003) when comparing to Hα- and radio-derived SFRs. The X-ray undetected quiescent galaxies were not detected with S/N> 3 in 24 μm either (except in one case) leading to a mean flux of $1.2 \pm 1.7 \mu$Jy, of which we adopted a 2σ upper limit for the remaining analysis.

In the bottom panel of Figure 9.2, $\mathrm{SFR}_{2\text{–}10\,\mathrm{keV}}$ is compared to $\mathrm{SFR}_{\mathrm{UV+IR}}$ with the dashed line indicating equality. It is no surprise that nearly all of the individual X-ray detections have very high $\mathrm{SFR}_{2\text{–}10\,\mathrm{keV}}$ as compared to $\mathrm{SFR}_{\mathrm{UV+IR}}$, as we were largely insensitive to individual purely star-forming galaxies, given the detection limits in the top panel of Figure 9.2 and the criteria in Table 9.2.

For the star-forming stack, the X-ray inferred SFR of $71 \pm 51 M_\odot\,\mathrm{yr}^{-1}$ is consistent with the IR+UV inferred SFR of $46 \pm 33 M_\odot\,\mathrm{yr}^{-1}$, whereas the quiescent stack shows an $\mathrm{SFR}_{2\text{–}10\,\mathrm{keV}}$ of $92 \pm 65 M_\odot\,\mathrm{yr}^{-1}$ ($89 \pm 17 M_\odot\,\mathrm{yr}^{-1}$ when bootstrapping this sample 200 times), well exceeding $\mathrm{SFR}_{\mathrm{UV+IR}} \leq 3 M_\odot\,\mathrm{yr}^{-1}$.

9.3 An overwhelmingly large AGN population

9.3.1 Luminous AGN Fraction

In total, 22 X-ray detected galaxies have emission consistent with containing a luminous (rest-frame $L_{0.5\text{–}8\mathrm{keV}} > 3 \times 10^{42}\,\mathrm{erg\,s^{-1}}$) and obscured ($10^{22} < N_\mathrm{H} < 10^{24}\,\mathrm{cm^{-2}}$) AGN, and a further five have emission consistent with a luminous unobscured ($N_\mathrm{H} < 10^{22}\,\mathrm{cm^{-2}}$) AGN. This leads to a luminous AGN fraction of the full sample of $22\% pm 5\% (27/123)$ and of the detected galaxies only, $53\% \pm 13\% (27/51)$. The AGN fraction among both quiescent and star-forming galaxies, according to their X-ray spectra, is measured to be around 20% as Table 9.3 shows, meaning that AGNs in massive $z \sim 2$ galaxies, even quiescent ones, are common, as proposed by Kriek et al. (2009) who studied the near-IR spectrum of one quiescent galaxy.

	Quiescent (27)	Star-forming (96)
Luminous AGNs	5	22
Low-luminosity AGNs	2 (det) 12–19 (non-det)	19 (det) 0–21 (non-det)
Luminous AGN fraction	$19\% \pm 9\%$	$23\% \pm 5\%$
Total AGN fraction	70%–100%	43%–65%

Table 9.3 X-Ray derived AGN Numbers and Fractions for Quiescent and Star-forming Galaxies, Divided into Luminous AGNs and Detected and Non-detected Low-luminosity AGNs

This luminous AGN fraction is high when compared to the 5% found by Rubin et al. (2004) (see the introduction), but this is likely a consequence of their 4σ detection limit of $1.2 \times 10^{43}\,\mathrm{erg\,s^{-1}}$ in rest-frame 2–10 keV being about twice as high as our limit of $5.5 \times 10^{42}\,\mathrm{erg\,s^{-1}}$ (at $\Gamma = 1.4$), as calculated from the average background noise in the observed soft band. Adopting the detection limit of Rubin et al. (2004) and requiring an S/N of at least 4, we reduce our fraction of luminous AGN to $8\% \pm 3\% (10/123)$, consistent with the results of Rubin et al. (2004). Alexander et al. (2011), using also the 4 Ms CDF-S data, found a much lower X-ray detection fraction of $21\% \pm 3\%$ as compared to ours ($53\% \pm 7\%$), and a luminous AGN fraction of only $9\% \pm 2\% (20/222)$. We believe that the discrepancies have several reasons, the main ones being: (1) our use of a mass-complete sample, whereas the BzK selection technique used by Alexander et al. (2011) includes galaxies down to $M_* \sim 10^{10} M_\odot$ for which the total AGN fraction, assuming a fixed Eddington ratio, is expected to be lower above our detection limit,[6] (2) our updated source count extraction and stacking method leading to higher S/N, and (3) the use of Γ instead of HR in the AGN identification conducted by Alexander et al. (2011). For comparison, Tanaka et al. (2012) recently discovered a group of quiescent galaxies at $z = 1.6$ with only one main-sequence star-forming galaxy. This group differed from local groups in having a remarkably high AGN fraction of $38^{+23}_{-20}\%$, consistent with our result, and which they interpret as possible evidence for AGN activity quenching star formation.

9.3.2 Importance of Low-luminosity AGNs

As seen in Figure 9.2, the X-ray-identified luminous AGNs in general show an excess in SFR compared to that inferred from IR+UV emission. Among the galaxies classified as being dominated by either low-luminosity AGN or star formation, about $\sim 90\%(21/24)$ have $\mathrm{SFR}_{2\text{–}10\,\mathrm{keV}}$ more than 1σ above $\mathrm{SFR}_{\mathrm{UV+IR}}$.

Surprisingly, the quiescent stack also has a much larger $\mathrm{SFR}_{2\text{–}10\,\mathrm{keV}}$ than $\mathrm{SFR}_{\mathrm{IR+UV}}$. Even when removing the marginally undetected galaxies with 2 <S/N< 3, the resulting $\mathrm{SFR}_{2\text{–}10\,\mathrm{keV}} = 62 \pm 19 M_\odot\,\mathrm{yr}^{-1}$ is still more than 3σ above $\mathrm{SFR}_{\mathrm{IR+UV}}$. This discrepancy is only further aggravated if instead assuming the SFR$-L_X$ relation of Lehmer et al. (2010). If caused by obscured star formation, we would have expected an average $24\,\mu$m flux of $90\,\mu$Jy for the individual galaxies, in order to match the lower limit on $\mathrm{SFR}_{2\text{–}10\,\mathrm{keV}}$. This is far above the upper limit of $3.4\,\mu$Jy for the stack, suggesting that the X-ray flux of this stack is instead dominated by low-luminosity AGNs, but that their contribution to the $24\,\mu$m flux remains undetectable in the *Spitzer*–MIPS data.

We derived a lower limit on the low-luminosity AGN contribution for this stack of 19 objects by constructing a mock sample of the same size and with the same redshifts, but containing N low-luminosity AGNs with luminosities $L_{0.5\text{–}8\,\mathrm{keV}} = 10^{42}\,\mathrm{erg\,s^{-1}}$ just below the detection limit and $19 - \mathrm{N}$ galaxies with $L_{0.5\text{–}8\,\mathrm{keV}} = 10^{41}\,\mathrm{erg\,s^{-1}}$ (all of them with $\Gamma = 1.4$). From random realizations of this mock sample we found that at least $\mathrm{N} = 12$ low-luminosity AGNs are required to match the observed rest-frame 2–10 keV luminosity of the stack. Similarly, we found that by removing at least 12 randomly selected galaxies it is possible to match the low SFR predicted by IR+UV emission, though only with a small probability ($\sim 1\%$ of 200 bootstrappings). We therefore adopted $63\%(= 12/19)$ as a conservative lower limit on the low-luminosity AGN fraction among quiescent X-ray non-detections, but we note that the data were consistent with all the quiescent galaxies hosting low-luminosity AGNs if the luminosity of these was assumed to be only $L_{0.5\text{–}8\,\mathrm{keV}} = 7 \times 10^{41}\,\mathrm{erg\,s^{-1}}$.

Interestingly, the quiescent stack was only detected in the soft band, cf. Table 9.1, whereas one might expect a significant contribution to the hard band flux from a low-luminosity AGN population as the one proposed above. The lack of a hard band detection can be explained by the fact that the sensitivity of the CDF-S observations drops about a factor of six from the soft to the hard band (Xue et al., 2011), meaning that the low-luminosity AGN population must be relatively unobscured ($\Gamma > 1$, consistent with the value of 1.4 assumed here), as it would otherwise have been detected in the hard band with an S/N$\,> 2$.

The $\mathrm{SFR}_{2\text{–}10\,\mathrm{keV}}$ of the star-forming stack was consistent with its $\mathrm{SFR}_{\mathrm{UV+IR}}$, meaning that a strict lower limit to the low-luminosity AGN fraction here, is zero. However, performing the

[6] For a fixed Eddington ratio, and assuming that galaxy bulge mass increases with total stellar mass, the AGN X-ray luminosity is expected to scale with galaxy stellar mass according to the M_{bh}–M_{bulge} relation (Häring & Rix, 2004)

test above with the same model parameters, a maximum of $40\%(21/53)$ low-luminosity AGNs is possible, before the X-ray inferred SFR exceeds the upper limit on $\mathrm{SFR_{UV+IR}}$.

It should be mentioned that the $24\,\mu$m flux, especially at these high redshifts, is an uncertain estimator of the total rest-frame infrared luminosity, i.e., the entire dust peak, used in the conversion to SFR. As shown by Bell (2003), one should ideally use the entire 8–$1000\,\mu$m range, e.g., by taking advantage of Herschel data, which can lead to systematic downward correction factors up to ~ 2.5 for galaxies with $L_{\rm IR} \approx 10^{11} L_\odot$ (similar to the inferred IR luminosities of our sample galaxies detected in $24\,\mu$m, showing a median of $L_{\rm IR} = 10^{11.5} L_\odot$) as demonstrated by Elbaz et al. (2010). However, using the same conversion from $f_{24\mu\rm m}$ to $L_{\rm IR}$ as the one implemented in this study, Wuyts et al. (2011) showed that the resulting $L_{\rm IR}$ for galaxies out to $z \sim 3$ are consistent with those derived from PACS photometry with a scatter of 0.25 dex. Hence, we do not expect the inclusion of Herschel photometry in the this study to significantly impact any of our results, and we leave any such analysis for future work.

Table 9.3 gives an overview of the derived AGN fractions, both at high and low X-ray luminosity. Adding the numbers of luminous AGN, X-ray-detected low-luminosity AGNs as well as the estimated lower limit on the low-luminosity AGN fraction among non-detections, we arrive at a lower limit on the total AGN fraction of

$$f_{\rm AGN} \geq \frac{27 + 21 + 0.6 \cdot 19 + 0 \cdot 53}{123} = 0.48 \tag{9.7}$$

for all massive galaxies at $z \sim 2$. While for the star-forming galaxies this fraction lies in the range from 43%–65%, it must be 70%, and potentially 100%, for the quiescent galaxies. Using the upper limits on these numbers, a tentative upper limit on the total AGN fraction is 0.72.

9.3.3 Contribution from Hot Gas Halos

We have so far considered star formation and AGN activity as causes of the X-ray emission observed, but a third possibility is an extended hot gas halo as seen around many nearby early-type galaxies in the same mass-range as our sample galaxies (Mulchaey & Jeltema, 2010) and predicted/observed around similar spirals (Toft et al., 2002; Rasmussen et al., 2009; Anderson & Bregman, 2011; Dai et al., 2012). AGN X-ray emission is expected to come from a very small, $R < 1\,$pc, accretion disk surrounding the central black hole of the host galaxy (Lobanov & Zensus, 2007), whereas very extended star formation in the galaxy or a hot gas halo surrounding it would lead to more extended emission. We investigated the possibilities for these latter cases by comparing radial surface brightness profiles of the 51 individually X-ray detected galaxies out to a radius of $8''$ in both the stacked observed image and a correspondingly stacked PSF image.

The profiles were calculated in full band only, because of the high S/N here as compared to the other bands (cf. Figure 9.1). For each galaxy, we extracted the background subtracted source count per pixel within 10 concentric rings of width $0''.8$ around the galaxy center positions from the FIREWORKS catalog, and each profile was normalized to the mean count rate in all rings. The same procedure was applied to the corresponding PSF images, extracted with the library and tools that come with CIAO,[7] allowing for extraction at the exact source positions on the detector. We verified the robustness of using PSF models from the CIAO calibration database

[7] `http://cxc.cfa.harvard.edu/ciao4.3/ahelp/mkpsf.html`

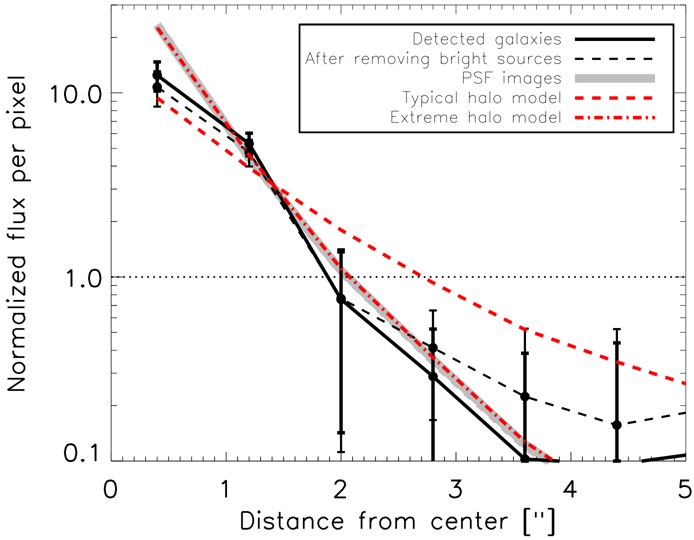

Figure 9.3 Comparison of the radial surface brightness profiles in PSF images vs. observed images in full band for all detected galaxies. Black: stacked observed image centered on K-band positions from FIREWORKS for all detected galaxies (solid line) and if excluding the three X-ray brightest sources (dashed line). Grey line: stacked PSF image. Red: stack of halo model images, with $\beta = 0.5$, $R_c = 2.5$ kpc (dashed) and $\beta = 1$, $R_c = 1$ kpc (dot-dashed).

for this purpose, by repeating the above procedure for 51 known X-ray bright point-like sources from the catalog of Xue et al. (2011), and confirming that the resulting mean profile was fully consistent with that of the corresponding model PSFs.

As can be observed in Figure 9.3, the combined radial profile of our X-ray detected galaxies in the full band is consistent with the PSF of point sources stacked at the same detector locations. A Kolmogorov-Smirnov (K-S) test yields a statistic of 0.2 and a probability of 99.96% that the two profiles are drawn from the same parent sample.

Omitting the three sources with $L_{0.5\text{–}8\,\mathrm{keV}} > 10^{44}\,\mathrm{erg\,s^{-1}}$ (cf. Figure 9.2) leads to a more extended profile (dashed black line in Figure 9.3), but the result still shows a high corresponding K-S probability of 70%. We also compared the profiles while recentering the images on the center of the X-ray emission as derived using WAVDETECT[8] instead of the K-band center positions listed in the FIREWORKS catalog, in order to test for the impact of any off-set between the X-ray and optical centroids. However, the recentering only resulted in small variations within the errorbars on the original profile. The same conclusions applied to the subsample of X-ray detected star-forming galaxies only, whereas the S/N was too low to perform a similar study on the quiescent, X-ray detected sample alone.

For comparison, we also simulated the stacked profile of extended hot gas halos, using for the surface brightness profile the β-model first introduced by Cavaliere & Fusco-Femiano (1976). With default parameters of $\beta = 0.5$ and core radius $R_c = 2.5$ kpc, both taken from the study of $z \lesssim 0.05$ early-type galaxies by O'Sullivan et al. (2003), the stacked profile of the halos, convolved with the corresponding PSFs, is well outside the errorbars of the measured profile. Only if assuming an extremely compact case of $\beta = 1$ and $R_c = 1$ kpc, does the halo

[8]WAVDETECT is part of the CIAO software.

emission become sufficiently compact to mimic that of the PSF profile (see dash-dotted line in Figure 9.3), but the halo model then overpredicts the observed surface brightness on scales smaller than $1''$. In conclusion, a hot gas halo alone, described by a β-model, cannot explain the emission, unless one chooses model parameters that render the profile indistinguishable from a point-like source.

9.3.4 Quenching of Star Formation by AGNs?

It remains debated whether the presence of AGN is connected with internal galaxy properties associated with secular evolution or, to a higher degree, with external processes (Darg et al., 2010). For example, the cosmic star formation rate density and the number density of AGN share a common growth history with a peak in activity around $z \sim 2$–3 (Treister & Urry, 2012; Dunlop, 2011), hinting at a co-evolution between SFR and supermassive black hole (SMBH) accretion (Schawinski, 2011). We investigated the correlation, if any, between the presence of AGNs and internal/external processes, treating luminous and low-luminosity AGNs separately. As typical internal properties governing secular evolution we focused on stellar mass, M_*, and SFR (Peng et al., 2010), while major mergers were taken as a likely case of external processes and as a phenomenon often associated with luminous AGNs (Treister et al., 2012).

Starting with our X-ray identified luminous AGNs, we found that the fraction of these does not correlate with star formation in our sample (cf. Table 9.3). In addition, the distribution of luminous AGNs and that of the rest with regards to their $\text{SFR}_{\text{IR+UV}}$ are similar, with a K-S test yielding a statistic of 0.21 with a probability of 59%. Similarly, Harrison et al. (2012) found no correlation between AGN luminosity and quenching of star formation, albeit at a higher luminosity ($L_{2-8\,\text{keV}} > 10^{44}\text{erg}\,\text{s}^{-1}$) than probed here. Dividing the sample according to M_* instead, by constructing two bins around the median mass of $1.1 \times 10^{11}\,M_\odot$, we arrived at similar luminous AGN fractions above and below this mass limit, namely $21\% \pm 7\%(13/61)$ and $23\% \pm 7\%(14/62)$, respectively. We thus find no clear evidence for the luminous AGN fraction of our sample to correlate with internal properties, suggesting that an external factor is of larger importance.

An alternative is that luminous AGNs are primarily triggered by non-secular processes such as major mergers. Treister et al. (2012) found that major mergers are the only processes capable of triggering luminous ($L_{\text{bol}} \gtrsim 10^{45}\,\text{erg}\,\text{s}^{-1}$) AGN at $0 < z < 3$. Our luminous AGN fraction is consistent with the major merger fraction of massive ($M_* > 10^{11}M_\odot$) galaxies at $1.7 < z < 3$ found by Man et al. (2012) to be $15\% \pm 8\%$ (compared to a luminous AGN fraction of $11 \pm 3\%(13/123)$ when excluding galaxies with $M_* < 10^{11}M_\odot$). This is consistent with the idea that our luminous AGNs are triggered by major mergers, but a more direct test of this scenario would be to search for major mergers using the imaging data available in CDF-S. Indeed, Newman et al. (2012) used *HST* CANDELS imaging in the GOODS-South field residing within CDF-S (along with the UKIRT Ultra Deep Survey) to arrive at roughly equal pair fractions when comparing massive ($M_* > 10^{10.7}M_\odot$) quiescent to massive star-forming galaxies at $0.4 < z < 2$. Again, this is in agreement with our result that the luminous AGN fraction does not vary between quiescent and star-forming galaxies. A detailed morphological study of our X-ray identified luminous AGN using the *HST*/WFC3 data to search for evidence of merging is an interesting extension to the work presented here, which we leave for a future study.

Turning toward our low-luminosity AGNs, we *do* see X-ray evidence for an enhanced population among the quiescent galaxies when compared to their star-forming equivalents. The mean masses of our non-detected samples of quiescent and star-forming galaxies are similar (14.6 ± 1.6 and $12.7 \pm 1.0 \times 10^{10}\ M_\odot$ respectively), suggesting that the relevant factor here is SFR. At $0.01 < z < 0.07$, Schawinski et al. (2009) found that massive ($M_* \gtrsim 10^{10} M_\odot$) host galaxies of low-luminosity AGNs all lie in the green valley, that is, at some intermediate state after star formation quenching has taken place and before the SED is truly dominated by old stellar populations. The observation that these host galaxies had been quiescent for ~ 100 Myr, ruled out the possibility that one short-lived, luminous AGN suppressed star formation and, at the same time, made it unlikely that the same AGN quenching star formation was still active, given current AGN lifetime estimates of $\sim 10^7$–10^8 yr (Di Matteo et al., 2005). Rather, the authors favored a scenario in which a low-luminosity AGN already shut down star formation, followed by a rise in luminosity, making the AGN detectable. At $z \sim 2$, SED fits of massive ($M_* > 10^{11} M_\odot$) quiescent galaxies show that the quenching typically took place ~ 1 Gyr before the time of observation (Toft et al., 2012; Krogager, J.-K. et al., in preparation), demanding an even longer delay *or* an episodic AGN activity as frequently applied in models (Croton et al., 2006). Episodic AGN activity could explain why we see evidence for a higher low-luminosity AGN fraction among quiescent as compared to star-forming galaxies, but it would also require the low-luminosity AGN phase in quiescent galaxies to last at least as long as the dormant phase. Future modeling and observations will show whether this is in fact possible.

We conclude that our data are consistent with a scenario in which luminous AGNs in massive galaxies at $z \sim 2$ are connected with major mergers or other non-secular processes, while the presence of low-luminosity AGNs in the majority of quiescent galaxies suggests that these AGNs present an important mechanism for quenching star formation and keeping it at a low level. Ultimately what happens at $z \sim 2$ has to agree with the subsequent evolution that changes size and morphology of quiescent galaxies (Barro et al., 2013).

9.4 CONCLUSIONS

Our main conclusions are on the following two topics:

1. *Luminous AGN fraction*
   We find a luminous AGN fraction of $22\% \pm 5\%$ among massive ($M_* > 5 \times 10^{10} M_\odot$) galaxies at redshifts $1.5 \leq z \leq 2.5$, using their X-ray properties extracted from the 4 Ms Chandra Deep Field South observations. Among the X-ray detected galaxies, $53\% \pm 13\%$ harbor high-luminosity AGNs, while stacking the galaxies not detected in X-ray, leads to mean detections consistent with low-luminosity AGNs or pure star formation processes. The luminous AGN fraction among quiescent and star-forming galaxies is similar ($19\% \pm 9\%$ and $23\% \pm 5\%$, respectively) and does not depend on galaxy M_*.
   We confirmed that extended X-ray emission from a hot gaseous halo is not a viable explanation for the observed X-ray emission of the X-ray detected galaxies.

2. *Limits on total AGN fraction*
   We convert the rest-frame hard band X-ray luminosity into an upper limit on the star formation rate, $\mathrm{SFR}_{2\text{–}10\,\mathrm{keV}}$ and compare to that derived from the rest-frame IR+UV emission, $\mathrm{SFR}_{\mathrm{IR+UV}}$. All luminous AGNs show an excess in $\mathrm{SFR}_{2\text{–}10\,\mathrm{keV}}$ as expected, and so does a large fraction ($\sim 90\%$) of the remaining detected galaxies. While the star-forming galaxies not detected in X-ray have a mean X-ray inferred SFR of $71 \pm 51 M_\odot\ \mathrm{yr}^{-1}$, consistent with their $\mathrm{SFR}_{\mathrm{IR+UV}}$, the stack of quiescent galaxies shows an excess in $\mathrm{SFR}_{2\text{–}10\,\mathrm{keV}}$ of

a factor > 10 above the upper limit on $\mathrm{SFR_{IR+UV}}$. For these galaxies, we find that a minimum fraction of $\sim 60\%$ must contain low-luminosity ($L_{0.5\text{–}8\,\mathrm{keV}} \approx 10^{42}\,\mathrm{erg\,s^{-1}}$) AGNs if the SFR estimates from X-ray are to be explained, and that low-luminosity AGNs might be present in all of them. On the other hand, for the star-forming stack, we derive a low-luminosity AGN fraction of 0–40%.
Gathering all low- and high-luminosity AGNs, we derive a lower limit to the total AGN fraction of 48%, with a tentative upper limit of 72%.

Our study was the first to present observational evidence that, at $z \sim 2$, the majority of quiescent galaxies host a low- to a high-luminosity AGN, while the AGN fraction is significantly lower in star-forming galaxies. These findings are consistent with an evolutionary scenario in which low-luminosity AGN quench star formation via the energetic output from SMBH accretion, which, if believed to continue in an episodic fashion as often invoked by models, would need to have 'dormant' phases at least as long as 'active' phases.

We find that the high-luminosity AGNs are likely related to non-secular processes such as major mergers. In the future, examining the X-ray properties of galaxies in a larger sample, cross-correlated with signs of major mergers, may shed further light on the co-evolution of AGNs and host galaxy.

10

OUTLOOK

Since we published these results in 2013, many additional observational studies have been carried out with the aim of shedding light on AGN-galaxy co-evolution at $z \sim 2$. A short summary is provided here together with future directions in this field.

10.1 THE AGN-MORPHOLOGY CONNECTION

First of all, we found no clear evidence for a correlation between the presence of a luminous AGN and the internal properties of massive galaxies at $z \sim 2$. This was interpreted as an argument for the need of external factors triggering the luminous AGN phase rather than events associated with secular evolution. However, we only considered stellar mass and SFR, whereas more recent observations have established a clear correlation between the presence (and strength) of AGN and the morphology of its host galaxy.

In this regard, Barro et al. (2013) analysed the morphologies and SFRs of $\mathrm{M}_* > 10^{10}\,\mathrm{M}_\odot$ galaxies at $z = 1.4 - 3$ in the GOODS-S and CANDELS UDS fields, for comparison with AGN activity as a function of redshift. Barro et al. (2013) found a population of compact star-forming galaxies (cSFGs; defined as having $\log\left(\mathrm{M}_*/r_e^{1.5}\right)$ below $10.3\,\mathrm{M}_\odot\,\mathrm{kpc}^{-1.5}$) at $z = 2.6 - 3.0$ that dissappears before the compact quiescent galaxies (CQGs) of similar structural properties appear at lower redshifts. At the same time, the AGN fraction among cSFGs is higher at $z > 2$ than at lower redshifts and X-ray luminous ($L_{2-8\,\mathrm{keV}} > 10^{43}\,\mathrm{erg\,s^{-1}}$) AGNs are found $\sim 30\,\%$ more frequently in cSFGs than in non-compact ones at $z > 2$. This was interpreted as a sign that at least some cSFGs evolve directly into the CQGs observed at $z \sim 2$ via the evolutionary path described in Section 2.1.5, whereas non-compact quiescent galaxies, formed later on, are the result of normal SFGs that are quenched by other mechanisms which partially preserve the structural properties.

Deriving the total IR luminosity directly from the $24\,\mu$m flux only, is a rough approximation that could possibly affect our results and those of Barro et al. (2013), as the possible contribution from an AGN to the FIR luminosity can lead to overestimates of the SFR. Mancini et al. (2015) did a more careful estimate of L_{IR} with (*Spitzer*+*Herschel*) photometry from $24\,\mu$m to $250\,\mu$m of 56 $\mathrm{M}_* \geq 10^{11}\,\mathrm{M}_\odot$ galaxies at $1.4 \leq z \leq 2$ in the GOODS-S field, for a better estimate of $\mathrm{SFR}_{\mathrm{IR+UV}}$. Defining AGN as those with excess X-ray and/or radio (VLA 1.4 GHz) luminosity with respect to the expected $\mathrm{SFR}_{\mathrm{IR+UV}}$ or $\mathrm{SFR}_{\mathrm{SED}}$, and classifying galaxies as star-forming/quiescent based on sSFR as well as UVJ color, the authors found relatively high AGN fractions of $\sim 40 \pm 10\,\%$ and $\sim 22 \pm 7\,\%$ for star-forming and quiescent galaxies, respectively (though fractions very close to ours when adopting the same criteria). In agreement with Barro et al. (2013), Mancini et al. (2015) also found that the presence of an AGN correlates with compactness as probed by a steep radial surface brightness profile in rest-frame optical. Over a wider redshift range, $1.4 < z < 3$ but with a similar method, Rangel et al. (2014) concluded that compact galaxies, both quiscent and star-forming, display higher intrinsic $2-8$ keV luminosities and levels of obscuration that in extended galaxies.

These studies show that of out massive galaxies at $z \sim 2$, compact ones contain the most powerful AGN, and that when studying quiescent/star-forming galaxy samples across redshift, observations seem to promote a picture in which cSFGs evolve directly into CQGs via a relatively obscured AGN phase, albeit of high (absorption-corrected) X-ray luminosity.

10.2 Direct observations of AGN feedback

Direct evidence for the radiative and quasar mode of AGN feedback is now existing for a few, mostly nearby, objects (see review by Fabian, 2012). For example, in a study of the UV absorption line profiles of 226 $M_* \geq 10^{11}\,M_\odot$ galaxies at $1 < z < 3$, Cimatti et al. (2013) found possible gas outflow velocities of up to $\sim 500\,\mathrm{km\,s^{-1}}$, but only in galaxies classified as luminous AGNs (with $L_{2-8\,\mathrm{keV}} > 10^{42.3}\,\mathrm{ergs\,s^{-1}}$). This indicates that the gas here is moving faster than the escape velocity of active galaxies, resulting in the ejection of part of the ISM possible decrease in SFR. With the X-ray satellite Nustar, sensitive to high energy X-rays of $3-79$ keV, it is also possible to see such outflows in X-ray absorption and emission lines as demonstrated by Nardini et al. (2015). Likewise but at high redshift, Nesvadba et al. (2011) observed evidence for outflows of turbulent gas traced by narrow-line emission in the rest-frame UV and optical of two quasars at $z \sim 3.4$ and ~ 3.9. In addition to observations in UV, AGN feedback has been confirmed with radio and sub-mm observations, in particular in the form of strong molecular outflows (e.g. Feruglio et al., 2010; Cicone et al., 2014; Tombesi et al., 2015). Comparing the mass outflow (or inflow) rates of ionized or molecular gas to the accretion rate to the AGN, hints at the effect that these might have on the global SFR, as summarized by e.g. Bergmann (2012) and Storchi-Bergmann (2014). However, *more observations of both jets and outflows, observationally confirmed in at least some AGNs at redshifts out to almost $z \sim 4$, are needed in order to settle how they affect the ISM of their host galaxies as a whole.*

10.3 Future directions: Adding variability with time

In particular the arrival of new oberving facilities, will open up this field towards high redshift by studying both individual cases and global properties of large samples.

Seeing the strong connection between compactness and AGN activity at high-z, as revealed over recent years, this field will benefit tremendously from the arrival of JWST, that will enable rest-frame optical imaging out to $z \sim 10$ with 3 times better angular resolution than HST at 1.6μm (Beichman et al., 2012). That means being able to see whether AGNs are associated with compact galaxies all the way out to Epoch of Re-ionization (EoR). With the high NIR spectral resolution of JWST, the absence of poly-aromatic hydrocarbon (PAH) emission at $\sim 6-11\,\mu$m can also be used to select possibile AGN candidates without the need of X-ray observations (Windhorst et al., 2009; Hanami et al., 2011). The combined forces of JVLA, JWST and ALMA will also allow detections of molecular outflows at high-z by measuring gas kinematics as traced by molecular and fine structure lines (Fabian, 2012).

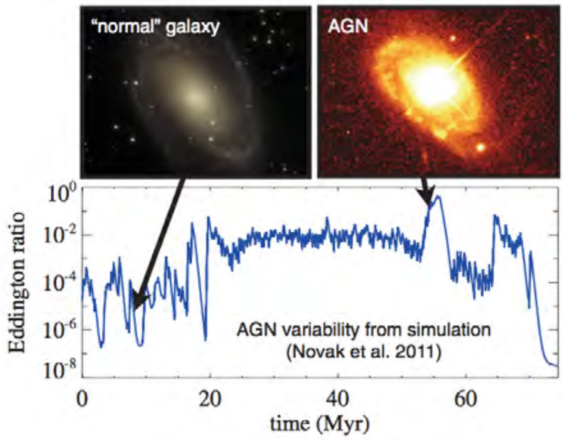

Figure 10.1 Illustration of AGN variability from Hickox et al. (2014) who took the Eddington ratio, a measure of BHAR, as a function of time from a hydrodynamic simulation presented by Novak et al. (2011) (*bottom*). Depending on the time of observation, the same galaxy can happen to be in an inactive state or a bright AGN state.

A potentially very important factor, but not completely revealed in any of the above studies, is time variation. As mentioned in Section 9.3.4, major mergers at $0 < z < 3$ have been associated with the most luminous AGNs (Treister et al., 2012), whereas moderate-luminosity ($L_{0.5\text{-}8\,\mathrm{keV}} \sim 10^{42-44}\,\mathrm{ergs\,s^{-1}}$) AGNs at $z \sim 2$ are not associated with disturbed morphologies, indicative of recent mergers, any more than non-active galaxies are (Kocevski et al., 2012). This said, the apparent lack of merger signatures in AGNs cannot rule out a connection between AGNs and mergers. First of all, if mergers in the initial phase generally produce obscured AGNs, then these will be harder to detect in X-rays, unless one has access to the hard X-rays that penetrate the obscuring gas better than the soft ones. One would then expect moderate AGNs to be primarily observed in post-starburst galaxies, in agreement with our stacking of un-detected X-ray sources, that revealed a *higher* signal from quiescent galaxies than from SFGs. Another exception would be if there exists a time delay between the merger and the actual onset of the luminous AGN phase. With JWST and upcoming X-ray observatories (see Section 1.5), we can start to piece together the redshift distribution of AGNs and mergers/pairs to look for a possible delay. A second time-related issue, possibly blurring the observable relationship between AGNs and their hosts, is variability of the AGN luminosity as shown in Fig. 10.1. Models show, that when reasonable variability for the AGN luminosity is assumed, the weak correlations between SFR and L_{AGN} can be reproduced, even if there is a tight underlying correlation between SFR and BHAR (Novak et al., 2012; Hickox et al., 2014).

In conclusion, new observatories can explore the presence of AGNs at $z > 2$, with particular focus on compactness, jets and in/outflows that are crucial for the overall SFR of the host galaxy. We also need to understand the time domain of AGNs in more detail, and as Fig. 10.1 illustrates, such observations of AGN variability will be aided by a wealth of emerging simulations attempting to model the AGN-host co-evolution (e.g. Vogelsberger et al., 2013; Gabor & Bournaud, 2014; DeGraf et al., 2014).

10.4 REFERENCES

Alexander, D. M., Bauer, F. E., Brandt, W. N., et al. 2011, ApJ, 738, 44

Anderson, M. E., & Bregman, J. N. 2011, ApJ, 737, 22

Arnaud, K. A. 1996, in Astronomical Society of the Pacific Conference Series, Vol. 101, Astronomical Data Analysis Software and Systems V, ed. G. H. Jacoby & J. Barnes, 17

Barro, G., Faber, S. M., Pérez-González, P. G., et al. 2013, ApJ, 765, 104

Bauer, F. E., Alexander, D. M., Brandt, W. N., et al. 2004, AJ, 128, 2048

Beichman, C. A., Rieke, M., Eisenstein, D., et al. 2012, in Society of Photo-Optical Instrumentation Engineers (SPIE) Conference Series, Vol. 8442, Society of Photo-Optical Instrumentation Engineers (SPIE) Conference Series, 2

Bell, E. F. 2003, ApJ, 586, 794

Bergmann, T. S. 2012, in Astronomical Society of the Pacific Conference Series, Vol. 460, AGN Winds in Charleston, ed. G. Chartas, F. Hamann, & K. M. Leighly, 133

Bruzual, G., & Charlot, S. 2003, MNRAS, 344, 1000

Cardamone, C. N., Urry, C. M., Damen, M., et al. 2008, ApJ, 680, 130

Cavaliere, A., & Fusco-Femiano, R. 1976, A&A, 49, 137

Cicone, C., Maiolino, R., Sturm, E., et al. 2014, A&A, 562, A21

Cimatti, A., Brusa, M., Talia, M., et al. 2013, ApJ, 779, L13

Cowie, L. L., Barger, A. J., & Hasinger, G. 2012, ApJ, 748, 50

Croton, D. J., Springel, V., White, S. D. M., et al. 2006, MNRAS, 365, 11

Daddi, E., Dickinson, M., Morrison, G., et al. 2007, ApJ, 670, 156

Dai, X., Anderson, M. E., Bregman, J. N., & Miller, J. M. 2012, ApJ, 755, 107

Darg, D. W., Kaviraj, S., Lintott, C. J., et al. 2010, MNRAS, 401, 1552

DeGraf, C., Dekel, A., Gabor, J., & Bournaud, F. 2014, ArXiv e-prints

Di Matteo, T., Springel, V., & Hernquist, L. 2005, Nature, 433, 604

Done, C., Davis, S. W., Jin, C., Blaes, O., & Ward, M. 2012, MNRAS, 420, 1848

Donley, J. L., Koekemoer, A. M., Brusa, M., et al. 2012, ApJ, 748, 142

Dunlop, J. S. 2011, Science, 333, 178

Elbaz, D., Hwang, H. S., Magnelli, B., et al. 2010, A&A, 518, L29

Fabian, A. C. 2012, ARA&A, 50, 455

Feruglio, C., Maiolino, R., Piconcelli, E., et al. 2010, A&A, 518, L155

Franx, M., van Dokkum, P. G., Schreiber, N. M. F., et al. 2008, ApJ, 688, 770

Gabor, J. M., & Bournaud, F. 2014, MNRAS, 441, 1615

Gilli, R., Comastri, A., & Hasinger, G. 2007, A&A, 463, 79

Grimm, H.-J., Gilfanov, M., & Sunyaev, R. 2003, MNRAS, 339, 793

Hanami, H., Ishigaki, T., & Ishigaki. 2011, in IAU Symposium, Vol. 277, IAU Symposium, ed. C. Carignan, F. Combes, & K. C. Freeman, 182–185

Häring, N., & Rix, H.-W. 2004, ApJ, 604, L89

Harrison, C. M., Alexander, D. M., Mullaney, J. R., et al. 2012, in press (ArXiv:1209.3016)

Hickox, R. C., Mullaney, J. R., Alexander, D. M., et al. 2014, ApJ, 782, 9

Kocevski, D. D., Faber, S. M., Mozena, M., et al. 2012, ApJ, 744, 148

Kriek, M., van Dokkum, P. G., Franx, M., Illingworth, G. D., & Magee, D. K. 2009, ApJ, 705, L71

Kurczynski, P., Gawiser, E., Huynh, M., et al. 2012, ApJ, 750, 117

Laird, E. S., Nandra, K., Pope, A., & Scott, D. 2010, MNRAS, 401, 2763

Lamareille, F. 2010, A&A, 509, A53

Lehmer, B. D., Alexander, D. M., Bauer, F. E., et al. 2010, ApJ, 724, 559

Lobanov, A., & Zensus, J. A. 2007, Active Galactic Nuclei at the Crossroads of Astrophysics

(Springer-Verlag), 147–162
Man, A. W. S., Toft, S., Zirm, A. W., Wuyts, S., & van der Wel, A. 2012, ApJ, 744, 85
Mancini, C., Renzini, A., Daddi, E., et al. 2015, ArXiv e-prints
Matt, G., Marinucci, A., Guainazzi, M., et al. 2014, MNRAS, 439, 3016
Mulchaey, J. S., & Jeltema, T. E. 2010, ApJ, 715, L1
Nandra, K., & Pounds, K. A. 1994, MNRAS, 268, 405
Nardini, E., Reeves, J. N., Gofford, J., et al. 2015, Science, 347, 860
Nesvadba, N. P. H., Polletta, M., Lehnert, M. D., et al. 2011, MNRAS, 415, 2359
Newman, A. B., Ellis, R. S., Bundy, K., & Treu, T. 2012, ApJ, 746, 162
Novak, G. S., Ostriker, J. P., & Ciotti, L. 2011, ApJ, 737, 26
—. 2012, MNRAS, 427, 2734
O'Sullivan, E., Ponman, T. J., & Collins, R. S. 2003, MNRAS, 340, 1375
Papovich, C., Moustakas, L. A., Dickinson, M., et al. 2006, ApJ, 640, 92
Peng, Y.-j., Lilly, S. J., Kovač, K., et al. 2010, ApJ, 721, 193
Persic, M., Rephaeli, Y., Braito, V., et al. 2004, A&A, 419, 849
Piconcelli, E., Jimenez-Bailón, E., Guainazzi, M., et al. 2005, A&A, 432, 15
Ranalli, P., Comastri, A., & Setti, G. 2003, A&A, 399, 39
Rangel, C., Nandra, K., Barro, G., et al. 2014, MNRAS, 440, 3630
Rasmussen, J., Sommer-Larsen, J., Pedersen, K., et al. 2009, ApJ, 697, 79
Reeves, J. N., & Turner, M. J. L. 2000, MNRAS, 316, 234
Risaliti, G., & Elvis, M. 2004, in Astrophysics and Space Science Library, Vol. 308, Supermassive Black Holes in the Distant Universe, ed. A. J. Barger, 187
Rubin, K. H. R., van Dokkum, P. G., Coppi, P., et al. 2004, ApJ, 613, L5
Schawinski, K. 2011, in New Horizons in Astronomy, Proceedings of the Frank N. Bash Symposium 2011, held October 9-11, 2011. Austin, Texas, USA. Edited by S. Salviander, J. Green, and A. Pawlik. Published online at `http://pos.sissa.it/cgi-bin/reader/conf.cgi?confid=149`
Schawinski, K., Virani, S., Simmons, B., et al. 2009, ApJ, 692, L19
Stark, A. A., Gammie, C. F., Wilson, R. W., et al. 1992, ApJS, 79, 77
Stern, D., Eisenhardt, P., Gorjian, V., et al. 2005, ApJ, 631, 163
Storchi-Bergmann, T. 2014, ArXiv e-prints
Szokoly, G. P., Bergeron, J., Hasinger, G., et al. 2004, ApJS, 155, 271
Tajer, M., Polletta, M., Chiappetti, L., et al. 2007, A&A, 467, 73
Tanaka, M., Finoguenov, A., Mirkazemi, M., et al. 2012, PASJ, in press (ArXiv:1210.0302)
Taylor, E. N., Franx, M., van Dokkum, P. G., et al. 2009, ApJS, 183, 295
Toft, S., Franx, M., van Dokkum, P., et al. 2009, ApJ, 705, 255
Toft, S., Gallazzi, A., Zirm, A., et al. 2012, ApJ, 754, 3
Toft, S., Rasmussen, J., Sommer-Larsen, J., & Pedersen, K. 2002, MNRAS, 335, 799
Tombesi, F., Melendez, M., Veilleux, S., et al. 2015, ArXiv e-prints
Treister, E., Schawinski, K., Urry, C. M., & Simmons, B. D. 2012, ApJ, 758, L39
Treister, E., & Urry, C. M. 2012, Advances in Astronomy, Seeking for the Leading Actor on the Cosmic Stage: Galaxies versus Supermassive Black Holes, 35
Treister, E., Cardamone, C. N., Schawinski, K., et al. 2009, ApJ, 706, 535
Vanzella, E., Cristiani, S., Dickinson, M., et al. 2008, A&A, 478, 83
Vasudevan, R. V., Mushotzky, R. F., Reynolds, C. S., et al. 2014, ApJ, 785, 30
Vogelsberger, M., Genel, S., Sijacki, D., et al. 2013, MNRAS, 436, 3031
Wang, J. X., Malhotra, S., Rhoads, J. E., & Norman, C. A. 2004, ApJ, 612, L109

Williams, R. J., Quadri, R. F., Franx, M., van Dokkum, P., & Labbé, I. 2009, ApJ, 691, 1879
Windhorst, R. A., Mather, J., Clampin, M., et al. 2009, in Astronomy, Vol. 2010, astro2010: The Astronomy and Astrophysics Decadal Survey, 317
Wuyts, S., Labbé, I., Schreiber, N. M. F., et al. 2008, ApJ, 682, 985
Wuyts, S., Förster Schreiber, N. M., van der Wel, A., et al. 2011, ApJ, 742, 96
Xue, Y. Q., Luo, B., Brandt, W. N., et al. 2011, ApJS, 195, 10
Zheng, Z.-Y., Malhotra, S., Wang, J.-X., et al. 2012, ApJ, 746, 28

SUMMARY

Looking back in time at galaxies in different phases of their lifetimes, it is possible to reconstruct their evolution across cosmic time. A galaxy can be viewed as a gargantuan machinery converting gas into stars at a star formation rate (SFR) that is in principle only set by the amount and properties of the gas. At redshift $z \sim 2$, some $10\,$Gyr ago, galaxies were more gas-rich than today and the cosmic SFR density was peaking. Yet, while most massive galaxies resided on the main sequence of star formation, some were quenched with vanishingly low SFRs and compact morphologies. Different evolutionary sequences, with much observational and theoretical support, have been proposed in order to explain this, but with no final conclusion at hand yet.

Piecing together the puzzle of galaxies observed at different redshifts requires precise knowledge about *the shape of the pieces to the puzzle*, i.e. the physical conditions of the galaxies, not just of the stellar component, but of the interstellar medium (ISM) and black hole as well. This thesis focuses on deriving the actual shape of those puzzle pieces, with particular focus on characterising the ISM as well as the gas accretion onto the central black hole, in order to better understand their effects on the SFR and general evolution of massive galaxies. With this aim in mind, three studies were carried out, listed below together with the main conclusions from each:

Amount and distribution of molecular gas in the ISM

A combination of density and temperature sets the shape of the CO spectral line energy distribution (SLED), and observations thereof can consequently be used to probe the conditions of the star-forming, molecular gas in the ISM. However, detailed modeling is needed in order to interpret observations. For that purpose, a new method is constructed and presented here; SImulator of GAlaxy Millimeter/submillimeter Emission (`SÍGAME`). The method is combined with the radiative transfer code `LIME` in order to simulate CO line emission, and by applying `SÍGAME` to three galaxies from cosmological simulations, the following conclusions are drawn for simulated massive galaxies at $z \sim 2$:

- The CO SLED resembles the low-excitation one of the Milky Way (MW), in that it peaks at CO$(3-2)$, but also with significant line intensity at higher transitions, not seen in the MW.
- Global α_{CO} factors range from 2.36 to 2.61 $\mathrm{M}_\odot\ \mathrm{pc}^{-2}\,(\mathrm{K\,km\,s^{-1}})^{-1}$ or about half the typically assumed MW values.
- Total CO$(3-2)$ luminosities are about $\sim 1-2\,\sigma$ below the mean of observations of corresponding $z \sim 1-2.5$ star-forming galaxies, most likely due to relatively low molecular gas masses in our model galaxies.

- Radial profiles of line ratios within each galaxy reveal more excited gas towards the center, in agreement with observations of nearby galaxies, and suggesting ULIRG-like environments in the central ($R < 5\,\mathrm{kpc}$) regions.
- The α_{CO} factor displays a decrease towards the center of each model galaxy, however, by a factor that is lower than what is observed in local spiral galaxies.

Tracing SFR on local and global scales

SÍGAME is expanded and adapted in order to model [CII] – the fine-structure line of singly ionized carbon (C^+), thereby being the first code to simulate the [CII] emission reliably on kpc-scales in normal star-forming galaxies. [CII] is typically the strongest cooling line in neutral ISM, and correlates strongly with SFR on global and local scales, but its origin is so far unclear. These are the major findings from applying SÍGAME to seven $z = 2$ star-forming galaxies from another simulation:

- SÍGAME is able to reproduce the observed $L_{[\mathrm{CII}]}$-SFR relation of normal galaxies at $z > 0.5$.
- The [CII] emission that originates in molecular gas tends to dominate the total [CII] luminosity, with the contributions from PDRs coming next and HII regions contributing with a negligible amount.
- On resolved (1 kpc) scales, an expression is provided for the $\Sigma_{[\mathrm{CII}]}$-Σ_{SFR} relation.
- No metallicity dependency is found in the scatter around the $L_{[\mathrm{CII}]}$-SFR relation, but SFR/$L_{[\mathrm{CII}]}$ does increase towards the center of each galaxy together with metallicity, as also observed in local spiral galaxies.

Importance of AGNs in massive galaxies at $z \sim 2$

The deep *Chandra* X-ray survey CDF-S is analysed, and AGNs of high and low X-ray luminosity are extracted via AGN classification methods, and stacking techniques of non-detections, in X-ray. The galaxies investigated come from a mass-complete (at $M_* > 5 \times 10^{10}\,M_\odot$) sample at $1.5 \leq z \leq 2.5$ with stellar masses from fits of stellar population synthesis models to their spectral energy distribution. By statistical analysis, the following results are obtained:

- Among both star-forming and quiescent galaxies, a similar fraction of $22 \pm 5\,\%$ is found to have rest-frame X-ray luminosities ($L_{0.5\text{-}8\,\mathrm{keV}} > 3 \times 10^{42}\,\mathrm{erg\,s^{-1}}$) consistent with hosting luminous AGNs.
- An excess in X-ray-inferred SFR compared to that from infrared and ultraviolet emission for the stacked non-detections, converts into even higher fractions of low- or high-luminosity AGNs among these. This fraction is higher ($70 - 100\,\%$) among quiescent galaxies than among star-forming ones ($43 - 65\,\%$).
- Hot gas halos are rejected as potential sources for the strong X-ray emission in the detected galaxies, based on the very limited spatial extent of their X-ray emission.
- The fraction of luminous AGNs does not depend on SFR nor stellar mass, suggesting that external effects are triggering the AGNs.

SAMMENFATNING

En galakse kan opfattes som et kæmpemæssigt maskineri, der omdanner gas til stjerner ved en stjernedannelses-rate (SFR; Star Formation Rate) der i princippet kun afhænger af mængden af og egenskaberne ved gassen. Omkring 10 Gyr år siden, ved rødforskydning $z \sim 2$, indeholdt galakser mere gas end de gør i dag, og den kosmiske SFR tæthed havde sit maksimum. Men skønt de fleste massive galakser levede på hovedserien bestående af stjernedannende galakser, var der også nogle med forsvindende lave SFRs og kompakte strukturer. Forskellige evolutionsteorier, alle med god opbakning fra observationer of teoretiske modeller, er blevet foreslået som svar på dette fænomen, men indtil nu er en endelig konklusion ikke nået.

Det er et sandt puslespil at stykke galakse-udviklingen sammen ud fra observationer af galakser ved forskellige rødforskydninger. For at løse puslespillet er det først of fremmest afgørende at kende formen af brikkerne, dvs. den fysiske tilstand af galakserne – ikke bare af deres stellare del men også af det interstellare medium (ISM) og deres centrale sorte hul. Med dette mål for øje, består denne afhandling af følgende tre projekter:

Mængde o fordeling af molekylær gas i ISM af galakser

Den spektrale linie energi fordeling (SLED; Spectral Line Energy Distribution) for CO molekylet er bestemt af tæthed og temperatur af den gas hvor linien udsendes fra, og observationer af CO SLEDs kan derfor bruges til at bestemme tilstanden af den stjerne-dannende, molekylære gas i ISM af galakser. For at kunne oversætte observationer af SLED'en til sådanne gas tilstande, er detaljeret modellering nødvendig. Til det formål bliver en ny metode skabt og præsenteret her; SImulator of GAlaxy Millimeter/submillimeter Emission (`SÍGAME`). Denne metode kombineres med en kode for strålingstransport af millimeter of infrarød stråling (`LIME`) for at kunne simulere CO linie emission, og ved at anvende `SÍGAME` på tre galakser fra kosmologiske simulationer, bliver de følgende konklusioner draget for massive galakser ved $z \sim 2$:

- CO SLED'en minder om den lavt eksiterede SLED i Mælkevejen, i og med at den har maksimum i CO$(3-2)$, men også signifikant linie intensitet ved højere overgange, hvilket ikke ses i Mælkevejen.

- Globale $\alpha_{\rm CO}$ faktorer ligger på omkring 50 % af Mælkevejens, nemlig fra 2.26 til 2.61 $\rm M_\odot$ $\rm pc^{-2}\,(K\,km\,s^{-1})^{-1}$.

- De totale CO$(3-2)$ luminositeter er alle omkring $1-2\,\sigma$ under middel af observationer af sammenlignelige $z \sim 1-2.5$ stjerne-dannende galakser, højst sandsynlig pga. relativt lave molekylære gas masser i vores model galakser.

- Radielle profiler af CO linie forhold viser at hver model galakse indeholder mere eksiteret gas i de centrale dele sammenlignet med længere ude i disken. Dette er i overensstemmelse med observationer af lokale galakser og antyder at de centrale ($R < 5$ kpc) områder minder om de forhold man finder i ULIRGs (Ultra-Luminøse infrarøde galakser).
- $\alpha_{\rm CO}$ faktoren aftager mod centrum i galakserne som også observeret, dog med et mindre relativt fald ift. til dét set i lokale spiral-galakser.

Afdækning af SFR på små og store skalaer

`SÍGAME` udvides og adapteres til at modellere [CII]– fin-struktur linien i enkelt-ioniseret carbon (C^+), og er dermed den første kode til troværdigt at simulere [CII] emission på kpc-skaler i normale stjernedannende galakser. [CII] er typisk den linie der kraftigst køler neutral ISM, og den skalerer med SFR på globale såvel som på lokale skalaer. Men dens fysiske oprindelse i gassen er stadig uklar. Disse er de før ste konklusioner, som `SÍGAME` indtil nu har ført til på det område:

- `SÍGAME` kan reproducere den observerede relation mellem $L_{\rm [CII]}$ og SFR for normale galakser ved $z > 0.5$.
- [CII] emission udspringer hovedsageligt fra molekylær gas. Derefter kommer PDR (Photon Dominated Region) områderne og tilsidst HII gassen, der bidrager med et neglicibel [CII] intensitet.
- På opløste (1 kpc) skalaer, opstilles et udtryk for $\Sigma_{\rm [CII]}$ som funktion af $\Sigma_{\rm SFR}$.
- Der ses ikke nogen metallicitets-afhængighed for spredningen omkring $L_{\rm [CII]}$-SFR relationen, men SFR/$L_{\rm [CII]}$ raten stiger imod centrum af galakserne sammen med metalliciteten, hvilket også er blevet observeret i lokale spiral-galakser.

En vigtig rolle af AGNs i massive galakser ved $s \sim 2$

Aktive galaksekerner (AGNs; Active Galactic Nucleui) af høj og lav X-ray luminositet afdækkes i feltet CDF-S, der er blevet studeret i røntgen med lang eksponering (4 Ms) af *Chandra* rumobservatoriet. Gruppen af galakser som undersøges dækker fuldstændigt stellar masser over $5 \times 10^{10}\,{\rm M}_\odot$ ved $1.5 \leq z \leq 2.5$. Ved brug af AGN klassificerings-teknikker (og opsummeringsmetoder for de galakser der ikke detekteres individuelt i rœntgen), opnåes de fæl gende resultater:

- En brøkdel på $22 \pm 5\,\%$ blandt stjerne-dannende såvel som blandt passive galakser, har X-ray lystyrker svarende til lysstærke AGNs.
- En endnu større brøkdel blandt de ikke-detekterede galakser, viser tegn på at indeholde AGNs af lav- til høj-luminositet, med højere brøkdel ($70 - 100\,\%$) blandt passive galakser sammenlignet med de stjerne-dannende ($43 - 65\,\%$).
- Grundet den rumligt koncentrerede X-ray emission fra de undersøgte galakser, kan en ekstremt varm gas halo udelukkes som årsag til X-ray emissionen i de detekterede galakser.
- Brøkdelen af lysstærke AGNs afhænger ikke af SFR eller stellar masse, hvilket tyder på at eksterne faktorer spiller ind på antændelsen af deres AGNs.

ACKNOWLEDGMENT

My passion for astronomy was sparked during long, cold nights in the observatory of my high school, AGS, in Sønderborg. I am thankful for having benefitted from an educational system that incorporates astronomy, and more particularly from the incredible enthusiasm of my first astronomy teacher, Mogens Winther, and those classmates that made it fun to stay up at night. Since then, so many inspirational people have opened up the sky for me, both in Aarhus, where I finished my bachelors in physics, and later on in Copenhagen. These past 4 years, that journey has been eased and guided by two amazing people, my supervisors Thomas and Sune. In your own very separate ways, you have taught me how to believe in myself as a researcher.

From the moment I hand in my thesis, I will miss life at Dark. Dark Cosmology Centre is nothing less of a paradise for any astronomer; daily provisions of coffee and fruit and a non-tiring staff of administration and support. Thank you for patiently answering all of my stupid questions and fixing my mistakes (even on weekends). And to the rest of my 'darklings'; thank you for all those great moments; excursions, movie nights, alleviating lunch breaks, partiess or laughters at the coffee machine.

I would not have gotten very far, in astronomy or anything else, without my friends. First thanks to my 'old' friends in Copenhagen that I occasionally forget how lucky I am to have; Tomatito, Lotte (x2), Helene. Thanks to my dear friends spread across the world – your warmth, generosity and wisdom still reaches and amazes me; Marty, Cat, Urs and papa-J, Sam, Chang, Rosa, Scott (the dad and the pilot), Fan-Fan, Hannah, Carol, Lila, Henry, Charlotte, Britta and Kaare to name a few, but certainly not all! I will also not forget my flamenco girls; Rut, Rebecka, Elisabeth and all those crazy, lovely people I meet doing capoeira or aerial acrobatics, in Denmark and accross the world.

Towards the end of my PhD, I was blessed by meeting my own 'curandero'. From the other side of the ocean, you supported me in everything I did and made me laugh on my most solemn days. I will never know how many bruises and dangers you saved me from.

Finally, I can't wait to thank my family (yes, that includes you guys, tía mía and Erk who I always wish to see more). You've been there with love and encouragement (and sund fornuft), even when Als seemed light years away. In particular, thank you mamita for taking those field trips to Copenhagen and reminding me of how to go shopping.

Tak, gracias, obrigada, thank you!

Karen

Appendices

A

APPENDIX TO CHAPTER 4

A.1 THERMAL BALANCE OF THE ATOMIC GAS PHASE

As explained in §4.3.2, we cool the initial hot SPH gas down by considering the following heating and cooling mechanisms and equating their energy rates: $\Gamma_{\rm CR,HI} = \Lambda_{\rm ions+atoms} + \Lambda_{\rm rec} + \Lambda_{\rm f-f}$.

$\Gamma_{\rm CR,HI}$ is the heating rate of the atomic gas due to cosmic ray ionizations (Draine, 2011):

$$\begin{aligned}\Gamma_{\rm CR,HI} =& 1.03 \times 10^{-27} n_{\rm HI} \left(\frac{\zeta_{\rm CR,HI}}{10^{-16}}\right) \\ & \times \left[1 + 4.06 \left(\frac{x_{\rm e}}{x_{\rm e} + 0.07}\right)^{1/2}\right] \ {\rm erg\,cm^{-3}\,s^{-1}},\end{aligned} \tag{A.1}$$

where $\zeta_{\rm CR,HI}$ is the primary CR ionization rate of HI atoms (determined locally in our simulations according to eq. 4.10), and $x_{\rm e}$ is the hydrogen ionization fraction calculated with a procedure kindly provided by I. Pelupessy; see also Pelupessy (2005). The term containing $x_{\rm e}$ in eq. **??** accounts for the fact that in gas of high ionization, the electron created by the primary CR ionization has a high probability of transferring its kinetic energy into heat via long-range Coulomb scattering off free electrons. In the case of low ionization, this term becomes insignificant as a higher fraction of its energy will go to secondary ionizations or excitation of bound states in stead of heating.

$\Lambda_{\rm ions+atoms}$ is the total cooling rate due line emission from H, He, C, N, O, Ne, Mg, Si, S, Ca, and Fe, calculated using the publically available code of Wiersma et al. (2009) which takes $T_{\rm k}$, $n_{\rm H}$ and the abundances of the above elements as input. Wiersma et al. (2009) compute the cooling rates with the photoionization package `CLOUDY` assuming CIE. They also adopt a value for the meta-galactic UV and X-ray field equal to that expected at $z \sim 2$ (Haardt & Madau, 2001). At $z \sim 2$, the emission rate of HI ionizing radiation is higher by a factor of about ~ 30 than at $z = 0$ (Puchwein et al., 2014), and thus plays an important role in metal line cooling calculations.

$\Lambda_{\rm rec}$ is the cooling rate due to hydrogen recombination emission (Draine, 2011):

$$\Lambda_{\rm rec} = \alpha_B n_{\rm e} n_{\rm H^+} \langle E_{rr} \rangle \ \ {\rm ergs\,cm^{-3}\,s^{-1}}, \tag{A.2}$$

where α_B is the radiative recombination rate for hydrogen in the case of optically thick gas in

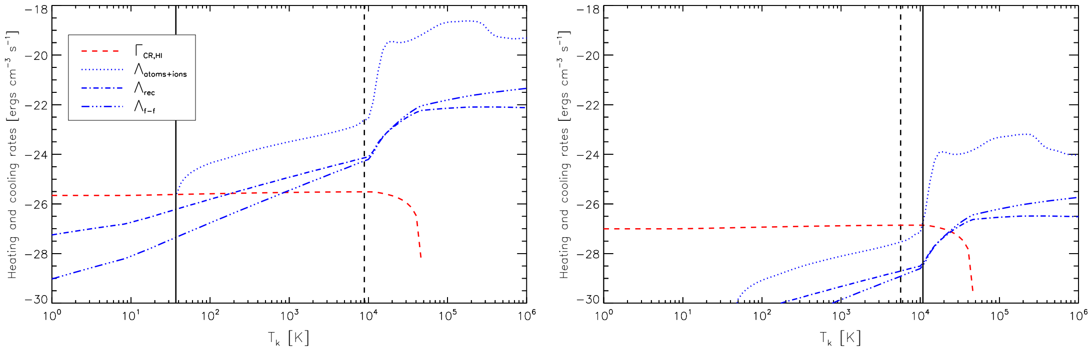

Figure A.1 Heating and cooling rates as functions of temperature for two SPH gas particles with [$n_{\rm H} = 14.62\,{\rm cm}^{-3}$, $\zeta_{\rm CR} = 4.02 \times 10^{-16}\,{\rm s}^{-1}$, $x_{\rm e}$ ($T_{\rm k,SPH} = 8892\,K$) $= 0.006$] (left) and [$n_{\rm H} = 0.09\,{\rm cm}^{-3}$, $\zeta_{\rm CR} = 3.92 \times 10^{-16}\,{\rm s}^{-1}$, $x_{\rm e}$ ($T_{\rm k,SPH} = 5649\,K$) $= 0.001$] (right). The left-hand side plot illustrates the case of an SPH particle of high gas density and metallicity leading to relatively high metal line cooling as compared to the heating from cosmic rays of moderate intensity. This results in a low temperature for the WCNM of $T_{\rm k} = 37\,{\rm K}$. The right-hand side plot shows a case of lower density and metallicity causing less cooling by metal lines, hence a higher equilibrium temperature for a similar cosmic ray field strength. Vertical black solid lines mark the resulting temperature of the neutral gas phase in each SPH particle, found where the difference between heating and cooling rate is smallest, when starting at the original SPH gas temperature, indicated with vertical black dashed lines.

which ionizing photons emitted during recombination are immediately reabsorbed. We adopt the approximation for α_B given by Draine (2011):

$$\alpha_{\rm B} = 2.54 \times 10^{-13} T_4^{(-0.8163-0.0208\ln T_4)}\ \ {\rm cm}^3\,{\rm s}^{-1}, \tag{A.3}$$

where T_4 is defined as $T_{\rm k}/10^4\,{\rm K}$. The density of ionised hydrogen, $n_{\rm H^+}$, is set equal to the electron density, $n_{\rm e}$, and E_{rr} is the corresponding mean kinetic energy of the recombining electrons:

$$\langle E_{rr} \rangle = [0.684 - 0.0416\ \ln T_4]\ k_{\rm B} T_{\rm k}\ \ {\rm ergs}. \tag{A.4}$$

$\Lambda_{\rm f-f}$ is the cooling rate due to free-free emission from electrons in a pure H plasma (i.e., free electrons scattering off H$^+$), and is given by (Draine, 2011):

$$\Lambda_{\rm f-f} = 0.54 T_4^{0.37} k_B T_{\rm k} n_{\rm e} n_{\rm H^+} \alpha_{\rm B}\ \ {\rm ergs\,cm}^{-3}\,{\rm s}^{-1}, \tag{A.5}$$

where the recombination rate, $\alpha_{\rm B}$, is calculated in the same way as for $\Lambda_{\rm rec}$.

Figure A.1 shows the above heating and cooling rates pertaining to two example SPH particles with similar initial temperatures ($\sim 10^4$ K). Because of different ambient conditions (i.e., $n_{\rm HI}$, $x_{\rm e}$, Z', and $\zeta_{\rm CR}$) the equilibrium temperature solutions for the two gas particles end up being significantly different.

A.2 Thermal balance of the molecular gas phase

As described in Section 4.3.4 `SÍGAME` assumes the molecular gas resides exclusively in giant molecular clouds that have Plummer radial density profiles (i.e., given by eq. 4.9). Throughout the clouds the gas temperature is solved for according to the heating and cooling equilibrium requirement $\Gamma_{\rm PE} + \Gamma_{\rm CR,H_2} = \Lambda_{\rm H_2} + \Lambda_{\rm CO} + \Lambda_{\rm CII} + \Lambda_{\rm OI} + \Lambda_{\rm gas-dust}$ (eq. 4.12).

$\Gamma_{\rm PE}$ is the heating rate of the gas due to photo-electric ejection of electrons from dust grains by FUV photons, and is given by (Bakes & Tielens, 1994):

$$\Gamma_{\mathrm{PE}} = 10^{-24}\epsilon G_{0,\mathrm{att}} n_{\mathrm{H}} \ \ \mathrm{ergs\,cm^{-3}\,s^{-1}}, \tag{A.6}$$

where $G_{0,\mathrm{att}}$ is the local attenuated FUV field in Habing units, derived following eq. 4.11, and ϵ is the heating efficiency:

$$\begin{aligned}\epsilon =& \frac{4.87\times10^{-2}}{1+4\times10^{-3}(G_{0,\mathrm{att}}T^{0.5}/n_e)^{0.73}} \\ &+ \frac{3.65\times10^{-2}}{1+4\times10^{-3}(G_{0,\mathrm{att}}T^{0.5}/n_e)^{0.73}},\end{aligned} \tag{A.7}$$

where n_{e} is the electron density, calculated as $x_{\mathrm{e}} n_{\mathrm{H}}$, with x_{e} again calculated using the procedure of I. Pelupessy.

$\Gamma_{\mathrm{CR,H_2}}$ is the heating rate by cosmic rays traveling through molecular gas (Stahler & Palla, 2005):

$$\Gamma_{\mathrm{CR,H_2}} = 1.068\times10^{-24}\left(\frac{\zeta_{\mathrm{CR,H_2}}}{10^{-16}}\right)\left(\frac{n_{\mathrm{H_2}}}{10^3\,\mathrm{cm^{-3}}}\right) \ \ \mathrm{ergs\,cm^{-3}\,s^{-1}} \tag{A.8}$$

where $\zeta_{\mathrm{CR,H_2}}$ is the local CR primary ionization rate of H_2 molecules, which is approximately $1.6\times$ higher that of H I atoms (Stahler & Palla, 2005).

$\Lambda_{\mathrm{H_2}}$ is the H_2 line cooling rate, and we use the parameterization made by Papadopoulos et al. (2014) that includes the two lowest H_2 rotational lines (S(0) and S(1), the only lines excited for $T_{\mathrm{k}} \lesssim 1000\,\mathrm{K}$):

$$\begin{aligned}\Lambda_{\mathrm{H_2}} =& 2.06\times10^{-24}\frac{n_{\mathrm{H_2}}}{1+\mathrm{r_{op}}}\left[1+\frac{1}{5}e^{510\mathrm{K}/T_{\mathrm{k}}}\left(1+\frac{n_0}{n_{\mathrm{H_2}}}\right)\right]^{-1} \\ &\times(1+R_{10}) \ \ \mathrm{ergs\,cm^{-3}\,s^{-1}},\end{aligned} \tag{A.9}$$

where R_{10} is defined as:

$$\mathrm{R}_{10} = 26.8\,\mathrm{r_{op}}\left[\frac{1+(1/5)e^{510\mathrm{K}/T_{\mathrm{k}}}\left(1+\frac{n_0}{n_{\mathrm{H_2}}}\right)}{1+(3/7)e^{845\,\mathrm{K}/T_{\mathrm{k}}}\left(1+\frac{n_1}{n_{\mathrm{H_2}}}\right)}\right], \tag{A.10}$$

and $n_0 \sim 54\,\mathrm{cm^{-3}}$ and $n_1 \sim 10^3\,\mathrm{cm^{-3}}$ are the critical densities of the S(0):2-0 and S(1):3-1 rotational lines. $\mathrm{r_{op}}$ is the ortho-H_2/para-H_2 ratio (set to 3 which is the equilibrium value).

For the cooling rates due to the [C II]158 μm and [O I]63 μm+146 μm fine-structure lines we adopt the parameterizations by Röllig et al. (2006). The C II cooling rate (Λ_{CII}) is:

$$\begin{aligned}\Lambda_{\mathrm{CII}} =& 2.02\times10^{-24} n Z' \\ &\times\left[1+\frac{1}{2}e^{92\mathrm{K}/T_{\mathrm{k}}}\left(1+1300/n_{\mathrm{H}}\right)\right]^{-1} \ \ \mathrm{ergs\,cm^{-3}\,s^{-1}},\end{aligned} \tag{A.11}$$

where a carbon to hydrogen abundance ratio that scales with metallicity according to $\chi_{[\mathrm{C}]} = 1.4\times10^{-4}\,Z'$ is assumed. For the parameterization of the O I cooling rate ($\Lambda_{\mathrm{OI}} = \Lambda_{63\mu\mathrm{m}}+\Lambda_{146\mu\mathrm{m}}$) we refer to eqs. A.5 and A.6 in Röllig et al. (2006) and simply note that we adopt (in accordance with Röllig et al. (2006)) an oxygen to hydrogen abundance ratio of $\chi_{[\mathrm{O}]} = 3\times10^{-4}\,Z'$.

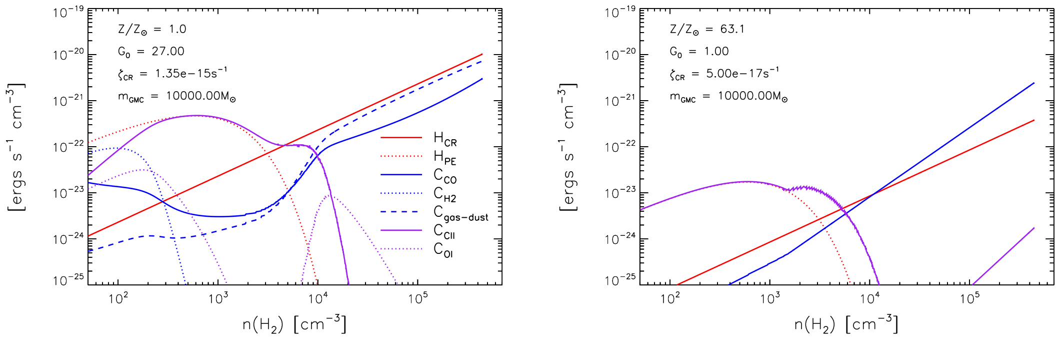

Figure A.2 Equilibrium heating (red curves) and cooling (blue+purple curves) rates as functions of H_2 density for two different GMC models with [$m_{\rm GMC} = 10^4\,{\rm M}_\odot$, $Z' = 1$, $G_0 = 27$] (left) and [$m_{\rm GMC} = 10^4\,{\rm M}_\odot$, $Z' = 63$, $G_0 = 1$] (right). In the case of high FUV and cosmic ray fields (left), heating and cooling in the outer region ($n_{\rm H_2} \lesssim 1500\,{\rm cm}^{-3}$) are dominated by photoelectric heating (red dotted) and [[CII]] line cooling (purple solid), while in the inner region ($n_{\rm H_2} \gtrsim 10000\,{\rm cm}^{-3}$), cosmic ray heating (red solid) and gas-dust interactions (blue dashed) are the important mechanisms in determining the temperature. In the case of high metallicity (right), photoelectric heating and [[CII]] line cooling are also dominating in the outer region, but cooling in the inner region is mainly controlled by CO line emission.

$\Lambda_{\rm CO}$ is the cooling rate due to CO rotational transitions. We use the parameterization provided by Papadopoulos & Thi (2013):

$$\Lambda_{\rm CO} = 4.4 \times 10^{-24} \left(\frac{n_{\rm H_2}}{10^4}\right)^{3/2} \left(\frac{T_{\rm k}}{10\,{\rm K}}\right)^2 \left(\frac{\chi_{\rm CO}}{\chi_{\rm [C]}}\right) {\rm ergs\,cm^{-3}\,s^{-1}}, \tag{A.12}$$

where $\chi_{\rm CO}/\chi_{\rm [C]}$ is the relative CO to neutral carbon abundance ratio, the value of which we determine by interpolation, assuming that $\chi_{\rm CO}/\chi_{\rm [C]} = (0.97, 0.98, 0.99, 1.0)$ for $n_{\rm H_2} = 5 \times 10^3, 10^4, 10^5, 10^6\,{\rm cm}^{-3}$, respectively (Papadopoulos & Thi, 2013).

$\Lambda_{\rm gas-dust}$ is the cooling rate due to gas-dust interactions and is given by (Papadopoulos et al., 2011):

$$\Lambda_{\rm gas-dust} = 3.47 \times 10^{-33} n_{\rm H}{}^2 \sqrt{T_{\rm k}}(T_{\rm k} - T_{\rm dust})\,{\rm ergs\,cm^{-3}\,s^{-1}}, \tag{A.13}$$

where the dust temperature ($T_{\rm dust}$) is calculated using eq. B.2 (Section 4.3.4).

A.3 GMC MODELS

Each SPH particle is divided into several GMCs as described in §4.3.4, and we derive the molecular gas density and temperature within each from three basic parameters which are SFR density, GMC mass, $m_{\rm GMC}$, and metallicity, $Z'/Z_\odot$. Derived from these basic parameters are the far-UV and cosmic ray field strengths, the H_2 gas mass fraction of each SPH particles, as well as the GMC properties used to derive the CO excitation and emission; H_2 density and temperature. Histograms of the basic parameters are shown in Figure A.3, while properties derived thereof can be found in Figure A.4.

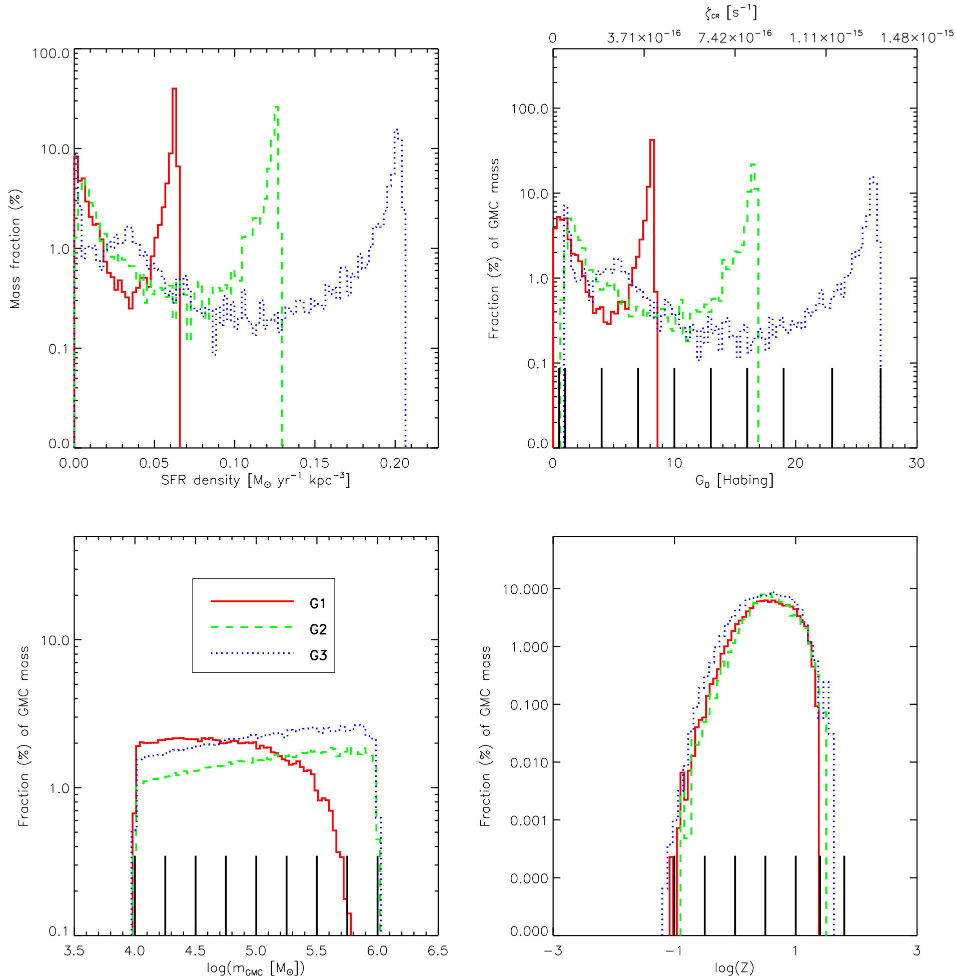

Figure A.3 Mass-weighted histograms of the basic parameters of the GMCs in G1 (red solid), G2 (green dashed), and G3 (blue dotted). From top left and clockwise: the local SFR density ($\mathrm{SFRD_{local}}$), the local far-UV field (G_0) (or CR ionization rate, $\zeta_{\mathrm{CR}} \propto G_0$), GMC mass ($m_{\mathrm{GMC}}$), and metallicity ($Z'$). Black vertical lines indicate the G_0, m_{GMC}, and Z'-values for which $T_{\mathrm{k}} - n_{\mathrm{H_2}}$ curves were calculated (see Figure A.4) – a total of 630 GMCs which make up our grid GMC models. Each GMC in the galaxies is assigned the $T_{\mathrm{k}} - n_{\mathrm{H_2}}$ curve of the GMC model at the closest grid point.

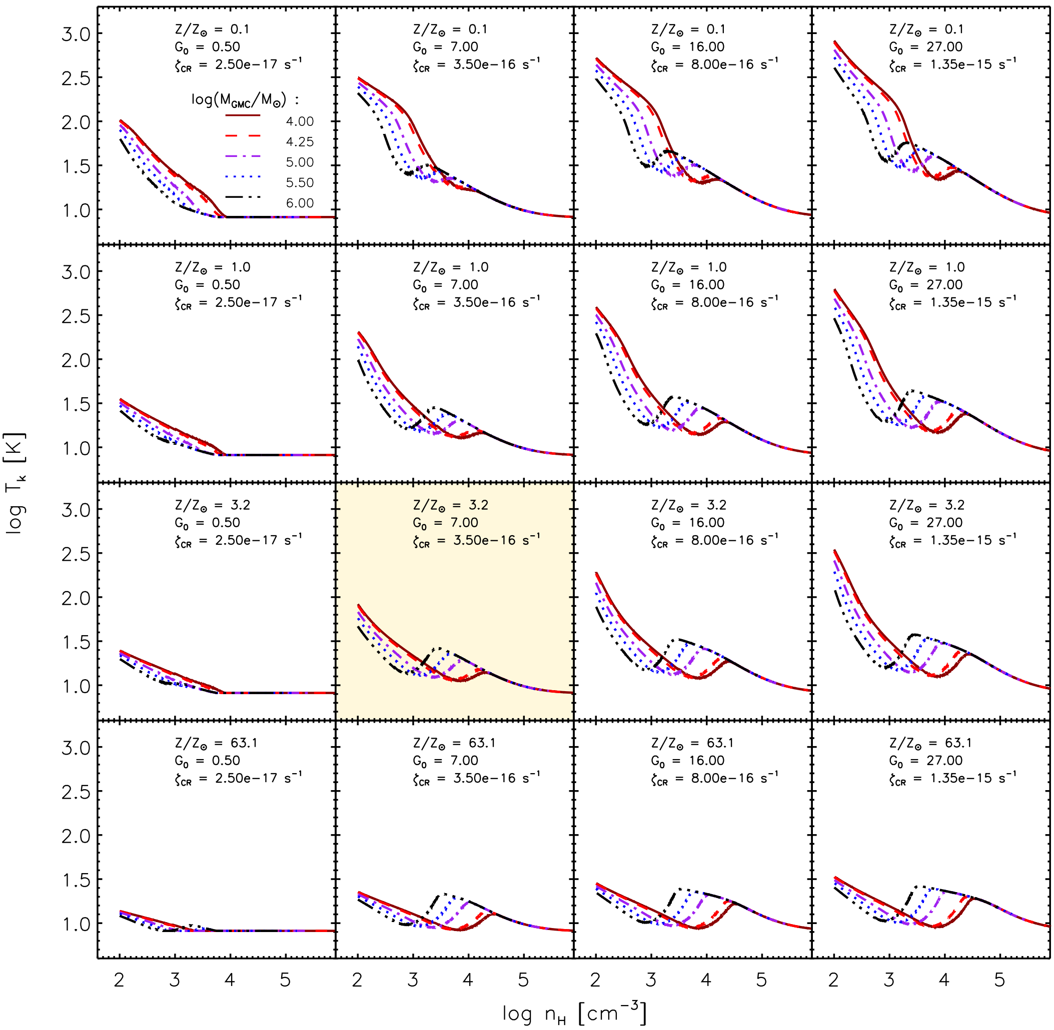

Figure A.4 Kinetic temperature versus H_2 density curves for 80 out of the 630 grid model GMCs that span the full (G_0, $M_{\rm GMC}$, Z') parameter space defined by the distributions in Figure A.3 (see also Section 4.3.4). The grid model most often assigned to GMCs in G1 is indicated by the red dashed curve in the highlighted panel and corresponds to $G_0 = 7.0$ ($\zeta_{\rm CR} = 3.5 \times 10^{-16}\,{\rm s}^{-1}$), $\log m_{\rm GMC}/{\rm M}_\odot = 4.25$, and $Z' = 3.2$. In general, higher metallicity (from top to bottom) leads to more cooling via emission lines of ions, atoms and molecules, and hence lower temperatures. On the other hand, higher UV and CR fields (from left to right) cause more heating and therefore higher $T_{\rm k}$. The decreasing trend of $T_{\rm k}$ with higher values of $n_{\rm H_2}$ is mainly caused by the gradual attenuation of the UV field as one moves into the cloud. The 'bump' at $n_{\rm H_2} \sim 10^3 - 10^4\,{\rm cm}^{-3}$ corresponds to the transition from CII line cooling to the less efficient CO line cooling at higher densities. At densities above $n_{\rm H_2} = 10^4\,{\rm cm}^{-3}$, gas-dust interactions set in and eventually cools the gas down to the CMB temperature in all GMC cores.

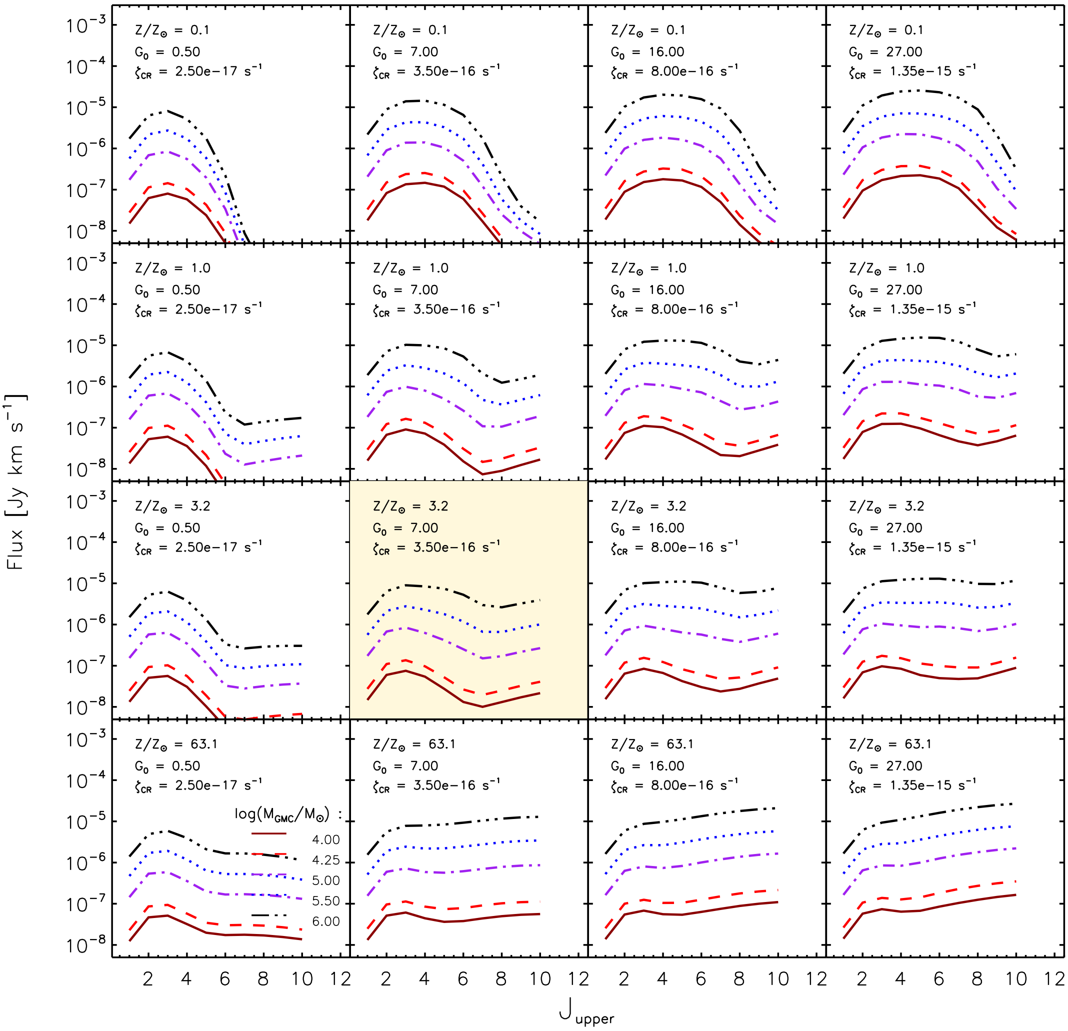

Figure A.5 CO SLEDs obtained with `LIME` for the 80 model GMCs whose $T_{\rm k} - n_{\rm H_2}$ curves are shown in Figure A.4. The CO SLED used most often in G1 is shown as the red dashed curve in the highlighted panel.

B

Appendix to Chapter 6

B.1 Density of singly ionized carbon

The strength of the [CII] emission from any gas phase depends on the fraction of total carbon atoms that are singly ionized, f_{CII}. For calculating f_{CII}, we chose to employ the microphysics code `CLOUDY` v13.03, that simultaneously solves the equations for statistical and thermal equilibrium for a wide range of optional elements. We set up `CLOUDY` to work on a small parcel of gas with a single temperature and a constant density across its volume. The incident radiation field on the gas parcel is set to the local interstellar radiation field, as provided by `CLOUDY`, but scaled by a factor (in practice, our G_0). In addition, a cosmic ray ionization rate can be specified in units of s^{-1}.

As a test to judge whether we are using CLOUDY correctly, the fraction of CIV, f_{CIV}, as a function of density and temperature was compared to the work of Oppenheimer & Schaye (2013) by reproducing their CIV fractions at $z = 1$ for a Haardt & Madau (2001) background radiation field. This comparison is shown in Fig. B.1 with plots of the CIV abundance (rela-

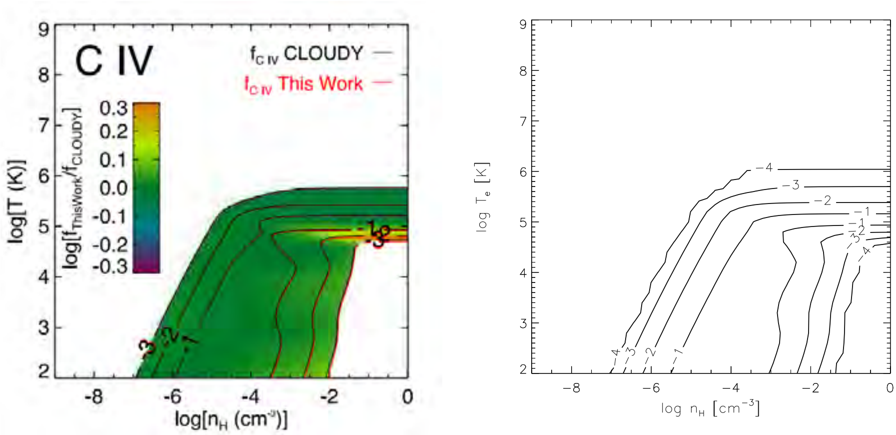

Figure B.1 A comparison of f_{CIV} as calculated by Oppenheimer & Schaye (2013) using `CLOUDY` v10.00 (left) and by `SÍGAME` using `CLOUDY` v13.03 (right). In both cases a Haardt & Madau 2005 background radiation field (embedded in `CLOUDY`) at $z = 1$ was used together with solar abundances. A good agreement is seen, in particular with decreasing f_{CIV} towards high densities and low temperatures, where carbon exists in lower ionizational states such as CII, see Fig. B.2 below.

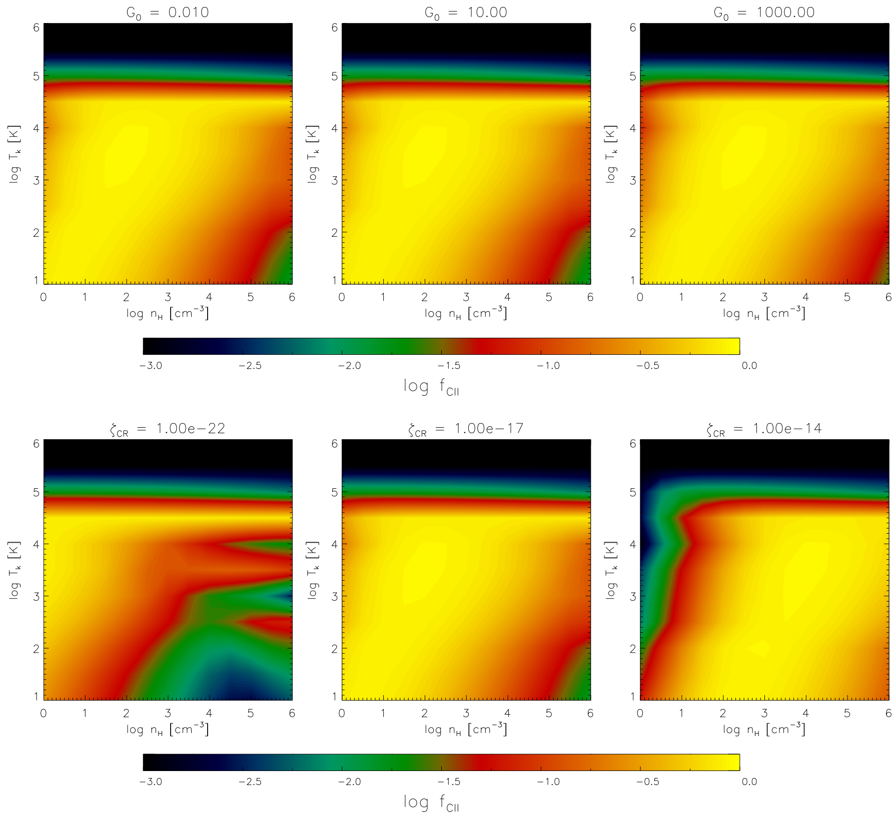

Figure B.2 Maps of f_{CII} as function of gas temperature and hydrogen density made with CLOUDY v13.03 as part of the grid used in SÍGAME to derive x_{e} and f_{CII} in the ISM. *Top row:* For three values of G_0 (and ζ_{CR} fixed at $10^{-17}\,\mathrm{s}^{-1}$). *Bottom row:* For three values of ζ_{CR} (with G_0 fixed to 1 Habing). Note how f_{CII} drops at $T_{\mathrm{k}} \gtrsim 10^5$ K in all cases, and depends on ζ_{CR} while being largely insensitive to changes in G_0.

tive to the total number of carbon atoms) as a function of hydrogen density and kinetic gas temperature. A good agreement with the figure of Oppenheimer & Schaye (2013) is achieved when using the build-in Haardt & Madau 2005 background of CLOUDY ('HM05' command in CLOUDY, including galaxies and quasars but not the CMB) at $z = 1$ together with default solar abundances.

In order to keep the computing time of SÍGAME low, we set up a grid in [n_{H}, T_{k}, ζ_{CR}, G_0] and calculated f_{CII} with CLOUDY for each grid point. Though metallicity and element abundances (of C, O, Si and Fe) are followed in our simulated galaxies, we chose the default solar composition that comes with CLOUDY for the sake of having fewer parameters in the grid. Visualizations of this grid are shown in Fig. B.2 for three values of G_0 (and ζ_{CR} fixed at $10^{-17}\,\mathrm{s}^{-1}$, close to the adopted $\zeta_{\mathrm{CR,MW}} = 10^{-17}\,\mathrm{s}^{-1}$) in the top row and three values of ζ_{CR} (with G_0 fixed to 1 Habing, close to $G_{0,\mathrm{MW}} = 0.6$ Habing) in the bottom row. As can be seen, f_{CII} does not seem to depend at all on G_0, but much more on the intensity of cosmic rays.

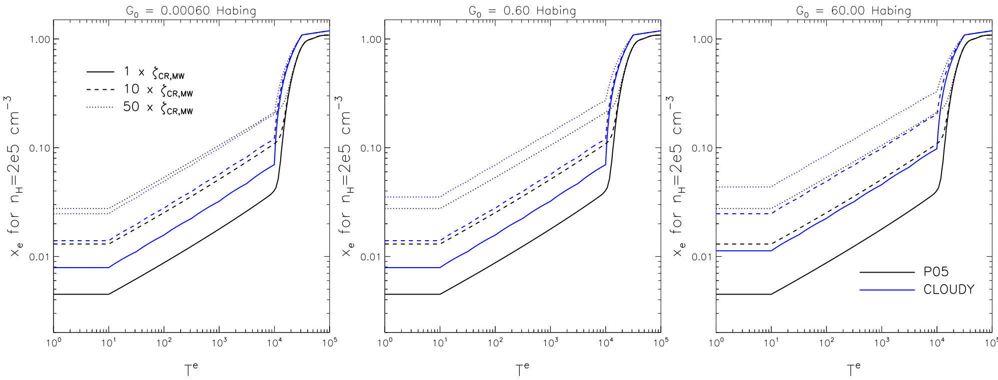

Figure B.3 A comparison of `CLOUDY` and the method described in Pelupessy (2005) for deriving x_e as a function of electron temperature, T^e, at a density of $n_\mathrm{H} = 2 \times 10^5\,\mathrm{cm}^{-3}$. The two methods agree about the shape of increasing x_e with T^e, including the sharp rise at $T_\mathrm{k} \sim 10^4\,\mathrm{K}$ due to Balmer lines. The P05 method does not include ionization by the FUV radiation field, meaning that it takes the same shape in each panel. Note that x_e rises above 1 due to the inclusion of other elements than hydrogen, that can contribute to the electron number.

B.2 Electron fraction

In order to be consistent with the calculation of f_CII, we also decided to calculate the electron fraction, x_e, with `CLOUDY` v13.03 rather than the method of Pelupessy (2005) (P05) used in the previous paper (Chapter 4). Fig. B.3 shows how `CLOUDY` and the P05 method compare as a function of electron temperature at a density of $n_\mathrm{H} = 2\times10^5\,\mathrm{cm}^{-3}$, for different combinations of interstellar radiation field (G_0) and cosmic ray ionization rate (ζ_CR). The P05 method is aimed for application in the interior of GMCs and therefore only considers ionization by cosmic rays that are expected to dominate the ionization of hydrogen, whereas `CLOUDY` takes G_0 and ζ_CR as separate variables.

Furthermore, P05 method does not depend on density, whereas the calculation with `CLOUDY` does. Fig. B.4 gives the same comparison as the previous figure, but for a lower density of $n_\mathrm{H} = 100\,\mathrm{cm}^{-3}$, where `CLOUDY` derives much larger electron fractions than the P05 model. This is expected, since at low densities, the gas is less shielded from the incident radiation field. We therefore consider the inclusion of the `CLOUDY`, with its sensitivity towards G_0 and n_H, an improvement to `SÍGAME` with respect to the electron fraction.

B.3 Heating and cooling rates of molecular and atomic gas inside GMCs

Table B.1 provides a quick look-up table for the methods and references behind the recipes adopted for the various heating and cooling mechanisms present inside our GMC models, as summarized in eqs. 6.19 - 6.21. All of these, except Λ_OI, Λ_CI and Λ_CII that will be described in this section and Appendix B.4, are the same as those used in Olsen et al. 2015, to which we refer for more details. For the heating mechanisms, we adopt the local dust-attenuated FUV field, $G_{0,\mathrm{att}}$ (as calculated in eq. 4.3 combined with eqs. 6.10 - 6.12) and the local cosmic ray ionization rate, ζ_CR, as calculated in eq. 6.13.

Λ_OI represents the cooling due to [OI] (63 μm+146 μm) line emission, for which we use the

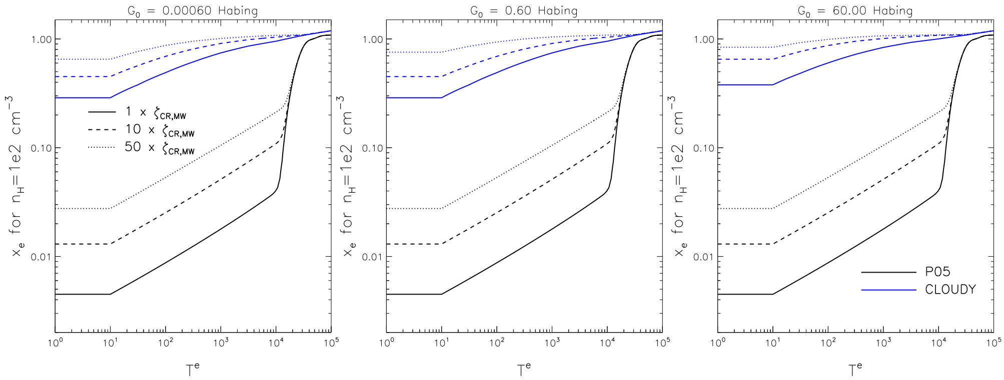

Figure B.4 Same as Fig. B.3, but for a density of $n_{\rm H} = 100\,{\rm cm}^{-3}$.

Cooling and heating rates in GMC models

Process		Parameters	Reference
$\Gamma_{\rm PE}$	Photo-electric heating	$G_{0,\rm att}$, $T_{\rm k}$, $n_{\rm e}$, $n_{\rm H}$	Bakes & Tielens (1994)
$\Gamma_{\rm CR,HI}$	Cosmic ray heating in atomic gas	$\zeta_{\rm CR}$, $n_{\rm HI}$, $x_{\rm e}$	Draine (2011)
$\Gamma_{\rm CR,H_2}$	Cosmic ray heating in molecular gas	$\zeta_{\rm CR}$, $n_{\rm H_2}$	Stahler & Palla (2005)
$\Lambda_{\rm H_2}$	H2 line cooling	$n_{\rm H_2}$, $T_{\rm k}$	Papadopoulos et al. (2014)
$\Lambda_{\rm CI}$	CI line cooling	$n_{\rm e}$, $T_{\rm k}$	Raga et al. (1997)
$\Lambda_{\rm OI}$	OI line cooling	$n_{\rm H}$, $T_{\rm k}$	Röllig et al. (2006)
$\Lambda_{\rm gas-dust}$	gas-dust interaction cooling	$n_{\rm H}$, $T_{\rm k}$	Papadopoulos et al. (2011)
$\Lambda_{\rm CII}$	[CII] line cooling in ionised gas	$n_{\rm H}$, $T_{\rm k}$, $X_{\rm C}$, G_0, σ_v	see Appendix B.4

Table B.1

parametrization of Röllig et al. (2006) who investigate the density range from 10^3 to $10^6\,{\rm cm}^{-3}$:

$$\Lambda_{\rm OI} = \Lambda_{63\,\mu m} + \Lambda_{146\,\mu m} \tag{B.1}$$

where

$$\Lambda_{63\,\mu m} = 3.15\times10^{-14} 8.46\times10^{-5}\frac{1}{2}X_O$$
$$\times \frac{n\exp(98\,{\rm K}/T_{\rm k})\,3\,n\left(n+\frac{1}{2}\frac{1.66\times10^{-5}}{1.35\times10^{-11}T_{\rm k}^{0.45}}\right)}{n^2+\exp(98\,{\rm K}/T_{\rm k})\left(n+\frac{1}{2}\frac{1.66\times10^{-5}}{1.35\times10^{-11}T_{\rm k}^{0.45}}\right)\left(3\,n+\exp(228\,K/T_{\rm k})5\left(n+\frac{1}{2}\frac{8.46\times10^{-5}}{4.37\times10^{-12}T_{\rm k}^{0.66}}\right)\right)}\ {\rm ergs\,cm^{-3}\,s^{-1}}$$
$$\Lambda_{146\,\mu m} = 1.35\times10^{-14} 1.66\times10^{-5}\frac{1}{2}X_O$$
$$\times \frac{3\times10^{-4}\,n\,n^2}{n^2+\exp(98\,{\rm K}/T_{\rm k})\left(n+\frac{1}{2}\frac{1.66\times10^{-5}}{1.35\times10^{-11}T_{\rm k}^{0.45}}\right)\left(3\,n+\exp(228\,{\rm K}/T_{\rm k})5\left(n+\frac{1}{2}\frac{8.46\times10^{-5}}{4.37\times10^{-12}T_{\rm k}^{0.66}}\right)\right)}\ {\rm ergs\,cm^{-3}\,s^{-1}}$$

Röllig et al. (2006) assume the relative oxygen abundance to scale with Z' as $X_O = 3\times10^{-4}\times Z$, whereas we have replaced it by its actual value from the simulation (mass fractions of oxygen are shown in histograms in Appendix B.5).

$\Lambda_{\rm CI}$ is cooling due to CI line emission, for which we use the tables of CI cooling rate of Raga et al. (1997) for temperatures in the range $100 < T_{\rm k} < 10^6$ K and electron densities of $1 < n_{\rm e} < 10^6\,{\rm cm}^{-3}$. At $T_{\rm k} < 100$ K, we fix the CI line cooling rate to its value at $T_{\rm k} = 100$ K, but this choice is not important, as cooling from H_2, [CII] and gas-dust interactions are expected to dominate here.

Finally, for the [CII] line cooling ($\Lambda_{\rm CII}$), we use the same formula as those applied to derive the [CII] luminosity and to be described in Appendix B.4.

B.3.1 A NOTE ON DUST TEMPERATURE

The dust temperature, $T_{\rm dust}$, used for cooling by gas-dust interactions at $R_{\rm CI}$ (see eq. 6.19) is set by the equilibrium between absorption of FUV and the emission of IR radiation by the dust grains. We adopt the approximation given by Tielens (2005):

$$T_{\rm dust} \simeq 33.5 \left(\frac{1\mu{\rm m}}{a}\right)^{0.2} \left(\frac{G_{0,\rm att}}{10^4}\right)^{0.2} {\rm K} \tag{B.2}$$

where $G_{0,\rm att}$ is the dust-attenuated FUV field (eq. 6.12) and a is the grain size, which we set to $1\,\mu$m for simplicity. Values for $T_{\rm dust}$ using the above equation range from 0 to 14.3 K, but we enforce a lower limit on $T_{\rm dust}$ equal to the $z = 2$ CMB temperature of 8.175 K.

B.4 THE [CII] COOLING RATE IN GAS OF DIFFERENT CONDITIONS

In the case that the gas in cuestion is not optically thin to the [CII] line frequency, we estimate the optical depth as it would be in a homogeneous static slab of gas of thickness ΔR (Draine, 2011):

$$\tau_0 = \frac{g_u}{g_l} \frac{A_{ul}\lambda^3_{\rm CII}}{4(2\pi)^{3/2}\sigma_v} n_l \Delta R \left(1 - \frac{n_u g_l}{n_l g_u}\right) \tag{B.3}$$

where A_{ul} is the rate of spontaneous emission of $2.3 \times 10^{-6}\,{\rm s}^{-1}$ for [CII][1], $\lambda_{\rm CII}$ is $157.74\,\mu$m and the fraction of statistical weights is $g \equiv g_u/g_l = 4/2 = 2$ for [CII]. In the diffuse gas regions, the velocity dispersion, σ_v, is calculated according to the local velocity dispersion in the SPH simulation, while inside the GMCs, we use σ_v as calculated in eq. 6.9. For the ratio of C^+ density in the upper $^2P_{3/2}$ level to that in the lower level, we use the formalism of Goldsmith et al. (2012):

$$\frac{n_u}{n_l} = \frac{B_{lu}U + C_{lu}}{A_{ul} + B_{ul}U + C_{ul}} = \frac{gB_{ul}U + gKC_{ul}}{A_{ul} + B_{ul}U + C_{ul}} \tag{B.4}$$

where we have invoked balance between the stimulated emission and absorption rates; $B_{lu}U = gB_{ul}U$, and the temperature dependence on the collision rate balance: $C_{lu} = gC_{ul}e^{-91.25\,{\rm K}/T_{\rm k}}$, defining $K \equiv e^{-91.25\,{\rm K}/T_{\rm k}}$. We can use the above equation to write down an expression for the

[1]Einstein coefficient for spontaneous emission taken from the LAMDA database: `http://www.strw.leidenuniv.nl/~moldata/`, Schöier et al. (2005)

fraction of C^+ in the upper level, f_u:

$$
\begin{aligned}
f_u &= \frac{n_u}{n_l + n_u} = \frac{1}{\frac{n_l}{n_u} + 1} \\
&= \frac{gB_{ul}U + gKC_{ul}}{A_{ul} + (1+g)B_{ul}U + C_{ul} + gKC_{ul}} \\
&= \frac{gK + gB_{ul}/C_{ul}U}{1 + gK + A_{ul}/C_{ul} + (1+g)B_{ul}U/C_{ul}}
\end{aligned}
\tag{B.5}
$$

The downward stimulated rate, $B_{ul}U$, can be written in terms of excitation temperature, T^{ex}, and background temperature, T^{bg}:

$$
B_{ul}U = \frac{(1-\beta)A_{ul}}{e^{-91.25\,\mathrm{K}/T^{\mathrm{ex}}} - 1} + \frac{\beta A_{ul}}{e^{-91.25\,\mathrm{K}/T^{\mathrm{bg}}} - 1} \tag{B.6}
$$

where the excitation temperature is related to the kinetic temperature via:

$$
e^{-91.25\,\mathrm{K}/T^{\mathrm{ex}}} = K\left[\frac{\frac{C_{ul}}{\beta A_{ul}} + 1 + G}{\frac{C_{ul}}{\beta A_{ul}} + GK}\right] \approx K\left(1 + \frac{\beta A_{ul}}{C_{ul}}\right) \tag{B.7}
$$

where we ignore any background (CMB) radiation field, hence setting the background term $G = \frac{1}{T^*/T^{\mathrm{bg}}-1}$ to 0. We expect that the ionized gas is diffuse and therefore close to being optically thin ($\beta = 1$), but inside GMCs this might not be true. However, as a first approximation, we ignore any background (CMB) radiation ($B_{ul}U = 0$) and set $\beta = 1$, simplifying the expression for f_u to:

$$
f_u = \frac{gK}{1 + gK + A_{ul}/C_{ul}} \tag{B.8}
$$

With this first estimate of f_u, we derive an optical depth via eq. B.3 and calculate β by adopting the LVG model for a spherical cloud with radial velocity gradient proportional to radius, so that $\beta = (1 - e^{-\tau_0})/\tau_0$. In order to account for a considerable optical depth, we go on to iteratively solve for consistent values for f_u and β. For that, we use the complete formula for f_u in eq. B.5 and calculate the downward stimulated rate as:

$$
B_{ul}U(T^{\mathrm{bg}} \to 0) = \frac{(1-\beta)A_{ul}}{e^{-91.25\,\mathrm{K}/T^{\mathrm{ex}}} - 1} \tag{B.9}
$$

The collisional deexcitation rate, C_{ul}, is calculated as a sum of contributions from collisions with electrons, hydrogen atoms and H_2 molecules as shown in eq. 6.24.

For the deexcitation collision rate with electrons, $C_{ul}(e^-)$, we will use a rate applicable to temperatures from $\simeq 100\,\mathrm{K}$ to 20,000 K, as presented by Goldsmith et al. (2012):

$$
C_{ul}(e^-) = n_{\mathrm{e}} 8.7 \times 10^{-8} (T^e/2000)^{-0.37}\,\mathrm{cm^{-3}\,s^{-1}} \tag{B.10}
$$

where electron density is calculated with a code kindly provided by I. Pelupessy, and the electron temperature assumed equal to the gas temperature, T_{k}. At $T_{\mathrm{k}} > 20{,}000\,\mathrm{K}$, we make $C_{ul}(e^-)$ drop as $(T^e)^{-0.85}$, motivated by the effective collision strength, υ_{ul}, calculated by Wilson & Bell (2002) up to $T^e = 10^{5.5}\,\mathrm{K}$, and its relation to R_{ul}: $R_{ul} \propto \upsilon_{ul}/\sqrt{T^e}$ (Langer et al., 2015).

The deexcitation rate coefficient with atomic hydrogen is found by interpolation of the values calculated by Keenan et al. (1986) for T^e from 1 to 10^5 K.

For collisions with molecular hydrogen, we adopt the deexcitation rate coefficient presented in Goldsmith et al. (2012):

$$C_{ul}(\mathrm{H}_2) = n_{\mathrm{H}_2} 3.8 \times 10^{-10} (T_\mathrm{k}/100)^{0.14}\,\mathrm{cm}^{-3}\,\mathrm{s}^{-1} \tag{B.11}$$

Once consistent values for f_u and τ have been achieved, we calculate the total cooling rate according to eq. 6.23. This cooling rate is used to determine the thermal balance at various points within the GMCs as well as the [CII] emission from the various ISM phases as described in Section 6.5.1.

B.5 SPH properties relevant for the [CII] emission

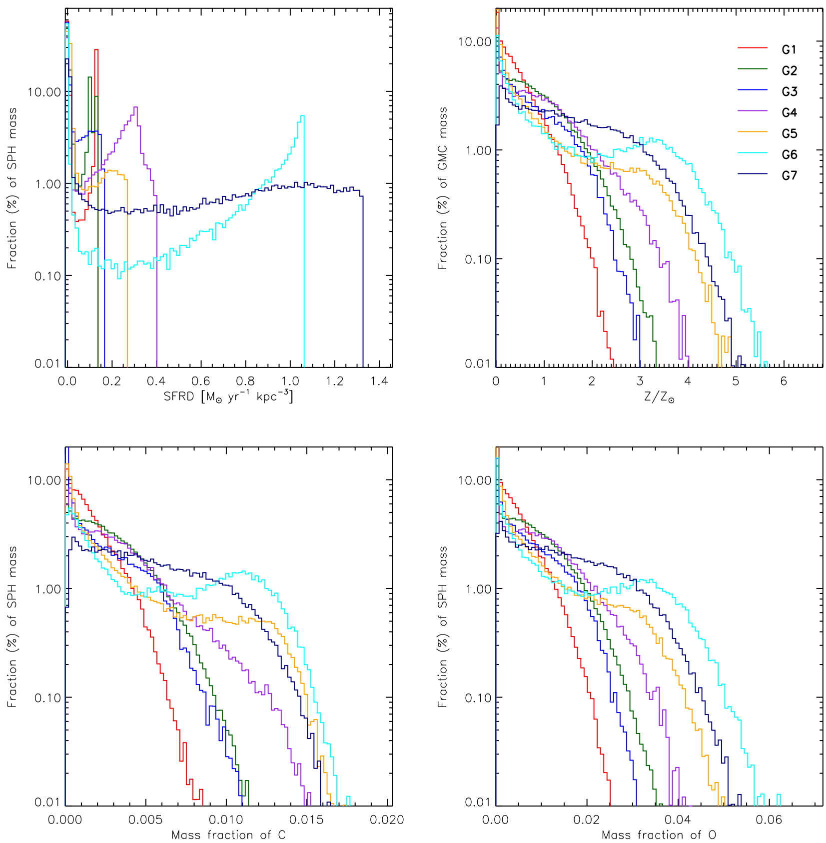

Figure B.5 Mass-weighted (by SPH mass) histograms of SPH gas properties in the simulations of our set of seven model galaxies at $z = 2$.

B.6 References

Bakes, E. L. O., & Tielens, A. G. G. M. 1994, ApJ, 427, 822

Draine, B. T. 2011, Physics of the Interstellar and Intergalactic Medium (Princeton University Press)

Goldsmith, P. F., Langer, W. D., Pineda, J. L., & Velusamy, T. 2012, ApJS, 203, 13

Haardt, F., & Madau, P. 2001, in Clusters of Galaxies and the High Redshift Universe Observed in X-rays, ed. D. M. Neumann & J. T. V. Tran

Keenan, F. P., Lennon, D. J., Johnson, C. T., & Kingston, A. E. 1986, MNRAS, 220, 571

Langer, W. D., Goldsmith, P. F., Pineda, J. L., et al. 2015, ArXiv e-prints

Oppenheimer, B. D., & Schaye, J. 2013, MNRAS, 434, 1043

Papadopoulos, P. P., & Thi, W.-F. 2013, in Advances in Solid State Physics, Vol. 34, Cosmic Rays in Star-Forming Environments, ed. D. F. Torres & O. Reimer, 41

Papadopoulos, P. P., Thi, W.-F., Miniati, F., & Viti, S. 2011, MNRAS, 414, 1705

Papadopoulos, P. P., Zhang, Z.-Y., Xilouris, E. M., et al. 2014, ApJ, 788, 153

Pelupessy, F. I. 2005, PhD thesis, Leiden Observatory, Leiden University, P.O. Box 9513, 2300 RA Leiden, The Netherlands

Puchwein, E., Bolton, J. S., Haehnelt, M. G., Madau, P., & Becker, G. D. 2014, ArXiv e-prints

Raga, A. C., Mellema, G., & Lundqvist, P. 1997, ApJS, 109, 517

Röllig, M., Ossenkopf, V., Jeyakumar, S., Stutzki, J., & Sternberg, A. 2006, A&A, 451, 917

Schöier, F. L., van der Tak, F. F. S., van Dishoeck, E. F., & Black, J. H. 2005, A&A, 432, 369

Stahler, S. W., & Palla, F. 2005, The Formation of Stars (Wiley)

Tielens, A. G. G. M. 2005, The Physics and Chemistry of the Interstellar Medium (Cambridge University Press)

Wiersma, R. P. C., Schaye, J., & Smith, B. D. 2009, MNRAS, 393, 99

Wilson, N. J., & Bell, K. L. 2002, MNRAS, 337, 1027